Title

Adventures in 3D Electron Crystallography

Author

Saha, Ambarneil

Publication Date

2023

UNIVERSITY OF CALIFORNIA

Los Angeles

Adventures in 3D Electron Crystallography

A dissertation submitted in partial satisfaction
of the requirements for the degree
Doctor of Philosophy in Chemistry

by

Ambarneil Saha

2023

ABSTRACT OF THE DISSERTATION

Adventures in 3D Electron Crystallography

by

Ambarneil Saha
Doctor of Philosophy in Chemistry
University of California, Los Angeles, 2023
Professor José A. Rodríguez, Co-Chair
Professor David S. Eisenberg, Co-Chair

This dissertation describes a set of experiments loosely unified under the general theme of 3D electron crystallography.

Chapter 1 provides a comprehensive overview of the scientific literature in the field, with particular emphasis on experiments aimed at using electron diffraction to elucidate the atomic structure of three-dimensional molecular crystals.

Chapter 2 focuses on the development of a publicly accessible web server, FAES (Factors of Atomic Electron Scattering, `http://srv.mbi.ucla.edu/faes`), containing a database of electron scattering factors parameterized into Gaussian approximations compatible with widely used least-squares refinement programs. These include all neutral and ionic species tabulated in the *International Tables for Crystallography*, as well as fractionally charged scattering factors calculated by computing linearly weighted sums of adjacent integral neighbors. FAES provides numerical fitting coefficients, statistical goodness-of-fit values, and elastic and estimated inelastic cross-sections at a range of accelerating voltages relevant to transmission electron microscopy.

Chapter 3 details rigorous studies involving the mapping of electron beam-induced radiolytic damage in molecular crystals using 4D scanning transmission electron microscopy (4D–STEM), conducted on a variety of organic and organometallic species spanning a wide gamut of chemical

space. By acquiring a series of consecutive 4D–STEM scans on the same crystal, we explicitly visualize the spatial evolution of coherently diffracting zones (CDZs) as a function of accumulating electron fluence, providing a detailed, time-resolved map of the internal lattice reorientation induced by radiolysis. These experiments also unveil the resolution-dependent propagation of tides of amorphization from impact craters created by asymmetric, localized delivery of incident electrons.

Chapter 4 relates the development of the 4D-STEM method nanobeam electron diffraction tomography into a technique capable of overcoming obstacles that thwart structural elucidation by conventional microcrystal electron diffraction (microED). 4D–STEM's unique ability to pinpoint a specific nanoscale volume for data analysis enables pixel-by-pixel spatial exclusion of unwanted signal from disordered or Bragg-silent regions, empowering us to simply pick and choose whichever CDZs generate the highest-quality diffraction patterns. These experiments represent the first 4D–STEM structures phased *ab initio* by direct methods.

The dissertation of Ambarneil Saha is approved.

Brian C. Regan

Todd O. Yeates

David S. Eisenberg, Committee Co-Chair

José A. Rodríguez, Committee Co-Chair

University of California, Los Angeles

2023

TABLE OF CONTENTS

LIST OF FIGURES

LIST OF TABLES

ACKNOWLEDGMENTS

I'd like to thank everyone who made a positive contribution to my journey as a scientist. First off, my advisor, José Rodríguez, who always entrusted me with the intellectual freedom to pursue essentially whatever scientific problem piqued my interest. If not for your timely intervention during a fragile period when I was feeling profoundly disillusioned with academia—i.e., the Kafkaesque TEMPO–N_3 episode of my first year—I would probably have abandoned science for good back in 2019. It took me a minute to tune my irony detector to your idiosyncratic frequency, but you're actually pretty funny, too. Sometimes.

Next up, my thesis committee: David Eisenberg, Todd Yeates, and Chris Regan. David, I remain awed by the breadth of your historical knowledge. Thanks for patiently listening to months of circuitous rants over Zoom during those COVID-era book club meetings, even when I decided to subject everyone to a vaguely Marxist reading of Ishiguro. Todd, I probably owe my understanding of space-group symmetry—as well as my ever-increasing familiarity with M. C. Escher's oeuvre—entirely to three consecutive years of your lectures in M230. I credit one particular post-M230 discussion we had during my first year (about energetic preferences for specific space groups) with strongly catalyzing my then-nascent interest in crystallography. Chris, my Ph.D. took an early detour into what I perceived as foreign physics territory, and your TEM course was instrumental in helping me navigate initially unfamiliar waters (in addition to fostering my growing skepticism toward $\hbar$). One day, I hope to emulate your ability to serenely yet productively break it to me that my newest idea was crazy.

Crystallography is sometimes castigated as an unwelcoming discipline—a minefield strewn with inscrutable black boxes, jealously patrolled by irascible gatekeepers. In that context, I've been lucky to learn from two remarkably selfless crystallographers, Michael Sawaya and Duilio Cascio. Mikey, I'd wager that any crystallographic query has an answer tucked away in a dusty corner of the DOE Institute's Library of Babel: `/home/sawaya/misc`. Your willingness to immediately share any of the myriad scripts you've painstakingly developed over the years is deeply inspirational to me. Duilio, thanks for all the stimulating political discourse. I trace my first steps in crystallography back to those action-packed early days in your office, where you whizzed through indexing and integration at breakneck speed while simultaneously formulating vulgar passwords and hatching secret plans to send verboten crystals to the synchrotron. Good times. I remain convinced that your *de facto* title as the crown emperor of endless tangents is beyond dispute.

Electron microscopy is another field somewhat notorious for dauntingly high barriers to entry. Thankfully, my practical understanding of TEM grew exponentially after working closely with Matthew Mecklenburg and Peter Ercius. In retrospect, it's mortifying just how little I knew about operating a TEM before Matt and Peter took me to school! Matt, you were instrumental in transforming the previously moribund dungeons of CNSI into a vibrant place to do science. Although I cannot reconcile your abject terror of innocuous organic compounds with your nonchalance around literal asbestos, I hope I managed to at least marginally alleviate your chemophobia. In your own unique, indefatigable way, you have somehow patiently and methodically answered every single question I've ever asked you—on any topic—for which you have earned my undying gratitude. Peter, thanks for letting me run amok on a multimillion-dollar instrument and pump what must at this point be several nanoamps into the central pixels of the poor 4DCamera. I'm very excited by the prospect that our body of work together is just beginning!

I've had the immense privilege of knowing almost every member of the Rodríguez group, past and present, all of whom contributed to making the lab a wonderful place to do science. I'd especially like to give a shoutout to my labmates María Flores, Logan Richards, Niko Vlahakis, and Shervin Nia—formidable scientists and great friends. Thanks for everything, guys. I sincerely hope the legendary repartee in our respective Slack group chats at 11 AM on Thursdays was genuinely private. I'm also deeply indebted to Madeline Evans and Thomas Holton, without whom the FAES web server—one of my proudest achievements in graduate school—would never have existed.

Although I've meandered a long way from synthetic organic chemistry, I've never forgotten my scientific roots. I'm grateful to my undergraduate advisor, Song Lin, who welcomed me into his laboratory as one of its founding members and taught me a tremendous amount about experimental rigor. I also couldn't have asked for better mentors than Niankai Fu, Keith Carpenter, and Juno Siu, all of whom played a pivotal role in my early development and convinced me that being in the lab was actually a lot of fun. Although the synthetic skills you guys taught me have laid dormant for quite some time, I now see a return to the fume hood looming in the near future... Yikes.

Reaching into the distant past, I'd be remiss not to thank my high school debate coach, Doug Dennis, for forging my battle-tested argumentative skills in the unforgiving crucible of innumerable practice rounds. I owe you, Mr. D. Although I argue about different subjects nowadays, you made arguing with people easy.

Finally, my most profound thanks go to my parents, Arindam and Suranjana Saha—simultaneously my most trenchant critics and my most ardent supporters. They came to a foreign country with $750 in their pockets and worked tirelessly to build a solid middle-class life. Their sacrifices empowered me to blaze my own anfractuous trail. Without their support, none of this would have been possible. I dedicate this work, obviously, to them.

VITA

2016	Harold Tanner Dean's List, College of Arts and Sciences, Cornell University
2016	Teaching Assistant at Five Points Correctional Facility, Department of Government, Cornell Prison Education Program
2017	American Chemical Society Summer Undergraduate Research Fellowship
2014–2018	A.B. in Chemistry, Cornell University
2018	National Science Foundation Graduate Research Fellowship
2018	Excellence in Chemistry Fellowship, UCLA
2018–2019	Teaching Assistant, Department of Chemistry and Biochemistry, UCLA
2020	Michael E. Jung Award for Excellence in Teaching, Department of Chemistry and Biochemistry, UCLA
2020	Poster Prize, Southern California CryoEM Symposium
2021–2022	Teaching Assistant, Department of Chemistry and Biochemistry, UCLA
2022	National Science Foundation BioPACIFIC Materials Innovation Platform Fellowship
2022	Herman R. Branson Poster Prize, American Crystallographic Association

PUBLICATIONS

A. Saha, S. S. Nia, and J. A. Rodríguez, Electron diffraction of 3D molecular crystals. *Chem. Rev.* **122**, 13883–13914 (2022). <DOI: 10.1021/acs.chemrev.1c00879>

H. M. Nelson, J. C. Siu, **A. Saha**, D. Cascio, S. N. MacMillan, S.-B. Wu, C. Lu, J. A. Rodríguez, K. N. Houk, and S. Lin, Isolation and X-ray crystal structure of an electrogenerated TEMPO–N_3 charge-transfer complex. *Org. Lett.* **23**, 454–458 (2021). <DOI: 10.1021/acs.orglett.0c03966>

C.-T. Zee, **A. Saha**, M. R. Sawaya, and J. A. Rodríguez, *Ab initio* determination of peptide structures by MicroED. In *Methods in Molecular Biology*, Chap. 17, pp. 329–348, T. Gonen and B. L. Nannenga, Eds. (Springer, New York, 2021). <DOI: 10.1007/978-1-0716-0966-8_17>

C. G. Jones, M. Asay, L. Kim, J. F. Kleinsasser, **A. Saha**, T. J. Fulton, K. R. Berkley, D. Cascio, A. G. Malyutin, M. P. Conley, B. M. Stoltz, V. Lavallo, J. A. Rodríguez, and H. M. Nelson, Characterization of reactive organometallic species *via* MicroED. *ACS Cent. Sci.* **5**, 1507–1513 (2019). <DOI: 10.1021/acscentsci.9b00403>

J. C. Siu, G. S. Sauer, **A. Saha**, R. L. Macey, N. Fu, T. Chauviré, K. M. Lancaster, and S. Lin, Electrochemical azidooxygenation of alkenes mediated by a TEMPO–N_3 charge-transfer complex. *J. Am. Chem. Soc.* **140**, 12511–12520 (2018). <DOI: 10.1021/jacs.8b06744>

N. Fu, G. S. Sauer, **A. Saha**, A. Loo, and S. Lin, Metal-catalyzed electrochemical diazidation of alkenes. *Science* **357**, 575–579 (2017). <DOI:10.1126/science.aan6206>

CHAPTER 1

Electron Diffraction of 3D Molecular Crystals: An Overview

This chapter contains material adapted from Saha, A.; Nia, S. S.; Rodríguez, J. A. Electron diffraction of 3D molecular crystals. *Chem. Rev.* **2022**, *122*, 13883—13914. `<DOI: 10.1021/acs.chemrev.1c00879>`

1.1 Abstract

Electron crystallography has a storied history which rivals that of its more established X-ray-enabled counterpart. Recent advances in data collection and analysis have sparked a renaissance in the field, opening a new chapter for this venerable technique. Burgeoning interest in electron crystallography has spawned innovative methods described by various interchangeable labels (3D ED, MicroED, cRED, etc.). This introductory chapter covers concepts and findings relevant to the practicing crystallographer, with an emphasis on experiments aimed at using electron diffraction to elucidate the atomic structure of three-dimensional molecular crystals.

1.2 Introduction and Historical Background

In 1927, Davisson and Germer conducted one of the most consequential experiments of the twentieth century [1, 2, 3]. Using a heated tungsten filament as a thermionic gun, they fired a collimated beam of slow-moving electrons (accelerated by a potential of 60 volts) at a polished chunk of crystalline nickel. As a makeshift detector, they installed a galvanometer enclosed within a Faraday box capable of rotating along a 135-degree arc. To their astonishment, Davisson and Germer observed that the reflected electrons displayed a discrete distribution of scattering angles, precisely analogous to diffraction of X-ray photons. Invoking Bragg's law, Davisson and Germer then found very good agreement between their putative electron wavelength and the theoretical value predicted by the de Broglie relation $\lambda = \frac{h}{mv}$, which de Broglie had proposed only three years earlier [4]. Their discovery—widely recognized as the first demonstration of electron diffraction (ED)—provided powerful experimental evidence that electrons conformed to wave-particle duality, an idea still nascent at the time. Several months later, Davisson and Germer's results were echoed by Thomson and Reid, who bombarded a thin film of polycrystalline celluloid using a beam of higher-energy electrons propagated through a greater potential drop (in the vicinity of 13 kilovolts) [5]. On a photographic plate, Thomson and Reid observed a series of concentric rings evocative of X-ray powder diffraction. In subsequent studies, Thomson went on to disclose similar ring-like patterns formed upon irradiation of metallic films composed of polycrystalline platinum, aluminum, and gold [6, 7]. Thomson's calculations, just like Davisson and Germer's, showed excellent agreement between the theoretical de Broglie wavelength and the experimental electron wavelength back-calculated from Bragg's law. Naturally, he concluded that such diffraction patterns could only have originated if the scattered electrons had behaved as waves. Merely a decade after the publication of these seminal papers, Davisson and Thomson received the 1937 Nobel Prize in Physics for "their experimental discovery of the diffraction of electrons by crystals." Their pioneering work created the field of electron crystallography.

Davisson and Thomson's results prompted a flurry of activity during the interwar period. In 1933, Laschkarew and Usyskin disclosed a painstaking electron-diffraction analysis of Debye lines generated by polycrystalline ammonium chloride (NH_4Cl), through which they managed to estimate the N—H covalent bond length with remarkable accuracy (0.95 $\pm$ 0.07 Å) [8]. Although very sporadically cited, Laschkarew and Usyskin's work represents the first (albeit indirect) detection and localization of hydrogen atoms by electron diffraction, a feat which was subsequently reinvestigated many times in later decades [9, 10, 11]. This early report explicitly underscored a key distinction between ED and conventional X-ray diffraction, where observation of H atoms is comparatively more difficult. Three years later, Rigamonti conducted an ED study of several straight-chain *n*-alkane crystals [12]. Intriguingly, Rigamonti's work paired quantitative experimental intensities alongside theoretical structure-factor amplitudes, foreshadowing later attempts at reconstruction by Fourier synthesis. Subsequently, Charlesby *et al.* carried out a detailed single-crystal investigation of anthracene, complete with photocopied electron diffraction patterns meticulously indexed by hand [13]. Their results largely confirmed unit cell vectors and angles previously measured by X-ray diffraction, providing a compelling validation of ED as a capable standalone method for crystallographic analysis. Taken in tandem, these three reports paint a portrait of early electron crystallography as a vibrant field of study already producing impactful discoveries only a few short years after its birth in 1927.

In the postwar years, however, progress in the field began to decelerate considerably. Electron diffraction never quite came into its own as a widely used means of structure determination. Instead, it was rapidly eclipsed by single-crystal X-ray diffraction, which by the mid-twentieth century had become well-established as the gold standard for crystallographic analysis. This remarkable shift in trajectory—which initially appears perplexing given the impressive heights scaled by ED in the 1930s—was spurred by increasingly strident fears over multiple scattering, a physical phenomenon intrinsic to ED [14]. These concerns were buttressed by historical constraints (such as low operating voltages) which amplified the probability of observing multiple scattering artifacts, ultimately inhibiting ED's development as an independent experimental technique. For decades, ED was relegated to a niche method championed mostly by Vainshtein and co-workers in the Soviet Union, who developed a specialized electron diffractometer capable of collecting so-called texture patterns from 3D crystallites. An excellent summary of their work is available in Vainshtein's 1964 monograph *Structure Analysis by Electron Diffraction*, which details >30 3D structures—ranging from inorganic salts to organic small molecules—methodically solved by electron diffraction [15]. Nevertheless, it was not until Dorset's retroactive validation of Vainshtein's work in the 1990s that the stigma surrounding multiple scattering began to dissipate [16]. ED then experienced a belated resurgence in activity in the mid-2010s, driven by methodological and hardware-based advances which enabled collection of diffraction patterns minimizing the deleterious influence of multiple scattering [17]. Nearly a century after Davisson and Germer, electron diffraction now appears poised to reclaim its mantle as one of the most promising techniques for structure elucidation of 3D molecular crystals.

1.3 Theoretical Foundations

1.3.1 Differences Between X-ray and Electron Scattering

In real space, X-ray photons scatter solely off the periodic charge density distribution $\rho(\vec{r})$, which emanates from the electron clouds encapsulating atoms within the crystal lattice. In chemistry parlance, $\rho(\vec{r})$ is often referred to simply as "electron density." Following Fourier synthesis, X-ray diffraction (XRD) ultimately recapitulates a real-space map of $\rho(\vec{r})$. As uncharged, massless quanta, however, incident X-rays interact with matter quite weakly. Practically, in a routine XRD experiment conducted on an in-house diffractometer, a macroscopic crystal at least 10^5 μm^3 in volume is desired to generate enough signal for structure determination. High-flux microfocus beamlines at third-generation synchrotron facilities can push this lower-size threshold down to 10^3 μm^3; these highly brilliant X-ray sources have enabled viable diffraction from crystals with dimensions as small as 1-10 μm on one side [18]. Below this 1 μm limit, crystals quickly become smaller than the wavelength of visible light, rendering them invisible to optical microscopy. At this submicrometric scale, only the exceptionally intense pulses produced by X-ray free-electron lasers (XFELs) can extract diffraction from slurries of submicron-sized crystals [19]. Nevertheless, XFELs currently do not present a widely accessible or convenient means for routine structure elucidation.

In this context, electron diffraction, typically conducted in a transmission electron microscope (TEM), provides a powerful alternative which empowers us to interrogate nanocrystals inaccessible to conventional XRD. Disparities in intrinsic physical properties cause X-rays and electrons to interact with atoms differently. Due to their nonzero rest mass and inherent negative charge, incident electrons experience electrostatic attraction toward protons in atomic nuclei in addition to repulsion from $\rho(\vec{r})$. As a direct consequence of this remarkably strong Coulombic interaction, incident electrons can produce tractable diffraction from minuscule crystals many orders of magnitude smaller in volume ($10^{-2}\ \mu\text{m}^3$) than those needed for conventional XRD. Unlike X-ray scattering, elastic electron scattering is dictated by electrostatic potential (ESP), or $V(\vec{r})$. $V(\vec{r})$ amalgamates contributions from both $\rho(\vec{r})$ and nuclear charge density $\delta(\vec{r})$, which is usually expressed as a point charge weighted by atomic number. The key relation between atomic charge density and ESP is given by Poisson's equation:

$$\nabla^2 V(\vec{r}) = \frac{-e[Z\,\delta(\vec{r}) - \rho(\vec{r})]}{\epsilon_0}, \tag{1.1}$$

where ∇^2 is the Laplace operator, e is the elementary charge, Z is the atomic number, $\delta(\vec{r})$ is a Dirac delta function representing nuclear charge density, and ϵ_0 is the permittivity of free space [20].

A central pillar of crystallography is the notion that every diffraction pattern encodes critical information about the Fourier transform of the periodic real-space density distribution which produced it. In Fourier space, the atomic scattering factor or formfactor $f(s)$ describes the scattering amplitude of an isolated, stationary atom by an incident wave, where $s = \frac{\sin\theta}{\lambda}$. Formally, $f(s)$ is defined as the probability amplitude of the exit spherical wave relative to the incoming plane wave. Informally, $f(s)$ simply provides us with a way to quantify the scattering power of different atoms in reciprocal space. It follows that $f(s)$ is highly dependent on the identity of the impinging quanta. Mathematically, $f(s)$ is derived via Fourier transform of its corresponding real-space counterpart: $\rho(\vec{r})$ for X-rays and $V(\vec{r})$ for electrons. To convert between X-ray and electron scattering factors, we invoke the Mott-Bethe formula, which functionally provides a reciprocal-space equivalent to Poisson's equation:

$$f_e(s) = \frac{m_0 e^2}{8\pi^2\hbar^2}\left(\frac{Z - f_x(s)}{s^2}\right), \tag{1.2}$$

where m_0 is the electron rest mass, $\hbar$ is the reduced Planck constant, we denote X-ray scattering factors as $f_x(s)$ and electron scattering factors as $f_e(s)$, and $\frac{m_0 e^2}{8\pi^2\hbar^2} = 0.023924$ [21].

Inspection of these equations unveils several key distinctions between X-ray and electron scattering factors. Firstly, the Mott-Bethe formula indicates no simple, monotonic relationship between $f_x(s)$ and $f_e(s)$. Instead, we observe a nonlinear scaling factor of s^{-2}. Secondly, unlike their X-ray counterparts, electron scattering amplitudes do not always scale linearly with Z. $f_e(s)$ is directly proportional to atomic number only at high spatial frequencies, where electron scattering is dominated by Z-weighted nuclear charge density. At low spatial frequencies, electron scattering is influenced by repulsion from outer-shell valence electrons, which causes $f_x(s)$ and $f_e(s)$ to exhibit disparate behavior in the limit as $s \to 0$. For instance, following a shared inflection point at 0.16 Å^{-1} (3 Å), boron becomes a stronger electron scatterer than carbon, nitrogen, and oxygen at low resolution, despite its smaller atomic mass. This order is reversed at scattering angles corresponding to high resolution (Figure 1.1A). Conversely, all X-ray scattering factors obey the constraint

$$\lim_{s\to 0} f_x(s) = Z_0, \tag{1.3}$$

where Z_0 is the number of electrons associated with each atom. A straightforward consequence of this limit is that heavier atoms always scatter X-rays more strongly than lighter atoms, regardless of resolution (Figure 1.1B). Furthermore, X-ray scattering amplitudes for adjacent neutral elements never converge to a shared point (apart from collectively dwindling to zero as $s \to \infty$), whereas this behavior is permissible for electron scattering amplitudes. As a result, in electrostatic potential maps generated from ED data, certain elements become physically indistinguishable at specific scattering angles (Figure 1.1C). Broadly, relative differences between elements shrink in ED; at 0.2 Å^{-1} (2.5 Å), for example, iron scatters electrons merely 2.4× more strongly than

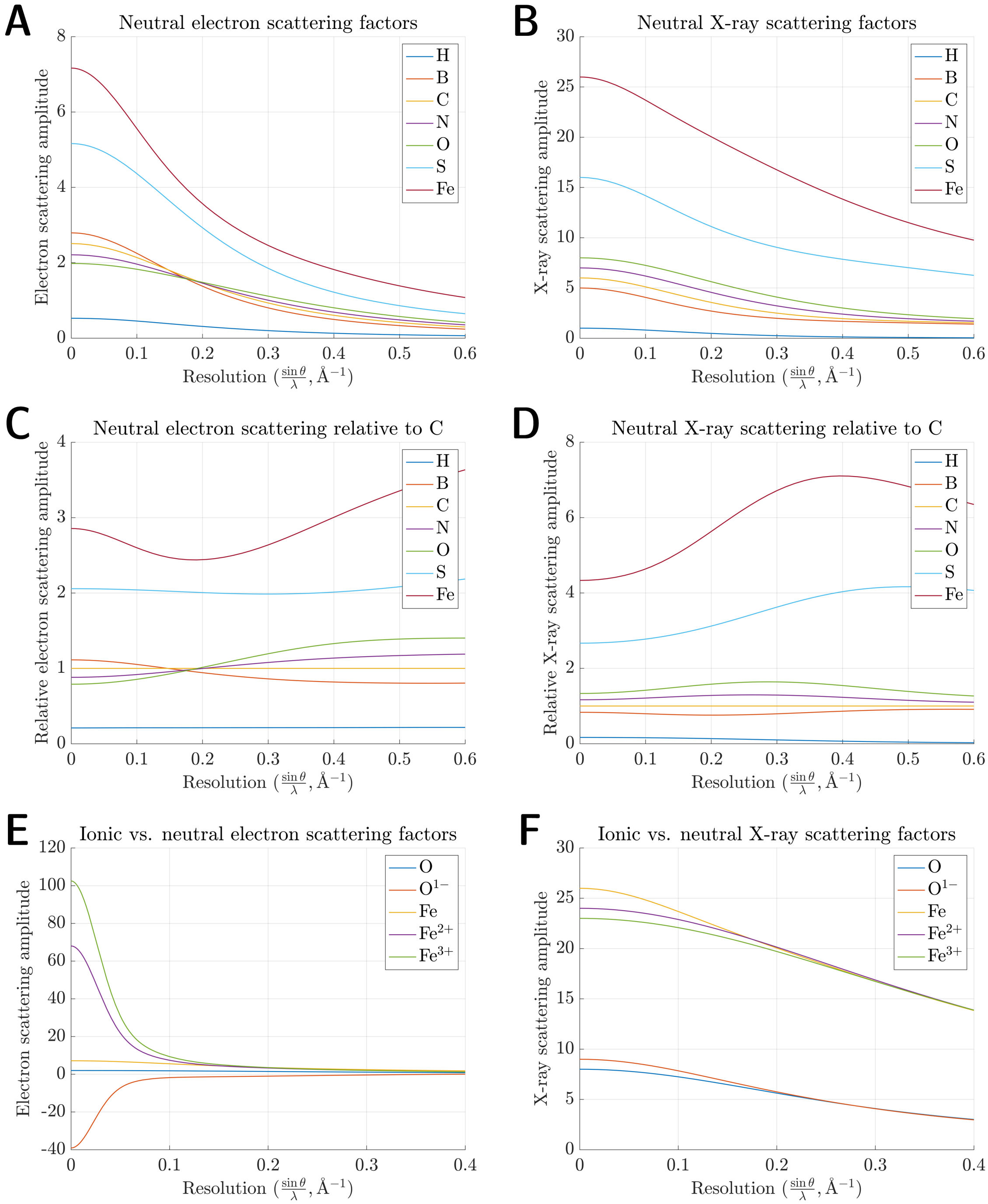

Figure 1.1: **Comparison of electron vs. X-ray scattering factors.** (A) Neutral electron scattering factors for 7 elements. All neutral scattering factors were parameterized into 5 Gaussians and plotted within the range $[0 < \frac{\sin\theta}{\lambda} < 0.6\,\text{Å}^{-1}]$, equivalent to $[\infty < d < 0.83\,\text{Å}]$. (B) Neutral X-ray scattering factors. (C) Neutral electron scattering relative to C. Relative scattering amplitudes were calculated by dividing each scattering factor by $f(s)$ for neutral C. (D) Neutral X-ray scattering relative to C. (E) Ionic vs. neutral electron scattering factors for O and Fe. (F) Ionic vs. neutral X-ray scattering factors.

carbon. This ratio grows to approximately 6× for X-rays, which is much more commensurate with the discrepancy in atomic mass between C and Fe. By the same token, however, lighter elements contribute a greater fraction of scattering signal in ED relative to XRD. This property empowers ED to detect and localize atoms such as hydrogen, which typically scatter X-rays very weakly. Finally, arguably the most drastic disparity between electron and X-ray scattering factors lies in electrons' ability to visualize charged states [22]. $V(\vec{r})$ contains an explicit contribution from nuclear charge density $\delta(\vec{r})$, which renders its Fourier transform $f_e(s)$ innately sensitive to the excess nuclear charge intrinsic to ionized atoms. Consequently, electron scattering amplitudes for neutral atoms diverge strikingly from those of their ionic counterparts, especially at low spatial frequencies. As $s \to 0$, $f_e(s)$ skyrockets toward ∞ for cations and plummets toward $-\infty$ for anions (Figure 1.1E). These differences materialize much more subtly in X-ray scattering, which remains comparatively uninfluenced by nuclear charge density (Figure 1.1F).

1.3.2 Differences Between X-ray and Electron Wavelengths

Conventional TEMs accelerate electrons to a significant fraction of the speed of light, exploiting voltage differences to produce a high-energy beam (i.e., 100–300 keV) in which each constituent electron is forcibly propagated through a potential drop. At these energies, an accurate calculation of the de Broglie electron wavelength must incorporate relativistic contraction, as follows:

$$\lambda = \frac{h}{\sqrt{2m_0E\left(1+\frac{E}{2m_0c^2}\right)}}, \tag{1.4}$$

where λ is the electron wavelength, h is Planck's constant, m_0 is the electron rest mass, E is the kinetic energy imparted by the accelerating voltage, and c is the speed of light in a vacuum. We can rearrange this expression to give a more intuitive formula with hc in the numerator:

$$\lambda = \frac{h}{\sqrt{2m_0E+\frac{E^2}{c^2}}} = \frac{hc}{\sqrt{2m_0c^2E+E^2}}. \tag{1.5}$$

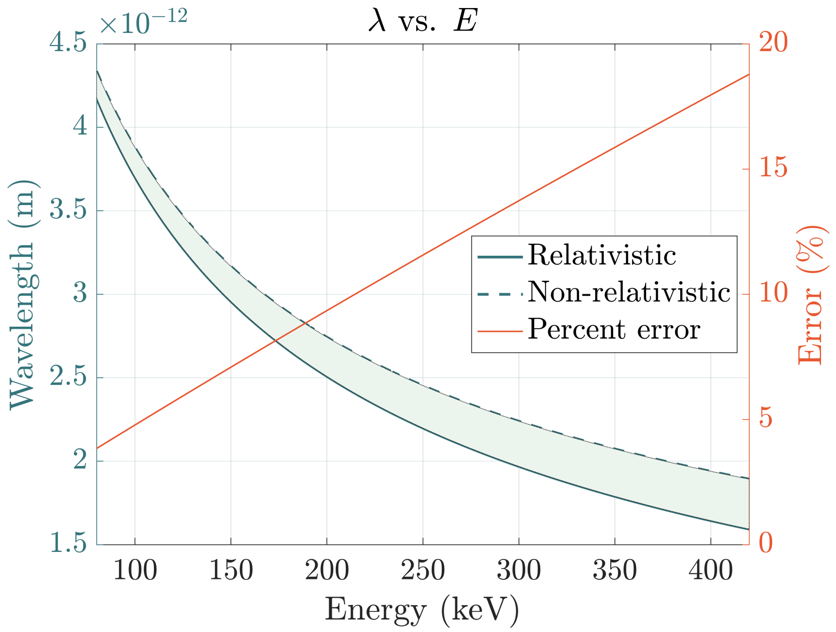

Figure 1.2: **Relativistic (solid blue line) and non-relativistic (dashed blue line) electron wavelengths plotted as a function of incident energy *E* at a range of accelerating voltages accessible to TEM.** Percent error between the two calculations is plotted in orange; characteristic values include 4.7% at 100 keV, 9.3% at 200 keV, 13.7% at 300 keV, and 17.9% at 400 keV.

Energy (keV)	Quanta	β ($\frac{v}{c}$)	Wavelength (Å)	Radius of Ewald sphere (Å^{-1})
8.042	X-rays (Cu K_α)	1	1.5418	0.6485
12.65	X-rays (Se K)	1	0.9795	1.0209
17.44	X-rays (Mo K_α)	1	0.7107	1.4070
100	Electrons	0.548	0.0370	27.027
200	Electrons	0.695	0.0251	39.840
300	Electrons	0.776	0.0197	50.761

Table 1.1: **Comparison of X-ray and electron wavelengths at a range of relevant energies.**

Discrepancies between the non-relativistic ($\lambda = \frac{h}{\sqrt{2m_0 E}}$) and relativistic calculations widen significantly as E rises (Figure 1.2). At 300 keV, for instance, the error grows to approximately 13.7%; these two wavelengths would generate distinct Ewald spheres with markedly different radii, underscoring the importance of using the relativistically corrected value.

For additional perspective, a systematic comparison of typical X-ray and electron wavelengths is given in Table 1.1. These numbers indicate that 100–300 keV electrons exhibit relativistic wavelengths roughly 50–100× shorter than their X-ray counterparts, which leads to an array of experimental consequences. Since the radius λ^{-1} of the Ewald sphere scales inversely with the wavelength of the impinging quanta, electrons at these energies divulge expansive Ewald spheres which intercept the reciprocal lattice along gently sloping arcs (Figure 1.3A). This geometry stands in stark contrast to X-ray diffraction, where inherently longer wavelengths produce smaller Ewald spheres featuring distinct surface curvature (Figure 1.3B). As a result, the cascades of circular lunes seen in X-ray diffraction patterns give way to nearly planar slices in electron diffraction patterns, which resemble canonical precession photographs (Figure 1.3C).

Each sampled Bragg peak represents an intersection between a reciprocal lattice vector and the surface of the Ewald sphere. A wider, flattened Ewald sphere causes electron diffraction patterns to accommodate different groups of reflections per scattering angle relative to X-ray diffraction. For instance, observation of several Friedel mates within a singular diffraction pattern is commonplace in ED, whereas the curvature of the X-ray Ewald sphere curtails this in XRD.

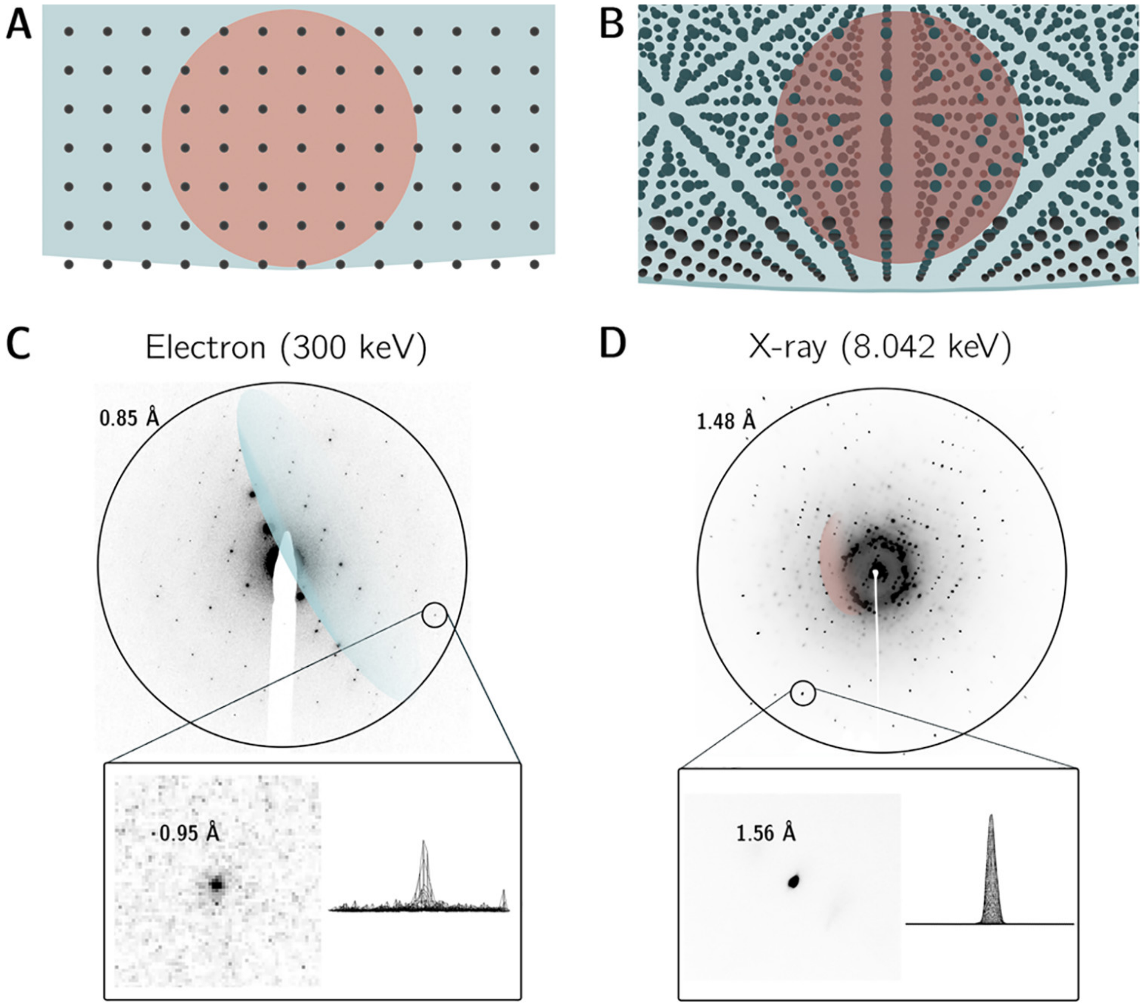

Figure 1.3: **Comparison of electron vs. X-ray Ewald spheres alongside representative experimental diffraction patterns.** Superimposed X-ray (rendered in blood orange, E = 8.042 keV, $\lambda = 1.541$ Å, radius = 0.6485 Å^{-1}, volume = 1.142 Å^{-3}) and electron (rendered in blue, E = 300 keV, $\lambda = 0.0197$ Å, radius = 50.76 Å^{-1}, volume = 5.478×10^5 Å^{-3}) Ewald spheres are drawn intersecting a cubic reciprocal lattice. The X-ray Ewald sphere is comfortably dwarfed by its much more voluminous electron counterpart. (A) 2D orthographic projection viewed normal to an arbitrary reciprocal lattice vector. (B) Alternate view revealing the three-dimensionality of the reciprocal lattice. (C) Electron diffraction pattern acquired using an accelerating voltage of 300 kV. Inset shows a close-up view and somewhat noisy 3D peak profile of a 0.95 Å resolution Bragg reflection. (D) X-ray diffraction pattern acquired on an in-house diffractometer equipped with a Cu Kα anode (8.042 keV). Inset shows a close-up view and strong 3D peak profile of a 1.56 Å Bragg reflection.

Furthermore, due to planarity, a singular ED pattern generally only permits the deduction of two unit cell vectors at once (exceptions include strongly diffracting samples in materials science, where higher-order Laue zone reflections can reveal three-dimensionality in the reciprocal lattice [23]). Conversely, a lone XRD pattern typically samples all three dimensions of the reciprocal lattice simultaneously. In practice, to reliably determine all three unit cell parameters, indexing requires comparatively more consecutive frames in ED (often covering a 15-25 degree angular wedge of reciprocal space) than it does in XRD, where one or two can theoretically suffice. Finally, the set of permissible scattering angles in ED (i.e., values of θ which satisfy the Bragg condition) encompasses a much smaller numerical range versus XRD, a direct consequence of substituting shorter wavelengths into Bragg's law. To compensate for this, ED requires a significantly longer detector distance than XRD to discriminate between Bragg peaks, often in the vicinity of 1 m. Another key experimental distinction is that adjustments to detector distance in XRD involve physically moving a piece of hardware. Conversely, in a transmission electron microscope, the physical distance between the sample and the detector is fixed. ED performed in TEMs utilizes a system of post-specimen electromagnetic lenses to generate virtual camera lengths, effectively either magnifying or demagnifying the reciprocal lattice projected onto the detector.

1.3.3 Multiple Scattering

As another consequence of their augmented cross-sections relative to X-rays, incident electrons have a higher relative likelihood of undergoing multiple scattering events while traversing an illuminated crystal [24, 25, 26, 27, 28]. This phenomenon—frequently referred to as "dynamical" scattering, a term which specifically encompasses multiple elastic events—was for decades considered a daunting bulwark against accurate structure determination by electron crystallography. Broadly, the probability of detecting multiple scattering is chiefly influenced by three factors: (a) the incident electron energy, (b) the irradiated crystal's density and thickness, and (c) its geometric orientation relative to the impinging beam. Within an energy range germane to transmission electron microscopy (i.e., accelerating voltages between 80–300 kV), electron cross-sections for all

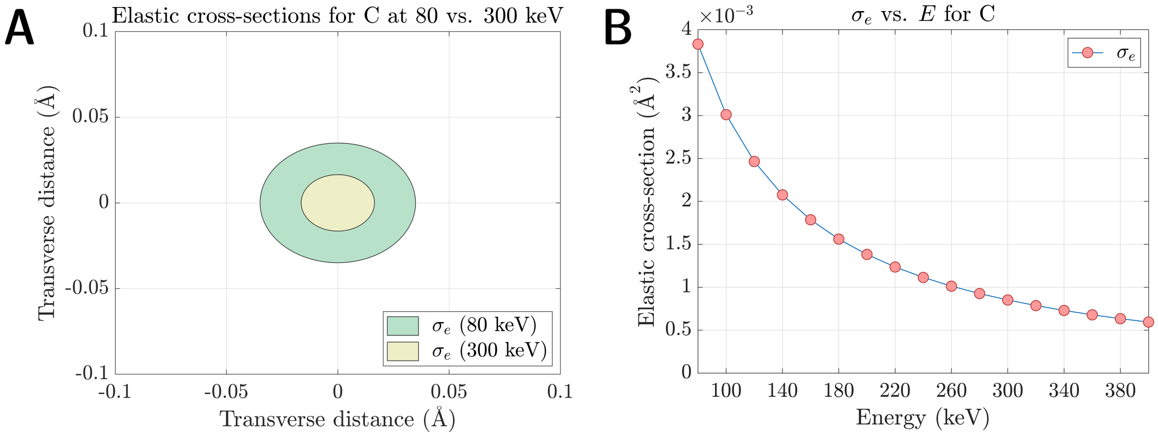

Figure 1.4: (A) Elastic cross-sections for neutral carbon at 80 keV (green) and 300 keV (yellow); cross-sectional areas expressed as concentric circles. (B) Elastic cross-section for neutral carbon decreasing as a monotonic function of incident energy, plotted at a range of accelerating voltages relevant to TEM.

neutral elements vary as a monotonic function of kinetic energy E (Figure 1.4B). As E becomes progressively larger (i.e., as the relativistic electron velocity asymptotically approaches c), the likelihood of any singular scattering event—and, by extension, the likelihood of multiple scattering—becomes progressively lower. For instance, the elastic cross-section of carbon at 300 keV is 4× smaller than its counterpart at 80 keV (Figure 1.4). In principle, the probability of multiple scattering is therefore diminished at higher incident energies and maximized at lower incident energies.

Furthermore, substrate-specific attributes such as crystal density determine the incident electrons' elastic and inelastic mean free paths (MFPs). MFPs provide a statistical estimate of the average distance traveled between each respective scattering event. Assuming a randomly distributed set of point scatterers, the MFP is defined as

$$\Lambda = \frac{1}{N\sigma}, \tag{1.6}$$

where N is the number of atoms per unit cell volume and σ is a weighted mean cross-section which represents an "average atom" within the unit cell. Clearly, MFPs scale inversely with N

and σ, indicating that the probability of multiple scattering is amplified if the incident electrons must penetrate (a) dense, tightly packed lattices or (b) unit cells containing strong scatterers such as heavy metals, whose cross-sections eclipse those of lighter elements. These scenarios lead to shorter MFPs. Theoretically, if the crystal under interrogation is several MFPs thick, multiple scattering becomes a statistical inevitability.

Finally, geometric orientations where the incident beam illuminates major zone axes can cause excitation of many Bragg reflections all at once. If an incident electron undergoes exclusively multiple elastic scattering, its ultimate fate likely lies within a Bragg peak, regardless of how many scattering events it experiences. Thus, since zone-axis diffraction patterns feature simultaneous excitation of a wide range of Bragg peaks, they effectively open many more avenues through which multibeam interference could potentially occur. This effect is intensified by low mosaicity. In sum, ED studies which report severe multiple scattering typically feature some combination of low accelerating voltages, near-perfect or minimally mosaic crystals, alignment at major zone-axis orientations, or thick and dense samples. All these experimental conditions maximize the occurrence of dynamical effects.

If singular elastic or "kinematical" scattering holds, the integrated intensity of each Bragg peak is proportional to the squared modulus of its corresponding structure factor:

$$I_{hkl} \propto F_{hkl} F^{*}_{hkl} = |F_{hkl}|^2. \tag{1.7}$$

In conventional X-ray crystallography, this relationship is almost universally observed. In ED, however, multiple elastic scattering stochastically redistributes some fraction of the diffracted intensities, a process mathematically described by self-convolution of I_{hkl} [29]. Such self-convolution breaks a key tenet of kinematical scattering, where the intensity of any random Bragg reflection is decoupled from that of its neighbor. Conversely, dynamical scattering imbues the intensities of compromised reflections with some degree of dependence on the intensities of their simultaneously excited counterparts. Two diagnostic markers of this effect include (a) violation of

Friedel's law [30, 31, 32] and (b) appearance of symmetry-forbidden Bragg peaks at reciprocal lattice points where glide planes, screw axes, or non-primitive lattices would normally mandate systematic extinctions [33, 34, 35, 36, 37, 38, 39, 40]. In space groups which contain these symmetry operators, a useful metric to quantify the extent of multiple scattering is the ratio between average intensities of symmetry-forbidden versus symmetry-allowed reflections within a particular zone axis [36, 38, 39]. If the recorded diffraction pattern is sufficiently marred by these artifacts, the fundamental link between I_{hkl} and $|F_{hkl}|^2$ becomes increasingly tenuous, undermining the validity of the measured intensities. In milder cases, multiple elastic scattering would simply intensify weaker reflections and attenuate stronger reflections. In severe cases, multiple scattering would theoretically sever this link altogether, producing a pseudouniform distribution of intensities which ablates distinctions between ideally independent reflections [40]. This homogenization of relative differences between Bragg peaks would render any structure-factor amplitudes derived from such intensities meaningless.

For many years, these concerns led to a self-imposed moratorium on structure elucidation by electron diffraction, as ED intensities were considered too corrupted to yield reliable atomic coordinates [41]. Such sentiments were succinctly expressed in *The Determination of Crystal Structures*, the classic 1966 textbook by Lipson and Cochran [42]. Following a perfunctory summary of Vainshtein's work, the authors concluded that electron diffraction was "inferior to the other two diffraction techniques [X-ray and neutron] because of the many difficulties which stand in the way of making accurate intensity measurements." In some laboratories, this belief rapidly ossified into dogma, and the steady stream of small-molecule ED structures solved by Vainshtein and co-workers in the Soviet Union was treated with suspicion. In 1968, Cowley [14] felt compelled to write that it was "perhaps significant that the first work on structure analysis by electron diffraction, and most of the subsequent work, was done in the U.S.S.R. and Australia, countries *well removed* [emphasis added] from the leading pre-war experimental electron diffraction groups in England and the groups in Japan which had the most complete knowledge of dynamical theory."

A key breakthrough was provided by Hauptman and Karle's development of direct methods, which supplied an objective means of phase retrieval from integrated intensities [43, 44, 45, 46]. Since direct methods leverage statistical relationships between accurately sampled structure-factor amplitudes, untethering I_{hkl} and $|F_{hkl}|^2$ should have nullified any possibility of *ab initio* phasing. Dynamically corrupted intensities would have led direct methods to formulate incorrect phase relationships between structure-factor amplitudes, ultimately generating a nonsense structure. However, in a seminal 1976 study, Dorset and Hauptman deployed *ab initio* phasing to successfully decipher the subcell structures of two organic compounds, *n*-hexatriacontane and racemic 1,2-dipalmitoyl-glycerophosphoethanolamine, via electron diffraction [47]. This work provided robust experimental evidence that structure elucidation using the kinematical approximation was plausible despite the countervailing influence of multiple scattering. Specifically, Dorset and Hauptman found that the utility of the triplet and quartet phase invariants (as well as the centrosymmetric phase restriction $\phi_{hkl} = 0$ or π) emerged unscathed, notwithstanding usage of amplitudes presumably distorted by multiple scattering. Dorset and Hauptman's results were especially compelling given their relatively low operating voltages of 80–100 kV (i.e., energies at which the probability of multiple scattering was already amplified). In a steadily increasing number of counterexamples, ominous predictions about multiple scattering have generally failed to hold true outside specific extenuating circumstances, and dynamical effects have not impeded structure solution by direct methods (Table 1.3). In sum, multiple elastic scattering rarely distorts intensities with enough severity to generate an experimental Patterson map out of sync with the autocorrelation function of the genuine structure [48].

An impactful portion of this dogma-busting work was conducted by Dorset, who embarked on a quest to apply direct methods to electron-diffraction amplitudes originally recorded at approximately 50 kV by Vainshtein, Zvyagin, and other pioneering Soviet crystallographers in the 1950s [49, 50, 51, 52, 53]. Since these ED data were collected prior to the advent of *ab initio* phasing, Vainshtein and co-workers usually relied on pairing experimental ED amplitudes with phases borrowed from corresponding X-ray structures. Naturally, this approach invited concerns regarding phase bias, despite its conceptual similarity to molecular replacement techniques commonly used today. Nevertheless, armed with the objectivity of direct methods, Dorset was able to replicate Vainshtein's structures of diketopiperazine, urea, and thiourea, all using a simple kinematical approximation. This resounding vindication of Vainshtein's early work, nearly three-and-a-half decades after it was first published, dispelled much of the stigma projected by dynamical scattering. In 2010, Dorset concluded the diketopiperazine saga with another reevaluation of Vainshtein's results, this time equipped with contemporary crystallographic software [54]. A full-matrix least-squares refinement of sixty-year-old data in SHELXL proved remarkably successful, yielding an R1 residual comparable to recent ED structures obtained using modern instrumentation.

1.4 Experimental Setup

1.4.1 Sample Preparation

Sample preparation for 3D electron crystallography involves dispersing a micro- or nanocrystalline powder onto an EM grid 3.05 mm in diameter. For a wide range of small molecules, this procedure is quite simple; it merely entails inserting an EM grid into a scintillation vial containing a few mg of substrate and vigorously shaking for 10 seconds or so (Figure 1.5B). If this "shake-n-bake" method produces an unduly sparse distribution of crystals, an alternative strategy involves immersing a small quantity of powder in a volatile solvent (ideally one in which the substrate is completely insoluble), drop-casting 2-3 μL of the resultant slurry directly onto the grid using a micropipette, and allowing it to air-dry at RT. Alternatively, crystals suitable for ED can be grown or annealed directly on EM grids by drop-casting a dilute solution of analyte and letting it evaporate, prompting *in situ* nucleation and crystallization [55, 56]. Optionally, excess solvent can be wicked away using filter paper or drained under reduced pressure by a vacuum pump [57]. Since the amorphous carbon surface of many grids is somewhat hydrophobic, it generally interferes with adherence of aqueous or polar organic solvents. This mismatch can prevent the drop-casted suspension from spreading uniformly across the film. A highly uneven distribution of crystallites can lead to a few overly congested grid squares, prohibiting isolation of a single crystal within the selected area aperture. To combat this, the surface of the grid can be rendered hydrophilic by glow-discharging both sides before use.

An added layer of complexity is presented by crystals which contain disordered channels of volatile solvent, such as proteins [58, 59, 60]. These species can undergo swift lattice collapse when subjected to the high vacuum (typically at least 10^{-4} Pa) of the TEM. Therefore, as a prophylactic measure, electron diffraction of solvated crystals is generally recorded under cryogenic (-175 °C) conditions facilitated by liquid nitrogen. Common practice involves implementing well-established cryo-preservation techniques borrowed from single-particle cryo-EM [61, 62, 63, 64]. Encasing susceptible crystals within a thin layer of vitreous ice shields them from the TEM vacuum and preserves the lattice in a frozen-hydrated state. Cryogenic temperatures also delay the onset and progression of radiation damage, which is frequently quite severe for macromolecular crystals at room temperature. For proteins and oligopeptides, several step-by-step protocols detailing cryo-preservation procedures have been published [65, 66]. A glow-discharged EM grid is first loaded with 2-3 μL of an aqueous suspension of protein crystals (usually immersed in mother liquor from a successful crystallization trial, such as the hanging drop in Figure 1.5C). Subsequently, the grid is blotted and rapidly plunged into a small reservoir (4 mL) of liquid ethane. Ethane's high specific heat capacity allows it to function as a ruthlessly efficient cryogen, ensuring complete vitrification of residual water without cocrystallization of adventitious ice. Since pure ethane solidifies upon prolonged exposure to liquid nitrogen, eutectic mixtures of ethane and propane have also been proposed as alternatives with depressed freezing points [67]. This step is typically carried out at high speed by automated vitrification robots, although manual plunge-freezing is also an option. Frozen grids can then be immediately cryo-transferred to the TEM or indefinitely stored in liquid nitrogen for future use. Finally, for substrates such as beam-sensitive, unsolvated small molecules, vitrification is generally unnecessary. Nonetheless, these crystals may still benefit considerably from the reduced radiation damage engendered by cryogenic conditions. A typical tactic therefore involves skipping vitrification and simply slow-cooling the sample within a cryo-

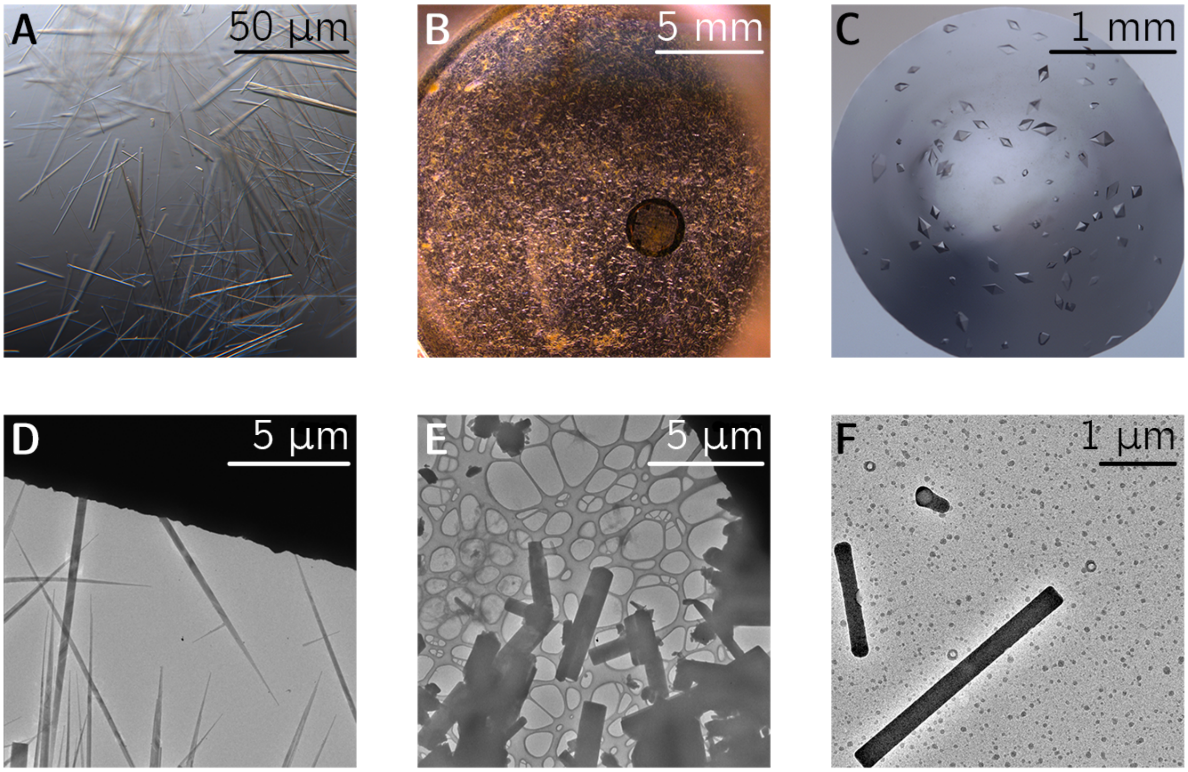

Figure 1.5: **Micrographs of crystals suitable and unsuitable for 3D ED.** (A–C) Optical microscopy of several crystalline compounds suitable for 3D electron crystallography. Panels A and C depict formally recrystallized material (an organic small molecule suspended in glycerol in A, an oligopeptide suspended in a hanging drop in C) requiring additional pulverization before ED due to their macroscopic size. Panel B shows an inherently microcrystalline powder amenable to a direct "shake-n-bake" approach with a standard 3.05 mm lacey carbon EM grid. (D–F) Transmission electron microscopy reveals micro- and nanocrystalline specimens with a range of morphologies, all suitable for ED analysis.

holder following insertion into the TEM.

Atomic-resolution ED data have been routinely recorded from crystals hundreds of nanometers thick [68]. Nevertheless, as crystal thicknesses approach the 1 μm mark, data quality rapidly deteriorates, largely due to prohibitive amounts of diffuse and inelastic scattering overwhelming productive signal from Bragg peaks. Thus, some form of mechanical deformation, such sonicating the microcrystalline slurry or vortexing with acid-washed glass beads, is often necessary to shatter crystals into smaller, thinner shards amenable to ED. In cases where a suitably inert drop-casting solvent is unavailable, simply grinding dry powder between two glass coverslips can achieve an analogous effect via shear force. Alternatively, focused ion-beam (FIB) milling can shave excessively thick crystals down to thin electron-transparent lamellae with precision [69, 70, 71]. Although quite powerful, FIB milling requires usage of specialized ancillary equipment (a scanning electron microscope), as well as multiple cumbersome cryo-transfer steps if dealing with vitrified samples.

1.4.2 3D ED Data Collection Procedures

Historically, electron diffraction patterns were recorded after tilting the crystal to a low-index zone-axis orientation [13]. In principle, in-zone diffraction patterns near-perfectly coincide with sets of parallel Bragg planes within the reciprocal lattice (Figure 1.6A). As a result, these slices of the Ewald sphere contain an especially high density of simultaneously excited reflections. Such circumstances present a double-edged sword. On one hand, a well-defined zone-axis geometry facilitates indexing and simplifies determination of unit cell parameters. By the same token, however, this method is blind to reflections located between zone axes, leaving interstitial corridors of reciprocal space undersampled. Furthermore, zone-axis orientations maximize the probability of observing multiple elastic scattering, impeding accurate integration of quasi-kinematical intensities needed for structure solution. To compound matters, merging intensities recorded solely from disparate still-frame in-zone patterns is often quite difficult. Excitation error can cause even small angular deviations to produce prohibitive variations in intensities recorded slightly outside their exact Bragg condition. As the relatively small handful of successful examples [72, 73, 74] attests, *ab initio* structure determination from oriented zone-axis patterns was never widely adopted as a robust means of solving 3D structures.

In 1994, Vincent and Midgley pioneered precession electron diffraction (PED), a novel means of data collection that mitigated some of these issues [75]. In their method, the incident electron beam is effectively precessed within a fixed, hollow cone whose vertex is coincident with the plane of the illuminated crystal [76]. The resultant diffraction patterns contain signal averaged over elongated conical sections of the Ewald sphere rather than planar slices through zone axes (Figure 1.6C). These cones encompass both in-zone reflections and several previously neglected off-zone reflections. Critically, since the gyrating beam captures most off-zone reflections sequentially and not all at once, they generally do not undergo simultaneous excitation. Consequently, PED reduces the number of plausible multibeam pathways for dynamical scattering. Furthermore, accurate measurement of PED intensities is facilitated by integration over a more complete snapshot of the Bragg condition for each observed reflection. As an ensemble, these intensities largely behave quasi-kinematically [77, 78, 79]. A straightforward tactic to further minimize dynamical effects involves widening the angle of precession [77], which has been shown to systematically diminish the intensities of symmetry-forbidden reflections [36]. PED also expands coverage of reciprocal space relative to sampling exclusively in-zone reflections. Nevertheless, this technique still favors locating zone-axis orientations and adds only a subset of off-zone reflections (i.e., those proximal to their in-zone counterparts). As a result, *ab initio* structures solved by zone-axis PED often relied on high-symmetry centrosymmetric space groups to simplify phasing and bolster completeness [80, 81].

A crucial step forward was taken by Kolb *et al.* in 2007 [82, 83]; these researchers proposed collecting a tomographic series of diffraction patterns, using the TEM goniometer to tilt the substrate in a sequence of discrete angular steps (Figure 1.6E). Since the axis of the TEM goniometer is geometrically arbitrary with respect to the orientation of the crystal, ED data collected in this way represent slices of the Ewald sphere which overlap "only accidentally" with

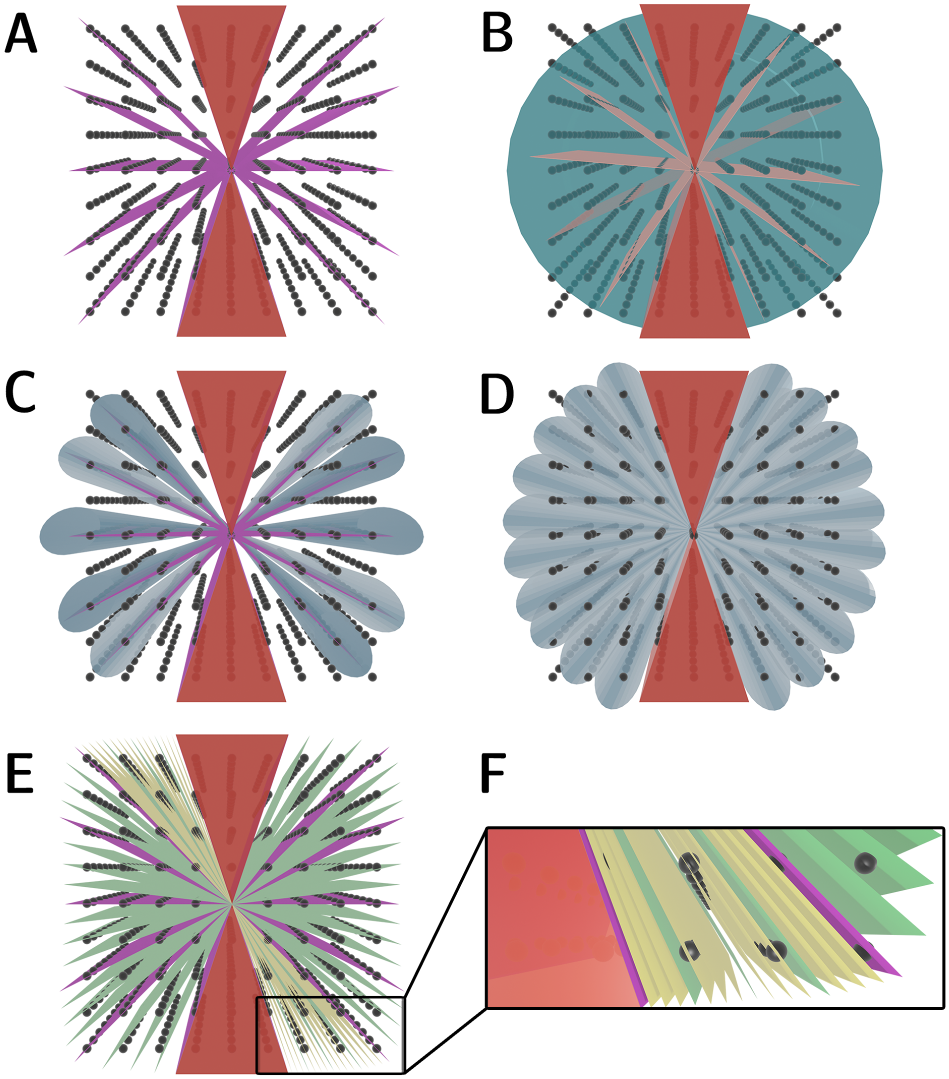

Figure 1.6: **Modalities of 3D ED data collection.** The hourglass-shaped missing wedge intrinsic to the TEM is depicted in red. (A) Zone-axis orientations (purple planes) accessed via stepwise angular tilts. This approach leaves corridors of reciprocal space between zone axes (white) unsampled. (B) Continuous-rotation electron diffraction. Blue wedges correspond to regions of reciprocal space sampled during the exposure time, whereas red planes represent gaps left unsampled while the TEM stage continues to rotate during the detector readout time. (C) Zone-axis precession electron diffraction (PED). Thanks to the precessing motion of the incident beam (blue cones), this method intercepts several off-zone reflections neglected in (A). (D) Precession electron diffraction tomography (PEDT). This technique combines beam precession with rotation about the goniometer axis. (E) Automated diffraction tomography (ADT). Stepwise tilts about the goniometer axis ensure that most diffraction patterns (green planes) represent off-zone orientations. (F) Rotation electron diffraction (RED). Exploitation of electron beam tilt enables finer sampling of reciprocal space (yellow planes) than relying on the mechanical precision of the TEM goniometer (green planes).

crystallographic zone axes [82]. Therefore, this approach, originally termed automated diffraction tomography (ADT), banished the persistent specter of zone-axis orientations amplifying multiple scattering. Indeed, ADT deliberately ensured that most diffraction patterns were collected off-zone, providing ideal conditions for quasi-kinematical scattering [84, 85].

ADT's most salient limitation was its tendency to leave unsampled gaps in reciprocal space between angular tilts: essentially a less severe version of the large swaths overlooked by zone-axis diffraction. Several subsequent strategies were developed to address this. ADT was swiftly combined with beam precession by Mugnaioli *et al.*, who developed a hybrid technique coined precession-assisted electron diffraction tomography [86] (PEDT; Figure 1.6D). PEDT represented the first ED technique to gain some level of traction as a generally applicable method for structure elucidation, despite the necessity of specialized external hardware to implement beam precession [87]. Alternatively, Hovmöller, Zou, and co-workers devised a means of slicing reciprocal space more finely by supplementing coarse mechanical tilts with electron beam tilts [88] (Figure 1.6F). This approach was dubbed rotation electron diffraction (RED); it utilized custom software to enable data collection in very granular angular steps ($\Delta\eta < 0.1°$) which eclipsed the precision of the TEM goniometer.

These developments paved the way for arguably the most impactful methodological advance in 3D electron crystallography: continuous rotation, which was formulated nearly in parallel by Nederlof *et al.* [89] and Nannenga *et al.* [90] in 2013 and 2014, respectively. Unlike PEDT or RED, no ancillary hardware or software is strictly required to implement continuous-rotation ED; most commercially available TEMs can collect continuous-rotation data with little to no reconfiguration. In this technique, reciprocal space is regularly sampled in periodic intervals while the irradiated crystal is unidirectionally rotated about the TEM goniometer axis (Figure 1.6B). Each diffraction pattern thus represents signal averaged over an oscillation range whose thickness in reciprocal space is given by

$$\Delta\eta = \omega_{\text{rot}}\tau_{\text{exp}}, \tag{1.8}$$

where ω_{rot} is the rotational velocity of the goniometer (typically expressed in degrees per second) and τ_{exp} is the exposure time (for instance, 2-3 seconds) [91]. In practice, since no detector operates instantaneously, $\Delta\eta$ is modified by adding a hardware-specific parameter τ_{dead}, which represents the readout time needed to store the data collected during τ_{exp}:

$$\Delta\eta = \omega_{\text{rot}}(\tau_{\text{exp}} + \tau_{\text{dead}}), \tag{1.9}$$

Especially in older systems containing slow-scan charge-coupled device (CCD) detectors, τ_{dead} can become significant. In such cases, each consecutive diffraction pattern is separated by a missing wedge ($\Delta\eta_{\text{dead}} = \omega_{\text{rot}}\tau_{\text{dead}}$) corresponding to the angular range left unsampled during the readout period. A viable tactic to minimize dead time entails spatial subsampling or binning each recorded frame, although this ultimately compromises the maximum achievable resolution. Nannenga *et al.* circumvented this issue by using a complementary metal–oxide–semiconductor (CMOS) detector in rolling-shutter mode, which provided a readout speed sufficiently high that τ_{dead} was rendered negligible relative to τ_{exp}. This breakthrough allowed continuous-rotation ED to fully sample all regions of reciprocal space accessible to the TEM goniometer. By integrating signal over an angular wedge, continuous-rotation ED also evaded all the canonical problems associated with multiple elastic scattering and partially recorded reflections. Nannenga *et al.* demonstrated this by using molecular replacement to solve a 2.5 Å ED structure of hen egg white lysozyme (HEWL), a protein frequently used as a standard in X-ray crystallography. HEWL crystallizes in the primitive tetragonal space group $P4_32_12$, which features several sets of systematic absences orchestrated by the 4_3 and 2_1 screw axes. Critically, Nannenga *et al.* hunted for symmetry-forbidden reflections and found that their intensities were quite weak, contributing only 2.5% of observed signal relative to their symmetry-allowed counterparts (vs. 5% for a previous ED investigation of HEWL [38] using still frames collected at discrete tilts).

These results sparked a renaissance in the field. In recent years, continuous rotation has clearly emerged as the method of choice for ED data collection. This has been accompanied by an alphabet soup of acronyms, including microcrystal electron diffraction or electron microdiffraction [90] (both condensed to "MicroED"), integrated electron diffraction tomography [91] (IEDT), and continuous-rotation electron diffraction [92] (cRED). Ultimately these all describe the same technique. Although "MicroED" has become the most popular moniker in the literature, especially in the United States, this is a rather unfortunate development. "Microcrystal electron diffraction" fails to communicate a key aspect of the technique: its ability to interrogate *nanocrystals*. Data collection from adequately sized microcrystals, of course, is also routinely conducted using synchrotron X-ray diffraction and is by no means unique to ED. Gemmi *et al.*'s adoption of the umbrella term 3D electron diffraction [17] (3D ED) is a more useful construct; it accurately conveys the central idea of sampling a 3D reciprocal lattice and also situates the technique within historical context by implicitly referencing its predecessor, 2D electron crystallography. For these reasons we follow this convention throughout.

1.4.3 Serial Electron Diffraction

To maximize sampling of reciprocal space, diffraction experiments have often relied on merging datasets collected from multiple crystals. Serial X-ray crystallography stretches this idea to its limit, exploiting X-ray free-electron lasers to collect and combine one-shot diffraction patterns extricated from hundreds of thousands of randomly oriented specimens [93]. Almost instantly after producing diffraction, these exceptionally brilliant lasers leave a bleak obliteration zone in their wake, vaporizing every crystal they touch. Ironically, XFELs come closest to generating diffraction patterns undistorted by radiation damage, since each successive crystal is exposed to a femtosecond-scale X-ray pulse only once before it is annihilated (as encapsulated in the mantra "diffraction before destruction") [94]. Ever-faster detectors at synchrotron facilities have driven serial X-ray crystallography's proliferation to many beamlines. Likewise, growing digitization and improved hardware have also enabled more ambitious, automated data collection strategies in ED [95, 96, 97]. Recent studies have exploited the automation capabilities of modern TEMs to collect data from thousands of crystals per hour. This approach, termed serial electron diffraction (serial ED), generally relies on merging unitary snapshots recorded from disparate crystals at distinct orientations, foregoing conventional sampling of a lone crystal at multiple angles. As with serial XRD, this technique exploits single exposures in an attempt to outrun radiation damage. With plenty of real estate on a typical EM grid, an experimentalist (or algorithm) can easily find dozens or possibly thousands of well-diffracting crystals during a routine search. Although many publications only report the number of crystals merged to produce a structure solution, hundreds more are typically probed and then belatedly abandoned.

Serial ED has successfully determined a small handful of structures, including HEWL, granulovirus occlusion bodies, and several highly symmetric zeolites [98, 99]. Elucidation of entirely novel structures remains a challenge, as it would require *ab initio* indexing, merging, and phasing. Nevertheless, serial ED has rapidly emerged as a potent microscopic alternative to the much larger-scale experiments conducted at synchrotrons or X-ray free-electron laser facilities. In addition to greater accessibility, the TEM unlocks another crucial advantage over conventional XFEL experiments: the power of real-space imaging. Indeed, the ability to visualize target crystals via imaging greatly streamlines the hunt for well-diffracting specimens, which for nanocrystals is a blind and comparatively inefficient process in serial X-ray crystallography.

In this context, 4D scanning transmission electron microscopy (4D–STEM) also merits discussion, since it too harmoniously combines real-space screening with reciprocal-space sampling [100]. This method leverages a scanning nanobeam to record ED patterns at an array of real-space points defined by a 2D raster scan across a user-selected region of a crystalline specimen [101, 102]. For instance, within an illuminated area of 500 nm^2, individual diffraction patterns can be collected every 20 nanometers. Conceptually, therefore, 4D–STEM provides an inherently serial approach to diffraction, simply localized with nanoscale precision onto the canvas of a single crystal. In principle, 4D–STEM's ability to digitally pinpoint a specific nanoscale volume for data collection is quite powerful; for instance, it could allow facile deconvolution of signal from twinned, metamict, or otherwise imperfect regions present within an already submicrometric crystal. 4D–STEM analysis can reveal complex mosaic substructures even in crystals anticipated to contain monolithic lattices. A conventional selected-area aperture is far too large to permit such granular spatial subsampling. Thanks to cryogenic conditions, 4D–STEM has also proved compatible with a range of beam-sensitive materials [103], and stepwise rotation of the TEM stage has allowed for tomographic data collection amenable to 3D structure determination. In sum, this approach permits *ex post facto* extraction and summation of diffraction signal from arbitrary regions of a 4D–STEM scan. These slices can subsequently be assembled into a more conventional tilt series comprehensible to standard data processing pipelines.

1.5 Data Processing

1.5.1 Data Reduction

Prior to the widespread adoption of continuous rotation, 3D ED data processing was non-trivial and somewhat opaque to the non-specialist; it was typically handled by a suite of dedicated programs developed by a coterie of seasoned electron crystallographers [104, 105, 106, 107]. Continuous-rotation 3D ED, however, is directly analogous to rotation of a mounted crystal on an X-ray diffractometer equipped with a single-axis goniometer. As a result, 3D ED data collected in this way can undergo indexing, integration, merging, and scaling routines implemented in several software packages originally written for X-ray crystallography. With minimal modification, well-established programs such as iMosflm [108], DIALS [109], and XDS [110] have all been successfully applied to continuous-rotation 3D ED data reduction. Detailed tutorials (such as for DIALS [111] and XDS [66]) easily comprehensible to any practicing X-ray crystallographer have subsequently appeared in the literature. Likewise, current processing pipelines for serial diffraction (such as crystFEL [112]) have also been ported to ED data [113]. Indexed lists of integrated intensities generated by these programs can directly serve as input for phasing algorithms.

1.5.2 Phasing by Direct Methods

It is a truth universally acknowledged that any diffraction experiment must overcome the phase problem, and ED is no exception. Since its initial demonstration by Dorset and Hauptman in 1976 [47], *ab initio* phasing has been successfully deployed on virtually all small-molecule substrates solved by 3D ED. If Sheldrick's criterion [114, 115] is met (i.e., if the illuminated crystal diffracts to at least 1.2 Å resolution and completeness in the outermost 1.2-1.1 Å shell exceeds 50%) or exceeded, direct methods (DM) has proved a robust and reliable means of phasing ED data. As in X-ray diffraction, the presence of (a) centrosymmetry, (b) sparsely populated unit cells, and (c) heavy atoms often permits some relaxation of Sheldrick's criterion (which is simply a conservative empirical estimate). Prior to the advent of automated software, venerable statistical approaches such as the Sayre equation and the tangent formula were applied manually, phase-by-phase. Today, widely used programs such as SHELXT [116] and SHELXD [117] have also found routine utility in ED data processing.

As currently implemented, DM algorithms generally hinge on two key constraints: atomicity and positivity. Since X-ray scattering amplitudes for all atoms remain non-negative regardless of resolution, positivity is a clearly justified postulate in X-ray crystallography. Indeed, the periodic electron density function recapitulated from X-ray diffraction is universally positive. An intriguing phenomenon intrinsic to ED, however, is that electron scattering amplitudes for negatively charged ions dip well below zero at low resolution, analogous to the negative scattering lengths exhibited by elements like H or Li in neutron diffraction. Consequently, in ED, anionic species can legally contribute negative density to electrostatic potential maps, a nuance to which *ab initio* phasing intended for X-ray diffraction is currently blind. As discussed in detail by Altomare *et al.* [118], violation of the positivity postulate is expected to alter the triplet phase invariant relationships traditionally exploited by direct methods. Evidence from difference Fourier maps indicates that this limitation may have contributed to erroneous assignment of charged moieties (such as deprotonated carboxylates) as neutral atoms [119, 120, 121].

Nevertheless, *ab initio* phasing by DM remains the gold standard in 3D ED, and the diverse array of structures determined by this approach has played a pivotal role in dispelling doomsday predictions about multiple scattering. *Ab initio* phasing has proved remarkably successful even on 3D ED data recorded from crystals hundreds of nanometers thick, despite multislice simulations suggesting a much lower thickness threshold for purportedly irreversible dynamical corruption [122]. This yawning chasm between theory and experiment is fueled by many factors, such as complex mosaicity at the nanoscale [102], unmodeled inelastic scattering [123], and the now-widespread usage of off-zone data collection. DM continues to face a stiff, often insurmountable challenge from macromolecular crystals containing >50% disordered solvent, which generally fail to diffract to atomic resolution. For lower-quality diffraction data extracted from small molecules, phasing by simulated annealing [124] has also proved a useful approach in 3D ED, often in conjunction with DM [125, 126].

1.5.3 Phasing by Molecular Replacement

Intrinsic disorder often prevents macromolecular crystals from diffracting to a resolution sufficiently high for direct methods. In such cases, if a search model with adequate sequence homology (generally at least 25%) is available, molecular replacement (MR) is a tried-and-tested means of phasing 3D ED data. Programs such as Phaser [127] and MOLREP [128] have been applied relatively seamlessly to ED; almost all protein structures solved by 3D ED have been phased via MR using an existing X-ray structure as a template. A substantial fraction originates from studies demonstrating new methodological approaches to 3D ED; this has resulted in well-studied proteins typically used as standards in X-ray crystallography (especially proteinase K, lysozyme, and catalase) accounting for over 40% of macromolecular structures deposited in the PDB. Comparatively few *de novo* structures have been determined by MR; currently, these remain limited to a handful of oligopeptides (with a maximum sequence length of 11 residues—see Table 1.2) and a single novel protein, R2lox [129] (which was later supplanted by a higher-quality X-ray structure [130]).

If existing models prove insufficient for MR and >1.2 Å resolution nullifies DM, fragment-based phasing (FBP) [131] has emerged as a potential alternative enabling structure determination. As implemented in the ARCIMBOLDO suite of programs, this approach mines focused fragment libraries derived from distant homologues or idealized elements of secondary structure (such as polyalanine α–helices). Iterative omission or placement of these fragments into a nascent structure solution allows for assessment of their respective phasing power. Ultimately, structures phased by this method fall conceptually closer to MR than to DM, although not quite as phase-biased as MR from a unitary model. Originally demonstrated on a variety of X-ray datasets by Usón and co-workers [132], FBP has recently been extended to a few ED cases where MR and DM had collectively proved ineffective [133], in addition to a proof-of-concept FBP structure of proteinase K [134]. Interestingly, FBP appears uniquely suited to probe smaller species with less predictable folds, including polymorphic amyloid oligopeptides. Like MR, FBP is also theoretically compatible with fragments harvested from computationally generated models (i.e., AlphaFold [135] or RoseTTAFold [136] for proteins, or DFT for small molecules), removing the need for an experimentally determined template.

1.6 Structure Refinement

1.6.1 Theoretical Background

A survey of published 3D ED structures—encompassing oligopeptides (Table 1.2), small molecules (Table 1.3), and proteins (Table 1.4)—reveals average refinement residuals in the 20-30% range, markedly greater than values typically observed in XRD (Figure 1.7). To a certain extent, however, this gap is cosmetic. In many cases, structures generated by 3D ED have yielded stubbornly inflated refinement *R*-factors despite featuring no errors in atomic assignment or placement. Additional validation of these ESP maps is provided by all-atom RMSD analyses relative to known X-ray structures, which often compare very favorably. Especially if initial data reduction statistics (such as R_{meas}, $<I/\sigma(I)>$, and $CC_{1/2}$) appear well-behaved, elevated refinement *R*-factors may partially reflect systematic inaccuracies in computation of F_{calc} rather than any genuine deficiencies in the atomic model itself. For instance, although 3D ED modalities such as continuous rotation and precession minimize the effects of multiple elastic scattering, dynamical diffraction can still distort structure-factor amplitudes. Conventional refinement procedures (in programs originally written for X-ray diffraction) neglect this and simply assume singular elastic scattering. To rectify this oversight, a series of studies by Palatinus and co-workers has formulated a refinement approach which incorporates dynamical diffraction theory into calculation of model structure factors [107, 137, 138]. As implemented in Jana2006, this procedure has diminished refinement R-factors for 3D ED data and seemingly enhanced the ability to detect granular details such as H atoms in Fourier difference maps [139]. Nevertheless, dynamical refinement is not yet a routine procedure, partially because its computational expense renders it currently unsuitable for larger systems like macromolecules. Alternative approaches involve application of various correction factors to measured intensities [140], including off-label use of a primary extinction parameter originally intended for X-ray diffraction [141]. These methods may help compensate for lingering dynamical effects.

Another potential source of error lies in $f_e(s)$ itself. Inverse Fourier transforms of conventional electron scattering factors ultimately yield spherical, isotropic distributions capable of accommodating a Gaussian model. This is emblematic of electrostatic potential projected by an isolated atom. In real systems, however, ESP almost always experiences perturbations due to environmental effects. Specifically, low-angle scattering is especially sensitive to the redistribution of valence electrons which accompanies ionization or chemical bonding. Isolated scattering factors disregard these effects. Chang *et al.* analyzed this issue by conducting Hartree-Fock molecular orbital calculations at the 6-31G* level of theory, which they then transformed into substrate-specific molecular electron scattering factors [142]. Yamashita and Kidera developed a similar treatment using the hybrid functional B3LYP, decomposing output from DFT into parameterized, atom-specific contributions. Both investigations concluded that ESP is represented more accurately by aspherical, anisotropic scattering factors, particularly at low spatial frequencies [143]. However,

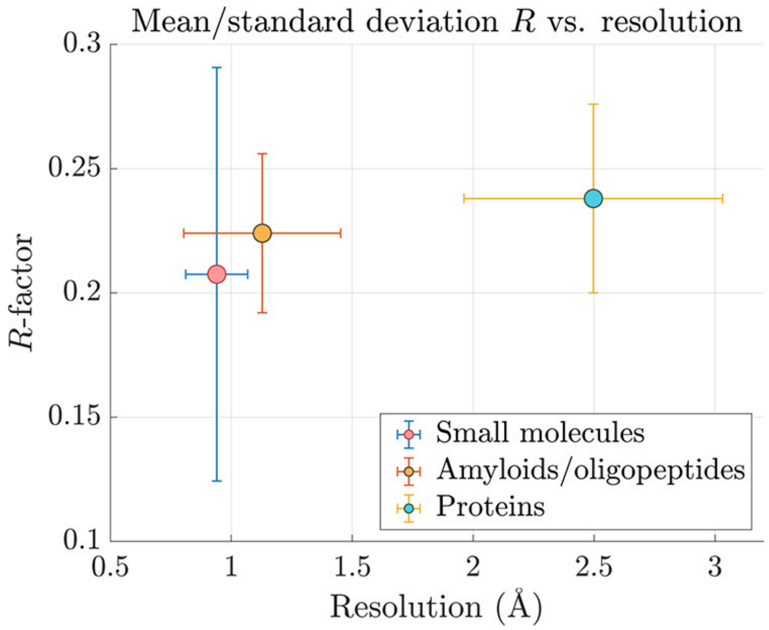

Figure 1.7: Circles represent the mean resolution and refinement R-factor ($R1$ for small molecules, R_{work} for peptides and proteins) for each category of substrate, whereas error bars signify one standard deviation in each direction. Data were taken from Tables 1.2, 1.3, and 1.4.

neither of these approaches has since been applied in a generalizable or user-friendly fashion to experimental 3D ED datasets. More recent work by Dominiak and co-workers [144, 145] has focused on refining 3D ED data against aspherical ESP produced by applying the Mott-Bethe formula to multipolar electron density distributions tabulated in databases such as ELMAM2 [146]. Nonetheless, this method ultimately led only to an incremental (1-2%) improvement in refinement R-factors, suggesting that the isolated atom model—although imperfect—is fairly accurate for neutral atoms, particularly at high resolution. For charged species, however, isolated electron scattering factors' sharp divergence to infinity is likely a significant exaggeration of ionic ESP in crystal structures, where excess charge is either balanced by the presence of proximal counterions or diluted by non-covalent interactions such as hydrogen bonding. To indirectly account for this, it is helpful to introduce fractionally charged scattering factors, which can provide a proxy for modelling effective, partial, or delocalized charge.

1.6.2 Charged Species

Historically, several 2D electron crystallographic studies had already demonstrated that ionic electron scattering factors' divergent behavior as $s \rightarrow 0$ renders ED uniquely capable of differentiating neutral atoms and ionized states. Grigorieff *et al.* observed effects consistent with negative charge in their 3.5 Å 2D ED structure of bacteriorhodopsin, where they visualized weakly resolved electrostatic potential enveloping the carboxylate termini of aspartate and glutamate side chains [147]. Similar findings were reported by Fujiyoshi and co-workers, who recorded systematically absent ESP for several putatively deprotonated Asp and Glu residues in bacteriorhodopsin at 3.0 Å [148]. These artifacts materialized most prominently in low-resolution shells, where ionic electron scattering amplitudes diverge strikingly from their neutral counterparts. Kimura *et al.* provided a compelling validation of theory by calculating experimental ESP maps omitting low-resolution reflections, which regenerated positive density around ionized carboxylates [149]. Intriguingly, Fujiyoshi and co-workers also visualized negative peaks on backbone carbonyl O atoms in Fourier difference maps computed assuming neutral electron scattering factors, suggesting experimentally observable partial charge even on formally neutral moieties. Indeed, Fujiyoshi and co-workers obtained slightly diminished refinement R-factors by assigning fractional charges of +0.5 and –0.5 to carbonyl C and O atoms, respectively. Later work by Hirai *et al.* further validated a range of these observations via computational simulations of charged states [150]. In addition to these extensive studies on proteins, ionic ESP has also been analyzed quantitatively in inorganic salts, where bonding features far less covalent character [151, 152].

A string of investigations by Yonekura and co-workers has propelled the study of ionized states into 3D ED territory [153, 154, 155]. Their results have largely reproduced the effects previously observed by their 2D predecessors: anions contribute negative density to ESP maps, whereas cations lead to modest enhancements in scattering power. In parallel, Wang has catalogued a variety of artifacts in ESP maps which may indicate the presence of deprotonated carboxylates incorrectly modeled as neutral oxygen atoms [119]. Specifically, several experimental 3D ED structures feature (a) strong negative peaks localized on carboxylate O atoms in Fourier difference maps calculated presuming neutral electron scattering factors, (b) weak or nonexistent density enveloping these O atoms in experimental ESP maps, and (c) aberrantly high, physically absurd *B*-factors associated with the offending atoms. Ions mistreated in this way would also increase refinement *R*-factors. Yonekura and co-workers managed to mitigate this via implementation of fractionally charged scattering factors [154]. Collectively, these studies underscore the necessity of integrating treatment of charged states as a routine facet of 3D ED analysis. Although this has been thwarted by the nonexistence of appropriately parameterized scattering factors, we hope tools like FAES and the ScatCurve package [154] developed by Yonekura and Maki-Yonekura clear a path toward refinement of ionic species in 3D ED data.

Finally, a currently underexplored strategy to unequivocally validate differences resulting from charge is joint refinement [156] of 3D ED structures alongside corroborating X-ray diffraction data. Since electron density in X-ray structures is universally positive and comparatively insensitive to charge, ESP from 3D ED could potentially convey complementary information about ionized states. Furthermore, 3D ED usually suffers from relatively low completeness; this is easily rectified by addition of X-ray data, which is typically highly redundant and much more complete. More uncharted territory is also provided by the prospect of joint refinement with neutron diffraction, which could serve as a useful cross-validation metric for localization of hydrogen atoms [157, 158]. For instance, 3D ED has already demonstrated its potential to elucidate structures of transition-metal hydrides [159], a family of organometallic complexes which has historically relied on single-crystal neutron diffraction for solid-state detection of H atoms [160]. Although the hydride ligand carries a formal negative charge, many species classified as "hydrides" nevertheless display acidic properties. 3D ED offers the tantalizing possibility of evaluating hydridic character via analysis of ionic ESP, whereas neutron diffraction can easily corroborate spatial positions of H atoms. Interestingly, however, bond lengths involving H atoms will likely prove slightly inconsistent between ED, XRD, and neutron diffraction, as these three forms of incident quanta all interact with hydrogen in appreciably different ways. Incident electrons experience perturbation due to both positively charged nuclei and atomic charge density projected by the electron cloud, placing them in between the two extremes of X-rays (which interact solely with the cloud) and neutrons (which interact solely with atomic nuclei). Such variability has already been noted in a 0.75 Å ED structure of a prion protofibril [161], as well as a 1.22 Å single-particle cryo-EM structure of apoferritin [162]. In both these cases, individual H atoms in Fourier difference maps appeared consistently different from their putative X-ray positions, indicating observable deviation from the idealized geometry of the riding model. Joint refinement would allow for a detailed analysis of such discrepancies.

1.6.3 Energy Filtration

Every practical aspect of crystallography is substantially influenced by the energy of the incident quanta. Thanks to the energy-time uncertainty principle, a perfectly coherent beam is forbidden by quantum mechanics, and the incident energy of the impinging electrons is properly described as a statistical distribution (with a full-width half-maximum of ΔE) in lieu of a discrete value E [15]. Typical TEM instruments suitable for 3D ED employ either field-emission guns (FEGs) or thermionic cathodes (containing tungsten hairpin filaments or lanthanum hexaboride crystals) as electron sources, all of which feature their own characteristic ΔE ranges. FEGs generate an especially coherent beam, with an energy spread ΔE of <0.7 eV; W filaments and LaB_6 crystals exhibit less monochromatic ΔE values of 1.5-3 eV and 1-2 eV, respectively [15]. Nevertheless, 3D ED structures have been routinely solved using instruments employing all three sources, which compare favorably to the monochromaticity obtained using an in-house X-ray diffractometer. In HRTEM imaging, ΔE has direct experimental repercussions; in reciprocal space, its influence on phase contrast is captured by a damped envelope function which delineates the maximum achievable resolution for an image. Such chromatic aberration (resulting from inherent fluctuations in energy within the incident beam) is also reflected in measured diffraction patterns, albeit more indirectly; it effectively causes the surface of the Ewald sphere to thicken. However, its influence on diffraction is not quite as consequential as its impact on imaging. Indeed, ΔE is quite small compared to the energy dispersion induced by the complex set of elastic and inelastic scattering events arising from the beam impinging upon an illuminated crystal.

In this context, post-specimen energy filtration (achieved, for example, via installation of a post-column bent electromagnet between the TEM's intermediate and projector lenses) is an impactful and currently underutilized strategy in 3D ED. Energy filtration allows selective exclusion of any scattered electrons which suffered some degree of energy loss (resolved, for instance, within windows of 10, 50, or 100 eV). Theoretically, diffraction signal is contributed largely by elastically scattered quanta residing within or very near the zero-loss peak, whereas inelastically scattered electrons mostly generate diffuse noise. Zero-loss energy filtration purges any evidence of inelastic scattering events polluting regions of reciprocal space proximal to Bragg reflections. Consequently, it significantly augments the accuracy of integrated intensities [164].

This phenomenon is especially well-illustrated by filtration of diffraction recorded from thick, frozen-hydrated specimens. In these systems, a substantial fraction of scattering signal is contributed by amorphous solvent and vitreous ice. For instance, in protein crystals, unfiltered ED patterns often feature a dense halo of low-frequency noise protruding radially from the central beam. By using an in-column energy filter, Yonekura and co-workers demonstrated that much of this detrimental noise is easily eliminated; energy filtration (with a slit width of 10 eV relative to the zero-loss peak) resulted in a pronounced enhancement in signal-to-noise for all reflections [164, 165, 166]. Furthermore, removal of inelastically scattered electrons disinterred a range of low-resolution reflections previously occluded by the diffuse penumbra emanating from the central beam (a dramatic illustration is provided by Figure 4 in reference [166]). Since Bragg peaks at mid-to-low spatial frequencies encipher crucial information about scattering differences between elements (as well as distinctions between neutral atoms and charged states), unveiling these reflections could have deeper consequences beyond more accurate integration of intensities. For instance, in addition to enabling proper refinement of ionized species, accentuation of scattering differences could potentially facilitate experimental phasing by multiple isomorphous replacement (MIR). Since discrepancies between elements become comparatively muted in ED versus XRD, MIR has been proposed [167] but never convincingly demonstrated in ED. Presumably the likelihood of reliably detecting these discrepancies would grow if energy filtration enabled facile detection and integration of low-resolution reflections. Similar logic applies to radiation-induced phasing, which has been attempted [168] but rather unconvincingly.

Intriguingly, inelastically scattered electrons which undergo relatively small energy losses can also end up within the vicinity of Bragg peaks. In fact, unfiltered Bragg reflections really represent a coalescence of signal from singular and multiple elastic scattering in tandem with a non-negligible fraction of inelastic scattering events. By removing any contributions from inelastic collisions, zero-loss energy filtration would in principle provide a more accurate measurement of multiple elastic scattering [123]. Dynamical refinement would presumably profit considerably from this. Although dynamical refinement explicitly seeks to treat effects arising from multiple elastic scattering, it is currently challenged by the prospect of accurately accounting for inelastically scattered electrons also contributing to individual integrated intensities. Finally, despite yielding cleaner diffraction patterns, energy filtration's extraction of inelastically scattered signal comes at the expense of attenuating the intensities of weak, high-resolution reflections. This tradeoff indicates that the net impact of energy filtration on 3D ED is likely to be nuanced, and future investigations would benefit from a systematic comparison of data reduction and refinement statistics against filter slit width.

1.6.4 Absolute Structure and Absolute Configuration

An especially impactful aspect of X-ray crystallography is its ability to routinely determine the absolute configuration of individual stereocenters in chiral molecules [169]. X-ray diffraction's sensitivity to chirality is conferred by anomalous dispersion, a resonant scattering effect which leads to enantiospecific violation of Friedel's law [170]. Analogously, in electron diffraction, a similar breakdown of Friedel symmetry is caused by multiple elastic scattering [30, 31]. Recent work by Brázda *et al.* has shown that this discrepancy is detectable using dynamical refinement, which permits discrimination between enantiomers via an R-factor comparison against the inverted structure [171]. This approach derives its sensitivity to chirality from an incorporation of dynamical effects into computation of F_{calc} (distinguishing it from a standard kinematical refinement, where enantiomorphic crystals would yield identical distributions of calculated structure factors and therefore identical R-values). Initially, however, this type of procedure may appear somewhat counterintuitive, as methodological developments in 3D ED have followed a trajectory specifically intended to diminish the effects of multiple scattering [17]. For instance, electron diffraction patterns collected via continuous rotation have proven generally devoid of dramatic dynamical artifacts. Today's status quo is a far cry from historical work, where aberrations such as violation of systematic absences were both very strong and routinely observed [14]. To quote Dorset [172], "certainly the existence of higher voltage sources than used in pioneering work allows the quasi-kinematical approximation to be satisfied for samples that would have caused problems" in the past. In this context, it remains somewhat unclear exactly how much dynamical diffraction is (a) quantifiably present in 3D ED patterns and (b) strictly necessary to reliably detect disruption of Friedel symmetry and confidently assign absolute structure.

To further develop the analogy to conventional X-ray crystallography, XRD's capacity to detect absolute chirality is directly tethered to the strength of the observed anomalous signal. As a result, X-ray methods did not always yield a reliable readout of absolute chirality in systems where resonant scattering was inherently weak, such as organic compounds composed entirely of lighter atoms. These cases necessitated the development of alternative statistical approaches with heightened sensitivity to differences in Bijvoet pair intensity, such as the Bayesian methods outlined by Hooft and co-workers [173]. In 3D ED, a rigorous examination of dynamical scattering's sensitivity to several similarly intertwined variables is currently lacking. For instance, parameters such as accelerating voltage, elemental composition, defects or imperfections in lattice structure, and variable thicknesses across datasets merged from several crystals would all systematically alter the probability of multiple elastic scattering. In cases where nanocrystals have been milled to thicknesses at or below the elastic mean free path of the material, dynamical scattering is expected to be weak or unobservable. Nevertheless, the outlook for 3D ED appears promising, as recent work by Klar *et al.* has extended the scope of dynamical refinement to a range of datasets collected using continuous rotation [174]. An encouraging experiment reported by Klar *et al.* involves a double-blind comparison against analogous X-ray data collected on a chiral zeolite. In this case, dynamical refinement on 3D ED data returned internally consistent results with an independent assessment of absolute structure made via the Flack parameter. Remaining challenges include implementation in a realistic case where absolute chirality is genuinely unknown, such as a crystalline sample obtained from a synthetic mixture with poor enantiomeric excess. Intriguingly, simulations by Spence and Donatelli have suggested that retrieval of chirality via exploitation of dynamical effects is thwarted both by very low thicknesses and by very high thicknesses [175]. A detailed experimental investigation of the conditions under which this approach is expected to falter is still required. Regardless, in the absence of appreciable dynamical signal, 3D ED remains perfectly capable of inferring stereochemistry relative to an internal chiral reference, such as another stereocenter whose absolute configuration is known *a priori*. One viable strategy to achieve this involves cocrystallization with enantiopure additives [176].

1.7 Applications

1.7.1 Amyloids and LARKS

Continuous-rotation 3D ED has emerged as a highly useful tool for studying the atomic structure of amyloid-forming peptides. A wide range of proteins can access the amyloid state, which is marked by dense fibrillar aggregates of interdigitated β-sheets cross-linked by hydrogen bonds [177, 178]. Accumulation of these aggregates is implicated in several fatal diseases, such as transmissible spongiform encephalopathy, Alzheimer's disease, Parkinson's disease, and Huntington's chorea. Amyloid fibrils exhibit a characteristic left-handed helical twist arising from their cross-β-sheet architecture. This makes it difficult for amyloidogenic proteins to crystallize in the fibrillar state, since the translational symmetry imposed by the Bravais lattice forcibly restricts their ability to twist [178]. Usually, the ensuing buildup of lattice strain prohibits the growth of X-ray-scale crystals. An analogous set of circumstances is presented by intrinsically disordered

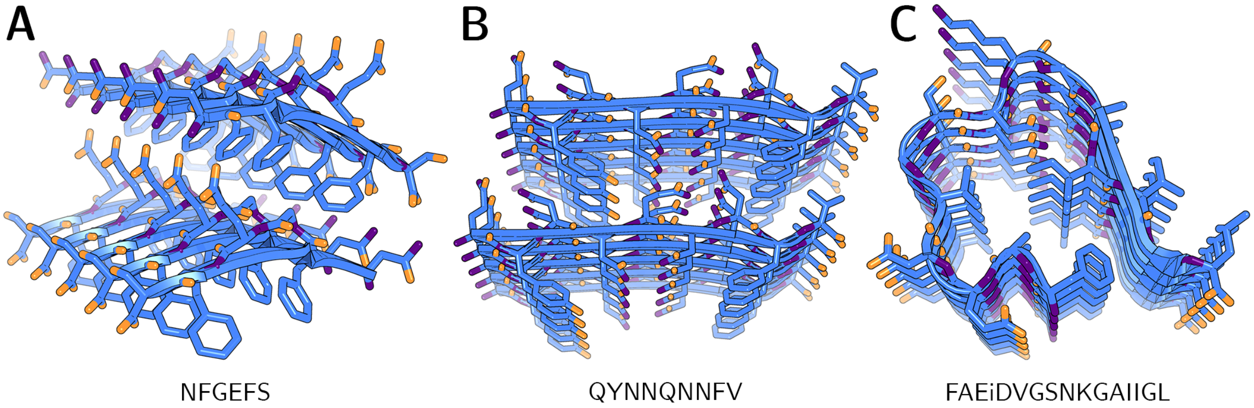

Figure 1.8: ***Ab initio* atomic-resolution 3D ED structures of three novel oligopeptide fragments derived from pathologically relevant proteins.** Carbon atoms and the peptide backbone are rendered in blue, oxygen atoms in orange, and nitrogen atoms in purple. (A) 1.0 Å resolution structure of ^{312}NFGEFS^{317} (PDB: 5WKB), a hexapeptide segment from the low-complexity domain of the A315E familial mutant of TAR DNA-binding protein 43. (B) 0.75 Å resolution structure of ^{168}QYNNQNNFV^{176} (PDB: 6AXZ), a nonapeptide segment from the $\beta2$–$\alpha2$ loop of the bank vole prion protein. (C) 1.1 Å resolution structure of ^{20}FAEiDVGSNKGAIIGL^{34} (PDB: 6OIZ), a 15-residue segment from wild-type amyloid-beta.

proteins (IDPs) containing low-complexity aromatic-rich kinked segments (LARKS), which often congeal into semi-solid hydrogels [179]. These species also exhibit amyloid-like cross-β-sheet morphology, although fibrils formed by LARKS appear more susceptible to chemically induced denaturation than their amyloid counterparts.

In 2001, Eisenberg and co-workers discovered that short oligopeptide fragments (4-7 residues) of amyloidogenic proteins do form microcrystals amenable to synchrotron X-ray diffraction at microfocus beamlines [180, 181]. Nevertheless, these peptides' propensity to crystallize tended to diminish with increasing sequence length, and a number of species continued to stubbornly resist X-ray-scale crystallization. These circumstances prompted a prescient attempt at electron diffraction of nanocrystalline GNNQQNY, a seven-residue peptide from the yeast prion protein Sup35 [35]. Remarkably, GNNQQNY nanocrystals divulged clear Bragg peaks at comfortably sub-angstrom (0.7 Å) resolution, and the corresponding diffraction patterns permitted indexing of reasonable orthorhombic unit cell parameters. Despite their ultrahigh resolution, these 3D ED data were recorded as a discrete tilt series of still frames, which apparently thwarted reliable integration of diffracted intensities. In addition to prohibitively partial sampling of Bragg reflections, Diaz-Avalos *et al.* observed weak violations of 2_1 systematic absences, suggesting some degree of distortion by multiple scattering.

Although this initial foray into electron diffraction did not allow full structure elucidation, this study clearly foreshadowed future success, which arrived twelve years later. For nearly a decade, the 11-residue core of the amyloidogenic protein alpha-synuclein (termed NACore), a key component of Lewy bodies in Parkinson's disease, had yielded only submicrometric crystals invisible to optical microscopy. Despite years of extensive attempts at X-ray-scale crystallization, this species exclusively formed nanocrystals with dimensions smaller than the wavelength of visible light. In 2015, Rodriguez *et al.* subjected frozen-hydrated NACore nanocrystals to electron diffraction using continuous rotation, which facilitated accurate integration of intensities out to a resolution of 1.4 Å [182]. These data were successfully phased via molecular replacement to yield the first novel solid-state structure solved by continuous-rotation ED. Subsequent reinvestigation of GNNQQNY by Sawaya *et al.* once again yielded high-resolution diffraction (1.0-1.1 Å), this time amenable to successful structure determination via direct methods [183]. Notably, continuous rotation greatly minimized the presence of dynamical scattering artifacts, which failed to impede *ab initio* phasing.

Since these proof-of-concept studies, a slew of amyloidogenic peptide fragments, as well as a smaller subset of LARKS, has been investigated by continuous-rotation 3D ED (Table 1.2). These include segments derived from human islet amyloid polypeptide [184], several isoforms of tau [185, 186], TAR DNA-binding protein 43 [187, 188], bank vole prion protein [161], the ice-nucleation protein InaZ [189], amyloid-beta [190, 191], heterogeneous nuclear ribonucleoprotein A1 [192], fused in sarcoma (FUS) [179, 193, 194], and nuclear pore complex protein 98 [179]. Several of these reports exploited the atomic-resolution information provided by 3D ED to design small-molecule or peptide inhibitors of amyloid fibril aggregation, highlighting 3D ED's potential to elucidate key structural details relevant to drug discovery. Many of these amyloidogenic peptide structures ultimately tell a similar story: in addition to collectively displaying canonical amyloid-like features such as steric zippers, several refused to yield X-ray-scale crystals despite considerable effort. A fairly typical example is Guenther *et al.*'s 1.0 Å structure of NFGEFS [187] (Figure 1.8A), which features face-to-back packing of parallel in-register sheets. Additionally, Gallagher-Jones *et al.*'s 0.75 Å structure of QYNNQNNFV [161] unveiled a unique structural motif termed a polar clasp (Figure 1.8B), whereas Warmack *et al.*'s 1.1 Å structure of the 15-residue peptide FAEiDVGSNKGAIIGL extended the scope of direct methods to the lengthiest sequence yet (Figure 1.8C). Finally, Zhou *et al.*'s 0.6 Å structure of SYSGYS [194], a hexapeptide derived from the low-complexity domain of FUS, is noteworthy for its unusually granular resolution, although this species has also been solved at 1.1 Å via synchrotron X-ray diffraction [179].

Parent protein	Amino acid sequence	PDB record	Phasing method	Resolution (Å)	Space group	$R_{\text{work}}/R_{\text{free}}$	Reference (DOI)
Alpha-synuclein (68-78)	GAVVTGVTAVA	4RIL	MR	1.4	C2	0.248/0.275	`10.1038/nature15368`
Alpha-synuclein (47-56)	GVVHGVTTVA	4ZNN	MR	1.4	$P2_1$	0.235/0.282	`10.1038/nature15368`
Amylin (19-29, S20G)	SGNNFGAILSS	5KNZ	MR	1.9	$P2_12_12_1$	0.228/0.275	`10.7554/eLife.19273`
Amylin (15-25)	FLVHSSNNFGA	5KO0	MR	1.4	P1	0.225/0.259	`10.7554/eLife.19273`
Sup35 (8-13)	Zn-NNQQNY	5K2E	DM	1.0	$P2_1$	0.152/0.194	`10.1073/pnas.1606287113`
Sup35 (8-13)	Cd-NNQQNY	5K2F	DM	1.0	$P2_1$	0.220/0.241	`10.1073/pnas.1606287113`
Sup35 (7-13)	GNNQQNY	5K2G	DM	1.1	$P2_1$	0.187/0.224	`10.1073/pnas.1606287113`
Sup35 (7-13)	GNNQQNY	5K2H	DM	1.05	$P2_12_12_1$	0.177/0.186	`10.1073/pnas.1606287113`
Tau (306-311)	VQIVYK	5K7N	DM	1.1	C2	0.210/0.223	`10.1038/nmeth.4178`
Tau (591-600)	KVQIINKKLD	5V5B	MR	1.5	$P2_1$	0.190/0.213	`10.1038/nchem.2889`
Tau (592-597)	VQIINK	5V5C	MR	1.25	$P2_12_12$	0.219/0.266	`10.1038/nchem.2889`
Tau (305-310)	SVQIVY	6ODG	DM	1.0	$P2_1$	0.245/0.266	`10.1074/jbc.RA119.009688`
TDP-43 (333-343)	SWGMMGMLASQ	6CFH	MR	1.5	P1	0.280/0.313	`10.1038/s41594-018-0064-2`
TDP-43 (312-317, A315pT)	NFGpTFS	6CF4	DM	0.75	$P2_12_12_1$	0.232/0.251	`10.1038/s41594-018-0064-2`
TDP-43 (312-317, A315E)	NFGEFS	5WKB	DM	1.0	$P2_12_12$	0.220/0.270	`10.1038/s41594-018-0064-2`
TDP-43 (247-257)	DLIIKGISVHI	5W52	MR	1.4	P1	0.262/0.306	`10.1038/s41594-018-0045-5`
BvPrP (168-176)	QYNNQNNFV	6AXZ	DM	0.75	P1	0.242/0.246	`10.1038/s41594-017-0018-0`
BvPrP (168-176, Y169F)	QFNNQNNFV	7RVF	DM	1.0	P1	0.221/0.251	`10.3389/fnins.2022.960322`
Mouse prion protein (168-176)	QYSNQNNFV	7RVD	DM	1.0	P1	0.201/0.250	`10.3389/fnins.2022.960322`
Human prion protein (168-176, S170N)	EYNNQNNFV	7RVE	DM	0.85	P1	0.218/0.266	`10.3389/fnins.2022.960322`
Human prion protein (169-175, Y169G)	GSNQNNF	6CLC	DM	1.01	P1	0.159/0.178	`10.1016/j.str.2018.03.021`
InaZ (707-712)	rac-GSTSTA	6M9J	DM	0.9	$P2_1/c$	0.233/0.252	`10.1107/S2052252518017621`
InaZ (707-712)	GSTSTA	6M9I	DM	0.9	$P2_12_12_1$	0.217/0.232	`10.1107/S2052252518017621`
Nup98 (116-123)	GFGNFGTS	6BZM	DM	0.9	P1	0.226/0.264	`10.1126/science.aan6398`
Amyloid-beta (20-34, D23iD)	FAEiDVGSNKGAIIGL	6NB9	DM	1.05	$P2_1$	0.198/0.246	`10.1038/s41467-019-11183-z`
Amyloid-beta (20-34)	FAEDVGSNKGAIIGL	6OIZ	DM	1.1	$P2_1$	0.194/0.213	`10.1038/s41467-019-11183-z`
Amyloid-beta (24-34)	VGSNKGAIIGL	5VOS	MR	1.42	$P2_1$	0.234/0.292	`10.1074/jbc.M117.806109`
HNRPA1 (209-217)	GFGGNDNFG	6J60	DM	0.96	$P2_12_12_1$	0.233/0.248	`10.1038/s41467-019-09902-7`
Fused in sarcoma (77-82)	STGGYG	6BZP	DM	1.1	$P2_12_12_1$	0.219/0.255	`10.1126/science.aan6398`
Fused in sarcoma (37-42)	SYSGYS	5XSG	DM	0.73	$P2_1$	0.261/0.289	`10.1038/s41594-018-0050-8`
Fused in sarcoma (37-42)	SYSGYS	6KJ1	DM	0.65	$P2_1$	0.229/0.240	`10.1021/acs.analchem.9b01162`
Fused in sarcoma (37-42)	SYSGYS	6KJ3	DM	0.6	$P2_1$	0.307/0.326	`10.1021/acs.analchem.9b01162`
Tau (591-599)	KVQIINKKL	6NK4	MR	1.99	$P6_1$	0.260/0.299	`10.1073/pnas.2014139118`
Amyloid-beta (16-26, D23N)	KLVFFAENVGS	6O4J	MR	1.4	$P2_1$	0.237/0.283	`10.7554/eLife.46924`
OsPYL/RCAR5 (24-29)	AVAAGA	6UOR	DM	0.9	$P2_12_12_1$	0.206/0.240	`10.1107/S2052252520004030`
LECT2 (63-71)	GSTVYAPFT	7N2I	FBP	1.4	C2	0.193/0.192	`10.1021/acsbiomedchemau.2c00082`
CPEB3 (154-161)	QIGLAQTQ	7N2F	FBP	1.2	$P2_1$	0.202/0.233	`10.1021/acsbiomedchemau.2c00082`
CPEB3 (154-161)	QIGLAQTQ	7N2G	FBP	1.2	$P2_12_12_1$	0.192/0.236	`10.1021/acsbiomedchemau.2c00082`
New1p (repeat)	NYNNYQ	7N2K	FBP	1.3	$P3_1$	0.161/0.185	`10.1021/acsbiomedchemau.2c00082`
BvPrP (168-176, Q172E)	QYNNENNFV	7N2J	FBP	1.5	P1	0.174/0.227	`10.1021/acsbiomedchemau.2c00082`
Human ZFP 292 (534-542)	FRNWQAYMQ	7N2D	FBP	1.5	C2	0.207/0.258	`10.1021/acsbiomedchemau.2c00082`

Table 1.2: **List of selected amyloid or amyloid-adjacent 3D ED structures deposited in the PDB**. Abbreviations used: MR = molecular replacement, DM = direct methods, FBP = fragment-based phasing, pT = phosphorylated L-threonine, rac = racemic, iD = L-isoaspartic acid, BvPrP = bank vole prion protein, HNRPA1 = heterogeneous nuclear ribonucleoprotein A1, CPEB3 = cytoplasmic polyadenylation element binding protein 3.

1.7.2 Small Molecules

In 2018, the near-simultaneous release of two papers by Gruene *et al.* [195] and Jones *et al.* [196] generated an abrupt resurgence of interest in applying continuous-rotation ED techniques to small molecules [197, 198, 199]. By this point, a considerable number of small-molecule structures had already been deciphered by 3D electron crystallography (by Dorset, Abrahams, Hovmöller, Kolb, and others, in addition to an extensive body of historical work by Vainshtein). Nevertheless, these two reports transformed the landscape of 3D electron crystallography by re-exposing its potential to a non-specialist audience. Synthetic chemists, for instance, frequently produce small quantities of seemingly amorphous powders recalcitrant to X-ray-scale crystallization. In this context, ED's ability to extract atomic-resolution diffraction from nanocrystals is potentially liberating.

For instance, Jones *et al.* [196] solved a 0.77 Å structure of synthetic (+)-limaspermidine from a few mg of solid residue obtained after *in vacuo* evaporation of eluent from flash column chromatography (Figure 1.9A). Furthermore, Jones *et al.* went on to determine four independent structures of biotin, acetaminophen, cinchonine, and brucine from a heterogeneous mixture of powders deposited on a single grid. At the bulk scale, overlapping signals from different components in this mixture would likely have prohibited clear disambiguation via X-ray powder diffraction or NMR spectroscopy. These results demonstrated how ED could function as a powerful addition to the synthetic chemist's toolbox. Not only does ED slot conveniently into established purification workflows—often obviating any need for formal recrystallization—it also offers elusive solid-state structural information potentially inaccessible via conventional methods.

A handful of small-molecule studies have rapidly delivered on this promise; two illustrative examples are highlighted here. Andrusenko *et al.* elucidated a 0.9 Å 3D ED structure of orthocetamol, a regioisomer of the antipyretic paracetamol (Figure 1.9B) [200]. This simple compound exhibits a bizarre morphology in which assemblies of nanocrystals coalesce into flat quadrilateral platelets up to 300 μm in length. To further complicate matters, these tetragonal conglomerates display high susceptibility to pseudo-merohedral twinning. These characteristics had thwarted

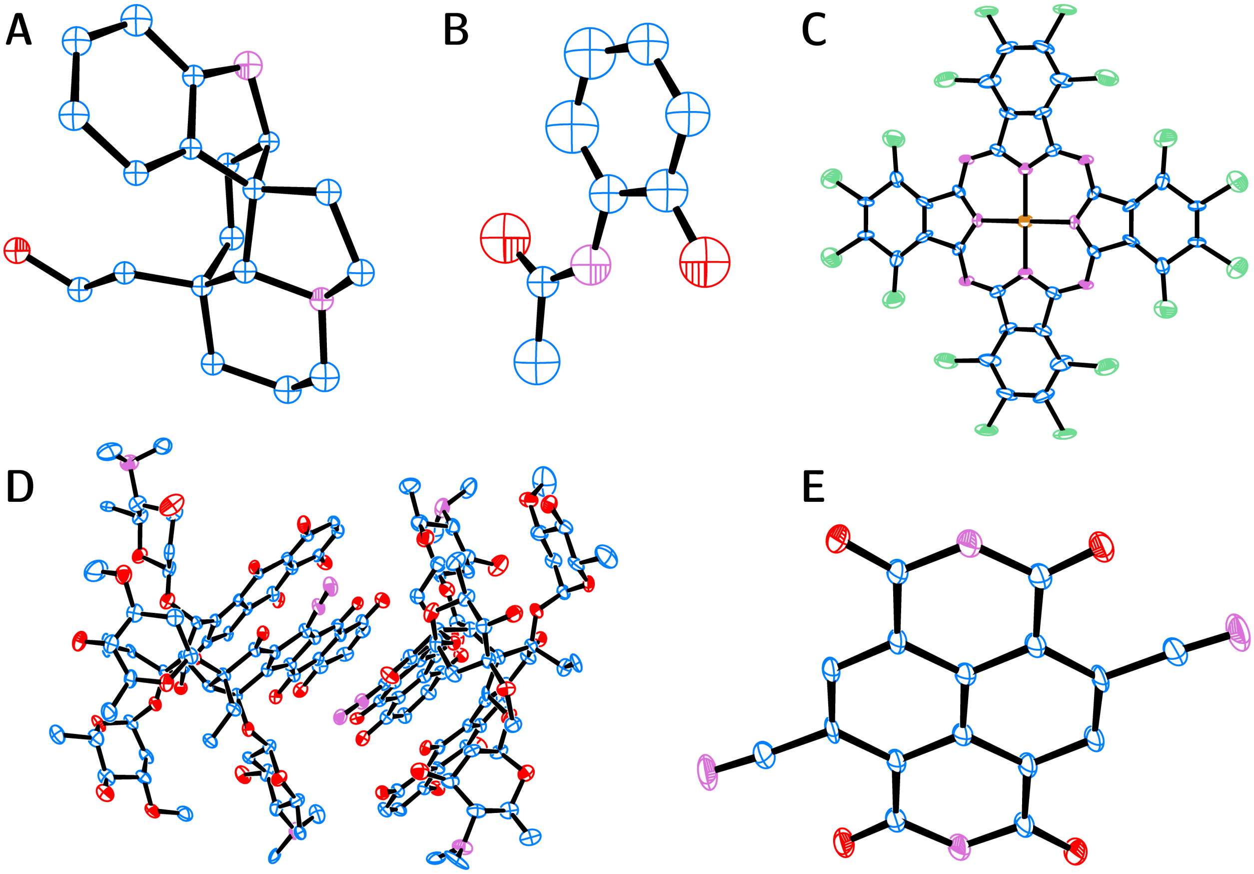

Figure 1.9: **ORTEP diagrams of five *ab initio* small-molecule 3D ED structures**, with H atoms omitted. Carbon atoms are rendered in blue, nitrogen atoms in lilac, oxygen atoms in red, chlorine atoms in sea green, and copper atoms in orange. All thermal ellipsoids are drawn at 50% probability except for compound D, which is depicted at 15% for clarity. (A) 0.77 Å resolution structure of synthetic (+)-limaspermidine (CSD: CAHKUU01), a monoterpene indole alkaloid featuring a *cis*-fused azadecalin core. Suitable microcrystals were obtained directly from flash column chromatography, without any formal recrystallization. (This compound did not undergo *B*-factor refinement, so its thermal ellipsoids do not carry any physical meaning.) (B) 0.9 Å resolution structure of the analgesic orthocetamol (CSD: WOFXEX), refined isotropically. (C) 0.8 Å resolution structure of the viridian pigment copper(II) perchlorophthalocyanine (CSD: UZEMIY), refined anisotropically. (D) 1.05 Å resolution structure of the genotoxic natural product (−)-lomaiviticin C (CSD: ERUHEH), featuring two independent molecules in the asymmetric unit. (E) 0.57 Å resolution structure of the organic semiconductor dicyanonaphthalene diimide (CSD: TUKVON), refined anisotropically. This entry represents one of the highest-resolution small-molecule structures currently solved by 3D ED.

structure determination of orthocetamol by X-ray crystallography for over a century. Andrusenko *et al.*'s ED structure supplied an unambiguous solution to this perennial problem.

In a similar vein, Gorelik *et al.* [201] solved a 0.8 Å 3D ED structure of copper(II) perchlorophthalocyanine (also known as phthalo green or viridian), a widely used synthetic pigment (Figure 1.9C). Phthalo green is stubbornly insoluble in a remarkably wide range of solvents, which effectively precludes X-ray-scale recrystallization. Thanks to prior investigations by Uyeda *et al.* [202] and Dorset [172], ED had already established a partially complete structure of this compound. Although several subtleties remained unclear, this organometallic species had nonetheless become something of a poster child for ED, appearing on the cover of Dorset's 1995 textbook *Structural Electron Crystallography*. Gorelik *et al.*'s data capped off the copper(II) perchlorophthalocyanine saga by confirming earlier results with a complete 3D structure. These cases demonstrated 3D ED's ability to resolve two longstanding quandaries in conventional X-ray crystallography with ease.

Compound name	Empirical formula	CSD record	Year	Resolution (Å)	Space group	$R1$	Reference (DOI)
Biotin	$C_{10}H_{16}N_2O_3S$	BIOTIN13	2018	0.9	$P2_12_12_1$	17.81	10.1021/acscentsci.8b00760
Carbamazepine	$C_{15}H_{12}N_2O$	CBMZPN28	2016	0.8	$P2_1/n$	25.45	10.1107/S2053273315022500
Epicorazine A	$C_{18}H_{16}N_2O_6S_2$	BISGAO	2019	0.83	$P2_12_12_1$	15.43	10.1107/S2053273318013918
Dehydrocurvularin	$C_{16}H_{18}O_5$	IRELOH01	2019	0.82	$P2_12_12_1$	14.95	10.1107/S2053273318013918
(+)-Limaspermidine	$C_{19}H_{26}N_2O$	CAHKUU01	2018	0.77	$P2_12_12_1$	18.22	10.1021/acscentsci.8b00760
Cimetidine	$C_{10}H_{16}N_6S$	CIMETD06	2019	1.0	$C2/c$	19.69	10.1038/s41467-019-11469-2
Cinchonine	$C_{19}H_{22}N_2O$	CINCHO11	2018	1.0	$P2_1$	17.80	10.1021/acscentsci.8b00760
Schwartz's reagent	$C_{24}H_{34}Cl_2Zr_2$	DIZZUK	2019	1.15	$Pnnm$	14.95	10.1021/acscentsci.9b00403
Pd(II) ethylene insertion product	$C_{36}H_{40}B_{18}O_2P_2Cl_{18}Pd_2$	DOBBEE	2019	0.9	$P\bar{1}$	18.22	10.1021/acscentsci.9b00403
Pd(dba)(PHOX)	$C_{43}H_{43}NO_2PPd$	DOBCAB	2019	1.0	$P2_12_12_1$	14.32	10.1021/acscentsci.9b00403
Paracetamol (orthorhombic)	$C_8H_9NO_2$	HXACAN41	2018	0.8	$Pcab$	8.89[a]	10.1126/science.aak9652
Ibuprofen	$C_{13}H_{18}O_2$	IBPRAC20	2018	0.9	$P2_1/c$	25.41	10.1021/acscentsci.8b00760
Ni(dppf)Cl_2	$C_{34}H_{28}Cl_2FeNiP_2$	KADXESO2	2019	1.0	$Pna2_1$	11.25	10.1021/acscentsci.9b00403
Methylene blue derivative (MBBF_4)	$(C_{30}H_{31}N_7S)^{2+}$, 2 $(C_{30}H_{30}N_7S)^{+}$, 4 $(BF_4)^{-}$	LIMZAL01	2018	0.9	$C2/c$	25.83	10.1002/anie.201811318
Brucine	$C_{23}N_2O_4$	MAJRIZ02	2018	0.9	$P2_1$	18.29	10.1021/acscentsci.8b00760
[Co(ddpd)$_2$] $(BF_4)_2$	$(C_{34}H_{34}N_{10}Co)^{2+}$, 2 $(BF_4)^{-}$	MOTNUG	2015	1.2	$P2_1/c$	28.81	10.1002/ejic.201403200
Nicotinic acid	$C_6H_5NO_2$	NICOAC05	2016	0.75	$P2_1/c$	30.26	10.1107/S2053273315022500
Ethisterone	$C_{21}H_{28}O_2$	POSJAI01	2018	0.9	$P2_1$	22.21	10.1021/acscentsci.8b00760
Grubbs' catalyst (1st gen.)	$C_{43}H_{72}Cl_2P_2Ru$	IKORIK03	2019	0.85	$P2_1/n$	15.95	10.1021/acscentsci.9b00403
Progesterone	$C_{21}H_{30}O_2$	PROGST15	2018	0.9	$P2_12_12_1$	17.65	10.1021/acscentsci.8b00760
HKL-I-029	$C_{19}H_{17}NO_5$	QILJUT	2018	1.0	$P2_1/n$	22.23	10.1021/acscentsci.8b00760
n-Tritriacontane	$C_{33}H_{68}$	QQQFVD03	1999	N/A	$A2_1am$	21.00	10.1524/zkri.1999.214.4.223
HRh(CO) $(PPh_3)_3$	$C_{55}H_{46}OP_3Rh$	RCOHPH04	2019	1.0	$P2_1/n$	13.24	10.1021/acscentsci.9b00403
Fe(acac)$_3$	$C_{15}H_{21}FeO_6$	XAQVIX01	2019	0.9	$Pbca$	16.07	10.1021/acscentsci.9b00403
C_{68}-warped nanographene	$C_{68}H_{28}$	AQETUO	2021	0.85	$P4_2$	16.47	10.1021/jacs.1c00863
Loratadine	$C_{22}H_{23}N_2O_2Cl$	BEQGIN08	2020	1.2	$C2/c$	57.58	10.1039/D0CE01216E
(-)-Lomaiviticin C	$C_{68}H_{82}N_4O_{24}$	ERUHEH	2021	1.05	$P2_1$	12.06	10.1021/jacs.1c01729
Sofosbuvir/L-proline cocrystal	$C_{22}H_{29}FN_3O_9P$, $C_5H_9NO_2$	EYIQEL	2019	1.0	$P2_12_12_1$	9.62[a]	10.1126/science.aaw2560
Polycyclic indole-derived ester	$C_{19}H_{14}N_4O_2$	FABTIP	2020	0.83	$R\bar{3}$	15.77	10.1002/anie.202011253
Remdesivir	$C_{27}H_{35}N_6O_8P$	IQIMAZ02	2021	0.9	$P2_1$	16.09	10.1039/D1RA03100G
Glycine (α-polymorph)	$C_2H_5NO_2$	KUFDIB	2020	0.703	$P2_1/n$	21.88	10.1107/S2052252519016105
Dipyrrolidine perylene diimide	$C_{32}H_{24}N_4O_4$	LACPAJ01	2020	0.6	Cc	19.91	10.1039/D0CC00119H
Dicyanonaphthalene diimide	$C_{16}H_4N_4O_4$	TUKVON	2020	0.57	$P2_1/c$	13.76	10.1039/D0CC00119H
Diketopyrrolopyrrole	$C_{54}H_{70}N_8O_6S_2$	TUKVUT	2020	0.9	$P2_1/n$	23.5	10.1039/D0CC00119H
L-histidine	$C_6H_9N_3O_2$	LHISTD15	2019	0.88	$P2_12_12_1$	19.81	10.1038/s41467-019-11469-2
Nickel carbene complex	$C_{27}H_{31}N_3O_2Ni$	LUZZUE	2020	0.85	Pca_1	24.63	10.5517/ccdc.csd.cc26m422
[Fe(bpy)$_3$] $(PF_6)_2$	$(C_{30}H_{24}FeN_6)^{2+}$, 2 $(PF_6)^{-}$	NUZKOI13	2020	N/A	$P\bar{3}c1$	N/A[b]	10.5517/ccdc.csd.cc26m422
[11]helicene derivative	$C_{88}H_{92}O_{10}$	QADMUH	2020	1.0	$P2_12_12_1$	11.73	10.1002/ange.202012213
B/N-doped *p*-arylenevinylene	$C_{102}H_{114}B_2N_2$	SADGEN	2020	0.95	$P\bar{1}$	24.29	10.1021/jacs.0c10337
Spirophenylenevinylene	$C_{42}H_{26}O$	SUVJOL	2020	0.95	$P\bar{1}$	24.29	10.1246/bcsj.20200065
Copper(II) perchlorophthalocyanine	$C_{32}N_8Cl_{16}Cu$	UZEMIY	2021	0.8	$C2/m$	27.85	10.1107/S2052520621006806
Olanzapine/phenol cocrystal	$C_{17}H_{20}N_4S$, C_6H_6O	WACDEN	2020	1.0	$P\bar{1}$	31.40	10.1107/S2052520620012779
Tryptophan-derived oxindole	$C_{12}H_{14}N_2O_3$	YOYXAO	2019	0.9	$P2_1/c$	17.77	10.1021/jacs.9b09864
Glucopyranosyl uric acid derivative	$C_{11}H_{14}N_4O_8$	YURNIL	2020	1.0	$P1$	14.01	10.1021/acs.orglett.0c02038
Metaxalone	$C_{12}H_{15}NO_3$	ZUQXIV	2020	0.78	$P2_12_12_1$	38.95	10.1021/acs.cgd.0c00497
Orthocetamol	$C_8H_9NO_2$	WOFXEX	2019	0.9	$C2/c$	32.70	10.1002/anie.201904564
Bismuth subgallate	$C_7H_5BiO_6$	JAXSUZ	2017	0.7	$Pmna$	11.80	10.1039/C7CC03180G
Teniposide	$C_{32}H_{32}O_{13}S$	KUXJUL	2021	0.9	$P2_12_12_1$	9.76	10.3389/fmolb.2021.648603
Thiophene-fused cyclooctatetraene	$C_{36}H_{36}O_{12}NS_4$	AQECOR	2021	0.8	$P\bar{1}$	23.96	10.1021/jacs.1c00823

Table 1.3: **List of selected small-molecule 3D ED structures deposited in the CSD** as of October 2021. [a]Cases applying dynamical refinement. [b]CIF files do not contain any structure-factor amplitudes or phases, simply atomic coordinates.

In these examples, however, the atomic connectivity of both compounds was already well-established; 3D ED simply contributed a solid-state structure that reinforced what was previously known. In this context, Kim *et al.*'s 1.05 Å structure of (–)-lomaiviticin C [203] provides a compelling case where ED data spurred reevaluation of an existing structural assignment (Figure 1.9D). (–)-Lomaiviticin C is a genotoxic bacterial metabolite which has evaded twenty years of efforts aimed at total synthesis and X-ray-scale crystallization [204]. Intriguingly, this natural product (NP) contains an unusual monomeric aglycon moiety in which only 6 out of 19 carbon atoms feature bonds to hydrogen. This dearth of proton-attached carbons, in tandem with a high degree of unsaturation, rendered inference of connectivity quite challenging based on NMR spectroscopy alone. Ultimately, Kim *et al.*'s ED structure—alongside high-field (800 MHz) NMR spectroscopic studies and DFT calculations which further substantiated the ED assignment—corrected several errors originally caused by misinterpretation of fortuitously misleading HMBC coupling constants. This study underscores ED's vast potential to make impactful contributions to the elucidation of NPs, many of which feature some combination of forbidding structural complexity, scarcely available source material, and potentially inconclusive NMR data. In a field continually grappling with the myriad pitfalls associated with the analysis of complex 2D NMR spectra [205], the clarity provided by a corroborating crystal structure seems almost cathartic. Furthermore, when applied in tandem with comparative genomics or metabolomics [206] (to mine relevant biosynthetic gene clusters) and synthetic biology [207] (to express those genes in model organisms), 3D ED could also significantly accelerate the rate of NP discovery. More broadly, 3D ED is rapidly finding a complementary niche within the wider context of synthetic chemistry; a growing number of reports now feature 3D ED structures of relevant synthetic targets or intermediates which proved unsuitable for single-crystal XRD [208, 209, 210, 211, 212, 213, 214, 215, 216, 217, 218]. These structures include two noncanonical amino acids bearing all-carbon quaternary stereocenters [209], a trio of organic semiconductors solved at ultrahigh resolution (one of which is depicted in Figure 1.9E) [215], a family of electron-deficient expanded helicenes [212], a pentacyclic indole-derived ester [213], and a synthetic mimic of the cuboidal subunit in the oxygen-evolving complex of photosystem II [217].

Finally, 3D ED has also tackled a bevy of small-molecule active pharmaceutical ingredients (APIs), including carbamazepine [196, 221], niacin (nicotinic acid) [221], bismuth subgallate [222], ibuprofen [196], ethisterone [196], progesterone [196], biotin [196], paracetamol (acetaminophen) [139, 195, 196], cimetidine [223], loratadine [125], sofosbuvir [139], ramelteon [224], tolvaptan [224], olanzapine [225], epicorazine A [140], dehydrocurvularin [140], metaxalone [226], teniposide [227], remdesivir [228], and indomethacin [126]. Since many APIs exist natively as microcrystalline powders, 3D ED could potentially revolutionize solid-state structure determination in the pharmaceutical industry [227], where size-limited single-crystal XRD is currently the gold standard. Specifically, 3D ED's sensitivity to variable polymorphism at the nanoscale could provide crucial insights into API stability and solubility, as different polymorphs of the same drug can often display drastically disparate pharmacokinetic profiles [230, 231, 232]. For instance, in orally administered drugs, an API's immediate bioavailability is controlled partially by its rate of dissolution in the gastrointestinal tract, which can vary considerably as a function of altered lattice packing [233]. Ultimately, structural information supplied by 3D ED could play a pivotal role in guiding crystal engineering efforts [234] aimed at designing solvates, cocrystals, or polymorphs of APIs with optimized pharmacokinetic properties.

Undoubtedly, 3D ED has plenty of potential in this area. Despite the considerable hype [197, 198, 199], however, the interested synthetic chemist is confronted with several issues that warrant caution. Firstly, electrostatic potential maps cannot always distinguish between disparate elements as unambiguously as atomic charge density maps derived from X-ray diffraction. Unlike their X-ray counterparts, elastic electron scattering factors do not scale linearly or monotonically with Z. As a result, relative differences between elements become diminished, as discussed earlier. Therefore, electrostatic potential alone does not necessarily provide a self-sufficient means of differentiating neutral C, N, and O, particularly if the diffraction dataset samples heavily within the vicinity of 3 Å resolution. Indeed, *ab initio* phasing algorithms frequently assign these atoms interchangeably, particularly since they typically presume X-ray-scale scattering differences between elements. In these cases, even at the refinement stage, elemental identity is frequently arduous or impossible to deduce based solely on experimental difference Fourier maps. Given these limitations, if attempting to solve a novel structure such as a complex natural product (generally replete with heteroatoms such as O and N) via 3D ED, rigorous corroboration with external data from NMR spectroscopy and mass spectrometry remains essential [203, 208].

Secondly, 3D ED always requires well-formed single crystals. Serendipitously, many compounds may inhabit a specific "Goldilocks zone" where they refuse to form X-ray-scale crystals yet grudgingly aggregate into crystalline assemblies at the nanoscale. ED is well-equipped to solve structures which fit this profile. Nevertheless, ED is not a panacea; it cannot salvage genuinely amorphous substrates. Species which systematically failed to form macroscopic crystals—especially if such reluctance reflects thermodynamic instability in the crystalline state—could just as easily fail at the microscopic level. Before attempting 3D ED on seemingly amorphous material, X-ray powder diffraction (XRPD) is strongly recommended as a simple, effective test to screen for the presence of microcrystalline domains. If XRPD fails to yield clear, well-resolved rings, structure determination by ED is unlikely to succeed.

Thirdly, *ceteris paribus*, current 3D ED data quality is often inferior to X-ray data quality by a range of metrics (R_{meas}, $<I/\sigma(I)>$, and $\text{CC}_{1/2}$), although this gap is beginning to contract quickly for small molecules. An especially relevant statistic is completeness, since ED's coverage of reciprocal space is inherently limited by the restricted tilt range available to the TEM goniometer. The resultant "missing wedge" becomes particularly problematic if the space-group symmetry of the crystal is low or if orientation bias is severe. X-ray diffractometers can easily collect 360 degrees of data, unlocking regions of the reciprocal lattice potentially inaccessible by continuous-rotation ED. Moreover, some fraction of small molecules deemed "impossible" to solve by XRD may simply indicate a lack of rigorous screening. In macromolecular crystallography, screening thousands of crystallization conditions via high-throughput hanging-drop vapor diffusion is routine. Similar methods have not yet percolated widely into small-molecule work, where venerable techniques such as slow evaporation of layered solvents usually reign supreme.

Thus, molecules seemingly "uncrystallizable" for XRD may benefit considerably from a broader, more systematic exploration of crystallization conditions [235], as well as attempts at derivatization with crystallogenic functional groups such as ferrocene [236]. In fact, belatedly discovering conditions suitable for macroscopic X-ray-scale crystal growth is fairly common during the course of a thorough 3D ED investigation [237]. If this occurs, XRD remains the technique of choice for small-molecule structure determination. Although ED's lower size constraint confers a distinct advantage over XRD, high-flux microfocus beamlines can now produce tractable X-ray diffraction from microcrystals with dimensions as small as 1-10 μm [18]. Nevertheless, if X-ray-scale crystals prove genuinely impossible to obtain *despite rigorous effort*, ED is a powerful alternative which can match or surpass the resolution achieved by XRD. As the technique continues to mature, the development of specialized hardware engineered exclusively for ED will undoubtedly alleviate many current issues with data quality [238].

1.7.3 Proteins

Continuous-rotation electron diffraction was originally developed specifically for the purpose of interrogating three-dimensional macromolecular crystals [38, 89]. This work traces its origins to a venerable tradition of two-dimensional electron crystallography, where amplitudes derived from 2D diffraction patterns were historically paired with phases obtained via direct Fourier transform of real-space images [239, 240, 241]. Key milestones in this field include Henderson *et al.*'s 3.5 Å structure of bacteriorhodopsin [242] and Gonen *et al.*'s 1.9 Å structure of aquaporin [243], two intermembrane proteins whose biological roles naturally predispose formation of 2D crystals. In this context, continuous rotation emerged as a method to analyze proteins not innately suited to aggregating into 2D arrays. Shi *et al.*'s 2.9 Å structure of HEWL [38] represented the first protein successfully solved by 3D electron crystallography; it was rapidly followed by a suite of canonical soluble proteins well-studied by conventional X-ray methods [65]. Since these pioneering studies, however, 3D ED of proteins appears to have progressed more slowly than expected, especially when juxtaposed against the explosion of interest in small molecules. This is largely because sample preparation in macromolecular electron crystallography is typically much more laborious, and most major advances have therefore focused on methodological development in lieu of elucidating novel structures. For instance, a series of reports by Gonen and co-workers have demonstrated that continuous-rotation ED is procedurally compatible with focused ion-beam milling [244] and *in meso* crystallogenesis within lipidic cubic phases (LCPs) [245]. These techniques were applied in tandem to solve a 1.9 Å structure of the human A_{2A} adenosine receptor [245], marking a significant breakthrough for ED given the inherent difficulty of working with lipophilic membrane proteins. Another emphasis has been placed on soaking protein nanocrystals with solutions of pharmacologically relevant ligands to visualize their substrate-binding pockets. These efforts have culminated in a 2.5 Å structure of human carbonic anhydrase bound to the sulfonamide inhibitor acetazolamide [246], as well as a 3.0 Å structure of an HIV-1 Gag polyprotein fragment bound to the steroidal inhibitor bevirimat [247].

Interestingly, when contrasted with analogous structures solved by single-crystal XRD, macromolecular crystals have historically diffracted to worse resolution by 3D ED, typically by a factor of 1.5-2. For instance, despite the considerable number of proteinase K ED structures currently deposited in the PDB, none have surpassed a resolution finer than 1.5 Å. Nevertheless, as of June 2023, the PDB is replete with just over 100 sub-1.5 Å resolution X-ray structures of proteinase K, including several determined to sub-angstrom resolution. No such discrepancy has been observed with small molecules, which routinely diffract to sub-angstrom resolution by both 3D ED and XRD. In fact, the average resolution of structures catalogued in Table 1.4 is only 2.5 Å (cf. 0.95 Å in Table 1.3). 2.5 Å is ultimately a rather underwhelming number, especially given the significant overrepresentation of well-diffracting crystallographic standards within the sample size. Relative to small molecules, protein crystals suffer from a couple of unique disadvantages in addition to innately higher disorder. Although signal-to-noise in ED is boosted by a greater number of repeating units, protein crystals' larger unit cells provide an inherently lower bound on the maximum thickness permissible before inelastic scattering overpowers Bragg peaks. Furthermore, vitrification and frozen hydration remain experimental necessities, and insulating layers of amorphous ice will always contribute noise.

An illustrative example is provided by Xu *et al.*'s multipart investigation of an R2-like ligand-binding oxidase (a metalloenzyme originally isolated from *Sulfolobus acidocaldarius*) [129, 130]. In 2018, Xu *et al.* disclosed a 3.0 Å 3D ED structure of R2lox, phased by molecular replacement using a homologous X-ray structure with 35% shared sequence identity as a template [129]. Although novel at the time, this structure nevertheless exhibited less-than-ideal completeness (62.8%, despite merging data from 21 crystals—suggesting stark orientation bias) and unusually high R_{meas} (56.1% overall) statistics. A subsequent reinvestigation of this species by synchrotron X-ray diffraction yielded a higher-quality 2.1 Å X-ray structure (featuring 99.4% completeness and 16.6% overall R_{meas}) which corrected several deficiencies in the 3D ED model [130]. Specifically, 3D ED had omitted the presence of a fatty acid ligand bound to the enzyme's active site, as well as the entirety of an 11-residue stretch between amino acids 249 and 261. While most general aspects of the 3D ED structure proved consistent with XRD, middling resolution and low completeness conspired to limit its utility in modelling biologically relevant details. Xu *et al.*'s commendable decision to pursue a corroborating X-ray structure in these circumstances reflects ED's current inability to consistently match XRD data quality in macromolecular crystallography.

A seemingly promising step forward has recently been contributed by Gonen and co-workers' 0.87 Å structure of triclinic HEWL [248]. This report exploited the heightened sensitivity of a direct electron detector operating in counting mode to break the sub-angstrom resolution barrier for 3D ED of proteins, albeit on a well-diffracting standard. Curiously, the authors do not disclose any attempt to phase these data by direct methods, even though DM has proved successful on triclinic HEWL determined to a similar resolution by X-ray diffraction [249]. In addition to improved hardware, a potential blueprint for macromolecular electron crystallography to overcome its current limitations is also provided by Yonekura and co-workers' development of energy-filtered 3D ED [166], as well as Bücker *et al.*'s serial approach to data collection [113]. These tactics could work in tandem to mitigate radiation damage and boost diffraction data quality, potentially allowing 3D ED to ultimately deliver novel macromolecular structures on par with XRD.

Protein	Sequence length	PDB record	Phasing method	Resolution (Å)	Space group	$R_{\mathbf{work}}/R_{\mathbf{free}}$	Reference (DOI)
Lysozyme	129	3J4G	MR	2.9	$P4_32_12$	0.255/0.278	10.7554/elife.01345
Lysozyme	129	3J6K	MR	2.5	$P4_32_12$	0.220/0.255	10.1038/nmeth.3043
Catalase	527	3J7B	MR	3.2	$P2_12_12_1$	0.262/0.308	10.7554/elife.03600
Calcium ATPase	994	3J7T	MR	3.4	C2	0.277/0.315	10.1073/pnas.1500724112
Lysozyme	129	5A3E	MR	2.5	$P2_12_12_1$	0.213/0.253	10.1038/nmeth.3043
Catalase	527	5GKN	MR	3.2	$P2_12_12_1$	0.251/0.304	10.1107/S1600576716011274
Proteinase K	279	5I9S	MR	1.75	$P4_32_12$	0.217/0.266	10.1107/S1600576716007196
Lysozyme	129	5K7O	MR	1.8	$P4_32_12$	0.239/0.284	10.1038/nmeth.4178
Xylanase	190	5K7P	MR	2.3	$P2_12_12_1$	0.230/0.267	10.1038/nmeth.4178
Thaumatin	207	5K7Q	MR	2.5	$P4_12_12$	0.251/0.294	10.1038/nmeth.4178
Trypsin	223	5K7R	MR	1.7	$P2_12_12_1$	0.248/0.281	10.1038/nmeth.4178
Proteinase K	279	5K7S	MR	1.6	$P4_32_12$	0.224/0.255	10.1038/nmeth.4178
Thermolysin	316	5K7T	MR	2.5	$P6_122$	0.290/0.310	10.1038/nmeth.4178
Lysozyme	129	5O4W	MR	2.11	$P2_12_12$	0.335/0.350	10.1107/S2059798317010348
Lysozyme	129	5OCV	MR	2.2	$P2_12_12$	0.236/0.270	10.7554/elife.03600
TGF receptor 2 complex	103/97	5TY4	MR	2.9	$P2_12_12_1$	0.292/0.328	10.1038/nmeth.4178
Proteinase K	279	6CL7	MR	1.71	$P4_32_12$	0.221/0.253	10.1016/j.str.2018.03.021
NaK ion channel	96	6CPV	MR	2.5	I4	0.218/0.263	10.1038/S42003-018-0040-8
Lysozyme	129	6H3V	MR	1.9	$P4_32_12$	0.291/0.283	10.1073/pnas.1809978115
Lysozyme	129	6HU5	MR	2.8	$P2_1$	0.297/0.339	10.1107/s2052252518017657
Catalase (energy-filtered)	527	6JNT	MR	3.0	$P2_12_12_1$	0.251/0.283	10.1016/j.jsb.2019.03.009
Catalase (energy-filtered)	527	6JNU	MR	3.0	$P2_12_12_1$	0.207/0.251	10.1016/j.jsb.2019.03.009
Thiostrepton	19	6MXF	MR	1.91	$P4_32_12$	0.190/0.218	10.1021/acscentsci.8b00760
CTD-SP1 fragment of HIV-1 Gag	110	6N3J	MR	3.0	C2	0.254/0.292	10.1073/pnas.1806806115
Proteinase K (FIB-milled)	279	6N4U	MR	2.75	$P4_32_12$	0.238/0.263	10.1016/j.str.2018.12.003
R2-like ligand-binding oxidase	328	6QRZ	MR	3.0	$P2_12_12$	0.318/0.335	10.1126/sciadv.aax4621
Proteinase K	279	6V8R	FBP	1.6	$P4_32_12$	0.195/0.232	10.1107/S2059798320008049
Human carbonic anhydrase II	260	6YMA	MR	2.5	$P2_1$	0.224/0.255	10.7554/elife.03600
Human carbonic anhydrase II	260	6YMB	MR	2.5	$P2_1$	0.249/0.276	10.1038/s42003-020-01155-1
Granulovirus occlusion body	248	6S2O	MR	1.55	I23	0.171/0.197	10.1038/s41467-020-14793-0
Lysozyme	129	6S2N	MR	1.8	$P4_32_12$	0.272/0.316	10.1038/s41467-020-14793-0
Catalase	527	7DI8	MR	3.2	$P2_12_12_1$	0.309/0.348	10.3389/fmolb.2020.612226
Thermolysin	316	6ZHJ	MR	3.26	$P6_122$	0.210/0.292	10.1107/S2059798320014540
Thaumatin	207	6ZHN	MR	2.76	$P4_12_12$	0.280/0.321	10.1107/S2059798320014540
VDAS channel protein 1	295	7KUH	MR	3.12	C2	0.257/0.287	10.1073/pnas.2020010117
Bovine insulin	21/30	6ZHB	MR	3.25	H3	0.181/0.319	10.1107/S2059798320014540
MyD88	151	7BEQ	MR	3.0	C2	0.223/0.280	10.1038/s41467-021-22590-6
Proteinase K (LCP)	279	6PQ0	MR	2.0	$P4_32_12$	0.217/0.267	10.1016/j.str.2020.07.006
Proteinase K (LCP)	279	6PQ4	MR	2.0	$P4_32_12$	0.244/0.282	10.1016/j.str.2020.07.006
CypA	165	6U5G	MR	2.5	$P2_12_12_1$	0.185/0.224	10.1107/S205225252000072X
Human adenosine receptor	447	7RM5	MR	2.79	$C222_1$	0.248/0.288	10.1073/pnas.2106041118
Vancomycin (triclinic polymorph)	7	7C4V	MR	1.05	P1	0.232/0.268	10.1002/anie.202003922
Vancomycin	7	7C4U	MR	1.2	$P22_12_1$	0.202/0.216	10.1002/anie.202003922
Granulovirus occlusion body	248	6YNG	MR	2.83	I23	0.184/0.226	10.2210/pdb6YNG/pdb
Proteinase K	279	6ZEV	MR	2.4	$P4_32_12$	0.200/0.243	10.3389/fmolb.2020.00179
Proteinase K	279	6ZET	MR	2.7	$P4_32_12$	0.225/0.268	10.3389/fmolb.2020.00179
Proteinase K	279	6ZEU	MR	2.0	$P4_32_12$	0.199/0.234	10.3389/fmolb.2020.00179

Table 1.4: **List of selected macromolecular 3D ED structures deposited in the PDB** as of October 2021. Vancomycin and thiostrepton, although more akin to small molecules, are categorized here because of their presence in the PDB.

1.7.4 Radioactive Minerals and Inorganic Compounds

Although slightly esoteric to chemists, mineralogy is a field replete with ideal samples for investigation by 3D ED. In fact, mineralogy has historically functioned as a key impetus behind research in 3D electron crystallography, dating back to Zvyagin's studies of celadonite and muscovite [52]. A detailed discussion on the applications of 3D ED to mineralogy has been provided by Mugnaioli and Gemmi. Here we would like to specifically highlight radioactive metamict minerals, which comprise a fascinating and seemingly tailor-made class of substrates for 3D ED. Metamict systems feature an intricate lattice structure punctuated by trace impurities of radioactive elements like uranium or thorium. Over geologic timescales, these interstitial radionuclides undergo alpha decay, selectively destroying certain regions of the lattice from within. This process, known as metamictization [251], gradually results in total amorphization of crystalline order. In a compelling study, Capitani *et al.* used the presence of Bragg peaks in ED patterns to spatially map metamict domains in the mineral samarskite at the nanoscale [250]. After targeting specific submicron-sized zones where crystallinity seemed best preserved, Capitani *et al.* collected a tomographic series of still-frame ED patterns. These 0.8 Å ED data successfully yielded a solution via direct methods, providing an elusive 3D structure of metamict samarskite. Critically, at the single-crystal X-ray scale, alpha decay had rendered the bulk sample mostly amorphous, carving a unique niche for ED.

In many ways, this work also echoes the more general blueprint formulated by Baybarz and coworkers at Oak Ridge National Laboratory in the 1970s [252, 253, 254]. These researchers worked primarily with inorganic salts formed by fully anthropogenic, superheavy elements like einsteinium, californium, or fermium. Synthetic Es and Fm typically decay so rapidly and destructively that formation of high-quality X-ray-scale crystals is a nonstarter; self-irradiation would likely cause lattices containing Es or Fm to collapse well before growing to X-ray size. Furthermore, synthesis of transplutonium elements is exceptionally arduous, generally divulging only nanogram-scale quantities of material (which then immediately begins to decay!). Undeterred, Baybarz and co-workers exploited ED's ability to interrogate submicron-sized crystals and deduced the unit

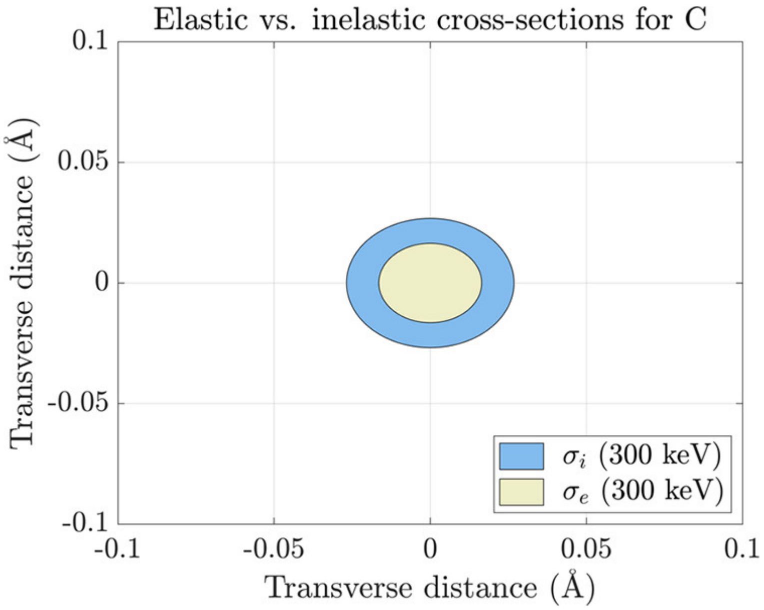

Figure 1.10: **Elastic vs. inelastic cross-sections for neutral carbon at 300 keV**, expressed as concentric circles.

cell parameters of several Es and Cf oxides from polycrystalline ED patterns recorded at 80 kV. Following a long hiatus, their torch has recently been lifted by Minor, Abergel, and co-workers [255]. Given contemporary advances in data collection and analysis, ED appears uniquely poised to deliver 3D structures of inorganic systems containing either superheavy or primordial radionuclides, an exciting prospect.

1.7.5 Radiation Damage: A Brief Overview

As with any diffraction experiment, the maximum achievable signal-to-noise in 3D ED is ultimately constrained by radiation damage, which begins as soon as the crystal of interest is exposed to the impinging beam. ED leverages information about structure-factor amplitudes encoded in Bragg peaks, which result from elastic scattering of incident electrons. Since the low-angle elastic collisions contributing to Bragg peaks involve negligible (<1 eV) energy loss, they leave the crystal lattice completely intact [256]. (At higher incident energies, elastic scattering can destructively dislocate atoms via knock-on displacement, but the likelihood of these events relative to radiolysis is negligible at TEM accelerating voltages [257].) Conversely, inelastic scattering causes impinging electrons to deposit a significant fraction (10-100 eV) of their incident energy within the sample, damaging the structural integrity of the lattice. Second-row elements such as carbon, nitrogen, and oxygen possess inelastic electron cross-sections roughly 3× greater than their elastic counterparts (Figure 1.10). On a per electron basis, therefore, any crystal composed primarily of C, N, and O atoms is 3× more likely to undergo unproductive inelastic scattering [258]. Although seemingly inauspicious, this ratio is actually superior to the corresponding fraction for X-ray diffraction; incident X-rays can inflict up to three orders of magnitude more collateral damage per useful elastic scattering event. (In principle, this advantage is attenuated somewhat by electrons' propensity for multiple scattering, since they interact with the substrate more frequently than X-rays.)

High-resolution information is especially sensitive to degradation of lattice structure. Therefore, in reciprocal space, radiation damage begins by consuming high-resolution reflections, causing Bragg peaks at the periphery of the detector to diminish in intensity until they become indistinguishable from noise. Ultimately, as crystalline order is totally destroyed, low-resolution reflections also recede into the void space of the noise floor. Statistically, this manifests as a monotonic decrease in $<I/\sigma(I)>$ which starts in the outermost resolution shell and spreads gradually inward. In real space, radiation damage results in two major global consequences: a uniform increase in B-factors and an expansion of unit cell volume [259]. Bloated B-factors represent growing uncertainty in atomic positions, whereas unit cell volume is thought to expand due to radiolytic generation of hydrogen gas within the lattice [260]. A systematic study by Hattne *et al.* [259] found that site-specific radiation damage inflicted upon particular functional groups largely mirrors the chronological progression observed in X-ray diffraction [261, 262]. In frozen-hydrated proteinase K, Hattne *et al.* observed perturbation of metal cations, elongation and lysis of disulfide bonds, and radiolytic decarboxylation of aspartate and glutamate side chains, all in quick succession. Loss of atomic-resolution (2 Å) information generally occurred after a total accumulated exposure of 3 e^{-} Å^{-2}. By collecting 3D ED data at an ultra-low flux density (<0.01 e^{-} Å^{-2} s^{-1}), staying well below this threshold is quite feasible. Furthermore, this cut-off is substrate-specific. For instance, organometallic complexes, which frequently exhibit denser packing and lattices free of solvent channels, could potentially tolerate equivalent levels of fluence quite easily, even at ambient temperatures [159]. Nevertheless, in virtually all cases, radiation damage is significantly abated by cryogenic temperatures, which presumably stall the thermal diffusion of destructive free radicals generated by radiolysis [263, 264]. Another bulwark against radical-induced decay is the presence of highly conjugated polyaromatic systems, which facilitate delocalization of errant secondary electrons via resonance [265, 266, 267]. This effectively provides a thermodynamic sink for radicals which would otherwise propagate freely throughout the crystal lattice.

Finally, some clarification on nomenclature is warranted (Table 1.5). Formally, dose refers to energy absorbed per unit mass (measured in units of MGy, or 10^6 J kg^{-1}) [268], whereas fluence corresponds to particles delivered per unit area (measured in units of e^- Å^{-2} for electrons, or γ μm^{-2} for X-ray photons). Regrettably, these two terms have become thoroughly muddled in the cryo-EM literature, where they're frequently used interchangeably. For instance, a substantial fraction of ED structures deposited in the PDB currently reports a "dose" tabulated in units of e^- Å^{-2}. This value is really a misrepresentation of total accumulated fluence. Although often strongly correlated, dose and fluence do not represent fungible observables, making their conflation incorrect and potentially misleading. The key distinction is that dose is a quantity specific to the substrate under interrogation. Conversely, fluence is a property of the incident beam, which is completely decoupled from the identity of the substrate. To illustrate this point, consider two identical, isomorphous protein crystals exposed to a fixed fluence: (a) one native and (b) one derivative intercalated with heavy metal cations. Because heavy metals feature significantly higher elastic-to-inelastic cross-section ratios than lighter elements such as C, N, and O, crystal B could experience a smaller proportion of inelastic scattering events than crystal A. In that case, crystal B would experience a lower dose than crystal A, notwithstanding being illuminated with the same fluence. In other words, despite being exposed to the same number of particles per unit area, crystal A's elevated susceptibility to inelastic scattering would cause it

Observable	Unit (electrons)	Unit (X-rays)	Description
Dose	MGy $\left(10^6 \text{ J kg}^{-1}\right)$	MGy $\left(10^6 \text{ J kg}^{-1}\right)$	Energy absorbed per unit mass
Fluence	$e^{-}\text{Å}^{-2}$	$\gamma\, \mu\text{m}^{-2}$	Particles delivered per unit area
Flux	$e^{-}\text{s}^{-1}$	$\gamma\, \text{s}^{-1}$	Particles delivered per unit time
Flux density	$e^{-}\text{Å}^{-2}\ \text{s}^{-1}$	$\gamma\, \mu\text{m}^{-2}\ \text{s}^{-1}$	Fluence delivered per unit time

Table 1.5: **Definitions and typical units for commonly conflated terms in dosimetry.**

to absorb more energy per unit mass than crystal B. In sum, different specimens exposed to an identical fluence can accumulate variable quantities of dose based on their chemical composition. Dose is a more suitable metric for assessing radiation damage than total accumulated fluence because it situates electron exposure within the specific context of the substrate itself.

1.8 Conclusion and Outlook

As a science born entirely in the quantum age, crystallographic analysis has been intimately shaped by our increasingly sophisticated understanding of incident quanta. Modern transmission electron microscopy is a powerful tool capable of generating highly coherent, atomically precise beams of electrons which would have been inconceivable to pioneering researchers like Davisson and Germer. Our ability to probe the atomic structure of 3D molecular nanocrystals at sub-angstrom resolution is a testament to electron diffraction's burgeoning relevance and vast potential. This introductory chapter has focused on pivotal concepts and experiments which have underpinned 3D electron crystallography's ongoing transformation from a somewhat esoteric subfield to an area of swiftly growing importance. We conclude with forward-looking recommendations organized around two central themes: increasing transparency and expanding access.

1.8.1 Increasing Transparency

It has become standard operating procedure to deposit fully refined structures to databases like the CSD or the PDB, although these resources have yet to flag 3D ED data in an easily identifiable or searchable way. To ensure maximum transparency, we also recommend concurrent deposition of raw, unprocessed data (i.e., a tilt series of diffraction patterns in a file format compatible with data reduction software) on public repositories such as Zenodo or *IUCrData*. Furthermore, automated validation routines, such as those embedded in checkCIF, typically raise an array of objections when presented with 3D ED structures, some of which reflect intrinsic disparities between 3D ED and XRD rather than genuine deficiencies in the deposited models. Moving forward, establishment of ED-specific validation criteria cognizant of the various differences between 3D ED and XRD would provide a more accurate record of the quality of 3D ED structures reported in the literature.

1.8.2 Expanding Access

Although ED is *en route* to becoming a more mainstream technique, its current practitioners remain limited to a relatively small (albeit growing) handful of specialists. Transmission electron microscopy presents a steeper economic barrier to entry than X-ray crystallography; a mid- to high-end TEM optimally equipped for ED carries a hefty six-digit price tag, whereas a standard X-ray diffractometer is usually up to an order of magnitude cheaper. Retrofitting used or refurbished TEMs for ED is usually a more viable option, although still expensive. Sadly, lack of widespread access to the appropriate instrumentation can thwart researchers otherwise interested in incorporating ED into their work. Furthermore, TEM maintenance is typically carried out by trained engineers or facility managers whom many institutions may not have the financial bandwidth to hire. Systemic inequities aside, however, the conceptual learning curve for ED is comparatively gentle, especially thanks to the advent of continuous rotation. Any practicing X-ray crystallographer has already attained the requisite skillset to start solving structures from continuous-rotation 3D ED data, leaving lack of access as the main bottleneck. To rectify this, investment in a subsidized infrastructure for ED data collection at dedicated user facilities, analogous to the now well-established network of synchrotron beamlines across the globe, will prove especially critical. ED will reach its considerable potential only when the technique proliferates to more users outside its current niche.

REFERENCES

[1] Davisson, C.; Germer, L. H. Diffraction of Electrons by a Crystal of Nickel. *Phys. Rev.* **1927**, 30 (6), 705–740. `<DOI: 10.1103/PhysRev.30.705>`

[2] Davisson, C.; Germer, L. H. The Scattering of Electrons by a Single Crystal of Nickel. *Nature* **1927**, 119 (2998), 558–560. `<DOI: 10.1038/119558a0>`

[3] Gehrenbeck, R. K. Electron Diffraction: Fifty Years Ago. *Physics Today* **1978**, 31 (1), 34–41. `<DOI: 10.1063/1.3001830>`

[4] de Broglie, L. XXXV. A Tentative Theory of Light Quanta. *Philosophical Magazine Letters* **1922**, 86 (7), 411–423. `<DOI: 10.1080/09500830600914721>`

[5] Thomson, G. P.; Reid, A. Diffraction of Cathode Rays by a Thin Film. *Nature* **1927**, 119 (3007), 890–890. `<DOI: 10.1038/119890a0>`

[6] Thomson, G. P. The Diffraction of Cathode Rays by Thin Films of Platinum. *Nature* **1927**, 120 (3031), 802–802. `<DOI: 10.1038/120802a0>`

[7] Thomson, G. P. Experiments on the Diffraction of Cathode Rays. *Proceedings of the Royal Society of London. Series A, Containing Papers of a Mathematical and Physical Character* **1928**, 117 (778), 600–609. `<DOI: 10.1098/rspa.1928.0022>`

[8] Laschkarew, W. E.; Usyskin, I. D. Die Bestimmung der Lage der Wasserstoffionen im NH_4Cl–Kristallgitter durch Elektronenbeugung. *Z. Physik* **1933**, 85 (9), 618–630. `<DOI: 10.1007/BF01331003>`

[9] Cowley, J. M. Structure Analysis of Single Crystals by Electron Diffraction. II. Disordered Boric Acid Structure. *Acta Cryst.* **1953**, 6 (6), 522–529. `<DOI: 10.1107/S0365110X53001423>`

[10] Honjo, G.; Shimaoka, K. Determination of Hydrogen Position in Cubic Ice by Electron Diffraction. *Acta Cryst.* **1957**, 10 (11), 710–711. `<DOI: 10.1107/S0365110X57002479>`

[11] Kuwabara, S. Accurate Determination of Hydrogen Positions in NH_4Cl by Electron Diffraction. *J. Phys. Soc. Jpn.* **1959**, 14 (9), 1205–1216. `<DOI: 10.1143/JPSJ.14.1205>`

[12] Rigamonti, R. La Struttura Della Catena Paraffinica Studiata Mediante i Raggi Di Elettroni. *Gazzeta Chimica Italiana* **1936**, 66, 174–182.

[13] Charlesby, A.; Finch, G. I.; Wilman, H. The Diffraction of Electrons by Anthracene. *Proc. Phys. Soc.* **1939**, 51 (3), 479–528. `<DOI: 10.1088/0959-5309/51/3/312>`

[14] Cowley, J. M. Crystal Structure Determination by Electron Diffraction. *Prog. Mat. Sci.* **1968**, 13, 267–321. `<DOI: 10.1016/0079-6425(68)90023-6>`

[15] Vainshtein, B. K. *Structure Analysis by Electron Diffraction*. Pergamon Press: Oxford, 1964.

[16] Dorset, D. L. Electron Crystallography. *Acta Cryst. B* **1996**, 52 (5), 753–769. `<DOI: 10.1107/S0108768196005599>`

[17] Gemmi, M.; Mugnaioli, E.; Gorelik, T. E.; Kolb, U.; Palatinus, L.; Boullay, P.; Hovmöller, S.; Abrahams, J. P. 3D Electron Diffraction: The Nanocrystallography Revolution. *ACS Cent. Sci.* **2019**, 5 (8), 1315–1329. `<DOI: 10.1021/acscentsci.9b00394>`

[18] Ji, X.; Axford, D.; Owen, R.; Evans, G.; Ginn, H. M.; Sutton, G.; Stuart, D. I. Polyhedra Structures and the Evolution of the Insect Viruses. *J. Struct. Biol.* **2015**, 192 (1), 88–99. `<DOI: 10.1016/j.jsb.2015.08.009>`

[19] Brewster, A. S.; Sawaya, M. R.; Rodriguez, J.; Hattne, J.; Echols, N.; McFarlane, H. T.; Cascio, D.; Adams, P. D.; Eisenberg, D. S.; Sauter, N. K. Indexing amyloid peptide diffraction from serial femtosecond crystallography: new algorithms for sparse patterns. *Acta Cryst. D* **2015**, 71, 357-366. `<DOI: 10.1107/S1399004714026145>`

[20] Zuo, J. M.; Spence, J. C. H. *Advanced Transmission Electron Microscopy: Imaging and Diffraction in Nanoscience*. Springer-Verlag: New York, 2017. `<DOI: 10.1007/978-1-4939-6607-3>`

[21] Peng, L.-M. Electron Scattering Factors of Ions and Their Parameterization. *Acta Cryst. A* **1998**, 54 (4), 481–485. `<DOI: 10.1107/S0108767398001901>`

[22] Zheng, J.-C.; Zhu, Y.; Wu, L.; Davenport, J. W. On the Sensitivity of Electron and X-Ray Scattering Factors to Valence Charge Distributions. *J. Appl. Cryst.* **2005**, 38 (4), 648–656. `<DOI: 10.1107/S0021889805016109>`

[23] Shi, H. L.; Li, Z. A. UnitCell Tools, a Package to Determine Unit-Cell Parameters from a Single Electron Diffraction Pattern. *IUCrJ* **2021**, 8 (5), 805–813. `<DOI: 10.1107/S2052252521007867>`

[24] Bethe, H. A.; Rose, M. E.; Smith, L. P. The Multiple Scattering of Electrons. *Proceedings of the American Philosophical Society* **1938**, 78 (4), 573–585.

[25] Blackman, M.; Thomson, G. P. On the Intensities of Electron Diffraction Rings. *Proceedings of the Royal Society of London. Series A. Mathematical and Physical Sciences* **1939**, 173 (952), 68–82. `<DOI: 10.1098/rspa.1939.0129>`

[26] Cowley, J. M.; Moodie, A. F. The Scattering of Electrons by Atoms and Crystals. I. A New Theoretical Approach. *Acta Cryst.* **1957**, 10 (10), 609–619. `<DOI: 10.1107/S0365110X57002194>`

[27] Fujiwara, K. Application of Higher Order Born Approximation to Multiple Elastic Scattering of Electrons by Crystals. *J. Phys. Soc. Jpn.* **1959**, 14 (11), 1513–1524. <DOI: 10.1143/JPSJ.14.1513>

[28] Stern, R. M.; Taub, H. An Introduction to the Dynamical Scattering of Electrons by Crystals. *C R C Critical Reviews in Solid State Sciences* **1970**, 1 (2), 221–302. <DOI: 10.1080/10408437008243421>

[29] Hu, H.; Dorset, D. L.; Moss, B. Space Group Symmetry and the Location of Forbidden Reflections Due to Incoherent Multiple Scattering from Epitaxially Oriented Paraffins. *Ultramicroscopy* **1989**, 27 (2), 161–169. <DOI: 10.1016/0304-3991(89)90084-3>

[30] Miyake, S.; Uyeda, R. An Exception to Friedel's Law in Electron Diffraction. *Acta Cryst.* **1950**, 3 (4), 314. <DOI: 10.1107/S0365110X5000080X>

[31] Goodman, P.; Lehmpfuhl, G. Observation of the Breakdown of Friedel's Law in Electron Diffraction and Symmetry Determination from Zero-Layer Interactions. *Acta Cryst. A* **1968**, 24 (3), 339–347. <DOI: 10.1107/S0567739468000677>

[32] Glaeser, R. M.; Ceska, T. A. High-Voltage Electron Diffraction from Bacteriorhodopsin (Purple Membrane) Is Measurably Dynamical. *Acta Cryst. A* **1989**, 45, 620–628. <DOI: 10.1107/S0108767389004599>

[33] Heidenreich, R. D. Theory of the "Forbidden" (222) Electron Reflection in the Diamond Structure. *Phys. Rev.* **1950**, 77, 271–283. <DOI: 10.1103/PhysRev.77.271>

[34] Cowley, J. M.; Rees, A. L. G.; Spink, J. A. Secondary Elastic Scattering in Electron Diffraction. *Proc. Phys. Soc. A* **1951**, 64, 609–619. <DOI: 10.1088/0370-1298/64/7/302>

[35] Diaz-Avalos, R.; Long, C.; Fontano, E.; Balbirnie, M.; Grothe, R.; Eisenberg, D.; Caspar, D. L. D. Cross-Beta Order and Diversity in Nanocrystals of an Amyloid-Forming Peptide. *J. Mol. Biol.* **2003**, 330, 1165-1175. <DOI: 10.1016/S0022-2836(03)00659-4>

[36] Ciston, J.; Deng, B.; Marks, L. D.; Own, C. S.; Sinkler, W. A Quantitative Analysis of the Cone-Angle Dependence in Precession Electron Diffraction. *Ultramicroscopy* **2008**, 108, 514–522. <DOI: 10.1016/j.ultramic.2007.08.004>

[37] Eggeman, A. S.; White, T. A.; Midgley, P. A. Is Precession Electron Diffraction Kinematical? Part II: A Practical Method to Determine the Optimum Precession Angle. *Ultramicroscopy* **2010**, 110, 771–777. <DOI: 10.1016/j.ultramic.2009.10.012>

[38] Shi, D.; Nannenga, B. L.; Iadanza, M. G.; Gonen, T. Three-Dimensional Electron Crystallography of Protein Microcrystals. *eLife* **2013**, 2, e01345. <DOI: 10.7554/eLife.01345>

[39] Nannenga, B. L.; Shi, D.; Leslie, A. G. W.; Gonen, T. High-Resolution Structure Determination by Continuous-Rotation Data Collection in MicroED. *Nat. Methods* **2014**, 11, 927–930. <DOI: 10.1038/nmeth.3043>

[40] Mugnaioli, E.; Gemmi, M. Single-Crystal Analysis of Nanodomains by Electron Diffraction Tomography: Mineralogy at the Order-Disorder Borderline. *Zeitschrift für Kristallographie* **2018**, 233, 163–178. <DOI: 10.1515/zkri-2017-2130>

[41] Cowley, J. M. Structure Analysis of Single Crystals by Electron Diffraction. I. Techniques. *Acta Cryst.* **1953**, 6, 516–521. <DOI: 10.1107/S0365110X53001411>

[42] Lipson, H.; Cochran, W. *The Determination of Crystal Structures*. Cornell University Press: Ithaca, New York, 1966.

[43] Hauptman, H.; Karle, J. Structure Invariants and Seminvariants for Noncentrosymmetric Space Groups. *Acta Cryst.* **1956**, 9, 45–55. <DOI: 10.1107/S0365110X56000097>

[44] Karle, J.; Hauptman, H. A Theory of Phase Determination for the Four Types of Non-Centrosymmetric Space Groups 1P222, 2P22, 3$P_1$2, 3$P_2$2. *Acta Cryst.* **1956**, 9, 635–651. <DOI: 10.1107/S0365110X56001741>

[45] Hauptman, H.; Karle, J. A Unified Algebraic Approach to the Phase Problem I. Space Group $P\bar{1}$. *Acta Cryst.* **1957**, 10, 267–270. <DOI: 10.1107/S0365110X57000833>

[46] Hauptman, H.; Karle, J. Phase Determination from New Joint Probability Distribution: Space Group $P\bar{1}$. *Acta Cryst.* **1958**, 11, 149–157. <DOI: 10.1107/S0365110X58000414>

[47] Dorset, D. L.; Hauptman, H. A. Direct Phase Determination for Quasi-Kinematical Electron Diffraction Intensity Data from Organic Microcrystals. *Ultramicroscopy* **1976**, 1, 195–201. <DOI: 10.1016/0304-3991(76)90034-6>

[48] Dorset, D. L. Comments on the Validity of the Direct Phasing and Fourier Methods in Electron Crystallography. *Acta Cryst. A* **1995**, 51, 869–879. <DOI: 10.1107/S0108767395005915>

[49] Dorset, D. L. Is Electron Crystallography Possible? The Direct Determination of Organic Crystal Structures. *Ultramicroscopy* **1991**, 38, 23–40. <DOI: 10.1016/0304-3991(91)90106-G>

[50] Dorset, D. L. Electron Diffraction Structure Analysis of Diketopiperazine—a Direct Phase Determination. *Acta Cryst. A* **1991**, 47, 510–515. <DOI: 10.1107/S0108767391003550>

[51] Dorset, D. L. Automated Phase Determination in Electron Crystallography: Thermotropic Phases of Thiourea. *Ultramicroscopy* **1992**, 45, 357–364. <DOI: 10.1016/0304-3991(92)90147-C>

[52] Dorset, D. L. Direct Phasing in Electron Crystallography: Determination of Layer Silicate Structures. *Ultramicroscopy* **1992**, 45, 5–14. <DOI: 10.1016/0304-3991(92)90033-G>

[53] Dorset, D. L.; McCourt, M. P. Automated Structure Analysis in Electron Crystallography: Phase Determination with the Tangent Formula and Least-Squares Refinement. *Acta Cryst. A* **1994**, 50, 287–292. `<DOI: 10.1107/S010876739300916X>`

[54] Dorset, D. L. Direct Methods and Refinement in Electron and X-Ray Crystallography—Diketopiperazine Revisited. *Zeitschrift für Kristallographie* **2010**, 225, 86–93. `<DOI: 10.1524/zkri.2010.1198>`

[55] Levine, A. M.; Bu, G.; Biswas, S.; Tsai, E. H. R.; Braunschweig, A. B.; Nannenga, B. L. Crystal Structure and Orientation of Organic Semiconductor Thin Films by Microcrystal Electron Diffraction and Grazing-Incidence Wide-Angle X-Ray Scattering. *Chem. Commun.* **2020**, 56, 4204–4207. `<DOI: 10.1039/D0CC00119H>`

[56] Levine, A. M.; He, G.; Bu, G.; Ramos, P.; Wu, F.; Soliman, A.; Serrano, J.; Pietraru, D.; Chan, C.; Batteas, J. D.; Kowalczyk, M.; Jang, S. J.; Nannenga, B. L.; Sfeir, M. Y.R.; Tsai, E. H. R.; Braunschweig, A. B. Efficient Free Triplet Generation Follows Singlet Fission in Diketopyrrolopyrrole Polymorphs with Goldilocks Coupling. *J. Phys. Chem. C* **2021**, 125, 12207–12213. `<DOI: 10.1021/acs.jpcc.1c02737>`

[57] Zhao, J.; Xu, H.; Lebrette, H.; Carroni, M.; Taberman, H.; Högbom, M.; Zou, X. A Simple Pressure-Assisted Method for MicroED Specimen Preparation. *Nat. Commun.* **2021**, 12, 5036. `<DOI: 10.1038/s41467-021-25335-7>`

[58] Matthews, B. W. Solvent Content of Protein Crystals. *J. Mol. Biol.* **1968**, 33, 491–497. `<DOI: 10.1016/0022-2836(68)90205-2>`

[59] Fraser, R. D. B.; MacRae, T. P.; Suzuki, E. An Improved Method for Calculating the Contribution of Solvent to the X-Ray Diffraction Pattern of Biological Molecules. *J. Appl. Cryst.* **1978**, 11, 693–694. `<DOI: 10.1107/S0021889878014296>`

[60] Weichenberger, C. X.; Afonine, P. V.; Kantardjieff, K.; Rupp, B. The Solvent Component of Macromolecular Crystals. *Acta Cryst. D* **2015**, 71, 1023–1038. `<DOI: 10.1107/S1399004715006045>`

[61] Dubochet, J.; McDowall, A. W. Vitrification of Pure Water for Electron Microscopy. *J. Microsc.* **1981**, 124, 3–4. `<DOI: 10.1111/j.1365-2818.1981.tb02483.x>`

[62] Dubochet, J.; Lepault, J.; Freeman, R.; Berriman, J. A.; Homo, J.-C. Electron Microscopy of Frozen Water and Aqueous Solutions. *J. Microsc.* **1982**, 128, 219–237. `<DOI: 10.1111/j.1365-2818.1982.tb04625.x>`

[63] Dubochet, J.; Adrian, M.; Chang, J.-J.; Homo, J.-C.; Lepault, J.; McDowall, A. W.; Schultz, P. Cryo-Electron Microscopy of Vitrified Specimens. *Q. Rev. Biophys.* **1988**, 21, 129–228. `<DOI: 10.1017/S0033583500004297>`

[64] Iancu, C. V.; Tivol, W. F.; Schooler, J. B.; Dias, D. P.; Henderson, G. P.; Murphy, G. E.; Wright, E. R.; Li, Z.; Yu, Z.; Briegel, A.; Gan, L.; He, Y.; Jensen, G. J. Electron Cryotomography Sample Preparation Using the Vitrobot. *Nat. Protoc.* **2006**, 1, 2813–2819. <DOI: 10.1038/nprot.2006.432>

[65] de la Cruz, M. J.; Hattne, J.; Shi, D.; Seidler, P.; Rodriguez, J.; Reyes, F. E.; Sawaya, M. R.; Cascio, D.; Weiss, S. C.; Kim, S. K.; Hinck, C. S.; Hinck, A. P.; Calero, G.; Eisenberg, D.; Gonen, T. Atomic-Resolution Structures from Fragmented Protein Crystals with the CryoEM Method MicroED. *Nat. Methods* **2017**, 14, 399–402. <DOI: 10.1038/nmeth.4178>

[66] Zee, C.-T.; Saha, A.; Sawaya, M. R.; Rodriguez, J. A. Ab Initio Determination of Peptide Structures by MicroED. In *CryoEM: Methods and Protocols; Methods in Molecular Biology*; Gonen, T., Nannenga, B. L., Eds.; Springer: New York, 2021; pp. 329–348. <DOI: 10.1007/978-1-0716-0966-817>

[67] Tivol, W. F.; Briegel, A.; Jensen, G. J. An Improved Cryogen for Plunge Freezing. *Microscopy and Microanalysis* **2008**, 14, 375–379. <DOI: 10.1017/S1431927608080781>

[68] Martynowycz, M. W.; Clabbers, M. T. B.; Unge, J.; Hattne, J.; Gonen, T. Benchmarking the Ideal Sample Thickness in Cryo-EM. *Proc. Natl. Acad. Sci. U. S. A.* **2021**, 118. <DOI: 10.1073/pnas.2108884118>

[69] Duyvesteyn, H. M. E.; Kotecha, A.; Ginn, H. M.; Hecksel, C. W.; Beale, E. V.; de Haas, F.; Evans, G.; Zhang, P.; Chiu, W.; Stuart, D. I. Machining Protein Microcrystals for Structure Determination by Electron Diffraction. *Proc. Natl. Acad. Sci. U. S. A.* **2018**, 115, 9569–9573. <DOI: 10.1073/pnas.1809978115>

[70] Martynowycz, M. W.; Zhao, W.; Hattne, J.; Jensen, G. J.; Gonen, T. Qualitative Analyses of Polishing and Precoating FIB Milled Crystals for MicroED. *Structure* **2019**, 27, 1594–1600. <DOI: 10.1016/j.str.2019.07.004>

[71] Martynowycz, M. W.; Zhao, W.; Hattne, J.; Jensen, G. J.; Gonen, T. Collection of Continuous Rotation MicroED Data from Ion Beam-Milled Crystals of Any Size. *Structure* **2019**, 27, 545–548. <DOI: 10.1016/j.str.2018.12.003>

[72] Nicolopoulos, S.; Gonzalez-Calbet, J. M.; Vallet-Regi, M.; Corma, A.; Corell, C.; Guil, J. M.; Perez-Pariente, J. Direct Phasing in Electron Crystallography: Ab Initio Determination of a New MCM-22 Zeolite Structure. *J. Am. Chem. Soc.* **1995**, 117, 8947–8956. <DOI: 10.1021/ja00140a008>

[73] Gemmi, M.; Righi, L.; Calestani, G.; Migliori, A.; Speghini, A.; Santarosa, M.; Bettinelli, M. Structure Determination of Φ-$Bi_8Pb_5O_{17}$ by Electron and Powder X-Ray Diffraction. *Ultramicroscopy* **2000**, 84, 133–142. <DOI: 10.1016/S0304-3991(00)00007-3>

[74] Weirich, T. E.; Zou, X. D.; Ramlau, R.; Simon, A.; Cascarano, G. L.; Giacovazzo, C.; Hovmöller, S. Structures of Nanometre-Size Crystals Determined from Selected-Area Electron Diffraction Data. *Acta Cryst. A* **2000**, 56, 29–35. `<DOI: 10.1107/S0108767399009605>`

[75] Vincent, R.; Midgley, P. A. Double Conical Beam-Rocking System for Measurement of Integrated Electron Diffraction Intensities. *Ultramicroscopy* **1994**, 53, 271–282. `<DOI: 10.1016/0304-3991(94)90039-6>`

[76] Eggeman, A. S.; Midgley, P. A. Precession Electron Diffraction. In *Advances in Imaging and Electron Physics*; Hawkes, P. W., Ed.; Elsevier, 2012; Chapter 1, Vol. 170, pp. 1–63. `<DOI: 10.1016/B978-0-12-394396-5.00001-4>`

[77] Own, C. S.; Marks, L. D.; Sinkler, W. Precession Electron Diffraction 1: Multislice Simulation. *Acta Cryst. A* **2006**, 62, 434–443. `<DOI: 10.1107/S0108767306032892>`

[78] Avilov, A.; Kuligin, K.; Nicolopoulos, S.; Nickolskiy, M.; Boulahya, K.; Portillo, J.; Lepeshov, G.; Sobolev, B.; Collette, J. P.; Martin, N.; Robins, A. C.; Fischione, P. Precession Technique and Electron Diffractometry as New Tools for Crystal Structure Analysis and Chemical Bonding Determination. *Ultramicroscopy* **2007**, 107, 431–444. `<DOI: 10.1016/j.ultramic.2006.09.006>`

[79] Midgley, P. A.; Eggeman, A. S. Precession Electron Diffraction—a Topical Review. *IUCrJ* **2015**, 2, 126–136. `<DOI: 10.1107/S2052252514022283>`

[80] Gjønnes, J.; Hansen, V.; Berg, B. S.; Runde, P.; Cheng, Y. F.; Gjønnes, K.; Dorset, D. L.; Gilmore, C. J. Structure Model for the Phase Al_mFe Derived from Three-Dimensional Electron Diffraction Intensity Data Collected by a Precession Technique. Comparison with Convergent-Beam Diffraction. *Acta Cryst. A* **1998**, 54, 306–319. `<DOI: 10.1107/S0108767397017030>`

[81] Gemmi, M.; Zou, X. D.; Hovmöller, S.; Migliori, A.; Vennström, M.; Andersson, Y. Structure of Ti_2P Solved by Three-Dimensional Electron Diffraction Data Collected with the Precession Technique and High-Resolution Electron Microscopy. *Acta Cryst. A* **2003**, 59, 117–126. `<DOI: 10.1107/S0108767302022559>`

[82] Kolb, U.; Gorelik, T.; Kübel, C.; Otten, M. T.; Hubert, D. Towards Automated Diffraction Tomography: Part I—Data Acquisition. *Ultramicroscopy* **2007**, 107, 507–513. `<DOI: 10.1016/j.ultramic.2006.10.007>`

[83] Kolb, U.; Gorelik, T.; Otten, M. T. Towards Automated Diffraction Tomography. Part II—Cell Parameter Determination. *Ultramicroscopy* **2008**, 108, 763–772. `<DOI: 10.1016/j.ultramic.2007.12.002>`

[84] Gorelik, T. E.; van de Streek, J.; Kilbinger, A. F. M.; Brunklaus, G.; Kolb, U. Ab-Initio Crystal Structure Analysis and Refinement Approaches of Oligo *p*-Benzamides

Based on Electron Diffraction Data. *Acta Cryst. B* **2012**, 68, 171–181. <DOI: 10.1107/S0108768112003138>

[85] Feyand, M.; Mugnaioli, E.; Vermoortele, F.; Bueken, B.; Dieterich, J. M.; Reimer, T.; Kolb, U.; de Vos, D.; Stock, N. Automated Diffraction Tomography for the Structure Elucidation of Twinned, Sub-Micrometer Crystals of a Highly Porous, Catalytically Active Bismuth Metal-Organic Framework. *Angew. Chem. Int. Ed.* **2012**, 51, 10373–10376. <DOI: 10.1002/anie.201204963>

[86] Mugnaioli, E.; Gorelik, T.; Kolb, U. "Ab Initio" Structure Solution from Electron Diffraction Data Obtained by a Combination of Automated Diffraction Tomography and Precession Technique. *Ultramicroscopy* **2009**, 109, 758–765. <DOI: 10.1016/j.ultramic.2009.01.011>

[87] Own, C. S.; Subramanian, A. K.; Marks, L. D. Quantitative Analyses of Precession Diffraction Data for a Large Cell Oxide. *Microscopy and Microanalysis* **2004**, 10, 96–104. <DOI: 10.1017/S1431927604040322>

[88] Zhang, D.; Oleynikov, P.; Hovmöller, S.; Zou, X. Collecting 3D Electron Diffraction Data by the Rotation Method. *Zeitschrift für Kristallographie* **2010**, 225, 94–102. <DOI: 10.1524/zkri.2010.1202>

[89] Nederlof, I.; van Genderen, E.; Li, Y.-W.; Abrahams, J. P. A Medipix Quantum Area Detector Allows Rotation Electron Diffraction Data Collection from Submicrometre Three-Dimensional Protein Crystals. *Acta Cryst. D* **2013**, 69, 1223–1230. <DOI: 10.1107/S0907444913009700>

[90] Nannenga, B. L.; Shi, D.; Hattne, J.; Reyes, F. E.; Gonen, T. Structure of Catalase Determined by MicroED. *eLife* **2014**, 3, e03600. <DOI: 10.7554/eLife.0360>

[91] Gemmi, M.; La Placa, M. G. I.; Galanis, A. S.; Rauch, E. F.; Nicolopoulos, S. Fast Electron Diffraction Tomography. *J. Appl. Cryst.* **2015**, 48, 718–727. <DOI: 10.1107/S1600576715004604>

[92] Wang, Y.; Yang, T.; Xu, H.; Zou, X.; Wan, W. On the Quality of the Continuous Rotation Electron Diffraction Data for Accurate Atomic Structure Determination of Inorganic Compounds. *J. Appl. Cryst.* **2018**, 51, 1094–1101. <DOI: 10.1107/S1600576718007604>

[93] Schlichting, I. Serial Femtosecond Crystallography: The First Five Years. *IUCrJ* **2015**, 2, 246–255. <DOI: 10.1107/S205225251402702X>

[94] Chapman, H. N.; Caleman, C.; Timneanu, N. Diffraction before Destruction. *Philosophical Transactions of the Royal Society B: Biological Sciences* **2014**, 369, 20130313. <DOI: 10.1098/rstb.2013.0313>

[95] Cichocka, M. O.; Ångström, J.; Wang, B.; Zou, X.; Smeets, S. High-Throughput Continuous Rotation Electron Diffraction Data Acquisition via Software Automation. *J. Appl. Cryst.* **2018**, 51, 1652–1661. <DOI: 10.1107/S1600576718015145>

[96] Roslova, M.; Smeets, S.; Wang, B.; Thersleff, T.; Xu, H.; Zou, X. InsteaDMatic: Towards Cross-Platform Automated Continuous Rotation Electron Diffraction. *J. Appl. Cryst.* **2020**, 53, 1217–1224, <DOI: 10.1107/S1600576720009590>

[97] Takaba, K.; Maki-Yonekura, S.; Yonekura, K. Collecting Large Datasets of Rotational Electron Diffraction with ParallEM and SerialEM. *J. Struct. Biol.* **2020**, 211, 107549. <DOI: 10.1016/j.jsb.2020.107549>

[98] Smeets, S.; Zou, X.; Wan, W. Serial Electron Crystallography for Structure Determination and Phase Analysis of Nanocrystalline Materials. *J. Appl. Cryst.* **2018**, 51, 1262–1273. <DOI: 10.1107/S1600576718009500>

[99] Bücker, R.; Hogan-Lamarre, P.; Mehrabi, P.; Schulz, E. C.; Bultema, L. A.; Gevorkov, Y.; Brehm, W.; Yefanov, O.; Oberthür, D.; Kassier, G. H.; Dwayne Miller, R. J. Serial Protein Crystallography in an Electron Microscope. *Nat. Commun.* **2020**, 11, 996. <DOI: 10.1038/s41467-020-14793-0>

[100] Ophus, C. Four-Dimensional Scanning Transmission Electron Microscopy (4D–STEM): From Scanning Nanodiffraction to Ptychography and Beyond. *Microscopy and Microanalysis* **2019**, 25, 563–582. <DOI: 10.1017/S1431927619000497>

[101] Gallagher-Jones, M.; Ophus, C.; Bustillo, K. C.; Boyer, D. R.; Panova, O.; Glynn, C.; Zee, C.-T.; Ciston, J.; Mancia, K. C.; Minor, A. M.; Rodriguez, J. A. Nanoscale Mosaicity Revealed in Peptide Microcrystals by Scanning Electron Nanodiffraction. *Commun. Biol.* **2019**, 2, 1–8. <DOI: 10.1038/s42003-018-0263-8>

[102] Gallagher-Jones, M.; Bustillo, K. C.; Ophus, C.; Richards, L. S.; Ciston, J.; Lee, S.; Minor, A. M.; Rodriguez, J. A. Atomic Structures Determined from Digitally Defined Nanocrystalline Regions. *IUCrJ* **2020**, 7, 490–499. <DOI: 10.1107/S2052252520004030>

[103] Bustillo, K. C.; Zeltmann, S. E.; Chen, M.; Donohue, J.; Ciston, J.; Ophus, C.; Minor, A. M. 4D–STEM of Beam-Sensitive Materials. *Acc. Chem. Res.* **2021**, 54, 2543–2551. <DOI: 10.1021/acs.accounts.1c00073>

[104] Kolb, U.; Mugnaioli, E.; Gorelik, T. E. Automated Electron Diffraction Tomography—a New Tool for Nano Crystal Structure Analysis. *Crystal Research and Technology* **2011**, 46, 542–554. <DOI: 10.1002/crat.201100036>

[105] Gemmi, M.; Oleynikov, P. Scanning Reciprocal Space for Solving Unknown Structures: Energy Filtered Diffraction Tomography and Rotation Diffraction Tomography Methods. *Zeitschrift für Kristallographie* **2013**, 228, 51–58. <DOI: 10.1524/zkri.2013.1559>

[106] Wan, W.; Sun, J.; Su, J.; Hovmöller, S.; Zou, X. Three-Dimensional Rotation Electron Diffraction: Software RED for Automated Data Collection and Data Processing. *J. Appl. Cryst.* **2013**, 46, 1863–1873. <DOI: 10.1107/S0021889813027714>

[107] Palatinus, L.; Brázda, P.; Jelínek, M.; Hrdá, J.; Steciuk, G.; Klementová, M. Specifics of the Data Processing of Precession Electron Diffraction Tomography Data and Their Implementation in the Program PETS2.0. *Acta Cryst. B* **2019**, 75, 512–522. <DOI: 10.1107/S2052520619007534>

[108] Battye, T. G. G.; Kontogiannis, L.; Johnson, O.; Powell, H. R.; Leslie, A. G. W. IMOSFLM: A New Graphical Interface for Diffraction-Image Processing with MOSFLM. *Acta Cryst. D* **2011**, 67, 271–281. <DOI: 10.1107/S0907444910048675>

[109] Winter, G.; Beilsten-Edmands, J.; Devenish, N.; Gerstel, M.; Gildea, R. J.; McDonagh, D.; Pascal, E.; Waterman, D. G.; Williams, B. H.; Evans, G. DIALS as a Toolkit. *Protein Sci.* **2022**, 31, 232–250. <DOI: 10.1002/pro.4224>

[110] Kabsch, W. XDS. *Acta Cryst. D* **2010**, 66, 125–132. <DOI: 10.1107/S0907444909047337>

[111] Clabbers, M. T. B.; Gruene, T.; Parkhurst, J. M.; Abrahams, J. P.; Waterman, D. G. Electron Diffraction Data Processing with DIALS. *Acta Cryst. D* **2018**, 74, 506–518. <DOI: 10.1107/S2059798318007726>

[112] White, T. A.; Mariani, V.; Brehm, W.; Yefanov, O.; Barty, A.; Beyerlein, K. R.; Chervinskii, F.; Galli, L.; Gati, C.; Nakane, T.; Tolstikova, A.; Yamashita, K.; Yoon, C. H.; Diederichs, K.; Chapman, H. N. Recent Developments in CrystFEL. *J. Appl. Cryst.* **2016**, 49, 680–689. <DOI: 10.1107/S1600576716004751>

[113] Bücker, R.; Hogan-Lamarre, P.; Miller, R. J. D. Serial Electron Diffraction Data Processing With Diffractem and CrystFEL. *Frontiers in Molecular Biosciences* **2021**, 8, 415. <DOI: 10.3389/fmolb.2021.624264>

[114] Sheldrick, G. M. Phase Annealing in SHELX-90: Direct Methods for Larger Structures. *Acta Cryst. A* **1990**, 46, 467–473. <DOI: 10.1107/S0108767390000277>

[115] Morris, R. J.; Bricogne, G. Sheldrick's 1.2 Å Rule and Beyond. *Acta Cryst. D* **2003**, 59, 615–617. <DOI: 10.1107/S090744490300163X>

[116] Sheldrick, G. M. SHELXT—Integrated Space-Group and Crystal-Structure Determination. *Acta Cryst. A* **2015**, 71, 3–8. <DOI: 10.1107/S2053273314026370>

[117] Schneider, T. R.; Sheldrick, G. M. Substructure Solution with SHELXD. *Acta Cryst. D* **2002**, 58, 1772–1779. <DOI: 10.1107/S0907444902011678>

[118] Altomare, A.; Giacovazzo, C.; Guagliardi, A.; Siliqi, D. Triplet and Quartet Relationships and the Positivity Postulate. *Acta Cryst. A* **1994**, 50, 311–317. `<DOI: 10.1107/S0108767393009857>`

[119] Wang, J. On the Appearance of Carboxylates in Electrostatic Potential Maps. *Protein Sci.* **2017**, 26, 396–402. `<DOI: 10.1002/pro.3093>`

[120] Wang, J. Experimental Charge Density from Electron Microscopic Maps. *Protein Sci.* **2017**, 26, 1619–1626. `<DOI: 10.1002/pro.3198>`

[121] Wang, J.; Moore, P. B. On the Interpretation of Electron Microscopic Maps of Biological Macromolecules. *Protein Sci.* **2017**, 26, 122–129. `<DOI: 10.1002/pro.3060>`

[122] Subramanian, G.; Basu, S.; Liu, H.; Zuo, J.-M.; Spence, J. C. H. Solving Protein Nanocrystals by Cryo-EM Diffraction: Multiple Scattering Artifacts. *Ultramicroscopy* **2015**, 148, 87–93. `<DOI: 10.1016/j.ultramic.2014.08.013>`

[123] Latychevskaia, T.; Abrahams, J. P. Inelastic Scattering and Solvent Scattering Reduce Dynamical Diffraction in Biological Crystals. *Acta Cryst. B* **2019**, 75, 523–531. `<DOI: 10.1107/S2052520619009661>`

[124] Brünger, A. T. Simulated Annealing in Crystallography. *Annu. Rev. Phys. Chem.* **1991**, 42, 197–223. `<DOI: 10.1146/annurev.pc.42.100191.001213>`

[125] Woollam, G. R.; Das, P. P.; Mugnaioli, E.; Andrusenko, I.; Galanis, A. S.; van de Streek, J.; Nicolopoulos, S.; Gemmi, M.; Wagner, T. Structural Analysis of Metastable Pharmaceutical Loratadine Form II, by 3D Electron Diffraction and DFT+D Energy Minimisation. *CrystEngComm* **2020**, 22, 7490–7499. `<DOI: 10.1039/D0CE01216E>`

[126] Lightowler, M.; Li, S.; Ou, X.; Zou, X.; Lu, M.; Xu, H. Indomethacin Polymorph Revealed To Be Two Plastically Bendable Crystal Forms by 3D Electron Diffraction: Correcting a 47-Year-Old Misunderstanding. *Angew. Chem. Int. Ed.* **2022**, 61, e202114985. `<DOI: 10.1002/anie.202114985>`

[127] McCoy, A. J.; Grosse-Kunstleve, R. W.; Adams, P. D.; Winn, M. D.; Storoni, L. C.; Read, R. J. Phaser Crystallographic Software. *J. Appl. Cryst.* **2007**, 40 (4), 658–674. `<DOI: 10.1107/S0021889807021206>`

[128] Vagin, A.; Teplyakov, A. Molecular Replacement with MOLREP. *Acta Cryst. D* **2010**, 66 (1), 22–25. `<DOI: 10.1107/S0907444909042589>`

[129] Xu, H.; Lebrette, H.; Clabbers, M. T. B.; Zhao, J.; Griese, J. J.; Zou, X.; Högbom, M. Solving a New R2lox Protein Structure by Microcrystal Electron Diffraction. *Science Advances* **2018**, 5 (8), eaax4621. `<DOI: 10.1126/sciadv.aax4621>`

[130] Xu, H.; Zou, X.; Högbom, M.; Lebrette, H. Redetermination of the First Unknown Protein MicroED Structure by High Resolution X-Ray Diffraction. *bioRxiv* **2021**. `<DOI: 10.1101/2021.04.07.438860>`

[131] Rodríguez, D. D.; Grosse, C.; Himmel, S.; González, C.; de Ilarduya, I. M.; Becker, S.; Sheldrick, G. M.; Usón, I. Crystallographic Ab Initio Protein Structure Solution below Atomic Resolution. *Nat. Methods* **2009**, 6 (9), 651–653. `<DOI: 10.1038/nmeth.1365>`

[132] Sammito, M.; Meindl, K.; de Ilarduya, I. M.; Millán, C.; Artola-Recolons, C.; Hermoso, J. A.; Usón, I. Structure Solution with ARCIMBOLDO Using Fragments Derived from Distant Homology Models. *FEBS J.* **2014**, 281 (18), 4029–4045. `<DOI: 10.1111/febs.12897>`

[133] Richards, L. S.; Flores, M. D.; Millán, C.; Glynn, C.; Zee, C.-T.; Sawaya, M. R.; Gallagher-Jones, M.; Borges, R. J.; Usón, I.; Rodriguez, J. A. Fragment-Based Ab Initio Phasing of Peptidic Nanocrystals by MicroED. *ACS Bio. Med. Chem. Au* **2023**, 3, 2, 201–210. `<DOI: 10.1021/acsbiomedchemau.2c00082>`

[134] Richards, L. S.; Millán, C.; Miao, J.; Martynowycz, M. W.; Sawaya, M. R.; Gonen, T.; Borges, R. J.; Usón, I.; Rodriguez, J. A. Fragment-Based Determination of a Proteinase K Structure from MicroED Data Using ARCIMBOLDO_SHREDDER. *Acta Cryst. D* **2020**, 76 (8), 703–712. `<DOI: 10.1107/S2059798320008049>`.

[135] Jumper, J.; Evans, R.; Pritzel, A.; Green, T.; Figurnov, M.; Ronneberger, O.; Tunyasuvunakool, K.; Bates, R.; Žídek, A.; Potapenko, A.; Bridgland, A.; Meyer, C.; Kohl, S. A. A.; Ballard, A. J.; Cowie, A.; Romera-Paredes, B.; Nikolov, S.; Jain, R.; Adler, J.; Back, T.; Petersen, S.; Reiman, D.; Clancy, E.; Zielinski, M.; Steinegger, M.; Pacholska, M.; Berghammer, T.; Bodenstein, S.; Silver, D.; Vinyals, O.; Senior, A. W.; Kavukcuoglu, K.; Kohli, P.; Hassabis, D. Highly Accurate Protein Structure Prediction with AlphaFold. *Nature* **2021**, 596 (7873), 583–589. `<DOI: 10.1038/s41586-021-03819-2>`

[136] Baek, M.; DiMaio, F.; Anishchenko, I.; Dauparas, J.; Ovchinnikov, S.; Lee, G. R.; Wang, J.; Cong, Q.; Kinch, L. N.; Schaeffer, R. D.; Millán, C.; Park, H.; Adams, C.; Glassman, C. R.; DeGiovanni, A.; Pereira, J. H.; Rodrigues, A. V.; van Dijk, A. A.; Ebrecht, A. C.; Opperman, D. J.; Sagmeister, T.; Buhlheller, C.; Pavkov-Keller, T.; Rathinaswamy, M. K.; Dalwadi, U.; Yip, C. K.; Burke, J. E.; Garcia, K. C.; Grishin, N. V.; Adams, P. D.; Read, R. J.; Baker, D. Accurate Prediction of Protein Structures and Interactions Using a Three-Track Neural Network. *Science* **2021**, 373 (6557), 871–876. `<DOI: 10.1126/science.abj8754>`

[137] Palatinus, L.; Petříček, V.; Corrêa, C. A. Structure Refinement Using Precession Electron Diffraction Tomography and Dynamical Diffraction: Theory and Implementation. *Acta Cryst. A* **2015**, 71, 235–244. `<DOI: 10.1107/S2053273315001266`

[138] Palatinus, L.; Corrêa, C. A.; Steciuk, G.; Jacob, D.; Roussel, P.; Boullay, P.; Klementová, M.; Gemmi, M.; Kopeček, J.; Domeneghetti, M. C.; Cámara, F.; Petříček, V.

Structure Refinement Using Precession Electron Diffraction Tomography and Dynamical Diffraction: Tests on Experimental Data. *Acta Cryst. B* **2015**, 71, 740–751. <DOI: 10.1107/S2052520615017023>

[139] Palatinus, L.; Brázda, P.; Boullay, P.; Perez, O.; Klementová, M.; Petit, S.; Eigner, V.; Zaarour, M.; Mintova, S. Hydrogen Positions in Single Nanocrystals Revealed by Electron Diffraction. *Science* **2017**, 355, 166–169. <DOI: 10.1126/science.aak9652>

[140] Clabbers, M. T. B.; Gruene, T.; van Genderen, E.; Abrahams, J. P. Reducing Dynamical Electron Scattering Reveals Hydrogen Atoms. *Acta Cryst. A* **2019**, 75, 82–93. <DOI: 10.1107/S2053273318013918>

[141] Yang, T.; Xu, H.; Zou, X. Improving data quality for three-dimensional electron diffraction by a post-column energy filter and a new crystal tracking method. *IUCrJ* **2022**, 55, 1583-1591. <DOI: 10.1107/S1600576722009633>

[142] Chang, S.; Head-Gordon, T.; Glaeser, R. M.; Downing, K. H. Chemical Bonding Effects in the Determination of Protein Structures by Electron Crystallography. *Acta Cryst. A* **1999**, 55, 305–313. <DOI: 10.1107/S0108767398009726>

[143] Yamashita, H.; Kidera, A. Environmental Influence on Electron Scattering from a Molecule. *Acta Cryst. A* **2001**, 57, 518–525. <DOI: 10.1107/S0108767301006778>

[144] Gruza, B.; Chodkiewicz, M. L.; Krzeszczakowska, J.; Dominiak. P. M. Refinement of Organic Crystal Structures with Multipolar Electron Scattering Factors. *Acta Cryst. A* **2020**, 76, 92–109. <DOI: 10.1107/S2053273319015304>

[145] Jha, K. K.; Gruza, B.; Chodkiewicz, M. L.; Jelsch, C.; Dominiak, P. M. Refinements on Electron Diffraction Data of β-Glycine in MoPro: A Quest for an Improved Structure Model. *J. Appl. Cryst.* **2021**, 54, 1234–1243. <DOI: 10.1107/S160057672100580X>

[146] Domagała, S.; Fournier, B.; Liebschner, D.; Guillot, B.; Jelsch, C. An Improved Experimental Databank of Transferable Multipolar Atom Models - ELMAM2. Construction Details and Applications. *Acta Cryst. A* **2012**, 68, 337–351. <DOI: 10.1107/S0108767312008197>

[147] Grigorieff, N.; Ceska, T. A.; Downing, K. H.; Baldwin, J. M.; Henderson, R. Electron-Crystallographic Refinement of the Structure of Bacteriorhodopsin. *J. Mol. Biol.* **1996**, 259 (3), 393–421. <DOI: 10.1006/jmbi.1996.0328>

[148] Mitsuoka, K.; Hirai, T.; Murata, K.; Miyazawa, A.; Kidera, A.; Kimura, Y.; Fujiyoshi, Y. The Structure of Bacteriorhodopsin at 3.0 Å Resolution Based on Electron Crystallography: Implication of the Charge Distribution. *J. Mol. Biol.* **1999**, 286 (3), 861–882. <DOI: 10.1006/jmbi.1998.2529>

[149] Kimura, Y.; Vassylyev, D. G.; Miyazawa, A.; Kidera, A.; Matsushima, M.; Mitsuoka, K.; Murata, K.; Hirai, T.; Fujiyoshi, Y. Surface of Bacteriorhodopsin Revealed by High-Resolution Electron Crystallography. *Nature* **1997**, 389 (6647), 206–211. `<DOI: 10.1038/38323>`

[150] Hirai, T.; Mitsuoka, K.; Kidera, A.; Fujiyoshi, Y. Simulation of Charge Effects on Density Maps Obtained by High-Resolution Electron Crystallography. *J. Electron Microsc.* **2007**, 56 (4), 131–140. `<DOI: 10.1093/jmicro/dfm019>`

[151] Anstis, G. R.; Lynch, D. F.; Moodie, A. F.; O'Keefe, M. A. N-Beam Lattice Images. III. Upper Limits of Ionicity in $W_4Nb_{26}O_{77}$. *Acta Cryst. A* **1973**, 29 (2), 138–147. `<DOI: 10.1107/S0567739473000379>`

[152] Tsirelson, V. G.; Avilov, A. S.; Lepeshov, G. G.; Kulygin, A. K.; Stahn, J.; Pietsch, U.; Spence, J. C. H. Quantitative Analysis of the Electrostatic Potential in Rock-Salt Crystals Using Accurate Electron Diffraction Data. *J. Phys. Chem. B* **2001**, 105 (21), 5068–5074. `<DOI: 10.1021/jp0015729>`

[153] Yonekura, K.; Kato, K.; Ogasawara, M.; Tomita, M.; Toyoshima, C. Electron Crystallography of Ultrathin 3D Protein Crystals: Atomic Model with Charges. *Proc. Natl. Acad. Sci. U. S. A.* **2015**, 112 (11), 3368–3373. `<DOI: 10.1073/pnas.1500724112>`

[154] Yonekura, K.; Maki-Yonekura, S. Refinement of Cryo-EM Structures Using Scattering Factors of Charged Atoms. *J. Appl. Cryst.* **2016**, 49 (5), 1517–1523. `<DOI: 10.1107/S1600576716011274>`

[155] Yonekura, K.; Matsuoka, R.; Yamashita, Y.; Yamane, T.; Ikeguchi, M.; Kidera, A.; Maki-Yonekura, S. Ionic Scattering Factors of Atoms That Compose Biological Molecules. *IUCrJ* **2018**, 5 (3), 348–353. `<DOI: 10.1107/S2052252518005237>`

[156] Afonine, P. V.; Mustyakimov, M.; Grosse-Kunstleve, R. W.; Moriarty, N. W.; Langan, P.; Adams, P. D. Joint X-Ray and Neutron Refinement with Phenix.Refine. *Acta Cryst. D* **2010**, 66 (11), 1153–1163. `<DOI: 10.1107/S0907444910026582>`

[157] Gardberg, A. S.; Del Castillo, A. R.; Weiss, K. L.; Meilleur, F.; Blakeley, M. P.; Myles, D. a. A. Unambiguous Determination of H-Atom Positions: Comparing Results from Neutron and High-Resolution X-Ray Crystallography. *Acta Cryst. D* **2010**, 66 (5), 558–567. `<DOI: 10.1107/S0907444910005494>`

[158] Schmidtmann, M.; Coster, P.; Henry, P. F.; Ting, V. P.; Weller, M. T.; Wilson, C. C. Determining Hydrogen Positions in Crystal Engineered Organic Molecular Complexes by Joint Neutron Powder and Single Crystal X-Ray Diffraction. *CrystEngComm* **2014**, 16 (7), 1232–1236. `<DOI: 10.1039/C3CE42070A>`

[159] Jones, C. G.; Asay, M.; Kim, L. J.; Kleinsasser, J. F.; Saha, A.; Fulton, T. J.; Berkley, K. R.; Cascio, D.; Malyutin, A. G.; Conley, M. P.; Stoltz, B. M.; Lavallo, V.; Rodríguez, J. A.; Nelson, H. M. Characterization of Reactive Organometallic Species via MicroED. *ACS Cent. Sci.* **2019**, 5 (9), 1507–1513. `<DOI: 10.1021/acscentsci.9b00403>`

[160] Bau, R.; Drabnis, M. H. Structures of Transition Metal Hydrides Determined by Neutron Diffraction. *Inorg. Chim. Acta* **1997**, 259 (1), 27–50. `<DOI: 10.1016/S0020-1693(97)89125-6>`

[161] Gallagher-Jones, M.; Glynn, C.; Boyer, D. R.; Martynowycz, M. W.; Hernandez, E.; Miao, J.; Zee, C.-T.; Novikova, I. V.; Goldschmidt, L.; McFarlane, H. T.; Helguera, G. F.; Evans, J. E.; Sawaya, M. R.; Cascio, D.; Eisenberg, D. S.; Gonen, T.; Rodriguez, J. A. Sub-Ångström Cryo-EM Structure of a Prion Protofibril Reveals a Polar Clasp. *Nat. Struct. Mol. Biol.* **2018**, 25 (2), 131–134. `<DOI: 10.1038/s41594-017-0018-0>`

[162] Nakane, T.; Kotecha, A.; Sente, A.; McMullan, G.; Masiulis, S.; Brown, P. M. G. E.; Grigoras, I. T.; Malinauskaite, L.; Malinauskas, T.; Miehling, J.; Uchański, T.; Yu, L.; Karia, D.; Pechnikova, E. V.; de Jong, E.; Keizer, J.; Bischoff, M.; McCormack, J.; Tiemeijer, P.; Hardwick, S. W.; Chirgadze, D. Y.; Murshudov, G.; Aricescu, A. R.; Scheres, S. H. W. Single-Particle Cryo-EM at Atomic Resolution. *Nature* **2020**, 587 (7832), 152–156. `<DOI: 10.1038/s41586-020-2829-0>`

[163] Reimer, L.; Kohl, H. *Transmission Electron Microscopy: Physics of Image Formation*, 5th ed. Springer: New York, **2008**.

[164] Yonekura, K.; Maki-Yonekura, S.; Namba, K. Quantitative Comparison of Zero-Loss and Conventional Electron Diffraction from Two-Dimensional and Thin Three-Dimensional Protein Crystals. *Biophys. J.* **2002**, 82 (5), 2784–2797. `<DOI: 10.1016/S0006-3495(02)75619-1>`

[165] Yonekura, K.; Braunfeld, M. B.; Maki-Yonekura, S.; Agard, D. A. Electron Energy Filtering Significantly Improves Amplitude Contrast of Frozen-Hydrated Protein at 300kV. *J. Struct. Biol.* **2006**, 156 (3), 524–536. `<DOI: 10.1016/j.jsb.2006.07.016>`

[166] Yonekura, K.; Ishikawa, T.; Maki-Yonekura, S. A New Cryo-EM System for Electron 3D Crystallography by EEFD. *J. Struct. Biol.* **2019**, 206 (2), 243–253. `<DOI: 10.1016/j.jsb.2019.03.009>`

[167] Burmester, C.; Schröder, R. R. SOLVING THE PHASE PROBLEM IN PROTEIN ELECTRON CRYSTALLOGRAPHY: MULTIPLE ISOMORPHOUS REPLACEMENT AND ANOMALOUS DISPERSION AS ALTERNATIVES TO IMAGING. *Scanning Microscopy* **1997**, 11, 323–334.

[168] Martynowycz, M. W.; Hattne, J.; Gonen, T. Experimental Phasing of MicroED Data Using Radiation Damage. *Structure* **2020**, 28 (4), 458-464. `<DOI: 10.1016/j.str.2020.01.008>`

[169] Flack, H. D.; Bernardinelli, G. The Use of X-Ray Crystallography to Determine Absolute Configuration. *Chirality* **2008**, 20 (5), 681–690. <DOI: 10.1002/chir.20473>

[170] Bijvoet, J. M.; Peerdeman, A. F.; van Bommel, A. J. Determination of the Absolute Configuration of Optically Active Compounds by Means of X-Rays. *Nature* **1951**, 168 (4268), 271–272. <DOI: 10.1038/168271a0>

[171] Brázda, P.; Palatinus, L.; Babor, M. Electron Diffraction Determines Molecular Absolute Configuration in a Pharmaceutical Nanocrystal. *Science* **2019**, 364 (6441), 667–669. <DOI: 10.1126/science.aaw2560>

[172] Dorset, D. L. *Structural Electron Crystallography*. Springer Science: New York, **1995**.

[173] Hooft, R. W. W.; Straver, L. H.; Spek, A. L. Determination of Absolute Structure Using Bayesian Statistics on Bijvoet Differences. *J Appl. Cryst.* **2008**, 41 (1), 96–103. <DOI: 10.1107/S0021889807059870>

[174] Klar, P.; Krysiak, Y.; Xu, H.; Steciuk, G.; Cho, J.; Zou, X.; Palatinus, L. Accurate structure models and absolute configuration determination using dynamical effects in continuous-rotation 3D electron diffraction data. *Nat. Chem.* **2023**, 15, 848–855. <DOI: 10.1038/s41557-023-01186-1>

[175] Spence, J. C. H.; Donatelli, J. J. Inversion of Dynamical Bragg Intensities to Complex Structure Factors by Iterated Projections. *Ultramicroscopy* **2021**, 222, 113214. <DOI: 10.1016/j.ultramic.2021.113214>

[176] Wang, B.; Bruhn, J.; Weldeab, A.; Wilson, T.; McGilvray, P.; Mashore, M.; Song, Q.; Scapin, G.; Lin, Y. Absolute Configuration Determination of Pharmaceutical Crystalline Powders by MicroED via Chiral Salt Formation. *Chem. Commun.* **2022**. <DOI: 10.1039/D2CC00221C>

[177] Eisenberg, D.; Jucker, M. The Amyloid State of Proteins in Human Diseases. *Cell* **2012**, 148, 1188–1203. <DOI: 10.1016/j.cell.2012.02.022>

[178] Eisenberg, D. S.; Sawaya, M. R. Structural Studies of Amyloid Proteins at the Molecular Level. *Annu. Rev. Biochem.* **2017**, 86, 69–95. <DOI: 10.1146/annurev-biochem-061516-045104>

[179] Hughes, M. P.; Sawaya, M. R.; Boyer, D. R.; Goldschmidt, L.; Rodriguez, J. A.; Cascio, D.; Chong, L.; Gonen, T.; Eisenberg, D. S. Atomic Structures of Low-Complexity Protein Segments Reveal Kinked β-Sheets That Assemble Networks. *Science* **2018**, 359, 698–701. <DOI: 10.1126/science.aan6398>

[180] Balbirnie, M.; Grothe, R.; Eisenberg, D. S. An Amyloid-Forming Peptide from the Yeast Prion Sup35 Reveals a Dehydrated β-Sheet Structure for Amyloid. *Proc. Natl. Acad. Sci. U. S. A.* **2001**, 98, 2375–2380. <DOI: 10.1073/pnas.041617698>

[181] Nelson, R.; Sawaya, M. R.; Balbirnie, M.; Madsen, A. Å.; Riekel, C.; Grothe, R.; Eisenberg, D. Structure of the Cross-β Spine of Amyloid-like Fibrils. *Nature* **2005**, 435, 773–778. <DOI: 10.1038/nature03680>

[182] Rodriguez, J. A.; Ivanova, M. I.; Sawaya, M. R.; Cascio, D.; Reyes, F. E.; Shi, D.; Sangwan, S.; Guenther, E. L.; Johnson, L. M.; Zhang, M.; Jiang, L.; Arbing, M. A.; Nannenga, B. L.; Hattne, J.; Whitelegge, J.; Brewster, A. S.; Messerschmidt, M.; Boutet, S.; Sauter, N. K.; Gonen, T.; Eisenberg, D. S. Structure of the Toxic Core of α-Synuclein from Invisible Crystals. *Nature* **2015**, 525, 486–490. <DOI: 10.1038/nature15368>

[183] Sawaya, M. R.; Rodriguez, J.; Cascio, D.; Collazo, M. J.; Shi, D.; Reyes, F. E.; Hattne, J.; Gonen, T.; Eisenberg, D. S. *Ab Initio* Structure Determination from Prion Nanocrystals at Atomic Resolution by MicroED. *Proc. Natl. Acad. Sci. U. S. A.* **2016**, 113, 11232–11236. <DOI: 10.1073/pnas.1606287113>

[184] Krotee, P.; Rodriguez, J. A.; Sawaya, M. R.; Cascio, D.; Reyes, F. E.; Shi, D.; Hattne, J.; Nannenga, B. L.; Oskarsson, M. E.; Philipp, S.; Griner, S.; Jiang, L.; Glabe, C. G.; Westermark, G. T.; Gonen, T.; Eisenberg, D. S. Atomic Structures of Fibrillar Segments of HIAPP Suggest Tightly Mated β-Sheets Are Important for Cytotoxicity. *eLife* **2017**, 6, e19273. <DOI: 10.7554/eLife.19273>

[185] Seidler, P. M.; Boyer, D. R.; Rodriguez, J. A.; Sawaya, M. R.; Cascio, D.; Murray, K.; Gonen, T.; Eisenberg, D. S. Structure-Based Inhibitors of Tau Aggregation. *Nat. Chem.* **2018**, 10 (2), 170–176. <DOI: 10.1038/nchem.2889>

[186] Seidler, P. M.; Boyer, D. R.; Murray, K. A.; Yang, T. P.; Bentzel, M.; Sawaya, M. R.; Rosenberg, G.; Cascio, D.; Williams, C. K.; Newell, K. L.; Ghetti, B.; DeTure, M. A.; Dickson, D. W.; Vinters, H. V.; Eisenberg, D. S. Structure-Based Inhibitors Halt Prion-like Seeding by Alzheimer's Disease–and Tauopathy–Derived Brain Tissue Samples. *J. Biol. Chem.* **2019**, 294 (44), 16451–16464. <DOI: 10.1074/jbc.RA119.009688>

[187] Guenther, E. L.; Ge, P.; Trinh, H.; Sawaya, M. R.; Cascio, D.; Boyer, D. R.; Gonen, T.; Zhou, Z. H.; Eisenberg, D. S. Atomic-Level Evidence for Packing and Positional Amyloid Polymorphism by Segment from TDP-43 RRM2. *Nat. Struct. Mol. Biol.* **2018**, 25 (4), 311–319. <DOI: 10.1038/s41594-018-0045-5>

[188] Guenther, E. L.; Cao, Q.; Trinh, H.; Lu, J.; Sawaya, M. R.; Cascio, D.; Boyer, D. R.; Rodriguez, J. A.; Hughes, M. P.; Eisenberg, D. S. Atomic Structures of TDP-43 LCD Segments and Insights into Reversible or Pathogenic Aggregation. *Nat. Struct. Mol. Biol.* **2018**, 25 (6), 463–471. <DOI: 10.1038/s41594-018-0064-2>

[189] Zee, C.; Glynn, C.; Gallagher-Jones, M.; Miao, J.; Santiago, C. G.; Cascio, D.; Gonen, T.; Sawaya, M. R.; Rodriguez, J. A. Homochiral and Racemic MicroED Structures of a Peptide Repeat from the Ice-Nucleation Protein InaZ. *IUCrJ* **2019**, 6 (2), 197–205. <DOI: 10.1107/S2052252518017621>

[190] Griner, S. L.; Seidler, P.; Bowler, J.; Murray, K. A.; Yang, T. P.; Sahay, S.; Sawaya, M. R.; Cascio, D.; Rodriguez, J. A.; Philipp, S.; Sosna, J.; Glabe, C. G.; Gonen, T.; Eisenberg, D. S. Structure-Based Inhibitors of Amyloid Beta Core Suggest a Common Interface with Tau. *eLife* **2019**, 8, e46924. `<DOI: 10.7554/eLife.46924>`

[191] Warmack, R. A.; Boyer, D. R.; Zee, C.-T.; Richards, L. S.; Sawaya, M. R.; Cascio, D.; Gonen, T.; Eisenberg, D. S.; Clarke, S. G. Structure of Amyloid-β (20-34) with Alzheimer's-Associated Isomerization at Asp23 Reveals a Distinct Protofilament Interface. *Nat. Commun.* **2019**, 10 (1), 3357. `<DOI: 10.1038/s41467-019-11183-z>`

[192] Gui, X.; Luo, F.; Li, Y.; Zhou, H.; Qin, Z.; Liu, Z.; Gu, J.; Xie, M.; Zhao, K.; Dai, B.; Shin, W. S.; He, J.; He, L.; Jiang, L.; Zhao, M.; Sun, B.; Li, X.; Liu, C.; Li, D. Structural Basis for Reversible Amyloids of HnRNPA1 Elucidates Their Role in Stress Granule Assembly. *Nat. Commun.* **2019**, 10 (1), 2006. `<DOI: 10.1038/s41467-019-09902-7>`

[193] Luo, F.; Gui, X.; Zhou, H.; Gu, J.; Li, Y.; Liu, X.; Zhao, M.; Li, D.; Li, X.; Liu, C. Atomic Structures of FUS LC Domain Segments Reveal Bases for Reversible Amyloid Fibril Formation. *Nat. Struct. Mol. Biol.* **2018**, 25 (4), 341–346. `<DOI: 10.1038/s41594-018-0050-8>`

[194] Zhou, H.; Luo, F.; Luo, Z.; Li, D.; Liu, C.; Li, X. Programming Conventional Electron Microscopes for Solving Ultrahigh-Resolution Structures of Small and Macro-Molecules. *Anal. Chem.* **2019**, 91 (17), 10996–11003. `<DOI: 10.1021/acs.analchem.9b01162>`

[195] Gruene, T.; Wennmacher, J. T. C.; Zaubitzer, C.; Holstein, J. J.; Heidler, J.; Fecteau-Lefebvre, A.; De Carlo, S.; Müller, E.; Goldie, K. N.; Regeni, I.; Li, T.; Santiso-Quinones, G.; Steinfeld, G.; Handschin, S.; van Genderen, E.; van Bokhoven, J. A.; Clever, G. H.; Pantelic, R. Rapid Structure Determination of Microcrystalline Molecular Compounds Using Electron Diffraction. *Angew. Chem. Int. Ed.* **2018**, 57 (50), 16313–16317. `<DOI: 10.1002/anie.201811318>`

[196] Jones, C. G.; Martynowycz, M. W.; Hattne, J.; Fulton, T. J.; Stoltz, B. M.; Rodriguez, J. A.; Nelson, H. M.; Gonen, T. The CryoEM Method MicroED as a Powerful Tool for Small Molecule Structure Determination. *ACS Cent. Sci.* **2018**, 4 (11), 1587–1592. `<DOI: 10.1021/acscentsci.8b00760>`

[197] Brown, A.; Clardy, J. Tiny Crystals Have Big Potential for Determining Structures of Small Molecules. *Nature* **2018**, 564 (7736), 348–349. `<DOI: 10.1038/d41586-018-07756-5>`

[198] Sitsel, O.; Raunser, S. Big Insights from Tiny Crystals. *Nat. Chem.* **2019**, 11 (2), 106–108. `<DOI: 10.1038/s41557-019-0211-3>`

[199] Filer, C. N. MicroED and Cannabinoid Research. *J. Cannabis Res.* **2021**, 3 (1), 14. `<DOI: 10.1186/s42238-021-00070-4>`

[200] Andrusenko, I.; Hamilton, V.; Mugnaioli, E.; Lanza, A.; Hall, C.; Potticary, J.; Hall, S. R.; Gemmi, M. The Crystal Structure of Orthocetamol Solved by 3D Electron Diffraction. *Angew. Chem. Int. Ed.* **2019**, 58 (32), 10919–10922. `<DOI: 10.1002/anie.201904564>`

[201] Gorelik, T. E.; Habermehl, S.; Shubin, A. A.; Gruene, T.; Yoshida, K.; Oleynikov, P.; Kaiser, U.; Schmidt, M. U. Crystal Structure of Copper Perchlorophthalocyanine Analysed by 3D Electron Diffraction. *Acta Cryst. B* **2021**, 77 (4), 662–675. `<DOI: 10.1107/S2052520621006806>`

[202] Uyeda, N.; Kobayashi, T.; Suito, E.; Harada, Y.; Watanabe, M. Molecular Image Resolution in Electron Microscopy. *J. Appl. Phys.* **1972**, 43 (12), 5181–5189. `<DOI: 10.1063/1.1661094>`

[203] Kim, L. J.; Xue, M.; Li, X.; Xu, Z.; Paulson, E.; Mercado, B.; Nelson, H. M.; Herzon, S. B. Structure Revision of the Lomaiviticins. *J. Am. Chem. Soc.* **2021**, 143 (17), 6578–6585. `<DOI: 10.1021/jacs.1c01729>`

[204] He, H.; Ding, W.-D.; Bernan, V. S.; Richardson, A. D.; Ireland, C. M.; Greenstein, M.; Ellestad, G. A.; Carter, G. T. Lomaiviticins A and B, Potent Antitumor Antibiotics from Micromonospora Lomaivitiensis. *J. Am. Chem. Soc.* **2001**, 123 (22), 5362–5363. `<DOI: 10.1021/ja010129o>`

[205] Burns, D. C.; Reynolds, W. F. Minimizing the Risk of Deducing Wrong Natural Product Structures from NMR Data. *Magn. Res. Chem.* **2019**, 59 (5), 500–533. `<DOI: 10.1002/mrc.4933>`

[206] Ghosh, R.; Bu, G.; Nannenga, B. L.; Sumner, L. W. Recent Developments Toward Integrated Metabolomics Technologies (UHPLC-MS-SPE-NMR and MicroED) for Higher-Throughput Confident Metabolite Identifications. *Front. Mol. Biosci.* **2021**, 8, 844. `<DOI: 10.3389/fmolb.2021.720955>`

[207] Kim, L. J.; Ohashi, M.; Zhang, Z.; Tan, D.; Asay, M.; Cascio, D.; Rodriguez, J. A.; Tang, Y.; Nelson, H. M. Prospecting for Natural Products by Genome Mining and Microcrystal Electron Diffraction. *Nat. Chem. Biol.* **2021**, 17 (8), 872–877. `<DOI: 10.1038/s41589-021-00834-2>`

[208] Park, J.-D.; Li, Y.; Moon, K.; Han, E. J.; Lee, S. R.; Seyedsayamdost, M. R. Structural Elucidation of Cryptic Algaecides in Marine Algal-Bacterial Symbioses by NMR Spectroscopy and MicroED. *Angew. Chem. Int. Ed.* **2022**, 61 (4), e202114022. `<DOI: 10.1002/anie.202114022>`

[209] Dick, M.; Sarai, N. S.; Martynowycz, M. W.; Gonen, T.; Arnold, F. H. Tailoring Tryptophan Synthase TrpB for Selective Quaternary Carbon Bond Formation. *J. Am. Chem. Soc.* **2019**, 141 (50), 19817–19822. `<DOI: 10.1021/jacs.9b09864>`

[210] Ting, C. P.; Funk, M. A.; Halaby, S. L.; Zhang, Z.; Gonen, T.; van der Donk, W. A. Use of a Scaffold Peptide in the Biosynthesis of Amino Acid–Derived Natural Products. *Science* **2019**, 365 (6450), 280–284. `<DOI: 10.1126/science.aau6232>`

[211] Curtis, B. J.; Kim, L. J.; Wrobel, C. J. J.; Eagan, J. M.; Smith, R. A.; Burch, J. E.; Le, H. H.; Artyukhin, A. B.; Nelson, H. M.; Schroeder, F. C. Identification of Uric Acid Gluconucleoside–Ascaroside Conjugates in *Caenorhabditis Elegans* by Combining Synthesis and MicroED. *Org. Lett.* **2020**, 22 (17), 6724–6728. `<DOI: 10.1021/acs.orglett.0c02038>`

[212] Samkian, A. E.; Kiel, G. R.; Jones, C. G.; Bergman, H. M.; Oktawiec, J.; Nelson, H. M.; Tilley, T. D. Elucidation of Diverse Solid-State Packing in a Family of Electron-Deficient Expanded Helicenes via Microcrystal Electron Diffraction (MicroED). *Angew. Chem.* **2021**, 133 (5), 2523–2529. `<DOI: 10.1002/ange.202012213>`

[213] Ghashghaei, O.; Pedrola, M.; Seghetti, F.; Martin, V. V.; Zavarce, R.; Babiak, M.; Novacek, J.; Hartung, F.; Rolfes, K. M.; Haarmann-Stemmann, T.; Lavilla, R. Extended Multicomponent Reactions with Indole Aldehydes: Access to Unprecedented Polyheterocyclic Scaffolds, Ligands of the Aryl Hydrocarbon Receptor. *Angew. Chem. Int. Ed.* **2021**, 60 (5), 2603–2608. `<DOI: 10.1002/anie.202011253>`

[214] Kato, K.; Takaba, K.; Maki-Yonekura, S.; Mitoma, N.; Nakanishi, Y.; Nishihara, T.; Hatakeyama, T.; Kawada, T.; Hijikata, Y.; Pirillo, J.; Scott, L. T.; Yonekura, K.; Segawa, Y.; Itami, K. Double-Helix Supramolecular Nanofibers Assembled from Negatively Curved Nanographenes. *J. Am. Chem. Soc.* **2021**, 143 (14), 5465–5469. `<DOI: 10.3389/fmolb.2021.720955>`

[215] Hall, C. L.; Andrusenko, I.; Potticary, J.; Gao, S.; Liu, X.; Schmidt, W.; Marom, N.; Mugnaioli, E.; Gemmi, M.; Hall, S. R. 3D Electron Diffraction Structure Determination of Terrylene, a Promising Candidate for Intermolecular Singlet Fission. *ChemPhysChem* **2021**, 22 (15), 1631–1637. `<DOI: 10.1002/cphc.202100320>`

[216] Cho, H. J.; Kim, K.; Kim, H.; Kim, T.; Malyutin, A. G.; Rees, D. C.; Yoo, B.-K.; Song, C. Microcrystal Electron Diffraction Elucidates Water-Specific Polymorphism-Induced Emission Enhancement of Bis-Arylacylhydrazone. *ACS Appl. Mater. Interfaces* **2021**, 13 (6), 7546–7555. `<DOI: 10.1021/acsami.0c21248>`

[217] Lee, H. B.; Shiau, A. A.; Marchiori, D. A.; Oyala, P. H.; Yoo, B.-K.; Kaiser, J. T.; Rees, D. C.; Britt, R. D.; Agapie, T. $\mathrm{CaMn_3^{IV}O_4}$ Cubane Models of the Oxygen-Evolving Complex: Spin Ground States $S<9/2$ and the Effect of Oxo Protonation. *Angew. Chem. Int. Ed.* **2021**, 60 (32), 17671–17679. `<DOI: 10.1002/anie.202105303>`

[218] Jellen, M. J.; Liepuoniute, I.; Jin, M.; Jones, C. G.; Yang, S.; Jiang, X.; Nelson, H. M.; Houk, K. N.; Garcia-Garibay, M. A. Enhanced Gearing Fidelity Achieved Through Macrocyclization of a Solvated Molecular Spur Gear. *J. Am. Chem. Soc.* **2021**, 143 (20), 7740–7747. `<DOI: 10.1021/jacs.1c01885>`

[219] Ueda, M.; Aoki, T.; Akiyama, T.; Nakamuro, T.; Yamashita, K.; Yanagisawa, H.; Nureki, O.; Kikkawa, M.; Nakamura, E.; Aida, T.; Itoh, Y. Alternating Heterochiral Supramolecular Copolymerization. *J. Am. Chem. Soc.* **2021**, 143 (13), 5121–5126. <DOI: 10.1021/jacs.1c00823>

[220] Doyle, L. R.; Thompson, E. A.; Burnage, A. L.; Whitwood, A. C.; Jenkins, H. T.; Macgregor, S. A.; Weller, A. S. MicroED Characterization of a Robust Cationic σ-Alkane Complex Stabilized by the $[B(3,5\text{-}(SF_5)_2C_6H_3)_4]^-$ Anion, via on-Grid Solid/Gas Single-Crystal to Single-Crystal Reactivity. *Dalton Trans.* **2022**, 51 (9), 3661–3665. <DOI: 10.1039/D2DT00335J>

[221] van Genderen, E.; Clabbers, M. T. B.; Das, P. P.; Stewart, A.; Nederlof, I.; Barentsen, K. C.; Portillo, Q.; Pannu, N. S.; Nicolopoulos, S.; Gruene, T.; Abrahams, J. P. *Ab Initio* Structure Determination of Nanocrystals of Organic Pharmaceutical Compounds by Electron Diffraction at Room Temperature Using a Timepix Quantum Area Direct Electron Detector. *Acta Cryst. A* **2016**, 72 (2), 236–242. <DOI: 10.1107/S2053273315022500>

[222] Wang, Y.; Takki, S.; Cheung, O.; Xu, H.; Wan, W.; Öhrström, L.; Inge, A. K. Elucidation of the Elusive Structure and Formula of the Active Pharmaceutical Ingredient Bismuth Subgallate by Continuous Rotation Electron Diffraction. *Chem. Commun.* **2017**, 53 (52), 7018–7021. <DOI: 10.1039/C7CC03180G>

[223] Guzmán-Afonso, C.; Hong, Y.; Colaux, H.; Iijima, H.; Saitow, A.; Fukumura, T.; Aoyama, Y.; Motoki, S.; Oikawa, T.; Yamazaki, T.; Yonekura, K.; Nishiyama, Y. Understanding Hydrogen-Bonding Structures of Molecular Crystals via Electron and NMR Nanocrystallography. *Nat. Commun.* **2019**, 10 (1), 3537. <DOI: 10.1038/s41467-019-11469-2>

[224] Das, P. P.; Mugnaioli, E.; Nicolopoulos, S.; Tossi, C.; Gemmi, M.; Galanis, A.; Borodi, G.; Pop, M. M. Crystal Structures of Two Important Pharmaceuticals Solved by 3D Precession Electron Diffraction Tomography. *Org. Process Res. Dev.* **2018**, 22 (10), 1365–1372. <DOI: 10.1021/acs.oprd.8b00149>

[225] Andrusenko, I.; Potticary, J.; Hall, S. R.; Gemmi, M. A New Olanzapine Cocrystal Obtained from Volatile Deep Eutectic Solvents and Determined by 3D Electron Diffraction. *Acta Cryst. B* **2020**, 76 (6), 1036–1044. <DOI: 10.1107/S2052520620012779>

[226] Hamilton, V.; Andrusenko, I.; Potticary, J.; Hall, C.; Stenner, R.; Mugnaioli, E.; Lanza, A. E.; Gemmi, M.; Hall, S. R. Racemic Conglomerate Formation via Crystallization of Metaxalone from Volatile Deep Eutectic Solvents. *Cryst. Growth Des.* **2020**, 20 (7), 4731–4739. <DOI: 10.1021/acs.cgd.0c00497>

[227] Bruhn, J. F.; Scapin, G.; Cheng, A.; Mercado, B. Q.; Waterman, D. G.; Ganesh, T.; Dallakyan, S.; Read, B. N.; Nieusma, T.; Lucier, K. W.; Mayer, M. L.; Chiang, N. J.; Poweleit, N.; McGilvray, P. T.; Wilson, T. S.; Mashore, M.; Hennessy, C.; Thomson, S.; Wang, B.; Potter, C. S.; Carragher, B. Small Molecule Microcrystal Electron Diffraction for

the Pharmaceutical Industry–Lessons Learned From Examining Over Fifty Samples. *Front. Mol. Biosci.* **2021**, 8, 354. <DOI: 10.3389/fmolb.2021.648603>

[228] Sekharan, S.; Liu, X.; Yang, Z.; Liu, X.; Deng, L.; Ruan, S.; Abramov, Y.; Sun, G.; Li, S.; Zhou, T.; Shi, B.; Zeng, Q.; Zeng, Q.; Chang, C.; Jin, Y.; Shi, X. Selecting a Stable Solid Form of Remdesivir Using Microcrystal Electron Diffraction and Crystal Structure Prediction. *RSC Adv.* **2021**, 11 (28), 17408–17412. <DOI: 10.1039/D1RA03100G>

[229] Das, P. P.; Pérez, A. G.; Galanis, A. S.; Nicolopoulos, S. Structural Characterization of Beam Sensitive Pharmaceutical Compounds Using 3D Electron Diffraction-Micro-ED at Low Dose with Pixelated Detectors. *Microscopy and Microanalysis* **2020**, 26 (S2), 1522–1522. <DOI: 10.1017/S1431927620018395>

[230] Bauer, J.; Spanton, S.; Henry, R.; Quick, J.; Dziki, W.; Porter, W.; Morris, J. Ritonavir: An Extraordinary Example of Conformational Polymorphism. *Pharm. Res.* **2001**, 18 (6), 859–866. <DOI: 10.1023/A:1011052932607>

[231] Lu, J.; Rohani, S. Polymorphism and Crystallization of Active Pharmaceutical Ingredients (APIs). *Current Medicinal Chemistry* **2009**, 16 (7), 884–905.

[232] Censi, R.; Di Martino, P. Polymorph Impact on the Bioavailability and Stability of Poorly Soluble Drugs. *Molecules* **2015**, 20 (10), 18759–18776. <DOI: 10.3390/molecules201018759>

[233] Lee, A. Y.; Erdemir, D.; Myerson, A. S. Crystal Polymorphism in Chemical Process Development. *Annual Review of Chemical and Biomolecular Engineering* **2011**, 2 (1), 259–280. <DOI: 10.1146/annurev-chembioeng-061010-114224>

[234] Blagden, N.; de Matas, M.; Gavan, P. T.; York, P. Crystal Engineering of Active Pharmaceutical Ingredients to Improve Solubility and Dissolution Rates. *Advanced Drug Delivery Reviews* **2007**, 59 (7), 617–630. <DOI: 10.1016/j.addr.2007.05.011>

[235] Tyler, A. R.; Ragbirsingh, R.; McMonagle, C. J.; Waddell, P. G.; Heaps, S. E.; Steed, J. W.; Thaw, P.; Hall, M. J.; Probert, M. R. Encapsulated Nanodroplet Crystallization of Organic-Soluble Small Molecules. *Chem.* **2020**, 6 (7), 1755–1765. <DOI: 10.1016/j.chempr.2020.04.009>

[236] Holstein, P. M.; Holstein, J. J.; Escudero-Adán, E. C.; Baudoin, O.; Echavarren, A. M. Ferrocene derivatives of liquid chiral molecules allow assignment of absolute configuration by X-ray crystallography. *Tetrahedron: Asymmetry* **2017**, 28, 1321–1329. <DOI: 10.1016/j.tetasy.2017.09.002>

[237] Nelson, H. M.; Siu, J. C.; Saha, A.; Cascio, D.; MacMillan, S. N.; Wu, S.-B.; Lu, C.; Rodríguez, J. A.; Houk, K. N.; Lin, S. Isolation and X-Ray Crystal Structure of an Electrogenerated TEMPO–N_3 Charge-Transfer Complex. *Org. Lett.* **2021**, 23 (2), 454–458. <DOI: 10.1021/acs.orglett.0c03966>

[238] Heidler, J.; Pantelic, R.; Wennmacher, J. T. C.; Zaubitzer, C.; Fecteau-Lefebvre, A.; Goldie, K. N.; Müller, E.; Holstein, J. J.; van Genderen, E.; De Carlo, S.; Gruene, T. Design Guidelines for an Electron Diffractometer for Structural Chemistry and Structural Biology. *Acta Cryst. D* **2019**, 75 (5), 458–466. <DOI: 10.1107/S2059798319003942>

[239] Glaeser, R. M.; Thomas, G. Application of Electron Diffraction to Biological Electron Microscopy. *Biophys. J.* **1969**, 9 (9), 1073–1099. <DOI: 10.1016/S0006-3495(69)86437-4>

[240] Unwin, P. N. T.; Henderson, R. Molecular Structure Determination by Electron Microscopy of Unstained Crystalline Specimens. *J. Mol. Biol.* **1975**, 94 (3), 425–440. <DOI: 10.1016/0022-2836(75)90212-0>

[241] Glaeser, R. M.; Downing, K. H. High-Resolution Electron Crystallography of Protein Molecules. *Ultramicroscopy* **1993**, 52 (3), 478–486. <DOI: 10.1016/0304-3991(93)90064-5>

[242] Henderson, R.; Baldwin, J. M.; Ceska, T. A.; Zemlin, F.; Beckmann, E.; Downing, K. H. Model for the Structure of Bacteriorhodopsin Based on High-Resolution Electron Cryo-Microscopy. *J. Mol. Biol.* **1990**, 213 (4), 899–929. <DOI: 10.1016/S0022-2836(05)80271-2>

[243] Gonen, T.; Sliz, P.; Kistler, J.; Cheng, Y.; Walz, T. Aquaporin-0 Membrane Junctions Reveal the Structure of a Closed Water Pore. *Nature* **2004**, 429 (6988), 193–197. <DOI: 10.1038/nature02503>

[244] Martynowycz, M. W.; Zhao, W.; Hattne, J.; Jensen, G. J.; Gonen, T. Qualitative Analyses of Polishing and Precoating FIB Milled Crystals for MicroED. *Structure* **2019**, 27 (10), 1594-1600. <DOI: 10.1016/j.str.2019.07.004>

[245] Martynowycz, M. W.; Shiriaeva, A.; Ge, X.; Hattne, J.; Nannenga, B. L.; Cherezov, V.; Gonen, T. MicroED Structure of the Human Adenosine Receptor Determined from a Single Nanocrystal in LCP. *Proc. Natl. Acad. Sci. U. S. A.* **2021**, 118 (36). <DOI: 10.1073/pnas.2106041118>

[246] Clabbers, M. T. B.; Fisher, S. Z.; Coinçon, M.; Zou, X.; Xu, H. Visualizing Drug Binding Interactions Using Microcrystal Electron Diffraction. *Commun. Biol.* **2020**, 3 (1), 1–8. <DOI: 10.1038/s42003-020-01155-1>

[247] Purdy, M. D.; Shi, D.; Chrustowicz, J.; Hattne, J.; Gonen, T.; Yeager, M. MicroED Structures of HIV-1 Gag CTD-SP1 Reveal Binding Interactions with the Maturation Inhibitor Bevirimat. *Proc. Natl. Acad. Sci. U. S. A.* **2018**, 115 (52), 13258–13263. <DOI: 10.1073/pnas.1806806115>

[248] Martynowycz, M. W.; Clabbers, M. T. B.; Hattne, J.; Gonen, T. Ab Initio Phasing Macromolecular Structures Using Electron-Counted MicroED Data. *Nat. Methods* **2022**, 19, 724–729. <DOI: 10.1038/s41592-022-01485-4>

[249] Deacon, A. M.; Weeks, C. M.; Miller, R.; Ealick, S. E. The Shake-and-Bake Structure Determination of Triclinic Lysozyme. *Proc. Natl. Acad. Sci. U. S. A.* **1998**, 95 (16), 9284–9289. <DOI: 10.1073/pnas.95.16.9284>

[250] Capitani, G. C.; Mugnaioli, E.; Guastoni, A. What Is the Actual Structure of Samarskite-(Y)? A TEM Investigation of Metamict Samarskite from the Garnet Codera Dike Pegmatite (Central Italian Alps). *American Mineralogist* **2016**, 101 (7), 1679–1690. <DOI: 10.2138/am-2016-5605>

[251] Woodhead, J. A.; Rossman, G. R.; Silver, L. T. The Metamictization of Zircon: Radiation Dose-Dependent Structural Characteristics. *American Mineralogist* **1991**, 76 (1–2), 74–82.

[252] Baybarz, R. D.; Haire, R. G.; Fahey, J. A. On the Californium Oxide System. *J. Inorg. Nucl. Chem.* **1972**, 34 (2), 557–565. <DOI: 10.1021/jacs.1c01885>

[253] Haire, R. G.; Baybarz, R. D. Identification and Analysis of Einsteinium Sesquioxide by Electron Diffraction. *J. Inorg. Nucl. Chem.* **1973**, 35 (2), 489–496. <DOI: 10.1016/0022-1902(73)80561-5>

[254] Haire, R. G.; Baybarz, R. D. Studies of Einsteinium Metal. *J. Phys. Colloques* **1979**, 40 (C4), C4-C4-102. <DOI: 10.1051/jphyscol:1979431>

[255] Müller, A.; Deblonde, G. J.-P.; Ercius, P.; Zeltmann, S. E.; Abergel, R. J.; Minor, A. M. Probing Electronic Structure in Berkelium and Californium via an Electron Microscopy Nanosampling Approach. *Nat. Commun.* **2021**, 12 (1), 948. <DOI: 10.1038/s41467-021-21189-1>

[256] Egerton, R. F. Radiation Damage to Organic and Inorganic Specimens in the TEM. *Micron* **2019**, 119, 72–87. <DOI: 10.1016/j.micron.2019.01.005>

[257] Egerton, R. F. Mechanisms of Radiation Damage in Beam-Sensitive Specimens, for TEM Accelerating Voltages between 10 and 300 KV. *Microsc. Res. Tech.* **2012**, 75 (11), 1550–1556. <DOI: 10.1002/jemt.22099>

[258] Henderson, R. The Potential and Limitations of Neutrons, Electrons and X-Rays for Atomic Resolution Microscopy of Unstained Biological Molecules. *Q. Rev. Biophys.* **1995**, 28 (2), 171–193. <DOI: 10.1017/S003358350000305X>

[259] Hattne, J.; Shi, D.; Glynn, C.; Zee, C.-T.; Gallagher-Jones, M.; Martynowycz, M. W.; Rodriguez, J. A.; Gonen, T. Analysis of Global and Site-Specific Radiation Damage in Cryo-EM. *Structure* **2018**, 26 (5), 759-766. <DOI: 10.1016/j.str.2018.03.021>

[260] Meents, A.; Gutmann, S.; Wagner, A.; Schulze-Briese, C. Origin and Temperature Dependence of Radiation Damage in Biological Samples at Cryogenic Temperatures. *Proc. Natl. Acad. Sci. U. S. A.* **2010**, 107 (3), 1094–1099. `<DOI: 10.1073/pnas.0905481107>`

[261] Ravelli, R. B.; McSweeney, S. M. The 'Fingerprint' That X-Rays Can Leave on Structures. *Structure* **2000**, 8 (3), 315–328. `<DOI: 10.1016/S0969-2126(00)00109-X>`

[262] Burmeister, W. P. Structural Changes in a Cryo-Cooled Protein Crystal Owing to Radiation Damage. *Acta Cryst. D* **2000**, 56 (3), 328–341. `<DOI: 10.1107/S0907444999016261>`

[263] Jeng, T.-W.; Chiu, W. Quantitative Assessment of Radiation Damage in a Thin Protein Crystal. *J. Microsc.* **1984**, 136 (1), 35–44. `<DOI: 10.1111/j.1365-2818.1984.tb02544.x>`

[264] Henderson, R.; Clarke, B. C. Cryo-Protection of Protein Crystals against Radiation Damage in Electron and X-Ray Diffraction. *Proceedings of the Royal Society of London. Series B: Biological Sciences* **1990**, 241 (1300), 6–8. `<DOI: 10.1098/rspb.1990.0057>`

[265] Fryer, J. R. The Effect of Dose Rate on Imaging Aromatic Organic Crystals. *Ultramicroscopy* **1987**, 23 (3), 321–327. `<DOI: 10.1016/0304-3991(87)90242-7>`

[266] Fryer, J. R.; McConnell, C. H.; Zemlin, F.; Dorset, D. L. Effect of Temperature on Radiation Damage to Aromatic Organic Molecules. *Ultramicroscopy* **1992**, 40 (2), 163–169. `<DOI: 10.1016/0304-3991(92)90057-Q>`

[267] Li, P.; Egerton, R. F. Radiation Damage in Coronene, Rubrene and p-Terphenyl, Measured for Incident Electrons of Kinetic Energy between 100 and 200kev. *Ultramicroscopy* **2004**, 101 (2), 161–172. `<DOI: 10.1016/j.ultramic.2004.05.010>`

[268] Dickerson, J. L.; McCubbin, P. T. N.; Garman, E. F. RADDOSE-XFEL: Femtosecond Time-Resolved Dose Estimates for Macromolecular X-Ray Free-Electron Laser Experiments. *J. Appl. Cryst.* **2020**, 53 (2), 549–560. `<DOI: 10.1107/S1600576720000643>`

CHAPTER 2

Factors of Atomic Electron Scattering (FAES): A Resource for Gaussian Parameterization of Integral Ionic, Fractionally Charged, and Neutral Electron Scattering Factors

This chapter contains material referenced in Saha, A.; Evans, M.; Holton, T.; Rodriguez, J. FAES (Factors of Atomic Electron Scattering): A resource for Gaussian parameterization of integral ionic, fractionally charged, and neutral electron scattering factors. *Acta Cryst.* **A77**, a50. `<DOI:10.1107/S0108767321099499>`

2.1 Abstract

Electrostatic potential maps derived from cryo–EM can contain a wealth of information about charged states. However, access to such information is obstructed by the absence of appropriately parameterized ionic electron scattering factors. Existing parameterizations remain either incomplete or incompatible with least-squares refinement programs. To rectify this, we introduce FAES (**F**actors of **A**tomic **E**lectron **S**cattering), a web server publicly accessible at `<srv.mbi.ucla.edu/faes>`. This resource supplies Gaussian parameterizations of elastic electron scattering factors into three forms and calculates fractionally charged scattering factors by computing linearly weighted sums of adjacent integral neighbors. Using atomic scattering amplitudes tabulated in the *International Tables for Crystallography*, FAES provides numerical fitting

coefficients, statistical goodness-of-fit values, and accompanying visual plots for all supported fits. We also derive elastic and estimated inelastic cross-sections from FAES parameterizations at a range of accelerating voltages relevant to transmission electron microscopy.

2.2 Theoretical Background

Under the aegis of cryogenic electron microscopy (cryo–EM), single-particle analysis and 3D electron crystallography have emerged as valuable techniques for structural elucidation of macromolecular assemblies. These methods recapitulate 3D maps of electrostatic potential (ESP) derived from interaction between an incident electron beam and the substrate under interrogation. Refinement of ESP maps is carried out by programs such as Phenix [1], REFMAC [2], and SHELXL [3], which attempt to iteratively minimize the discrepancy between theoretically calculated (F_{calc}) and experimentally observed (F_{obs}) structure factors in reciprocal space. Ultimately, the agreement between F_{calc} and F_{obs} is encapsulated in a residual or R-factor, which is defined as

$$R = \sum_{hkl} \frac{||F_{\text{obs}}| - |F_{\text{calc}}||}{|F_{\text{obs}}|} \tag{2.1}$$

and is generally reported as a universal validation metric to assess map quality. Computation of F_{calc} hinges on approximations of constituent atoms in terms of their parameterized electron scattering factors:

$$F_{hkl} = \sum_{j} f_j(s) \exp[-2\pi i\,(hx_j + ky_j + lz_j)], \tag{2.2}$$

where $f_j(s)$ is the individual scattering factor for the j^{th} atom, h, k, and l correspond to the Miller indices, and x_j, y_j, and z_j give the fractional coordinates of the j^{th} atom in real space. We can rewrite F_{hkl} in terms of the specific potential distribution which must have produced it

$$F_{hkl} = \int_0^c \int_0^b \int_0^a V(x, y, z) \exp[-2\pi i\,(hx + ky + lz)]\, dx\, dy\, dz, \tag{2.3}$$

where the limits of integration a, b, and c correspond to the dimensions of the unit cell and $V(x, y, z)$ is simply $V(\vec{r})$ expressed in terms of fractional Cartesian coordinates. From here we can reconstruct the electrostatic potential function $V(x, y, z)$ via inverse Fourier transform

$$V(x, y, z) = v^{-1} \sum_{hkl} F_{hkl} \exp[-2\pi i\,(hx + ky + lz)], \tag{2.4}$$

where v is the volume of the real-space unit cell. Just like XRD, each atomic scattering factor is treated as a sum of Gaussians, given the computational tractability of calculating Fourier transforms on Gaussian functions. These take the general form

$$f(s) = \sum_{j} a_j \exp(-b_j s^2), \tag{2.5}$$

where a_j and b_j represent arbitrary scaling coefficients. Some approximations also add a scalar constant

$$f(s) = \sum_{j} a_j \exp(-b_j s^2) + c, \tag{2.6}$$

which can augment the accuracy of the Gaussian fit. Specifically for ionic electron scattering factors, a divergent charge-correction term is historically used

$$f(s) = \sum_{j} a_j \exp(-b_j s^2) + \frac{m_0 e^2}{8\pi^2 \hbar^2} \left(\frac{\Delta Z}{s^2} \right), \tag{2.7}$$

where $\Delta Z = Z - Z_0$ and therefore represents excess nuclear charge. Equation 2.7 yields a very accurate fit for ionic electron scattering factors. Unfortunately, due to the resultant singularity at $s = 0$, inclusion of a divergent charge-correction term is incompatible with widely used refinement programs, rendering such parameterizations unusable for routine analysis of continuous-rotation 3D ED data. This dearth has forced groups interested in the process of refining charged species to compute their own parameterizations [4]. As a resource for the community, here we introduce a publicly accessible web server, FAES (Factors of Atomic Electron

Scattering, <srv.mbi.ucla.edu/faes>), which returns refinement-friendly parameterizations of all electron scattering factors currently tabulated in the *International Tables for Crystallography*, as well as fractionally charged scattering factors computed via linearly weighted combinations of integer parents. We also harness FAES' 5 Gaussian parameterization to derive elastic and estimated inelastic cross-sections for all neutral elements.

2.3 Curve-Fitting

Curve-fitting to a sum of Gaussian functions is treated as a nonlinear least-squares minimization problem and implemented using a Levenberg–Marquardt (`levmar`) algorithm in MATLAB [5, 6]. This algorithm iteratively optimizes an initial guess, which in our case originally consists of a pseudorandom set of values for a_j and b_j. As a result of these arbitrary starting points, the fitting procedure does not necessarily converge to a unique set of parameters for a_j and b_j across independent runs, even though the algorithm itself is formally deterministic. Effectively, `levmar` samples a cluster of local minima with negligibly different root-mean-squared error (RMSE) values. RMSE is used as a general measure of goodness-of-fit and is defined as

$$\mathrm{RMSE} = \sqrt{\frac{\sum_j (y_j - \hat{y}_j)^2}{v}}, \tag{2.8}$$

where v is the number of residual degrees of freedom and $\sum_j (y_j - \hat{y}_j)^2$ is the summed square of j residuals. We found that Levenberg–Marquardt systematically returned accurate fits for all six analytical approximations tested, despite starting from an uninformed initial guess. An exception arose in the specific case of I^-, where randomized starting points failed to generate a viable parameterization. Unlike their neutral and cationic counterparts, anions exhibit non-monotonic curves which hit a cusp and then abruptly plunge into negative scattering amplitudes as $s \to 0$. This behavior proved problematic to model for I^-. We rectified this by substituting initial a_j and b_j values from iodide's congener Br^-, allowing `levmar` to converge to an adequate solution

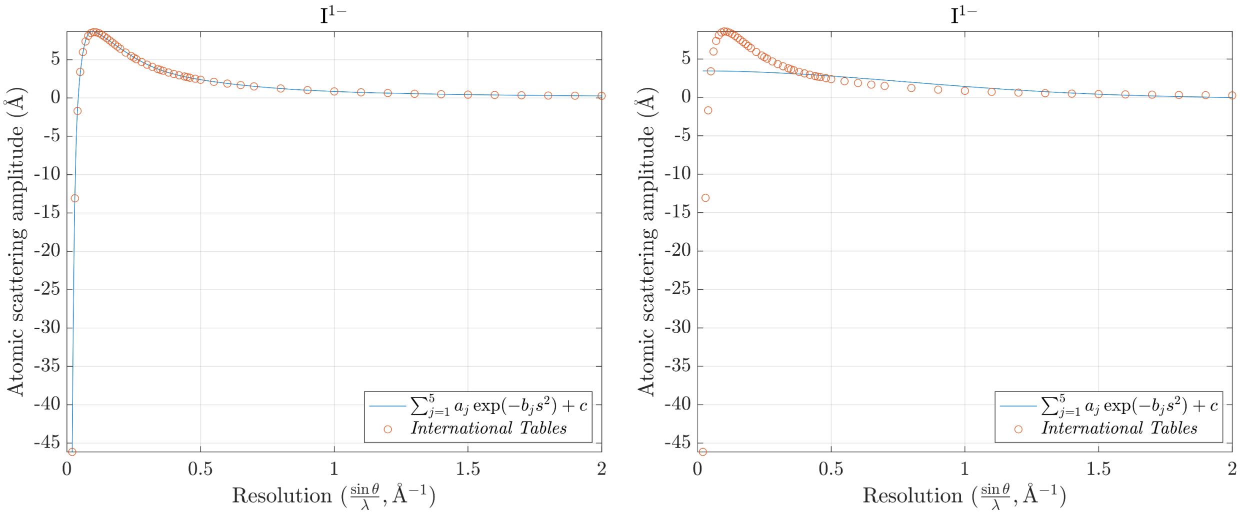

Figure 2.1: **Example of a problematic case, I$^-$, in which randomized starting points did not yield an accurate parameterization.** L: Results of Levenberg–Marquardt algorithm (RMSE = 0.051) for a 5 Gaussians + c parameterization (blue) applied to numerical data for I$^-$ (orange circles). This fit was obtained by substituting initial a_j and b_j values from iodide's congener Br$^-$, demonstrating the clear advantage conferred by supplying an informed initial guess. R: Analogous results of Levenberg–Marquardt algorithm (RMSE = 8.224) for a 5 Gaussians + c parameterization (blue) applied to numerical data for I$^-$ (orange circles), using randomized starting points for a_j and b_j.

(Figure 2.1). To avoid recurrence of these issues, we ultimately hard-coded proxy starting points for all ionic scattering factors.

An interesting artifact arose while curve-fitting numerical data to models involving a scalar constant c, as in equation 2.6. We observed that `levmar` frequently returned parameterizations in which one of the exponential terms contained a negative b coefficient very close to 0, yielding a non-Gaussian function resembling a flatline. By decomposing the relevant parameterizations into their individual components, we found that this non-Gaussian function and c were always offset equidistantly from the origin, effectively cancelling each other out (Figure 2.2). This redundancy, although diagnostic of an optimization procedure featuring an excessive number of degrees of freedom (i.e., more free variables than necessary), had no discernible effect on the quality of the fit. However, since direct summation quickly becomes intractable for large, macromolecular systems, structure-factor calculations in programs such as *Phenix* rely on a workaround involving fast Fourier transform (FFT) algorithms. As an intermediate step, these FFT routines use the *absolute value* of atomic charge density or ESP, obtained via analytical Fourier transform of scattering factors assumed to consist entirely of Gaussians:

$$\rho(|\vec{r}|) = \sum_j a_j \left(\frac{4\pi}{b_j}\right)^{\frac{3}{2}} \exp\left[-\frac{1}{2}\left(\frac{8\pi^2}{b_j}\right)\vec{r}^2\right], \tag{2.9}$$

where a_j and b_j represent the parameterized Gaussian coefficients [7, 8, 9]. Therefore, in cases where $b < 0$, since the Fourier transform of the resultant non-Gaussian function $a_j \exp(+b_j\vec{s}^2)$ is also non-Gaussian, FFT methods fail to return reliable results. To circumvent this, we applied a $b > 0$ constraint for all parameterizations involving equation 2.6. Because MATLAB's implementation of Levenberg–Marquardt cannot handle bound constraints, we switched to a trust-region algorithm for these approximations. This bug is fairly subtle and may have eluded previous authors; we note that existing parameterizations of ionic electron scattering factors did not necessarily apply such a constraint (for instance, see coefficients for H^{1+} in ref. [10]).

2.3.1 Resolution Range

FAES enforces a low-resolution cutoff at $\vec{s} = 0.05$ Å^{-1} for all cationic scattering factors and fits the remainder by extrapolation. We have relaxed this constraint to $\vec{s} = 0.02$ Å^{-1} only in the cases of the halide anions Cl^-, Br^-, and I^-, where a truncation at $\vec{s} = 0.05$ Å^{-1} failed to adequately capture the portion of the curve which becomes negative at low scattering angles. For neutral scattering factors, this value is set to 0.

We note that the ionic scattering amplitudes tabulated by Colliex *et al.* [11] in the *International Tables for Crystallography* often omit $f_e(0)$. Detailed calculations of $f_e(0)$ for a range of ions have been carried out by Rez, Rez, and Grant [12]. For charged scattering factors, however, Gaussian approximations cannot return accurate values for $f_e(0)$, as the sharp discontinuity between $f_e(0)$ and the first nonzero argument for s presents too great a challenge for fitting.

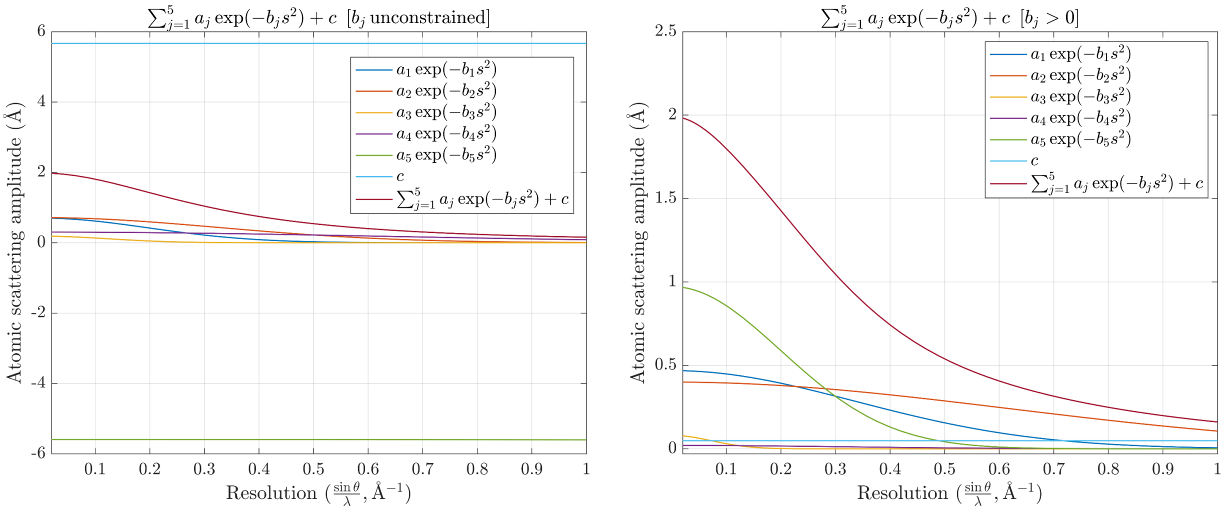

Figure 2.2: **Comparison between an unconstrained Levenberg–Marquardt algorithm and a trust-region approach in which the b_j terms were restricted to positive numbers.** L: Decomposition of an unconstrained 5 Gaussians + c parameterization for neutral O, obtained via Levenberg–Marquardt. Note how the Levenberg–Marquardt algorithm yields a non-Gaussian function $a_5 \exp(-b_5 s^2)$ (forest green), which is offset equidistantly from c (cyan): these two terms cancel each other out. R: Decomposition of a 5 Gaussians + c parameterization for neutral O, obtained via trust-region, in which the fitting procedure was restricted to positive b_j values. Note how the constrained trust-region approach removes the redundancy.

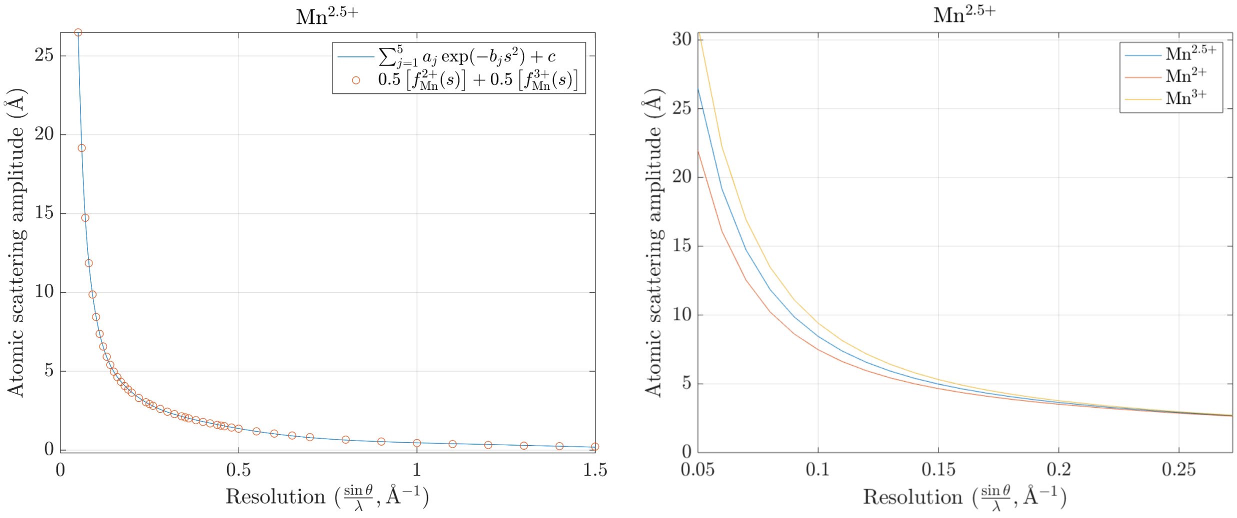

Figure 2.3: **Exemplary parameterization of a fractionally charged scattering factor, $\mathrm{Mn}^{2.5+}$.** L: 5 Gaussians + c parameterization (RMSE < 0.001) of $\mathrm{Mn}^{2.5+}$ (blue), a fractionally charged scattering factor formed via fitting numerical data (orange circles) synthesized from an equally weighted sum of Mn^{2+} and Mn^{3+}. R: $\mathrm{Mn}^{2.5+}$ (blue) interpolating between its integer parents, Mn^{2+} (orange) and Mn^{3+} (yellow).

2.3.2 Fractionally Charged Scattering Factors

In systems typically studied by cryo–EM methods, such as proteins, ionic species do not exist in an isolated vacuum. Generally, excess charge is either balanced by the presence of proximal counterions or diluted by non-covalent interactions such as hydrogen bonding. As a result, ESP projected by an individual ion will often experience perturbations due to its ambient environment. Specifically, low-angle scattering is especially sensitive to the redistribution of valence electrons which accompanies ionization. To indirectly account for this, it is helpful to introduce fractionally charged scattering factors, which can provide a proxy for modelling effective, partial, or delocalized charge.

Since multiconfigurational Dirac-Fock calculations may not provide stable results for non-integer charges, we approximate fractionally charged scattering factors by computing a weighted sum of their nearest integer neighbors. For an arbitrary element A, we can write

$$f_{\mathrm{A}}^{y}(\vec{s}) = w_1[f_{\mathrm{A}}^{x}(\vec{s})] + w_2[f_{\mathrm{A}}^{z}(\vec{s})], \tag{2.10}$$

$$|z| > |x|, \tag{2.11}$$

where y is some non-integer charge flanked by integers x and z. The weights w_1 and w_2 always sum to 1, but their individual values vary depending on y. As long as the inequality in equation 2.11 holds, we can construct a simple system of linear equations to solve for w_1 and w_2:

$$w_1 + w_2 = 1, \tag{2.12}$$

$$w_2 = |y| - |x|. \tag{2.13}$$

A simple illustrative example, $\mathrm{Mn}^{2.5+}$, is given in Figure 2.3. Fractionally charged scattering factors for 36 selected ions have been uploaded to the FAES database in increments of 0.1.

2.4 Derivation of Elastic Cross-Sections from Parameterized Scattering Factors

In crystallography, we typically express elastic X-ray or electron scattering amplitudes $f(s)$ as a function of $s = \frac{\sin\theta}{\lambda}$. This is convenient for our purposes, since it yields an x-axis interpretable in units of reciprocal distance (i.e., resolution in Å^{-1}). Transmission electron microscopy employs a different convention, where each scattering factor $f(\theta)$ is explicitly expressed as a function of the scattering angle θ in lieu of s. Once refactored into this form, we can derive the total elastic cross-section σ_e directly from $f(\theta)$ by integrating the differential cross-section $\frac{d\sigma}{d\Omega}$ over all unique scattering angles:

$$\sigma_e = 2\pi \int_0^\pi \frac{d\sigma}{d\Omega} \sin\theta \, d\theta = 2\pi \int_0^\pi |f(\theta)|^2 \sin\theta \, d\theta, \tag{2.14}$$

exploiting the key relationship $\frac{d\sigma}{d\Omega} = |f(\theta)|^2$. Using our 5 Gaussian approximation for $f(s)$ from FAES (<srv.mbi.ucla.edu/faes/data>), we can extract $f(\theta)$ and derive σ_e as follows:

```
import numpy as np
from scipy.integrate import quad
import csv

w = 0.019687  # relativistic wavelength in angstroms at 300 kV

a1 = []
a2 = []
a3 = []
a4 = []
a5 = []
b1 = []
b2 = []
b3 = []
b4 = []
b5 = []


# grab gaussian coefficients from FAES csv and store in arrays
for z in range(1, 2):
    zc = z - 1
    with open("FAES_neutral_5g.csv", "r") as ifile:
        y = csv.reader(ifile, delimiter=",")
        for col in y:
            a1.append(float(col[zc]))
            a2.append(float(col[zc + 1]))
            a3.append(float(col[zc + 2]))
```

```
            a4.append(float(col[zc + 3]))
            a5.append(float(col[zc + 4]))
            b1.append(float(col[zc + 5]))
            b2.append(float(col[zc + 6]))
            b3.append(float(col[zc + 7]))
            b4.append(float(col[zc + 8]))
            b5.append(float(col[zc + 9]))

for z in range(1, 99):
    zc = z - 1

    # define scattering factor as a function of sin(theta)/lambda
    def sfac(s):
        return a1[zc] * np.exp(-b1[zc] * (s ** 2)) + a2[zc] *
        np.exp(-b2[zc] * (s ** 2)) + a3[zc] * np.exp(-b3[zc]
        * (s ** 2)) + a4[zc] * np.exp(-b4[zc] * (s ** 2)) + a5[zc]
        * np.exp(-b5[zc] * (s ** 2))

    # rewrite scattering factor as a function of theta
    def sfac(theta):
        s = np.sin(theta) / w
        return a1[zc] * np.exp(-b1[zc] * (s ** 2)) + a2[zc] *
        np.exp(-b2[zc] * (s ** 2)) + a3[zc] * np.exp(-b3[zc]
        * (s ** 2)) + a4[zc] * np.exp(-b4[zc] * (s ** 2)) + a5[zc]
        * np.exp(-b5[zc] * (s ** 2))

    # calculate differential cross-section
    def diff_csection(theta):
        return abs(sfac(theta)) ** 2

    # multiply differential cross-section by 2pi and sin(theta)
    def diff_csection_int(theta):
        return 2 * np.pi * np.sin(theta) * diff_csection(theta)
```

```
    # integrate differential cross-section from 0 to pi
    int_csection, err = quad(diff_csection_int, 0, np.pi)
```

Listing 2.1: Code used to derive differential and total elastic cross-sections from FAES scattering factors.

Since this requires *ab initio* quantum mechanical calculations (e.g., relativistic Hartree-Fock, Dirac-Fock, etc.) for each element, a variety of analytical formulae have been derived to estimate σ_e. Langmore *et al.* [14] proposed the following expression in 1973:

$$\sigma_e \approx \frac{Z^{\frac{3}{2}}(1.5 \times 10^{-24}\,\mathrm{m}^2)}{\beta^2}\left(1 - \frac{Z}{596\beta}\right), \tag{2.15}$$

where Z is the atomic number, $\beta = \frac{v}{c}$, and $1 - \frac{Z}{596\beta}$ represents a correction to the first-order Born approximation. (Note that the presence of β renders all cross-sections inherently energy-dependent.) Langmore and Smith [15] later revised the above formula in 1992 to yield

$$\sigma_e \approx \frac{Z^{\frac{3}{2}}(1.4 \times 10^{-6}\,\mathrm{nm}^2)}{\beta^2}\left(1 - \frac{0.26Z}{137\beta}\right) \quad \text{if} \quad \frac{Z}{137\beta} \leq 1.5, \tag{2.16}$$

which is accurate for all elements lighter than U (with one notable exception, H). Calculation of the total inelastic cross-section σ_i from first principles is less straightforward. Empirically, however, Reimer and Ross-Messemer [15] found that σ_i exhibits a remarkably simple dependence on σ_e:

$$\sigma_i \approx \frac{20.2}{Z}\sigma_e. \tag{2.17}$$

Thankfully, therefore, we can easily estimate σ_i by multiplying σ_e by a scalar factor of $\frac{20.2}{Z}$. We can calculate all of these terms as follows:

```
import numpy as np
import matplotlib as mpl
import matplotlib.pyplot as plt
```

```
import matplotlib.patches as mpatches
from matplotlib.pyplot import figure

mpl.rc("text", usetex=True)

# define relevant constants
m = 1.5e-24
nm = 1.4e-6
c = 299792458  # speed of light in m/s
v = 2.3279e8 # relativistic electron velocity in m/s at 300 kV
# v = 2.0844e8 relativistic electron velocity in m/s at 200 kV
# v = 1.7587e8 relativistic electron velocity in m/s at 120 kV
# v = 1.6434e8 relativistic electron velocity in m/s at 100 kV
b = v / c
b2 = b ** 2
b596 = 596 * b
b137 = 137 * b

titles = ["H", "He", "Li", "Be", "B", "C", "N", "O", "F", "Ne",
    "Na", "Mg", "Al", "Si", "P", "S", "Cl", "Ar", "K", "Ca", "Sc",
    "Ti", "V", "Cr", "Mn", "Fe", "Co", "Ni", "Cu", "Zn", "Ga",
    "Ge", "As", "Se", "Br", "Kr", "Rb", "Sr", "Y", "Zr", "Nb",
    "Mo", "Tc", "Ru", "Rh", "Pd", "Ag", "Cd", "In", "Sn", "Sb",
    "Te", "I", "Xe", "Cs", "Ba", "La", "Ce", "Pr", "Nd", "Pm",
    "Sm", "Eu", "Gd", "Tb", "Dy", "Ho", "Er", "Tm", "Yb", "Lu",
    "Hf", "Ta", "W", "Re", "Os", "Ir", "Pt", "Au", "Hg", "Tl",
    "Pb", "Bi", "Po", "At", "Rn", "Fr", "Ra", "Ac", "Th", "Pa",
    "U", "Np", "Pu", "Am", "Cm", "Bk", "Cf"]

for z in range(1, 99):
    zc = z - 1
    z1p5 = z ** 1.5
```

```
# calculate elastic cross-section in m^2 according to equation(2)
sigma_el = ((m * z1p5) / b2) * (1 - (z / b596))

# convert m^2 to angstroms^2
sigma_el = sigma_el * 1e20

# estimate inelastic cross-section according to equation(4)
sigma_in = (sigma_el * 20.2) / z
ratio = sigma_el / sigma_in

# express cross-section as radius of a circle
r_el = np.sqrt(sigma_el / np.pi)
r_in = np.sqrt(sigma_in / np.pi)

# calculate elastic cross-section in nm^2 according to equation(3)
sigma_el2 = ((nm * z1p5) / b2) * (1 - (0.26 * z / b137))

# convert nm^2 to angstroms^2
sigma_el2 = sigma_el2 * 100

# estimate inelastic cross-section according to equation(4)
sigma_in2 = (sigma_el2 * 20.2) / z
ratio2 = sigma_el2 / sigma_in2

# express cross-section as radius of a circle
r_el2 = np.sqrt(sigma_el2 / np.pi)
r_in2 = np.sqrt(sigma_in2 / np.pi)

# plot as concentric superimposed circles
if r_el < r_in:

    # define circles
    c1 = plt.Circle((0, 0), r_el, color="#17becf", alpha=0.25)
```

```
        c2 = plt.Circle((0, 0), r_in, color="#bcbd22", alpha=0.25)

        # since r_el < r_in, plot inelastic cross-section first
        fig, ax = plt.subplots()
        ax.add_artist(c2)
        ax.add_artist(c1)

        # build plot and save to working directory in png format
        plt.axis([-0.5, 0.5, -0.5, 0.5])
        ax.set_title(titles[zc])
        plot_title = titles[zc] + "_300kV_csection_v2.png"
        inel = mpatches.Patch(color="#bcbd22", label="Inelastic cross-section ($\sigma_{i}$)", alpha=0.25)
        el = mpatches.Patch(color="#17becf", label="Elastic cross-section ($\sigma_{e}$)", alpha=0.25)
        plt.legend(handles=[inel, el])
        plt.xlabel(r"Transverse distance (A)")
        plt.ylabel(r"Transverse distance (A)")
        plt.savefig(plot_title, bbox_inches="tight", dpi=600)

    if r_in < r_el:
        c1 = plt.Circle((0, 0), r_el, color="#17becf", alpha=0.25)
        c2 = plt.Circle((0, 0), r_in, color="#bcbd22", alpha=0.25)

        # add circles in reverse order for r_in < r_el
        fig, ax = plt.subplots()
        ax.add_artist(c1)
        ax.add_artist(c2)

        # build plot and save to working directory in png format
        plt.axis([-0.5, 0.5, -0.5, 0.5])
        ax.set_title(titles[zc])
        plot_title = titles[zc] + "_300kV_csection_v2.png"
```

```
    inel = mpatches.Patch(color="#bcbd22", label="Inelastic cross-section ($\sigma_{i}$)", alpha=0.25)
    el = mpatches.Patch(color="#17becf", label="Elastic cross-section ($\sigma_{e}$)", alpha=0.25)
    plt.legend(handles=[inel, el])
    plt.xlabel(r"Transverse distance (A)")
    plt.ylabel(r"Transverse distance (A)")
    plt.savefig(plot_title, bbox_inches="tight", dpi=600)
```

Listing 2.2: Code used to compute analytical estimates of elastic and inelastic cross-sections and plot as concentric superimposed circles.

2.4.1 Comparison of FAES Cross-Sections to Results from Existing Models

These calculations divulge some interesting results. Using Langmore and Smith's analytical expression as a frame of reference, we find that the FAES-derived elastic cross-sections systematically give smaller numbers, although always within the same order of magnitude. This discrepancy narrows as we reduce the accelerating voltage (Table 2.1). On average, equation 2.16 returns σ_e values approximately 4× greater than equation 2.14 at 300 kV but only 2× greater at 80 kV. Furthermore, equation 2.16 is monotonic with respect to Z. In reality, each element's elastic cross-section should display some sensitivity to its corresponding outer-shell electronic structure, although this effect is increasingly attenuated at high Z. This should result in periodic deviations from monotonicity at low Z, especially for light noble gases such as He and Ne—elements with completely filled outer shells. Since our FAES scattering factors ultimately originate from relativistic Hartree-Fock wavefunctions, we should expect the σ_e values derived from equation 2.14 to break from monotonicity, particularly at junctures between noble gases and alkali metals (e.g., He to Li, Ne to Na, Ar to K, etc.). Conversely, we should anticipate Langmore and Smith's formula—an empirical estimate which is 'unaware' of the irregularities induced by outer-shell electronic structure—to overestimate σ_e for lighter atoms, especially first-row elements.

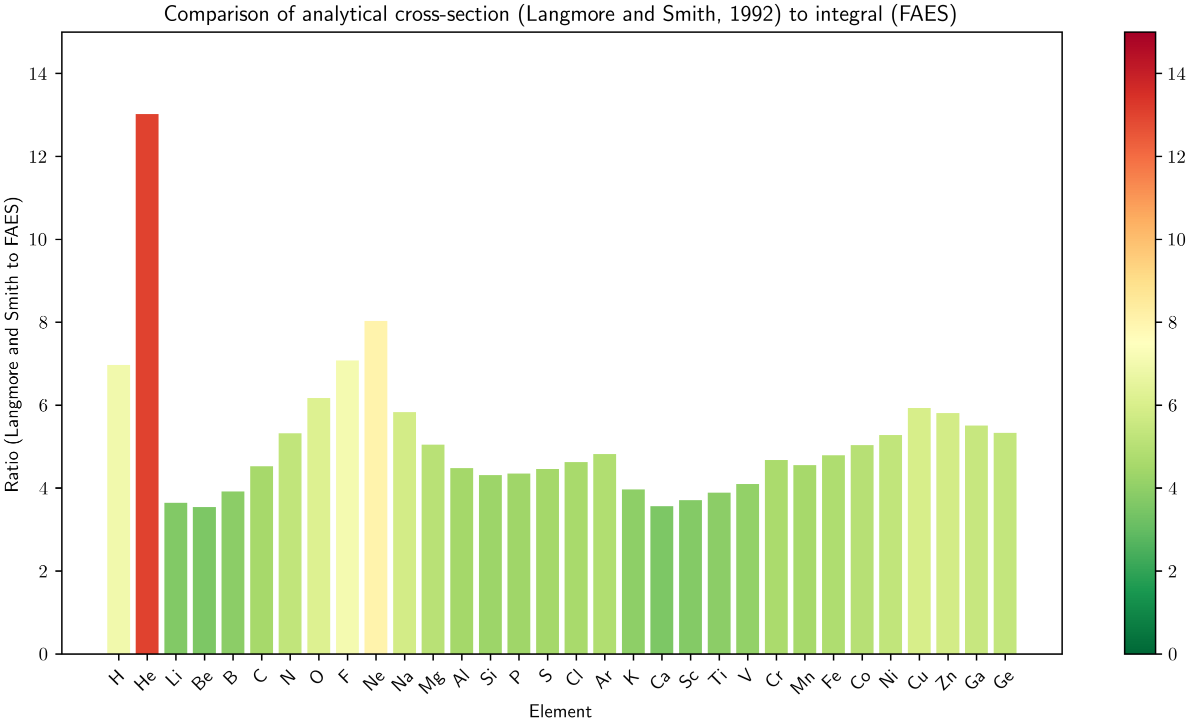

Figure 2.4: **Ratios between elastic cross-sections at 300 kV computed via Langmore and Smith's analytical estimate versus FAES' integral expression, plotted for elements H through Ge.** Non-monotonic trend reflects the intricacies of outer-shell electronic structure. Since Langmore and Smith's estimate is a linear approximation, it systematically overestimates σ_e for elements with completely filled outer shells, especially light atoms—thus the clear outliers at He and Ne.

Gratifyingly, this is exactly what we see. Plotting the ratio between Langmore and Smith's formula and FAES, we observe by far the most significant outliers at He and Ne, with a clear ascending pattern observed from B to Ne as we fill the *2p* valence shell. As Z gets larger and screening by outer-shell electrons becomes less consequential to elastic scattering, this discrepancy plateaus to a fairly consistent value. For nonmetals, this occurs at the third row. Critically, this trend appears physically meaningful and is reproducible across a range of accelerating voltages (80–400 kV). Plotting the calculated elastic cross-sections (in increments of 20 kV) for each element as a function of λ and β^{-2}, both consistent with the experimental results reported by Peet, Henderson, and Russo.

Accelerating voltage (kV)	FAES protein σ_e ($Å^2$)	Abrahams protein σ_e ($Å^2$)	FAES protein σ_i ($Å^2$)	Abrahams protein σ_i ($Å^2$)
100	0.00145	0.0042	0.00794	0.0174
200	0.000667	0.0026	0.00357	0.0108
300	0.000411	0.0021	0.00219	0.0087

Table 2.1: **Comparison of elastic cross-sections for an average atom in a protein crystal** ($Z = 3.77$, fractional empirical formula = $H_{0.57}C_{0.17}N_{0.05}O_{0.20}S_{0.01}$) derived from FAES vs. those estimated using the Lenz model by Latychevskaia and Abrahams (2019).

2.5 Features of the Web Server

Alongside a standard plot of the scattering factor itself, FAES also returns: (a) a 3D plot of the scattering factor recast as a function of two variables, (b) a 2D slice of the corresponding electrostatic potential $V(\vec{r})$, (c) a 2D slice of its Laplacian $\nabla^2 V(\vec{r})$, and (d) numerical coefficients corresponding to the relevant Gaussian approximation. For scattering factors parameterized into 4 Gaussians, FAES outputs Gaussian coefficients in a format which users can directly paste as an SFAC command into a SHELXL `.ins` file, as follows:

```
SFAC label a1 b1 a2 b2 a3 b3 a4 b4 c f' f" mu r wt
SFAC F 0.309 22.005 0.152 0.289 0.519 2.062 0.822 7.261 0 0 0 0 0.57
   18.998
```

Listing 2.3: Convention for specifying scattering factors in SHELXL. FAES automatically populates values for a1 through b4 (the coefficients from the corresponding Gaussian approximation), as well as r (covalent radius) and wt (atomic weight). Since c, f', f", and mu (real and imaginary components of expected anomalous dispersion, linear absorption coefficient) refer to terms unique to X-ray diffraction, FAES lists these as 0. Line 2 shows an illustrative example with the element fluorine. All covalent radii used in the SFAC commands were sourced from the values reported by Alvarez and co-workers [13].

To intuitively represent elastic and inelastic-cross sections in graphical form, FAES outputs a radial plot in which the cross-sectional areas σ_e and σ_i are expressed as concentric circles. For each element, FAES also returns: (a) a plot comparing elastic cross-sections at 100, 200, and 300 kV, (b) a plot showing the nonlinear dependence of σ_e on incident electron energy, (c) a plot showing the linear relationship between σ_e and β^{-2}, and (d) the numerical values obtained from equations 2.14 and 2.17.

Finally, to model the effects of thermal fluctuations and crystallographic disorder on electron scattering, we developed an interactive B-factor slider (`<srv.mbi.ucla.edu/faes/slider>`) which modifies the original scattering factor $f_e(s)$ as follows:

$$f_e^B(s) = \exp\left(\frac{-Bs^2}{4}\right) f_e(s), \tag{2.18}$$

where B is an isotropic Debye–Waller factor which can range from 0 to 200 Å^2. B is defined conventionally as

$$B = 8\pi^2\langle U^2\rangle, \tag{2.19}$$

where $\langle U^2\rangle$ is the mean square displacement of the atom in question from its listed set of 3D coordinates in the unit cell.

2.6 Potential Use Cases for Charged Scattering Factors

We examined 26 published 3D ED structures of oligopeptides to identify features potentially indicative of deprotonated carboxylates, ionized species frequently encountered in proteins. For each of these compounds, we tabulated the individual B-factors per atom and calculated the corresponding B-factor variance per residue. To reiterate, we searched for (a) strong negative peaks localized on carboxylate O atoms in Fourier difference maps calculated presuming neutral electron scattering factors, (b) weak or nonexistent density enveloping these O atoms in experimental ESP maps, and (c) aberrantly high B-factors associated with the offending atoms. Based on these diagnostic criteria, five of these structures—corresponding to PDB reference codes 4ZNN, 4RIL, 5WKB, 6BZM, and 5V5C—struck us as particularly promising candidates (Figures 2.5—2.14).

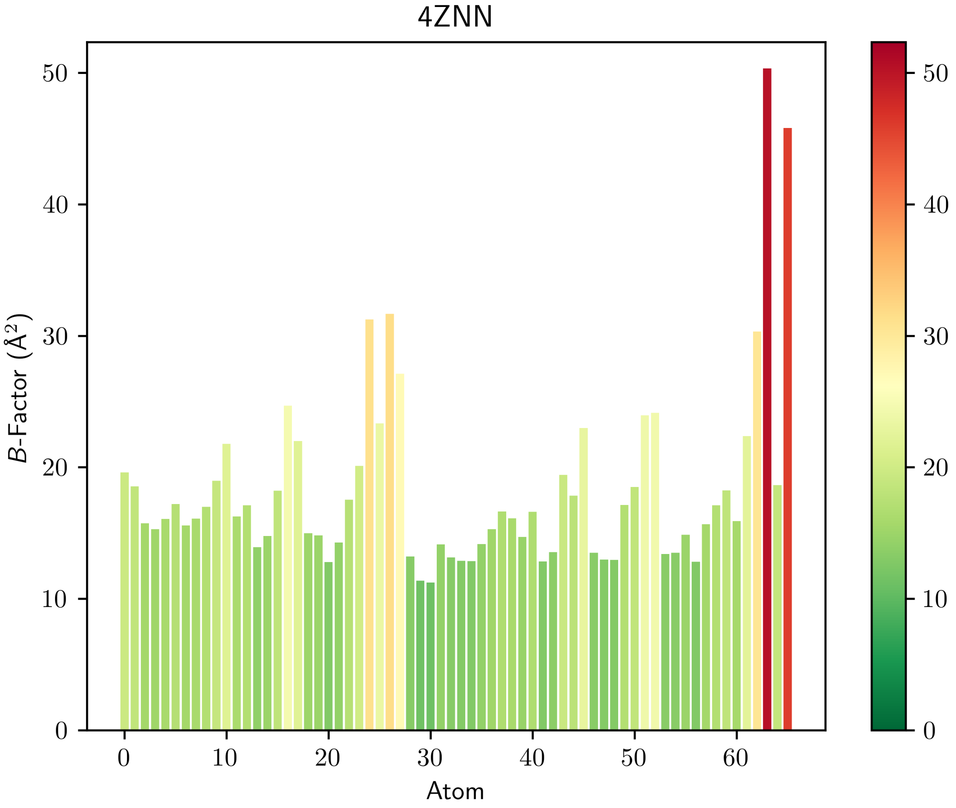

Figure 2.5: **Individual atomic *B*-factors refined in the deposited 3D ED structure of ^{47}GVVHGVTTVA^{56}** (PDB: 4ZNN), a segment from the toxic core of alpha-synuclein. Clear outliers observed for the two O atoms at the carboxylate terminus of the final alanine residue, A56. Interestingly, the carboxylate C atom on A56 (the last three atoms in the plot correspond to carboxylate O, C, O) features a *B*-factor comparable to an average atom in the remainder of the molecule, suggesting that beam-induced radiolytic decarboxylation was not yet operative to a significant extent given the dose absorbed by this crystal.

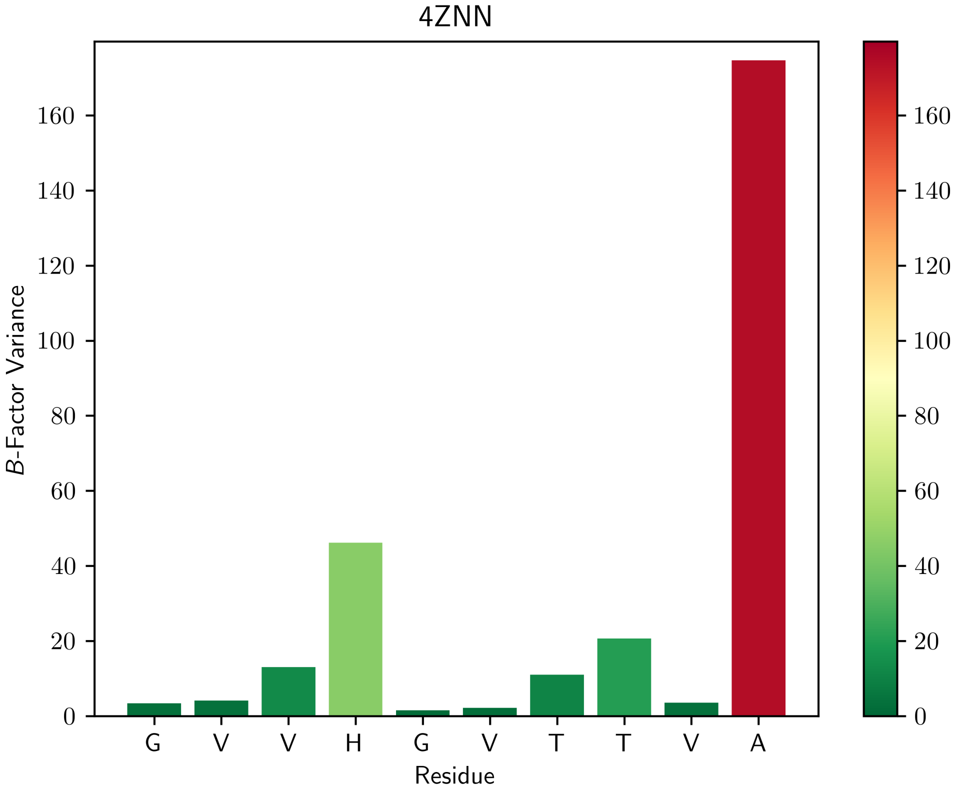

Figure 2.6: ***B*-factor variance calculated per residue for the deposited 3D ED structure of ^{47}GVVHGVTTVA^{56}** (PDB: 4ZNN), a segment from the toxic core of alpha-synuclein. A clear outlier is observed at the C-terminal alanine residue, A56, whose *B*-factor variance is 4× greater than the corresponding value for the next-highest amino acid, H50.

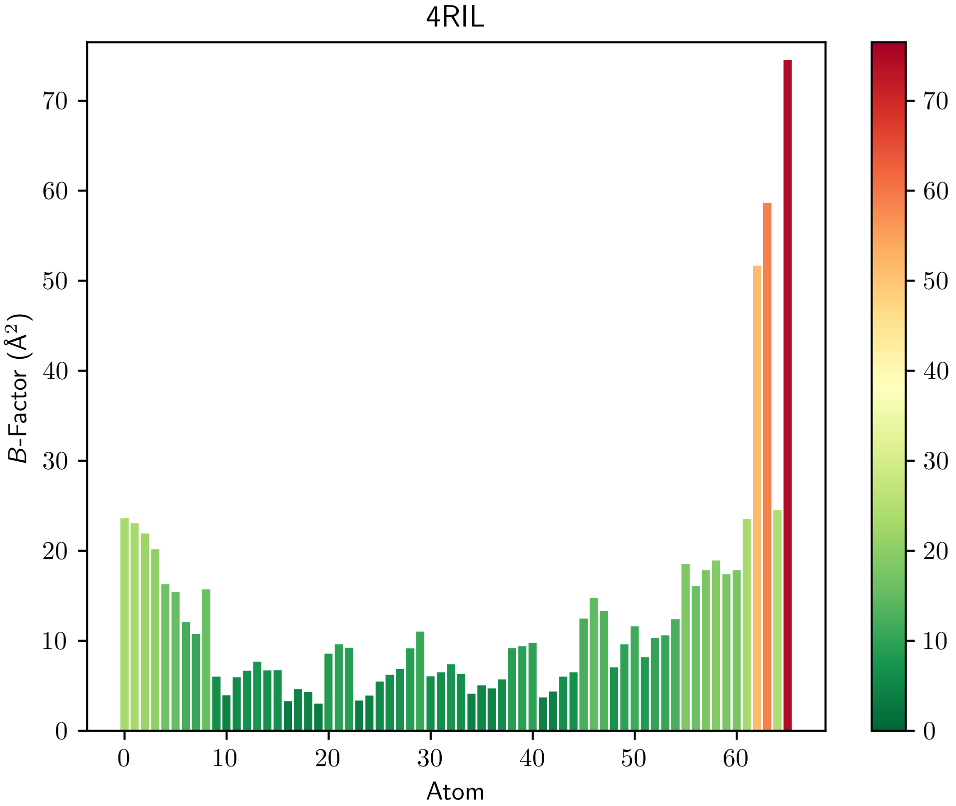

Figure 2.7: **Individual atomic *B*-factors refined in the deposited 3D ED structure of ^{68}GAVVTGVTAVA^{78}** (PDB: 4RIL), a segment from the toxic core of alpha-synuclein. Clear outliers observed for the two O atoms at the carboxylate terminus of the final alanine residue.

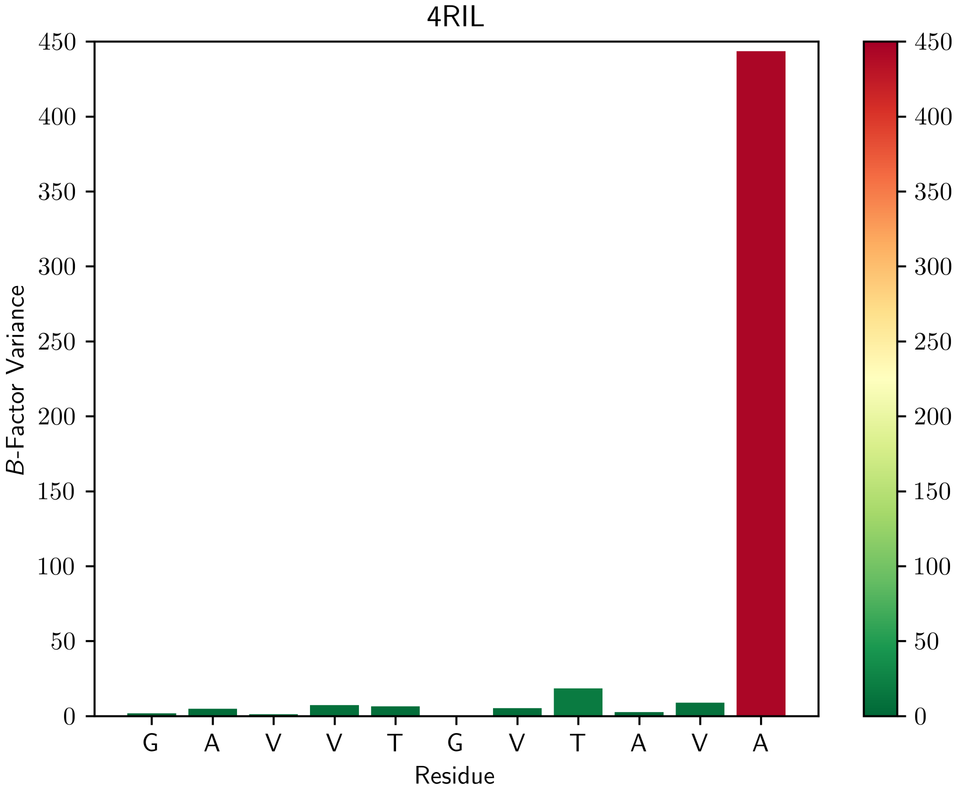

Figure 2.8: ***B*-factor variance calculated per residue for the deposited 3D ED structure of ^{68}GAVVTGVTAVA^{78}** (PDB: 4RIL), a segment from the toxic core of alpha-synuclein. A clear outlier is observed at the C-terminal alanine residue, A78, whose *B*-factor variance is a whopping 12× greater than the corresponding value for the next-highest amino acid, T75.

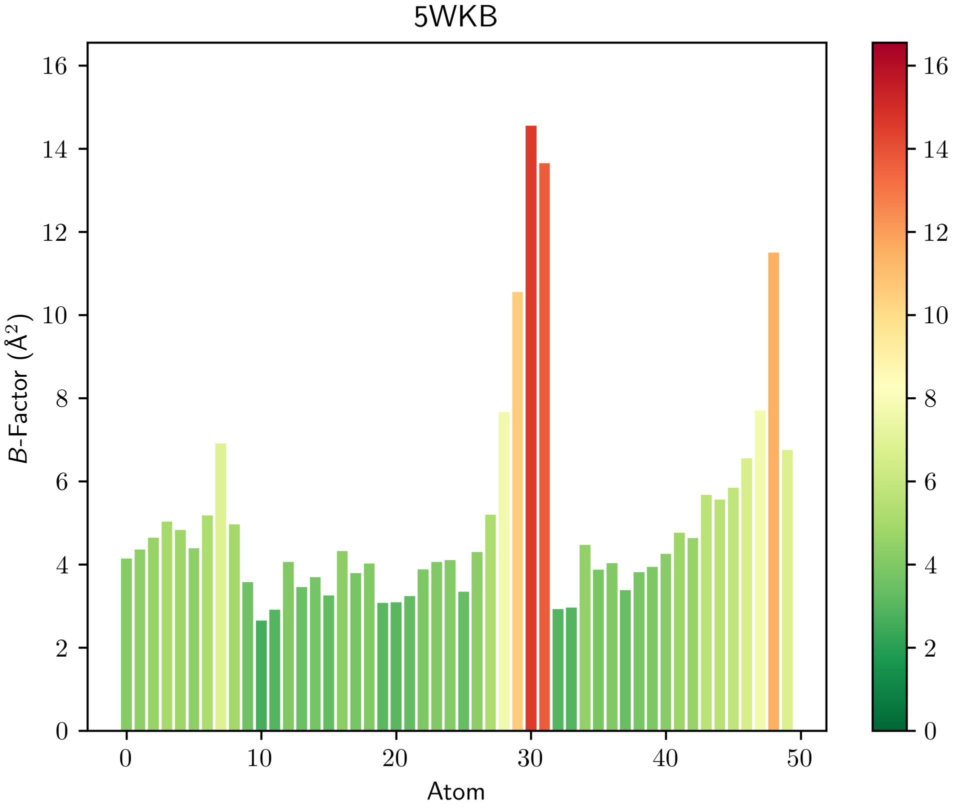

Figure 2.9: **Individual atomic *B*-factors refined in the deposited 3D ED structure of ^{312}NFGEFS^{317}** (PDB: 5WKB), featuring significant but remarkably less severe outliers than either 4ZNN or 4RIL for the O atoms on the carboxylate side chain of E315. This case presents a more ambiguous situation, since the *B*-factor on E315's carboxylate C atom is also comparably inflated—suggesting that radiolytic decarboxylation (i.e. ejection of the entire moiety as CO_2) is an equally plausible explanation as formal negative charge. Some combination of the two effects is also likely. Another intriguing aspect of this structure involves the corresponding *B*-factors for S317, the C-terminal serine residue, which appear less inflated than their counterparts on E315 (although they're still somewhat higher than the remainder of the molecule). This discrepancy could point to intrinsic differences between carboxylates in disparate chemical environments—both in terms of (a) susceptibility to radiolytic decarboxylation and (b) ability to partially neutralize negative charge via noncovalent interactions with proximal H-bond donors. In other words, not all carboxylates will (a) display the effects of charge equally or (b) accumulate radiolytic damage at precisely the same rate.

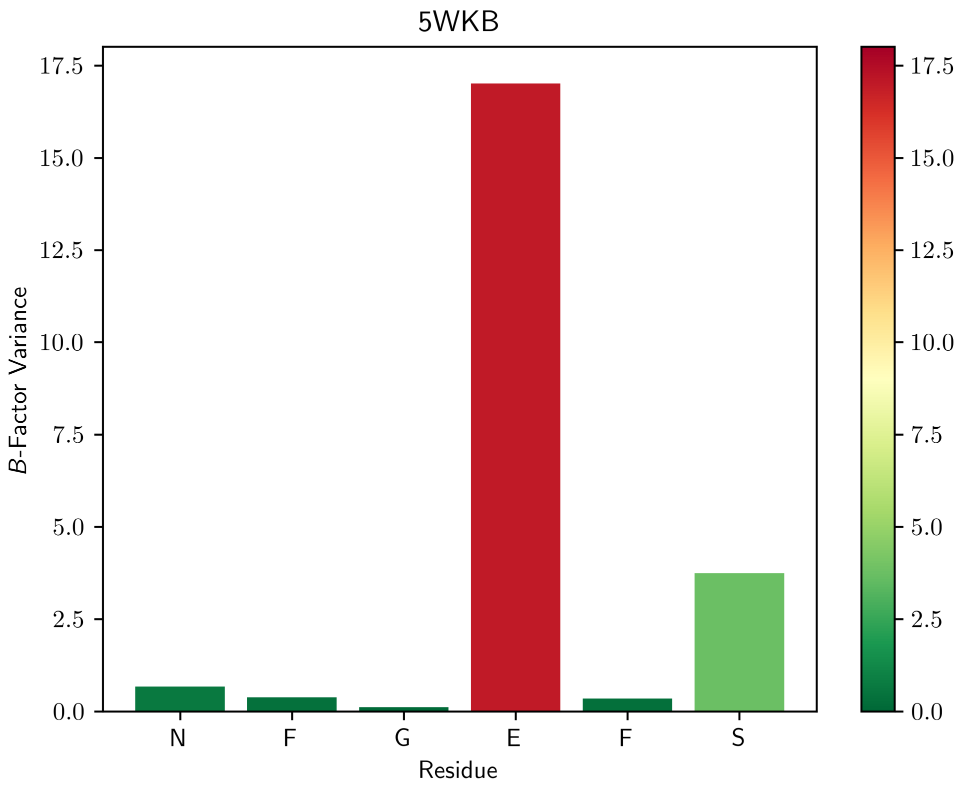

Figure 2.10: ***B*-factor variance calculated per residue for the deposited 3D ED structure of ^{312}NFGEFS^{317}** (PDB: 5WKB). A clear outlier is observed at mid-chain glutamate residue E315, whose *B*-factor variance is 5× greater than the corresponding value for the next-highest amino acid, S317. Since S317 is the C-terminal residue, its position as the second-highest offender is also logical.

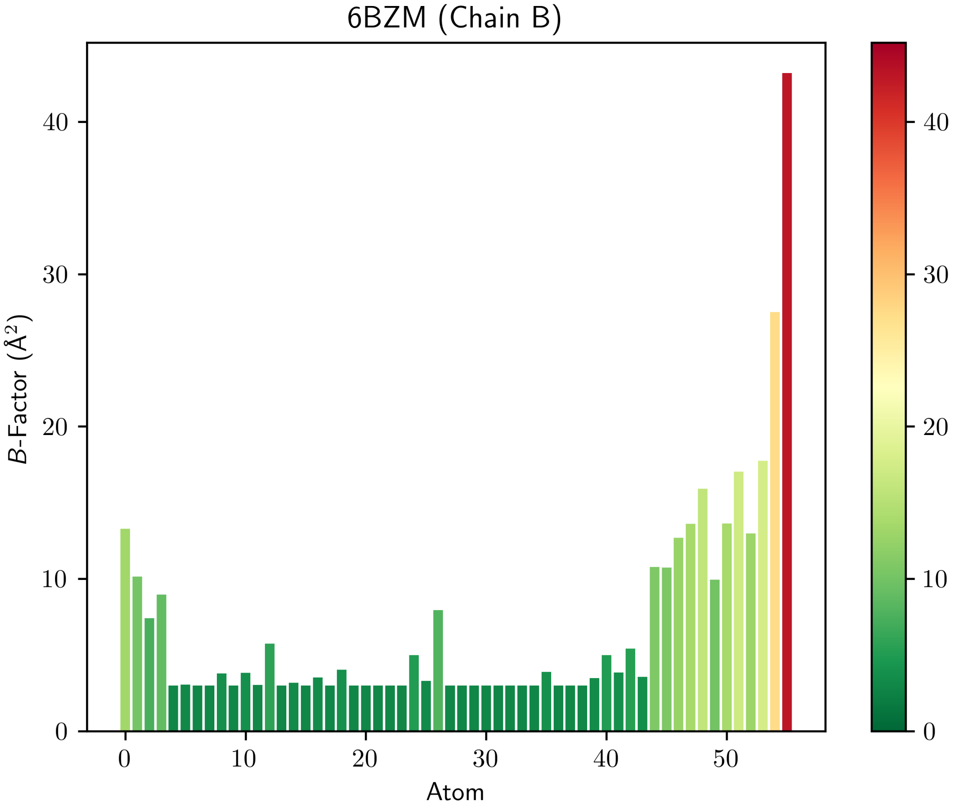

Figure 2.11: **Individual atomic *B*-factors refined in the deposited 3D ED structure of ^{116}GFGNFGTS^{123}** (PDB: 6BZM), a segment from the low-complexity domain of Nup98. Although a clear outlier is observed for one O atom at the carboxylate terminus of the final serine residue, S123, it's unclear why its counterpart is somewhat lower.

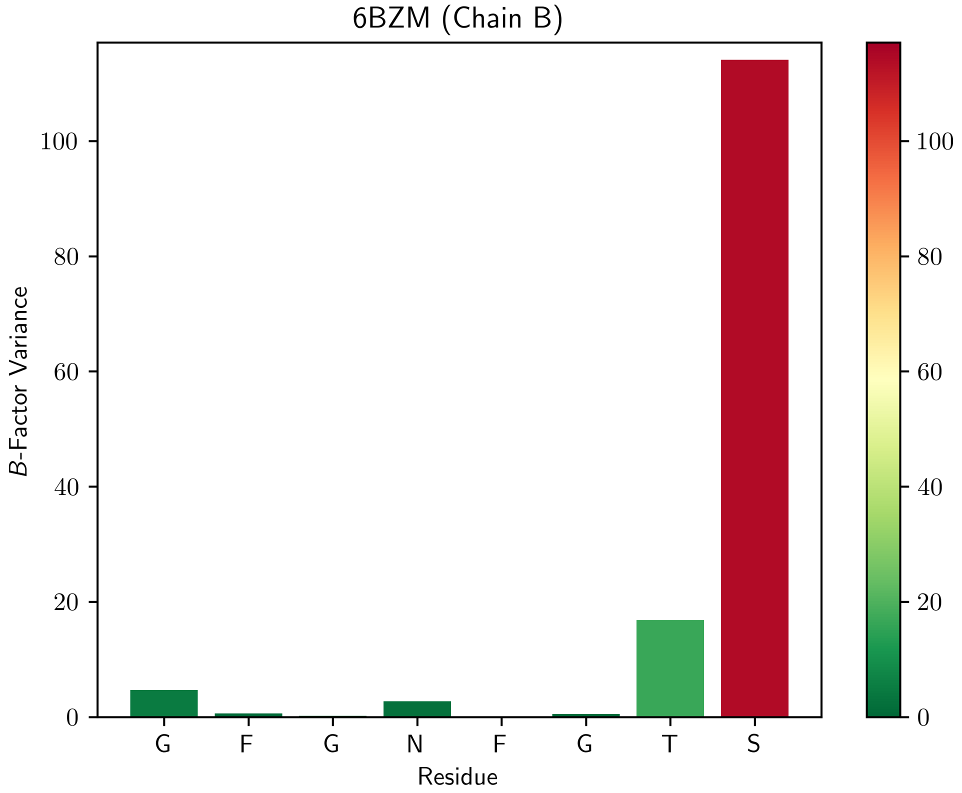

Figure 2.12: ***B*-factor variance calculated per residue for the deposited 3D ED structure of ^{116}GFGNFGTS^{123}** (PDB: 6BZM), a segment from the low-complexity domain of Nup98. A clear outlier is observed at the C-terminal serine residue, S123, whose *B*-factor variance is 5× greater than the corresponding value for the next-highest amino acid, T122.

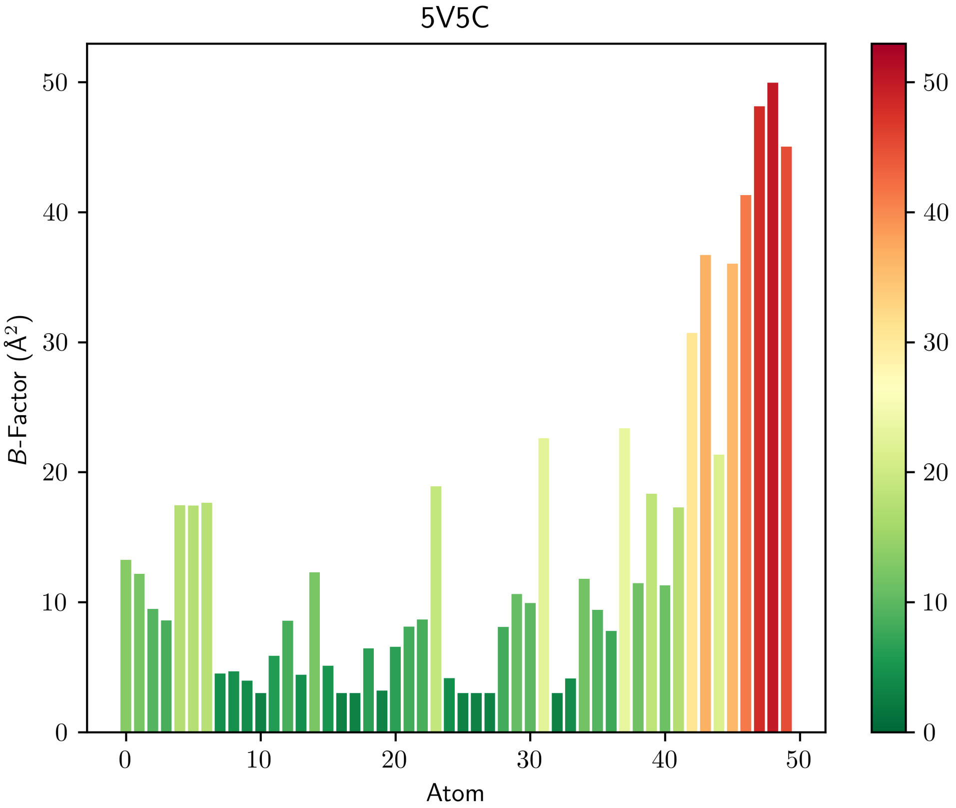

Figure 2.13: **Individual atomic *B*-factors refined in the deposited 3D ED structure of VQIINK** (PDB: 5V5C), a repeat segment from the amyloid spine of the microtubule-associated protein tau. Like 5WKB, this is another case where radiolytic decarboxylation is likely also a key confounding variable, since the corresponding B-factors appear consistently inflated throughout the entire C-terminal lysine residue (including all three atoms of the carboxylate moiety, indicating that ejection of CO_2 is plausible).

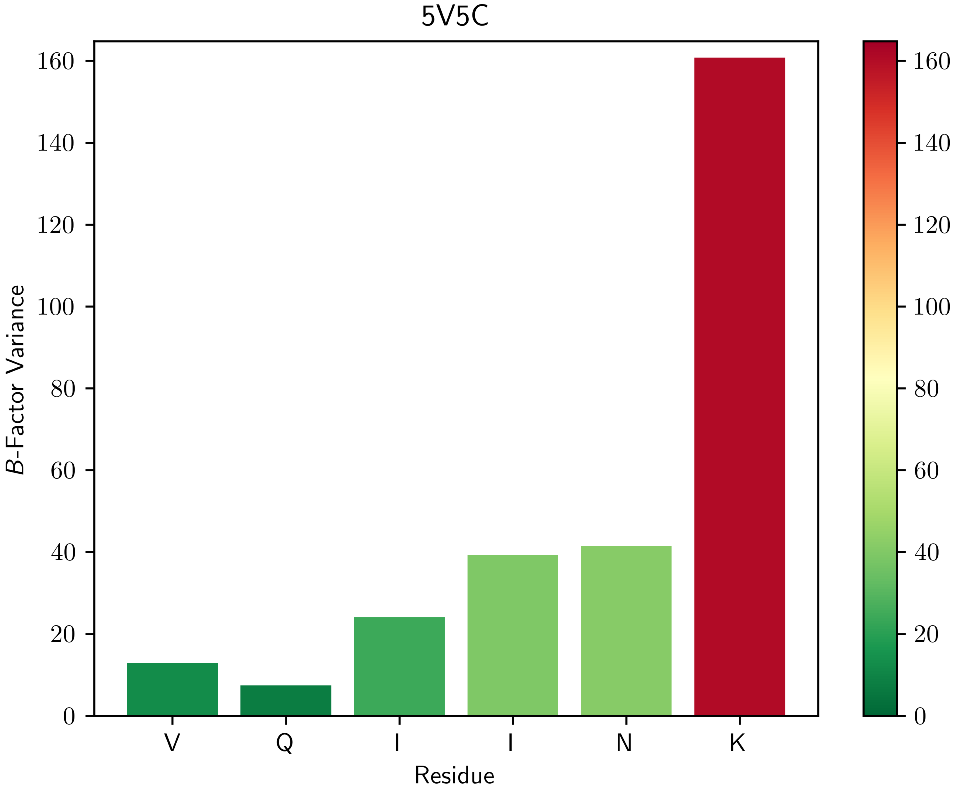

Figure 2.14: ***B*-factor variance calculated per residue for the deposited 3D ED structure of VQIINK** (PDB: 5V5C), a repeat segment from the amyloid spine of the microtubule-associated protein tau. A clear outlier is observed at the C-terminal lysine residue, K6, whose *B*-factor variance is 4× greater than the corresponding value for the next-highest amino acid, N5.

2.7 Errata in the *International Tables for Crystallography*

During the course of this work, we discovered several misprints in the electron scattering amplitudes tabulated by Colliex *et al.* in the *International Tables for Crystallography* (Table 2.2). Neutral Co, Ni, Te, La, At, and Cf contain clear outliers at 0.3 $Å^{-1}$, 1.8 $Å^{-1}$, 0.24 $Å^{-1}$, 1.3 $Å^{-1}$, 0.22 $Å^{-1}$, and 1.7 $Å^{-1}$, respectively. Neutral Ce, Sm, Gd, and Ho feature more subtle deviations from monotonicity at 0.26 $Å^{-1}$, 0.4 $Å^{-1}$, 1.5 $Å^{-1}$, and 0.7 $Å^{-1}$, respectively. These spurious values were omitted from the relevant parameterizations. Finally, neutral H and He contain potentially suspect duplicate values at 0.04 $Å^{-1}$ and 0.05 $Å^{-1}$ (H) and 0 $Å^{-1}$ and 0.01 $Å^{-1}$ (He). We have compiled a list of these errata at `<srv.mbi.ucla.edu/faes/?corrections>` and flagged each affected scattering factor accordingly in FAES.

2.8 Tables of Gaussian Coefficients from FAES Parameterizations

$\frac{\sin\theta}{\lambda}$ (Å^{-1})	H	Co	Ni	Te	Sm	Gd	Ho	At	Cf
0	0.529	6.854	6.569	11.003	15.897	15.266	14.355	13.473	16.841
0.01		6.836	6.552						
0.02		6.779	6.501						
0.03		6.687	6.418						
0.04	0.51	6.562	6.306	10.65	14.7	14.3	13.57	13.09	16.28
0.05	**0.51**	6.41	6.169	10.47	14.12	13.81	13.14	12.89	15.85
0.06	0.5	6.234	6.01	10.25	13.48	13.27	12.66	12.65	15.37
0.07	0.49	6.04	5.834	10.01	12.81	12.7	12.15	12.38	14.84
0.08	0.48	5.834	5.646	9.74	12.14	12.11	11.61	12.08	14.3
0.09	0.47	5.619	5.449	9.46	11.49	11.52	11.08	11.76	13.75
0.1	0.45	5.401	5.249	9.16	10.86	10.95	10.55	11.43	13.2
0.11	0.44	5.182	5.048	8.85	10.27	10.39	10.05	11.08	12.66
0.12	0.425	4.967	4.848	8.538	9.722	9.871	9.562	10.729	12.135
0.13	0.411	4.758	4.654	8.224	9.218	9.382	9.108	10.375	11.637
0.14	0.396	4.555	4.465	7.914	8.758	8.926	8.681	10.021	11.164
0.15	0.382	4.361	4.283	7.608	8.336	8.505	8.284	9.671	10.716
0.16	0.366	4.177	4.11	7.309	7.953	8.114	7.917	9.328	10.294
0.17	0.353	4.002	3.944	7.018	7.602	7.754	7.577	8.991	9.898
0.18	0.338	3.836	3.788	6.738	7.28	7.422	7.262	8.666	9.527
0.19	0.324	3.681	3.64	6.467	6.983	7.114	6.971	8.35	9.178
0.2	0.311	3.534	3.5	6.209	6.71	6.828	6.7	8.046	8.85
0.22	0.285	3.267	3.245	5.727	6.218	6.316	6.213	**3.474**	8.249
0.24	0.261	3.032	3.018	**3.291**	5.787	5.868	5.788	6.952	7.713
0.25	0.249	2.924	2.914	5.09	5.589	5.664	5.595	6.709	7.466
0.26	0.238	2.823	2.816	4.899	5.402	5.472	5.412	6.477	7.231
0.28	0.218	2.637	2.636	4.548	5.055	5.117	5.075	6.047	6.793
0.3	0.199	**1.471**	2.474	4.234	4.739	4.796	4.771	5.658	6.393
0.32	0.182	2.321	2.328	3.952	4.45	4.504	4.494	5.305	6.026
0.34	0.167	2.184	2.195	3.7	4.185	4.238	4.24	4.987	5.687
0.35	0.16	2.121	2.133	3.583	4.06	4.113	4.121	4.838	5.528
0.36	0.153	2.06	2.073	3.472	3.94	3.993	4.007	4.697	5.374
0.38	0.141	1.946	1.962	3.265	3.715	3.767	3.79	4.433	5.084
0.4	0.13	1.841	1.858	3.078	**3.306**	3.559	3.591	4.192	4.815
0.42	0.12	1.743	1.763	2.907	3.314	3.367	3.405	3.972	4.565
0.44	0.111	1.653	1.674	2.75	3.137	3.189	3.233	3.769	4.333
0.45	0.107	1.61	1.631	2.677	3.053	3.105	3.151	3.673	4.222
0.46	0.103	1.569	1.591	2.606	2.973	3.025	3.073	3.582	4.116
0.48	0.096	1.49	1.513	2.473	2.821	2.872	2.924	3.408	3.914
0.5	0.089	1.416	1.44	2.35	2.68	2.73	2.785	3.248	3.726
0.55	0.075	1.251	1.277	2.077	2.371	2.419	2.477	2.893	3.309
0.6	0.064	1.11	1.136	1.847	2.113	2.138	2.216	2.593	2.957
0.65	0.055	0.988	1.015	1.649	1.895	1.937	1.995	2.337	2.657
0.7	0.048	0.883	0.909	1.479	1.709	1.749	**1.085**	2.116	2.4
0.8	0.037	0.712	0.737	1.205	1.411	1.446	1.497	1.758	1.987
0.9	0.029	0.583	0.605	0.997	1.181	1.213	1.26	1.485	1.673
1	0.024	0.485	0.504	0.838	1	1.03	1.073	1.272	1.427
1.1	0.02	0.409	0.425	0.715	0.856	0.883	0.922	1.102	1.233
1.2	0.017	0.35	0.364	0.619	0.739	0.763	0.799	0.965	1.076
1.3	0.014	0.303	0.315	0.542	0.644	0.666	0.698	0.853	0.948
1.4	0.012	0.265	0.275	0.48	0.566	**0.383**	0.614	0.758	0.843
1.5	0.011	0.235	0.243	0.428	0.502	0.519	0.544	0.678	0.754
1.6		0.209	0.217	0.385	0.449	0.463	0.485	0.609	0.679
1.7		0.188	0.194	0.348	0.404	0.416	0.436	0.55	**0.165**
1.8		0.17	**1.176**	0.316	0.366	0.377	0.394	0.498	0.56
1.9		0.154	0.16	0.288	0.333	0.343	0.358	0.453	0.511
2		0.141	0.146	0.264	0.305	0.313	0.327	0.413	0.469

Table 2.2: **Errata in the electron scattering amplitudes tabulated in the *International Tables for Crystallography***, with suspicious values highlighted in boldface.

Atom	Z	a_1	a_2	a_3	a_4	b_1	b_2	b_3	b_4	RMSE
H	1	0.129	0.036	0.127	0.236	37.737	0.553	3.772	13.518	0.001
H^{1-}	1	-37.647	-4.391	0.351	-13.954	1537.902	177.243	5.666	553.026	0.013
He	2	0.078	0.04	0.125	0.174	19.191	0.309	2.053	6.989	0
Li	3	1.39	0.119	0.394	1.379	117.035	0.588	6.083	36.687	0.003
Li^{1+}	3	23.445	0.3	1.344	6.07	697.333	1.661	26.504	160.375	0.017
Be	4	1.065	0.118	0.439	1.428	66.144	0.461	4.485	21.589	0.002
Be^{2+}	4	47.441	0.486	2.899	12.592	719.569	2.261	30.72	171.613	0.028
B	5	0.765	0.13	0.521	1.377	51.783	0.419	3.927	16.688	0.002
C	6	0.6	0.136	0.547	1.225	40.938	0.374	3.278	13.013	0.001
N	7	0.482	0.135	0.519	1.075	31.526	0.324	2.607	10.017	0.001
O	8	0.392	0.144	0.511	0.937	25.675	0.306	2.272	8.27	0.001
O^{1-}	8	-23.228	0.383	1.281	-5.699	684.687	0.82	6.889	157.036	0.014
F	9	0.309	0.152	0.519	0.822	22.005	0.289	2.062	7.261	0.001
F^{1-}	9	-65.246	-5.474	1.383	-16.441	1913.852	150.335	3.163	573.682	0.056
Ne	10	0.256	0.158	0.504	0.733	19.19	0.272	1.841	6.313	0
Na	11	1.972	0.331	0.985	1.483	118.259	0.493	4.081	31.374	0.006
Na^{1+}	11	21.988	0.647	1.314	4.93	591.309	0.926	10.171	111.463	0.03
Mg	12	1.958	0.325	0.922	1.998	80.547	0.446	3.572	24.183	0.005
Mg^{2+}	12	45.955	0.898	2.424	11.391	661.678	1.253	20.279	143.191	0.044
Al	13	1.913	0.359	0.974	2.638	80.5	0.454	3.78	23.357	0.006
Al^{3+}	13	70.097	1.044	3.946	18.003	691.147	1.466	25.606	157.56	0.052
Si	14	1.762	0.362	0.974	2.725	64.441	0.428	3.553	19.406	0.005
Si^{4+}	14	93.814	1.149	5.414	24.39	699.961	1.556	27.251	162.042	0.064
P	15	1.567	0.354	0.941	2.622	49.607	0.394	3.189	15.68	0.004
S	16	1.39	0.348	0.915	2.506	40.169	0.365	2.89	13.043	0.003
Cl	17	1.232	0.341	0.893	2.391	33.612	0.339	2.625	11.095	0.002
Cl^{1-}	17	-120.636	3.287	0.666	-21.071	2803.538	9.276	0.647	429.353	0.118
Ar	18	1.075	0.341	0.9	2.263	28.97	0.323	2.487	9.764	0.002
K	19	3.532	0.566	2.414	2.457	150.836	0.507	5.768	31.814	0.015
K^{1+}	19	21.404	0.813	3.119	4.603	551.389	0.729	8.788	92.632	0.04
Ca	20	3.88	0.547	2.281	3.194	109.54	0.47	5.048	29.73	0.012
Ca^{2+}	20	43.972	1.016	3.338	9.863	590.914	0.879	10.27	111.139	0.06
Sc	21	3.431	0.539	2.211	3.117	98.119	0.444	4.574	26.467	0.011
Sc^{3+}	21	67.922	1.556	3.959	16.329	637.938	1.408	15.853	132.285	0.072
Ti	22	3.078	0.539	2.158	2.992	90.552	0.428	4.223	24.193	0.01
Ti^{2+}	22	44.391	1.378	3.305	10.205	605.298	1.172	11.843	117.047	0.057
Ti^{3+}	22	68.102	1.636	3.967	16.436	640.957	1.411	16.042	133.181	0.073
Ti^{4+}	22	92.443	1.843	5.142	23.098	669.282	1.626	20.734	146.166	0.085
V	23	2.792	0.542	2.109	2.854	84.561	0.414	3.932	22.411	0.009
V^{2+}	23	43.753	1.173	3.249	9.725	583.132	0.885	9.79	107.432	0.064
V^{3+}	23	68.061	1.7	3.933	16.367	639.296	1.398	16.111	132.795	0.073
V^{5+}	23	116.315	2.025	6.558	29.693	684.515	1.734	24.066	154.335	0.095
Cr	24	1.989	0.548	2.072	2.352	87.861	0.403	3.698	20.054	0.009
Cr^{2+}	24	44.348	1.493	3.173	10.163	603.76	1.16	11.729	116.79	0.058
Cr^{3+}	24	68.055	1.747	3.882	16.334	638.559	1.374	16.077	132.403	0.073
Mn	25	2.354	0.555	2.013	2.579	75.291	0.394	3.485	19.714	0.008
Mn^{2+}	25	43.699	1.257	3.106	9.674	581.489	0.871	9.523	106.837	0.065
Mn^{3+}	25	68.103	1.793	3.844	16.397	640.24	1.352	16.202	132.923	0.074
Mn^{4+}	25	92.167	1.968	5.049	22.918	665.233	1.513	20.603	144.881	0.085
Fe	26	2.177	0.563	1.966	2.453	71.621	0.387	3.307	18.67	0.007
Fe^{2+}	26	43.687	1.292	3.029	9.662	581.141	0.861	9.421	106.746	0.065
Fe^{3+}	26	67.162	1.603	3.65	15.701	618.91	1.091	13.661	123.602	0.082
Co	27	2.032	0.571	1.916	2.33	68.195	0.378	3.142	17.663	0.007
Co^{2+}	27	43.661	1.323	2.952	9.644	580.545	0.848	9.327	106.584	0.065
Co^{3+}	27	67.921	1.856	3.751	16.374	639.011	1.296	16.389	132.955	0.074
Ni	28	1.89	0.582	1.87	2.221	65.305	0.373	3.009	16.917	0.007
Ni^{2+}	28	43.654	1.348	2.877	9.634	580.253	0.833	9.246	106.515	0.065
Ni^{3+}	28	68.27	1.882	3.721	16.474	642.879	1.27	16.593	133.781	0.074
Cu	29	1.355	0.593	1.836	1.81	70.864	0.368	2.899	15.669	0.006
Cu^{1+}	29	21.11	1.128	2.534	4.419	532.756	0.673	6.703	84.838	0.045
Cu^{2+}	29	44.603	1.677	2.795	10.261	609.584	1.079	11.833	118.487	0.058
Zn	30	1.665	0.6	1.776	2.018	60.12	0.36	2.769	15.492	0.006
Zn^{2+}	30	43.655	1.395	2.733	9.631	580.403	0.805	9.176	106.588	0.065

Ga	31	1.931	0.671	1.849	2.649	74.503	0.388	3.024	19.106	0.008
Ga^{3+}	31	68.062	1.916	3.603	16.389	640.291	1.178	16.907	133.581	0.072
Ge	32	2.039	0.668	1.77	2.894	62.774	0.375	2.852	17.377	0.007
Ge^{4+}	32	92.523	2.024	4.808	23.271	670.285	1.228	20.484	145.151	0.084
As	33	2.015	0.651	1.665	2.985	50.642	0.355	2.611	15.035	0.006
Se	34	1.96	0.635	1.57	3.036	42.435	0.338	2.401	13.14	0.005
Br	35	1.861	0.624	1.495	3.075	36.786	0.323	2.244	11.727	0.004
Br^{1-}	35	-121.434	4.503	1.531	-22.068	2886.035	11.306	0.772	469.988	0.109
Kr	36	1.748	0.622	1.438	3.087	32.461	0.313	2.137	10.616	0.003
Rb	37	4.353	1.017	2.871	3.514	154.533	0.485	5.122	25.929	0.022
Rb^{1+}	37	20.889	1.376	4.168	4.551	517.741	0.658	8.758	75.721	0.052
Sr	38	5.135	1.01	2.938	4.007	116.292	0.47	4.963	26.868	0.019
Sr^{2+}	38	43.433	1.508	4.499	9.526	572.429	0.708	9.667	102.522	0.07
Y	39	4.642	0.976	2.871	4.159	99.298	0.445	4.567	24.096	0.017
Y^{3+}	39	66.164	1.653	4.839	14.877	593.682	0.766	10.642	111.893	0.089
Zr	40	4.151	0.957	2.852	4.178	89.731	0.426	4.312	22.129	0.015
Zr^{4+}	40	88.832	1.831	5.326	20.406	606.834	0.84	12.06	118.203	0.108
Nb	41	2.985	0.937	2.822	3.909	85.635	0.409	4.069	19.497	0.013
Nb^{3+}	41	65.614	1.697	5.089	14.628	583.555	0.754	10.283	107.761	0.093
Nb^{5+}	41	112.142	2.063	6.066	26.373	622.554	0.946	14.178	125.342	0.126
Mo	42	2.625	0.934	2.866	3.825	82.593	0.4	3.959	18.676	0.012
Mo^{3+}	42	65.604	1.727	5.141	14.542	581.818	0.753	10.108	106.792	0.096
Mo^{5+}	42	112.011	2.063	6.104	26.21	619.479	0.923	13.553	123.537	0.126
Mo^{6+}	42	136.072	2.31	7.109	32.755	639.79	1.063	16.752	133.099	0.141
Tc	43	3.114	0.929	2.894	3.897	74.66	0.389	3.828	18.356	0.012
Ru	44	2.2	0.916	2.873	3.548	74.517	0.377	3.643	16.48	0.011
Ru^{3+}	44	65.252	1.747	5.147	14.384	576.705	0.732	9.45	104.994	0.097
Ru^{4+}	44	88.372	1.935	5.52	20	597.49	0.819	11	113.874	0.115
Rh	45	1.932	0.921	2.958	3.413	75.303	0.371	3.603	16.371	0.014
Rh^{3+}	45	65.214	1.765	5.112	14.324	575.193	0.725	9.174	104.318	0.097
Rh^{4+}	45	88.302	1.96	5.487	19.894	595.487	0.813	10.722	112.857	0.116
Pd	46	1.413	0.784	2.175	3.199	37.395	0.31	2.588	9.848	0.005
Pd^{2+}	46	42.759	1.623	4.835	9.139	549.867	0.651	7.858	92.114	0.079
Pd^{4+}	46	87.908	1.986	5.438	19.778	592.089	0.808	10.466	111.946	0.118
Ag	47	1.713	0.907	2.939	3.105	70.45	0.353	3.325	14.732	0.009
Ag^{1+}	47	20.403	1.446	4.535	4.481	490.007	0.567	6.521	64.417	0.058
Ag^{2+}	47	42.702	1.637	4.77	9.085	548.663	0.644	7.611	92.04	0.079
Cd	48	2.19	0.906	2.945	3.183	62.472	0.347	3.225	14.804	0.009
Cd^{2+}	48	42.748	1.653	4.693	9.051	548.602	0.639	7.382	92.045	0.079
In	49	2.625	0.967	3.204	3.626	76.06	0.365	3.461	18.415	0.012
In^{3+}	49	65.092	1.858	4.847	14.169	571.695	0.708	8.314	102.705	0.101
Sn	50	2.882	0.953	3.115	3.901	66.558	0.354	3.269	17.617	0.011
Sn^{2+}	50	42.25	1.792	4.873	9.088	533.28	0.669	7.801	83.815	0.088
Sn^{4+}	50	87.659	2.098	5.083	19.507	586.366	0.791	9.608	109.281	0.121
Sb	51	2.975	0.931	2.987	4.073	56.336	0.34	3.047	16.205	0.009
Sb^{3+}	51	65.197	2.05	5.256	14.25	570.932	0.756	9.239	101.23	0.107
Sb^{5+}	51	110.972	2.465	5.759	25.505	606.758	0.928	12.353	118.599	0.139
Te	52	3.074	0.905	2.841	4.167	48.129	0.325	2.817	14.617	0.008
I	53	2.929	0.892	2.745	4.334	43.268	0.315	2.663	13.708	0.007
I^{1-}	53	-122.763	6.91	2.734	-23.906	3032.171	14.365	1.01	542.917	0.133
Xe	54	2.872	0.875	2.63	4.412	38.584	0.305	2.498	12.603	0.006
Cs	55	5.641	1.295	3.87	5.663	168.782	0.445	4.325	24.179	0.033
Cs^{1+}	55	19.82	1.803	5.375	5.463	456.075	0.616	7.313	47.623	0.073
Ba	56	7.125	1.315	3.933	5.861	128.365	0.446	4.313	24.199	0.031
Ba^{2+}	56	42.47	2.138	6.25	9.192	537.974	0.722	9.264	85.156	0.094
La	57	6.822	1.097	3.62	6.204	106.424	0.378	3.436	20.312	0.043
La^{3+}	57	65.22	2.3	6.623	14.35	573.363	0.768	10.063	102.573	0.109
Ce	58	5.85	1.376	4.124	5.991	113.777	0.45	4.424	25.207	0.04
Ce^{3+}	58	65.136	2.309	6.54	14.301	572.085	0.757	9.844	102.317	0.108
Ce^{4+}	58	87.734	2.444	6.971	19.683	589.003	0.807	10.758	110.645	0.125
Pr	59	6.409	1.334	3.882	5.306	117.398	0.43	4.048	22.279	0.029
Pr^{3+}	59	65.205	2.319	6.447	14.296	572.491	0.748	9.645	102.274	0.108
Pr^{4+}	59	87.943	2.459	6.867	19.69	589.756	0.798	10.577	110.447	0.125

Nd	60	6.228	1.344	3.854	5.129	114.834	0.426	3.969	21.81	0.028
Nd^{3+}	60	65.148	2.328	6.351	14.251	571.628	0.738	9.461	102.115	0.108
Pm	61	6.025	1.36	3.843	4.963	112.856	0.424	3.927	21.6	0.027
Pm^{3+}	61	65.024	2.334	6.247	14.201	570.299	0.728	9.275	101.794	0.107
Sm	62	5.858	1.366	3.801	4.819	110.724	0.42	3.843	21.183	0.027
Sm^{3+}	62	64.996	2.341	6.146	14.159	569.263	0.718	9.108	101.522	0.107
Eu	63	5.604	1.392	3.82	4.721	110.928	0.421	3.845	21.594	0.025
Eu^{2+}	63	42.534	2.207	5.759	9.065	541.827	0.665	8.125	87.869	0.089
Eu^{3+}	63	65.031	2.349	6.044	14.141	569.491	0.71	8.958	101.394	0.107
Gd	64	5.217	1.405	3.787	4.816	96.512	0.415	3.816	20.72	0.023
Gd^{3+}	64	64.962	2.357	5.944	14.12	568.385	0.701	8.818	101.186	0.107
Tb	65	5.284	1.413	3.766	4.452	107.388	0.415	3.74	21.13	0.026
Tb^{3+}	65	65.089	2.365	5.847	14.151	568.953	0.693	8.693	101.057	0.107
Dy	66	5.182	1.421	3.709	4.285	103.807	0.411	3.672	20.495	0.024
Dy^{3+}	66	64.737	2.369	5.748	14.051	566.075	0.684	8.556	100.659	0.106
Ho	67	5.012	1.379	3.544	4.412	86.953	0.393	3.414	18.523	0.019
Ho^{3+}	67	64.803	2.378	5.658	14.03	566.189	0.676	8.458	100.646	0.106
Er	68	4.894	1.443	3.639	4.061	100.711	0.405	3.581	20.167	0.023
Er^{3+}	68	64.948	2.387	5.57	14.068	567.98	0.67	8.37	100.894	0.106
Tm	69	4.774	1.45	3.595	3.949	98.69	0.401	3.523	19.872	0.022
Tm^{3+}	69	64.794	2.392	5.48	14.029	566.424	0.662	8.269	100.59	0.106
Yb	70	4.624	1.463	3.569	3.861	98.054	0.399	3.498	19.9	0.021
Yb^{2+}	70	42.334	2.246	5.134	8.931	539.714	0.611	7.305	88.702	0.086
Yb^{3+}	70	64.857	2.4	5.395	14.04	566.903	0.655	8.193	100.686	0.106
Lu	71	4.45	1.444	3.478	4.079	84.664	0.389	3.351	18.906	0.019
Lu^{3+}	71	64.853	2.403	5.311	14.019	566.629	0.647	8.1	100.454	0.106
Hf	72	4.104	1.427	3.396	4.224	76.01	0.379	3.221	17.769	0.017
Hf^{4+}	72	87.29	2.58	5.609	19.241	580.239	0.69	9.156	106.756	0.126
Ta	73	3.748	1.418	3.344	4.32	70.207	0.372	3.131	16.85	0.016
Ta^{5+}	73	109.901	2.785	6.089	24.722	592.446	0.741	10.592	112.367	0.146
W	74	3.452	1.408	3.295	4.366	65.57	0.365	3.043	15.906	0.015
W^{6+}	74	133.51	3.012	6.817	30.705	608.669	0.801	12.476	118.938	0.165
Re	75	3.248	1.391	3.231	4.373	60.608	0.356	2.934	14.832	0.013
Os	76	3.024	1.381	3.19	4.37	56.982	0.348	2.855	14.011	0.012
Os^{4+}	76	87.218	2.643	6.105	19.188	578.131	0.676	9.24	105.412	0.131
Ir	77	2.811	1.376	3.166	4.348	54.223	0.343	2.797	13.352	0.011
Ir^{3+}	77	64.538	2.5	5.947	13.891	559.455	0.629	8.252	96.897	0.112
Ir^{4+}	77	87.02	2.643	6.175	19.083	575.789	0.668	9.112	104.72	0.131
Pt	78	2.174	1.348	3.066	4.212	50.387	0.332	2.657	12.009	0.01
Pt^{2+}	78	42.137	2.356	5.806	8.903	529.169	0.584	7.376	82.518	0.093
Pt^{4+}	78	87.2	2.763	6.244	19.119	578.334	0.694	9.592	106.04	0.155
Au	79	1.994	1.345	3.064	4.163	48.63	0.327	2.618	11.55	0.009
Au^{1+}	79	20.087	2.132	5.5	4.802	467.165	0.521	6.192	53.162	0.07
Au^{3+}	79	64.738	2.501	6.026	13.886	560.803	0.616	7.991	97.01	0.112
Hg	80	2.27	1.357	3.134	4.195	47.992	0.326	2.641	11.706	0.009
Hg^{1+}	80	19.858	2.134	5.538	5.019	459.34	0.516	6.12	50.944	0.071
Hg^{2+}	80	42.074	2.35	5.845	8.807	529.002	0.571	7.098	83.251	0.092
Tl	81	2.61	1.47	3.613	4.392	64.497	0.349	3.065	14.762	0.013
Tl^{1+}	81	19.862	2.141	5.593	5.176	456.484	0.512	6.077	48.994	0.072
Tl^{3+}	81	64.437	2.494	6.029	13.765	557.836	0.602	7.657	96.348	0.112
Pb	82	2.909	1.469	3.636	4.573	60.255	0.345	3.03	14.85	0.013
Pb^{2+}	82	41.858	2.407	6.081	8.854	520.104	0.573	7.23	78.061	0.097
Pb^{4+}	82	86.775	2.649	6.254	18.872	571.412	0.635	8.317	102.692	0.133
Bi	83	3.192	1.465	3.644	4.784	56.775	0.34	2.982	14.85	0.012
Bi^{3+}	83	64.12	2.58	6.359	13.689	551.16	0.611	7.953	93.36	0.117
Bi^{5+}	83	109.291	2.843	6.59	24.17	582.547	0.679	9.257	107.544	0.155
Po	84	3.462	1.435	3.539	4.91	50.424	0.33	2.83	13.958	0.011
At	85	3.529	1.413	3.459	5.057	45.684	0.321	2.71	13.301	0.01
Rn	86	3.43	1.4	3.411	5.244	42.34	0.315	2.628	12.899	0.009
Fr	87	5.517	1.776	4.694	6.663	155.254	0.398	4.016	23.122	0.035
Ra	88	7.244	1.762	4.678	6.81	120.872	0.392	3.911	22.345	0.033
Ra^{2+}	88	41.351	2.641	7.209	9.13	504.452	0.596	8.009	69.61	0.111

Ac	89	7.04	1.735	4.601	7.051	102.298	0.382	3.749	21.186	0.03
Ac^{3+}	89	64.108	2.84	7.716	13.747	547.157	0.639	8.895	90.147	0.129
Th	90	6.594	1.706	4.509	7.251	89.501	0.372	3.585	19.932	0.027
Pa	91	6.346	1.73	4.635	6.803	95.871	0.374	3.634	19.828	0.028
U	92	5.991	1.741	4.7	6.66	95.173	0.373	3.628	19.64	0.027
U^{3+}	92	64.069	2.857	7.777	13.673	546.691	0.625	8.464	90.329	0.128
U^{4+}	92	86.545	2.987	8.061	18.801	567.154	0.656	9.108	100.406	0.145
U^{6+}	92	132.108	3.269	8.872	29.695	592.782	0.726	10.702	111.923	0.181
Np	93	5.86	1.728	4.672	6.45	91.511	0.367	3.528	18.791	0.026
Pu	94	5.615	1.75	4.789	5.987	100.875	0.368	3.565	18.854	0.027
Am	95	5.418	1.75	4.804	5.816	98.632	0.365	3.513	18.476	0.027
Cm	96	5.295	1.729	4.72	5.923	86.326	0.358	3.382	17.716	0.024
Bk	97	5.161	1.729	4.72	5.75	84.294	0.355	3.327	17.349	0.024
Cf	98	5.471	1.628	4.373	5.464	72.911	0.329	2.957	14.58	0.029

Table 2.3: **Fitting coefficients for the 4 Gaussian $[f(s) = \sum_{j=1}^{4} a_j \exp(-b_j s^2)]$ parameterizations from FAES, alongside corresponding RMSE values.**

Atom	Z	a_1	a_2	a_3	a_4	a_5	b_1	b_2	b_3	b_4	b_5	RMSE
H	1	0.041	0.266	0.154	-0.009	0.075	0.619	17.116	4.462	214.422	57.283	0.001
H^{1-}	1	0.351	-4.391	-199.271	-37.48	-13.95	5.666	177.241	4975.51	1536.194	552.975	0.013
He	2	0.029	0.155	0.076	0.017	0.141	0.229	4.185	1.328	31.441	12.292	0
Li	3	0.077	0.582	0.232	0.88	1.516	0.394	16.16	3.044	142.201	55.581	0.001
Li^{1+}	3	2.143	0.534	25.106	7.518	0.153	57.161	8.962	843.171	238.033	0.744	0.006
Be	4	0.079	0.7	0.226	0.654	1.392	0.318	10.489	2.296	80.004	31.845	0.001
Be^{2+}	4	4.576	1.096	50.718	15.53	0.219	63.429	11.406	868.725	252.676	0.838	0.01
B	5	0.091	0.783	0.257	0.449	1.213	0.3	8.465	2.127	63.745	24.397	0
C	6	0.094	0.796	0.275	0.318	1.026	0.26	6.842	1.832	52.535	19.684	0
N	7	0.093	0.706	0.282	0.273	0.857	0.223	5.39	1.556	39.145	14.786	0
O	8	0.101	0.718	0.307	0.176	0.68	0.215	4.938	1.448	34.137	13.464	0
O^{1-}	8	1.292	0.42	-27.455	-9.809	-3.525	7.436	0.893	1093.626	386.901	124.108	0.007
F	9	0.109	0.647	0.319	0.144	0.582	0.208	4.295	1.355	28.652	11.38	0
F^{1-}	9	1.383	-5.454	-139.58	-50.629	-16.025	3.163	150.116	4996.255	1774.931	567.743	0.058
Ne	10	0.132	0.625	0.387	0.097	0.411	0.229	4.532	1.468	26.086	11.251	0
Na	11	0.222	0.779	0.711	1.355	1.709	0.344	10.886	2.452	142.697	51.04	0.002
Na^{1+}	11	1.724	1.031	24.201	6.715	0.36	38.664	4.527	761.383	193.654	0.53	0.01
Mg	12	0.223	0.911	0.661	1.27	2.143	0.316	9.975	2.162	97.421	36.79	0.001
Mg^{2+}	12	3.79	1.182	49.273	14.177	0.459	47.404	5.88	799.542	214.025	0.61	0.016
Al	13	0.246	1.277	0.676	1.126	2.563	0.323	11.1	2.188	102.506	36.274	0.001
Al^{3+}	13	6.713	1.695	75.717	22.984	0.684	60.95	10.056	858.057	247.055	0.901	0.018
Si	14	0.254	1.423	0.645	0.999	2.506	0.31	9.927	2.047	82.154	30.137	0.001
Si^{4+}	14	9.212	2.26	101.327	31.135	0.741	63.953	11.383	870.175	253.93	0.92	0.021
P	15	0.257	1.496	0.619	0.804	2.313	0.293	8.718	1.901	64.584	24.936	0.001
S	16	0.257	1.463	0.582	0.709	2.151	0.275	7.382	1.739	51.912	20.367	0.001
Cl	17	0.249	1.434	0.551	0.623	2.001	0.252	6.333	1.567	43.243	17.115	0
Cl^{1-}	17	0.839	3.407	-127.402	-31.676	-8.978	0.834	11.178	3780.327	1009.429	251.832	0.034
Ar	18	0.249	1.409	0.522	0.548	1.852	0.238	5.528	1.446	36.797	14.742	0
K	19	0.401	2.287	1.316	2.418	2.56	0.361	12.307	3.209	186.495	63.87	0.004
K^{1+}	19	2.31	2.189	23.641	6.25	0.52	25.002	5.125	713.099	168.005	0.465	0.014
Ca	20	0.389	2.139	1.269	2.545	3.569	0.336	10.834	2.873	133.835	49.43	0.003
Ca^{2+}	20	3.638	2.522	48.598	13.584	0.605	39.078	5.769	768.396	196.901	0.519	0.02
Sc	21	0.384	2.07	1.258	2.283	3.31	0.318	9.927	2.655	119.109	43.135	0.002
Sc^{3+}	21	5.992	2.703	74.091	21.6	0.861	51.235	7.102	811.935	222.445	0.772	0.021
Ti	22	0.389	2.011	1.294	1.984	3.098	0.309	9.577	2.546	111.565	40.23	0.002
Ti^{2+}	22	3.874	2.566	48.916	13.87	0.841	43.37	6.314	784.553	206.22	0.723	0.017
Ti^{3+}	22	6.071	2.697	74.943	22	0.911	51.347	6.992	823.99	225.369	0.782	0.022
Ti^{4+}	22	8.281	2.858	100.1	29.509	0.968	54.337	7.64	830.714	230.646	0.829	0.026
V	23	0.396	1.934	1.327	1.767	2.879	0.303	9.276	2.461	105.031	37.788	0.002
V^{2+}	23	3.612	2.471	48.29	13.309	0.654	36.076	4.984	754.704	189.626	0.497	0.021
V^{3+}	23	5.947	2.642	74.269	21.593	0.949	49.978	6.769	810.775	220.696	0.78	0.022
V^{5+}	23	10.725	3.126	125.268	37.541	1.091	57.112	8.458	841.931	237.926	0.89	0.031
Cr	24	0.399	1.884	1.336	1.277	2.072	0.294	8.838	2.342	111.237	36.158	0.002
Cr^{2+}	24	3.842	2.486	48.923	13.918	0.921	43.158	6.014	785.101	206.532	0.728	0.018
Cr^{3+}	24	5.933	2.604	74.208	21.524	0.993	49.855	6.659	809.067	220.092	0.781	0.022
Mn	25	0.4	1.798	1.324	1.483	2.501	0.285	8.404	2.214	93.776	33.389	0.002
Mn^{2+}	25	3.533	2.4	48.224	13.251	0.699	35.537	4.651	751.857	188.091	0.492	0.021
Mn^{3+}	25	5.958	2.56	74.526	21.687	1.04	50.073	6.601	814.302	221.36	0.785	0.023
Mn^{4+}	25	8.173	2.744	99.382	29.163	1.111	53.305	7.361	821.535	227.526	0.835	0.027
Fe	26	0.406	1.738	1.333	1.337	2.351	0.28	8.173	2.132	90.264	32.17	0.002
Fe^{2+}	26	3.493	2.356	48.203	13.234	0.723	35.407	4.517	750.904	187.56	0.49	0.022
Fe^{3+}	26	5.381	2.471	73.203	20.636	0.789	42.263	5.041	777.91	202.198	0.532	0.027
Co	27	0.417	1.662	1.34	1.221	2.214	0.278	7.952	2.074	86.874	30.905	0.002
Co^{2+}	27	3.457	2.309	48.152	13.208	0.744	35.303	4.39	749.588	187.03	0.486	0.022
Co^{3+}	27	5.915	2.442	74.078	21.589	1.116	49.736	6.443	809.769	220.192	0.778	0.023
Ni	28	0.42	1.604	1.334	1.136	2.074	0.27	7.696	1.987	83.05	29.636	0.001
Ni^{2+}	28	3.423	2.26	48.132	13.194	0.767	35.304	4.287	748.87	186.734	0.483	0.022
Ni^{3+}	28	5.907	2.383	74.644	21.633	1.153	49.742	6.404	813.457	220.225	0.774	0.023
Cu	29	0.433	1.529	1.329	0.834	1.474	0.27	7.428	1.933	91.897	29.494	0.001
Cu^{1+}	29	2.01	2.072	23.509	6.138	0.699	24.345	3.581	702.137	162.367	0.429	0.015
Cu^{2+}	29	3.754	2.184	49.481	14.041	1.099	43.974	5.569	793.743	207.96	0.715	0.018
Zn	30	0.441	1.475	1.309	0.995	1.844	0.267	7.214	1.866	76.667	27.316	0.001
Zn^{2+}	30	3.385	2.157	48.174	13.214	0.814	35.577	4.127	749.958	187.059	0.479	0.022

Ga	31	0.48	1.655	1.399	1.105	2.468	0.282	8.701	1.969	98.693	32.462	0.002
Ga^{3+}	31	5.86	2.207	73.864	21.387	1.239	49.518	6.301	804.207	218.518	0.749	0.022
Ge	32	0.483	1.703	1.348	1.145	2.698	0.274	8.315	1.873	82.053	28.631	0.002
Ge^{4+}	32	6.883	2.262	97.382	27.055	1.266	45.667	6.473	773.183	200.367	0.743	0.04
As	33	0.472	1.694	1.272	1.106	2.776	0.261	7.505	1.73	65.527	24.093	0.001
Se	34	0.464	1.673	1.204	1.084	2.78	0.25	6.799	1.61	54.031	20.526	0.001
Br	35	0.455	1.696	1.146	0.997	2.766	0.238	6.271	1.502	46.972	18.178	0.001
Br^{1-}	35	1.664	4.602	-128.478	-34.083	-10.881	0.85	12.618	4012.566	1164.818	310.817	0.062
Kr	36	0.458	1.784	1.104	0.853	2.699	0.232	6.003	1.438	42.456	16.799	0.001
Rb	37	0.718	3.427	1.637	3.105	2.888	0.349	12.162	2.576	191.842	59.38	0.006
Rb^{1+}	37	3.554	2.396	23.225	5.922	0.91	19.562	4.1	679.274	150.71	0.436	0.018
Sr	38	0.699	3.264	1.564	3.424	4.154	0.332	10.733	2.387	143.599	50.651	0.005
Sr^{2+}	38	3.942	3.067	47.677	12.809	1.036	28.779	5.232	728.76	175.864	0.482	0.026
Y	39	0.685	3.233	1.529	3.032	4.192	0.317	9.869	2.261	123.952	43.434	0.004
Y^{3+}	39	5.461	3.461	73.106	20.341	1.118	38.594	5.837	768.32	195.905	0.509	0.031
Zr	40	0.687	3.219	1.529	2.687	4.036	0.31	9.343	2.218	112.202	38.981	0.004
Zr^{4+}	40	7.42	3.674	97.998	27.873	1.166	44.147	6.084	787.189	207.14	0.52	0.035
Nb	41	0.689	3.267	1.529	1.905	3.281	0.303	8.898	2.177	109.753	34.934	0.004
Nb^{3+}	41	5.604	3.633	72.414	20.072	1.121	36.657	5.586	757.586	191.786	0.489	0.031
Nb^{5+}	41	9.562	3.858	123.305	35.594	1.212	47.421	6.278	801.851	214.954	0.529	0.04
Mo	42	0.696	3.247	1.56	1.674	3.081	0.3	8.594	2.173	105.121	32.914	0.003
Mo^{3+}	42	5.59	3.652	72.419	19.957	1.11	35.326	5.346	754.113	189.478	0.475	0.031
Mo^{5+}	42	9.482	4.018	123.051	35.219	1.239	47.454	6.328	796.909	212.923	0.531	0.044
Mo^{6+}	42	11.601	4.033	148.138	42.867	1.255	48.83	6.44	805.384	217.511	0.537	0.045
Tc	43	0.699	3.182	1.601	1.942	3.427	0.294	8.315	2.157	95.02	32.269	0.003
Ru	44	0.699	3.175	1.619	1.375	2.683	0.288	7.963	2.124	97.061	29.668	0.003
Ru^{3+}	44	5.458	3.818	72.104	19.884	1.134	35.427	5.21	751.235	188.637	0.467	0.032
Ru^{4+}	44	7.296	3.954	97.84	27.562	1.188	41.517	5.569	778.962	201.891	0.49	0.037
Rh	45	0.73	3.199	1.815	0.978	2.52	0.294	8.492	2.28	111.656	33.099	0.009
Rh^{3+}	45	5.367	3.843	71.96	19.746	1.138	35.045	5.066	747.161	186.882	0.461	0.032
Rh^{4+}	45	7.194	3.973	97.553	27.279	1.192	40.873	5.406	773.127	199.373	0.483	0.037
Pd	46	0.621	2.769	1.292	0.717	2.179	0.245	5.651	1.642	51.028	17.378	0.002
Pd^{2+}	46	3.974	3.663	47.486	12.62	1.075	27.45	4.514	719.819	171.002	0.427	0.026
Pd^{4+}	46	7.159	3.99	97.129	27.297	1.2	40.692	5.268	771.535	199.166	0.477	0.037
Ag	47	0.711	2.981	1.777	1.057	2.143	0.276	7.413	2.102	92.261	27.449	0.002
Ag^{1+}	47	3.219	3.368	23.059	5.877	0.999	20.017	3.896	671.582	147.599	0.39	0.018
Ag^{2+}	47	3.879	3.69	47.518	12.68	1.085	27.656	4.422	721.877	172.044	0.424	0.026
Cd	48	0.704	2.869	1.782	1.346	2.53	0.267	7.072	2.033	79.643	26.643	0.002
Cd^{2+}	48	3.768	3.687	47.464	12.595	1.09	27.472	4.295	718.469	170.748	0.419	0.026
In	49	0.746	2.88	2.07	1.528	3.208	0.279	8.184	2.226	100.518	32.626	0.003
In^{3+}	49	5.199	3.857	72.493	19.951	1.175	35.415	4.585	753.86	188.222	0.445	0.033
Sn	50	0.743	2.786	2.089	1.656	3.584	0.273	7.998	2.171	86.56	30.004	0.002
Sn^{2+}	50	4.56	3.634	47.309	12.522	1.108	26.735	4.081	713.694	168.047	0.412	0.027
Sn^{4+}	50	7.099	3.95	97.362	27.332	1.25	41.388	4.791	773.378	199.974	0.465	0.039
Sb	51	0.729	2.684	2.03	1.687	3.844	0.263	7.451	2.054	72.252	26.438	0.002
Sb^{3+}	51	5.609	3.82	72.159	19.461	1.201	31.365	4.407	738.821	179.9	0.44	0.035
Sb^{5+}	51	8.897	3.982	121.412	34.219	1.304	42.512	4.887	774.228	201.741	0.477	0.044
Te	52	0.703	2.564	1.917	1.802	4.01	0.249	6.679	1.894	60.513	22.778	0.002
I	53	0.697	2.55	1.912	1.595	4.151	0.243	6.549	1.833	55.192	21.25	0.001
I^{1-}	53	2.819	6.962	-139.481	-45.551	-15.569	1.05	15.017	4996.293	1615.268	430.449	0.122
Xe	54	0.689	2.485	1.862	1.564	4.193	0.236	6.192	1.749	48.799	19.172	0.001
Cs	55	0.936	5.015	2.75	4.098	3.701	0.322	13.712	2.639	212.049	59.506	0.008
Cs^{1+}	55	5.605	3.323	22.851	5.744	1.112	18.835	3.426	651.038	135.624	0.383	0.022
Ba	56	0.882	4.855	2.582	4.788	5.156	0.301	12.009	2.373	161.687	53.915	0.008
Ba^{2+}	56	5.725	3.717	46.952	12.118	1.239	21.681	3.951	694.144	157.489	0.419	0.032
La	57	0.563	4.923	2.553	4.373	5.384	0.164	10.489	1.8	138.906	45.628	0.028
La^{3+}	57	6.157	4.198	71.14	18.844	1.381	26.309	4.594	717.04	169.646	0.458	0.04
Ce	58	0.818	4.468	2.294	4.187	5.607	0.267	9.537	2.003	138.654	42.216	0.028
Ce^{3+}	58	6.026	4.244	71.065	18.865	1.41	26.577	4.604	717.128	170.132	0.46	0.04
Ce^{4+}	58	7.276	4.718	95.872	26.29	1.529	33.293	5.3	744.53	184.891	0.498	0.046
Pr	59	0.922	4.574	2.563	4.168	4.75	0.298	11.073	2.286	151.43	51.036	0.007
Pr^{3+}	59	5.897	4.273	71.227	18.887	1.435	26.838	4.598	718.552	170.392	0.461	0.039
Pr^{4+}	59	7.201	4.718	96.298	26.316	1.551	33.607	5.258	746.677	185.136	0.497	0.046

Nd	60	0.925	4.44	2.532	4.162	4.538	0.295	10.652	2.226	145.866	48.842	0.006
Nd^{3+}	60	5.792	4.303	71.31	18.977	1.463	27.285	4.608	721.14	171.684	0.462	0.04
Pm	61	0.936	4.342	2.521	3.97	4.464	0.294	10.415	2.194	144.37	48.498	0.007
Pm^{3+}	61	5.689	4.322	71.242	19.018	1.49	27.754	4.614	722.215	172.574	0.464	0.04
Sm	62	0.945	4.24	2.514	3.799	4.388	0.292	10.204	2.163	142.893	48.154	0.007
Sm^{3+}	62	5.598	4.322	71.222	19.03	1.512	28.085	4.594	722.287	173.024	0.463	0.039
Eu	63	0.977	4.086	2.542	3.702	4.251	0.298	10.162	2.189	140.273	47.141	0.007
Eu^{2+}	63	4.703	3.892	46.822	12.047	1.408	21.766	3.944	692.018	156.842	0.426	0.031
Eu^{3+}	63	5.512	4.317	71.357	19.041	1.534	28.469	4.579	723.907	173.501	0.463	0.039
Gd	64	0.917	4.088	2.342	3.473	4.437	0.276	9.014	1.953	121.387	40.383	0.006
Gd^{3+}	64	5.449	4.307	71.367	19.122	1.555	28.888	4.558	725.372	174.423	0.462	0.039
Tb	65	1.026	3.946	2.597	3.08	4.309	0.304	10.298	2.226	146.379	50.215	0.009
Tb^{3+}	65	5.392	4.289	71.6	19.15	1.574	29.277	4.534	726.868	174.623	0.46	0.039
Dy	66	0.986	3.832	2.449	3.388	3.975	0.288	9.35	2.046	132.944	44.728	0.006
Dy^{3+}	66	5.311	4.258	71.002	19.071	1.589	29.417	4.492	723.135	174.528	0.458	0.038
Ho	67	0.937	3.642	2.274	3.705	3.812	0.269	8.145	1.852	103.001	34.058	0.006
Ho^{3+}	67	5.275	4.236	71.28	19.183	1.608	29.882	4.475	727.008	175.982	0.457	0.039
Er	68	1.013	3.645	2.426	3.163	3.826	0.287	9.07	2.01	129.586	43.764	0.006
Er^{3+}	68	5.235	4.211	71.666	19.275	1.628	30.34	4.459	731.523	177.01	0.456	0.038
Tm	69	1.026	3.561	2.419	3.035	3.76	0.287	8.977	1.998	127.898	43.592	0.006
Tm^{3+}	69	5.18	4.168	71.36	19.212	1.638	30.431	4.409	728.779	176.558	0.452	0.038
Yb	70	1.031	3.465	2.386	3.007	3.659	0.284	8.73	1.959	125.627	42.262	0.005
Yb^{2+}	70	4.021	3.835	46.617	12.167	1.544	23.345	3.872	695.378	160.423	0.421	0.03
Yb^{3+}	70	5.18	4.144	71.786	19.428	1.657	31.079	4.4	735.508	178.841	0.451	0.038
Lu	71	1.026	3.409	2.326	2.808	3.908	0.279	8.32	1.898	108.582	37.468	0.005
Lu^{3+}	71	5.112	4.095	71.557	19.258	1.666	31.026	4.347	731.214	177.408	0.447	0.037
Hf	72	1.02	3.404	2.275	2.522	3.954	0.273	7.994	1.84	98.172	33.887	0.004
Hf^{4+}	72	6.837	4.245	96.432	26.62	1.753	37.109	4.67	754.646	190.345	0.464	0.043
Ta	73	1.025	3.421	2.243	2.226	3.936	0.271	7.781	1.812	91.965	31.488	0.004
Ta^{5+}	73	8.771	4.357	121.048	33.956	1.818	40.853	4.908	768.248	198.357	0.475	0.048
W	74	1.031	3.464	2.222	1.972	3.853	0.269	7.627	1.79	87.424	29.747	0.004
W^{6+}	74	10.792	4.48	146.689	41.409	1.876	43.307	5.136	781.066	203.981	0.484	0.053
Re	75	1.017	3.429	2.147	1.956	3.711	0.262	7.137	1.717	78.502	26.544	0.003
Os	76	1.027	3.485	2.139	1.723	3.606	0.26	7.048	1.71	75.701	25.619	0.003
Os^{4+}	76	7.031	4.509	96.676	26.607	1.806	35.438	4.748	753.943	188.473	0.455	0.044
Ir	77	1.029	3.475	2.092	1.631	3.488	0.258	6.735	1.674	71.405	23.83	0.003
Ir^{3+}	77	5.563	4.41	71.531	19.204	1.739	29.245	4.404	728.502	175.316	0.433	0.039
Ir^{4+}	77	6.995	4.581	96.18	26.426	1.814	35.133	4.744	749.136	187.266	0.452	0.044
Pt	78	1.03	3.534	2.06	1.147	3.042	0.255	6.523	1.645	70.461	22.192	0.003
Pt^{2+}	78	4.648	4.224	47.124	12.298	1.658	23.204	3.998	702.193	161.323	0.408	0.032
Pt^{4+}	78	7.095	4.357	96.519	26.549	1.703	31.685	4.196	748.876	184.65	0.419	0.074
Au	79	1.021	3.521	2.01	1.09	2.931	0.249	6.199	1.595	66.077	20.672	0.002
Au^{1+}	79	4.239	3.91	23.136	5.761	1.556	17.853	3.506	656.944	136.241	0.378	0.022
Au^{3+}	79	5.447	4.554	71.909	19.21	1.753	29.194	4.389	730.293	175.037	0.427	0.039
Hg	80	1.04	3.52	2.038	1.281	3.085	0.25	6.181	1.619	63.491	20.88	0.002
Hg^{1+}	80	4.411	3.995	22.893	5.808	1.575	18.438	3.544	652.623	134.993	0.379	0.023
Hg^{2+}	80	4.426	4.339	46.727	12.142	1.665	22.731	3.952	694.792	159.533	0.401	0.031
Tl	81	1.134	3.747	2.313	1.504	3.406	0.269	7.228	1.856	87.578	26.844	0.003
Tl^{1+}	81	4.605	4.038	22.873	5.728	1.582	18.572	3.532	646.433	132.356	0.376	0.023
Tl^{3+}	81	5.321	4.676	71.561	19.189	1.765	29.475	4.346	729.054	175.382	0.42	0.038
Pb	82	1.129	3.701	2.318	1.672	3.776	0.265	7.058	1.831	79.449	26.059	0.003
Pb^{2+}	82	4.951	4.402	46.762	12.068	1.675	22.654	3.897	692.053	157.744	0.394	0.031
Pb^{4+}	82	6.846	4.871	96.334	26.426	1.839	35.351	4.594	749.848	187.049	0.434	0.044
Bi	83	1.139	3.647	2.357	1.812	4.14	0.264	7.011	1.843	74.242	25.463	0.003
Bi^{3+}	83	5.75	4.712	71.02	18.94	1.77	27.7	4.247	719.19	171.542	0.413	0.039
Bi^{5+}	83	8.659	4.988	121.244	33.71	1.893	39.192	4.743	764.318	194.834	0.443	0.05
Po	84	1.109	3.507	2.26	2.068	4.415	0.254	6.433	1.739	64.027	22.729	0.003
At	85	1.102	3.427	2.244	2.019	4.678	0.249	6.206	1.704	58.596	21.353	0.002
Rn	86	1.097	3.382	2.241	1.897	4.874	0.245	6.062	1.675	54.122	20.242	0.002
Fr	87	1.392	5.555	3.389	4.05	4.317	0.31	12.711	2.569	196.741	50.441	0.01
Ra	88	1.362	5.52	3.282	4.866	5.518	0.3	11.796	2.438	154.439	49.505	0.009
Ra^{2+}	88	6.698	4.534	46.584	11.948	1.72	20.916	3.736	683.224	152.265	0.382	0.034

Ac	89	1.328	5.426	3.16	4.549	6.012	0.289	10.861	2.299	131.211	43.597	0.007
Ac^{3+}	89	7.046	4.901	70.767	18.443	1.82	23.61	4.098	704.109	162.844	0.401	0.043
Th	90	1.301	5.365	3.069	4.142	6.224	0.28	10.168	2.191	115.212	38.839	0.007
Pa	91	1.315	5.399	3.125	4.102	5.616	0.281	10.126	2.208	123.017	40.335	0.006
U	92	1.322	5.375	3.145	3.84	5.434	0.28	9.938	2.197	121.621	39.84	0.006
U^{3+}	92	6.736	5.147	70.619	18.374	1.863	23.379	4.109	701.575	161.901	0.4	0.044
U^{4+}	92	7.543	5.507	94.908	25.291	1.966	27.848	4.539	720.882	172.295	0.423	0.051
U^{6+}	92	10.608	6.096	145.281	40.223	2.143	37.1	5.311	759.582	191.955	0.462	0.063
Np	93	1.31	5.321	3.133	3.747	5.24	0.275	9.607	2.147	118.146	38.705	0.006
Pu	94	1.326	5.269	3.213	3.751	4.624	0.276	9.629	2.174	129.083	40.607	0.006
Am	95	1.334	5.208	3.248	3.521	4.518	0.275	9.514	2.17	128.065	40.732	0.007
Cm	96	1.31	5.079	3.163	3.363	4.787	0.267	8.934	2.076	111.801	36.61	0.006
Bk	97	1.308	4.996	3.169	3.257	4.665	0.265	8.725	2.048	109.425	36.04	0.006
Cf	98	1.162	4.249	2.638	4.776	4.124	0.23	6.322	1.664	79.157	21.827	0.025

Table 2.4: **Fitting coefficients for the 5 Gaussian $[f(s) = \sum_{j=1}^{5} a_j \exp(-b_j s^2)]$ parameterizations from FAES, alongside corresponding RMSE values.** An RMSE of “0” is a MATLAB artifact which indicates a rounding issue for a negligible value.

Atom	a_1	a_2	a_3	a_4	a_5	b_1	b_2	b_3	b_4	b_5	c	RMSE
H	0.098	0.267	-0.006	0.141	-10.25	47.316	15.011	252.987	3.601	-0.001	10.277	0.001
H^{1-}	-2.453	-27.017	0.109	-8.939	0.304	134.104	1054.39	2.218	374.597	12.019	0.011	0.001
He	0.144	0.158	0.019	0.076	-4.727	11.972	3.974	30.408	1.128	-0	4.747	0
Li	1.509	0.538	0.968	0.221	-15.607	51.84	13.909	137.241	2.356	-0.001	15.658	0.001
Li^{1+}	24.486	1.813	-95.176	0.445	6.952	785.535	44.319	-0	5.384	206.345	95.256	0.009
Be	1.412	0.668	0.698	0.22	-12.032	30.493	9.594	78.291	1.861	-0.001	12.087	0.001
Be^{2+}	49.545	3.932	-91.085	0.854	14.43	812.306	50.286	-0	7.269	221.138	91.201	0.015
B	1.249	0.752	0.485	0.244	-10.72	23.248	7.732	62.096	1.72	-0.001	10.784	0
C	1.058	0.778	0.342	0.263	-7.859	18.872	6.351	51.228	1.528	-0.001	7.926	0
N	0.88	0.703	0.284	0.275	-5.513	14.404	5.11	38.644	1.352	-0.001	5.583	0
O	0.702	0.715	0.188	0.302	-5.592	13.03	4.691	33.445	1.266	-0.002	5.668	0
O^{1-}	-2.941	-26.666	0.568	-8.927	1.122	110.973	1012.8	1.886	342.122	9.084	0.072	0.002
F	0.601	0.651	0.152	0.316	-5.374	11.062	4.089	28.174	1.19	-0.002	5.455	0
F^{1-}	-2.581	-26.027	0.55	-8.411	0.974	91.814	948.98	1.635	302.518	7.477	0.073	0.002
Ne	0.447	0.623	0.113	0.373	-5.588	10.471	4.152	25.032	1.254	-0.002	5.684	0
Na	1.685	0.815	1.443	0.684	-17.304	47.943	9.288	138.848	1.983	-0.001	17.453	0.002
Na^{1+}	23.79	1.57	-105.861	1.045	6.365	725.957	30.94	-0	3.358	174.942	106.075	0.013
Mg	2.148	0.904	1.348	0.654	-15.145	35.081	8.794	95.246	1.795	-0.001	15.298	0.001
Mg^{2+}	48.345	3.325	-137.356	1.152	13.358	757.814	38.263	-0	3.837	191.438	137.61	0.02
Al	2.609	1.223	1.205	0.681	-17.403	34.533	9.946	99.773	1.809	-0.001	17.573	0.002
Al^{3+}	74.072	5.81	-216.771	1.491	21.435	805.606	49.066	-0.001	6.381	217.906	217.201	0.024
Si	2.573	1.347	1.084	0.65	-6.7	28.527	8.912	79.693	1.67	-0.004	6.874	0.001
Si^{4+}	99.267	8.07	-127.122	1.9	29.177	820.025	52.227	-0.001	7.507	225.85	127.6	0.029
P	2.404	1.375	0.919	0.615	-13.374	23.079	7.68	61.621	1.523	-0.002	13.549	0.001
S	2.234	1.381	0.783	0.585	-10.504	19.233	6.679	50.219	1.411	-0.002	10.681	0.001
Cl	2.065	1.389	0.665	0.563	-17.763	16.482	5.901	42.348	1.303	-0.001	17.94	0.001
Cl^{1-}	-8.385	-127.084	1.025	-31.007	3.187	236.585	3715.5	1.725	966.444	12.821	0.122	0.018
Ar	1.912	1.373	0.587	0.534	-13.637	14.211	5.166	36.037	1.191	-0.001	13.812	0
K	2.508	2.439	2.622	1.137	-83.972	57.713	10.64	179.655	2.401	-0.001	84.247	0.005
K^{1+}	23.217	2.523	-169.924	1.915	5.905	679.674	19.568	-0	3.834	151.502	170.267	0.018
Ca	3.514	2.255	2.76	1.11	-14.222	46.02	9.367	129.442	2.199	-0.003	14.493	0.004
Ca^{2+}	47.671	3.394	-112.042	2.342	12.795	728.525	30.172	-0.001	4.412	175.857	112.428	0.026
Sc	3.296	2.168	2.432	1.134	-30.908	40.717	8.767	116.067	2.112	-0.001	31.182	0.003
Sc^{3+}	73.115	5.462	-247.188	2.672	20.681	780.212	43.643	-0.001	5.62	204.565	247.76	0.026
Ti	3.096	2.098	2.122	1.179	-12.635	37.924	8.458	108.552	2.055	-0.003	12.914	0.003
Ti^{2+}	48.221	3.625	-105.6	2.548	13.258	752.899	35.963	-0.002	5.032	188.873	106.164	0.021
Ti^{3+}	73.745	5.516	-125.517	2.682	20.974	788.821	43.521	-0.002	5.454	206.416	126.114	0.027
Ti^{4+}	98.663	7.511	-139.544	2.802	28.218	797.226	46.584	-0.001	5.793	212.013	140.164	0.032
V	2.888	2.014	1.895	1.221	-12.421	35.556	8.174	102.102	2.007	-0.003	12.707	0.003
V^{2+}	47.536	3.422	-113.53	2.387	12.674	722.713	29.254	-0.001	3.887	172.872	113.948	0.026
V^{3+}	73.177	5.403	-125.343	2.645	20.601	776.893	42.187	-0.002	5.211	202.001	125.957	0.027
V^{5+}	123.189	9.59	-161.547	2.98	35.599	802.448	48.247	-0.001	6.064	216.086	162.22	0.039
Cr	2.107	1.964	1.363	1.244	-28.087	33.775	7.853	107.995	1.935	-0.001	28.376	0.003
Cr^{2+}	48.181	3.573	-109.521	2.512	13.26	751.677	35.593	-0.002	4.698	188.458	110.126	0.022
Cr^{3+}	73.121	5.378	-259.633	2.626	20.527	774.973	41.971	-0.001	5.068	201.168	260.271	0.027
Mn	2.52	1.862	1.585	1.248	-26.379	31.498	7.481	91.292	1.849	-0.002	26.671	0.002
Mn^{2+}	47.481	3.336	-114.692	2.362	12.627	720.565	28.938	-0.001	3.605	171.796	115.134	0.027
Mn^{3+}	73.313	5.372	-55.711	2.597	20.624	777.9	41.899	-0.004	4.941	201.533	56.373	0.028
Mn^{4+}	97.876	7.326	-149.194	2.725	27.746	785.151	44.858	-0.002	5.308	207.086	149.886	0.034
Fe	2.371	1.795	1.432	1.27	-25.253	30.349	7.3	87.796	1.797	-0.002	25.55	0.002
Fe^{2+}	47.467	3.291	-116.793	2.34	12.617	719.965	28.88	-0.001	3.487	171.472	117.249	0.027
Fe^{3+}	72.073	4.889	-134.412	2.455	19.66	744.827	34.989	-0.001	3.77	184.501	134.892	0.033
Co	2.239	1.718	1.314	1.28	-24.828	29.04	7.052	84.339	1.744	-0.002	25.131	0.002
Co^{2+}	47.425	3.249	-118.039	2.312	12.597	718.952	28.84	-0.001	3.375	171.1	118.507	0.027
Co^{3+}	72.887	5.315	-135.919	2.511	20.506	772.962	41.468	-0.002	4.708	200.054	136.627	0.028
Ni	2.097	1.651	1.221	1.291	-9.549	27.907	6.882	80.69	1.691	-0.004	9.856	0.002
Ni^{2+}	47.41	3.208	-119.49	2.282	12.586	718.408	28.859	-0.001	3.279	170.884	119.971	0.027
Ni^{3+}	73.38	5.298	-137.621	2.465	20.55	776.155	41.377	-0.002	4.616	199.952	138.352	0.028
Cu	1.511	1.59	0.895	1.29	-9.709	27.447	6.627	89.025	1.634	-0.004	10.022	0.002
Cu^{1+}	23.157	2.049	-185.583	2.082	5.856	674.758	20.002	-0	2.817	148.973	186.039	0.018
Cu^{2+}	48.64	3.435	-118.387	2.309	13.361	758.525	36.132	-0.002	4.155	189.279	119.101	0.022
Zn	1.872	1.521	1.078	1.274	-21.856	25.522	6.377	74.235	1.575	-0.002	22.174	0.001
Zn^{2+}	47.443	3.152	-122.066	2.213	12.602	719.282	29.099	-0.001	3.115	171.129	122.575	0.027

Ga	2.512	1.669	1.185	1.395	-28.624	30.741	7.767	95.727	1.676	-0.002	28.97	0.002
Ga^{3+}	72.722	5.238	-285.931	2.315	20.312	767.627	41.111	-0.001	4.402	198.112	286.727	0.028
Ge	2.755	1.683	1.244	1.348	-10.945	26.984	7.369	79.355	1.587	-0.004	11.291	0.002
Ge^{4+}	96.524	6.363	-134.252	2.326	26.369	752.012	39.046	-0.002	4.458	187.662	135.073	0.044
As	2.845	1.651	1.212	1.275	-8.946	22.688	6.637	63.33	1.465	-0.005	9.284	0.001
Se	2.859	1.625	1.172	1.215	-18.051	19.486	6.073	52.563	1.369	-0.002	18.384	0.001
Br	2.838	1.657	1.06	1.173	-15.219	17.488	5.75	46.021	1.297	-0.003	15.55	0.001
Br^{1-}	-9.525	-127.67	1.896	-32.307	4.293	279.393	3853.868	1.642	1063	14.92	0.233	0.028
Kr	2.775	1.737	0.915	1.139	-14.015	16.162	5.544	41.518	1.24	-0.003	14.346	0.001
Rb	2.893	3.487	3.307	1.606	-58.708	53.394	10.892	185.721	1.945	-0.001	59.188	0.007
Rb^{1+}	22.788	3.863	-119.582	2.177	5.593	646.465	16.333	-0.001	2.826	134.927	120.169	0.022
Sr	4.103	3.331	3.655	1.543	-21.808	47.269	9.706	139.566	1.827	-0.003	22.281	0.006
Sr^{2+}	46.626	4.12	-157.739	2.662	11.945	686.717	21.072	-0.001	3.464	154.868	158.393	0.033
Y	4.173	3.29	3.23	1.507	-19.952	40.821	8.957	120.559	1.748	-0.003	20.42	0.005
Y^{3+}	71.385	5.072	-389.05	3.113	18.925	720.435	28.058	-0	4.014	170.877	389.761	0.041
Zr	4.047	3.275	2.863	1.498	-45.27	36.675	8.47	109.151	1.72	-0.002	45.744	0.005
Zr^{4+}	95.928	6.593	-216.852	3.403	26.089	741.571	33.837	-0.001	4.328	182.663	217.601	0.047
Nb	3.352	3.317	2.039	1.486	-18.149	32.59	8.043	106.309	1.684	-0.004	18.626	0.004
Nb^{3+}	70.983	5.313	-196.362	3.333	18.844	716.554	27.948	-0.001	4.024	170.254	197.094	0.041
Nb^{5+}	120.906	8.449	-233.963	3.62	33.492	759.002	37.934	-0.001	4.528	191.873	234.741	0.053
Mo	3.173	3.306	1.794	1.499	-42.351	30.645	7.736	101.819	1.679	-0.002	42.836	0.004
Mo^{3+}	71.269	5.389	-196.6	3.434	18.973	721.207	28.256	-0.001	4.008	172.164	197.342	0.04
Mo^{5+}	120.395	8.196	-231.716	3.708	32.902	748.991	36.575	-0.001	4.481	186.758	232.503	0.057
Mo^{6+}	145.57	10.298	-104.269	3.788	40.565	766.166	40.04	-0.002	4.642	196.073	105.071	0.058
Tc	3.486	3.253	2.099	1.521	-17.485	30.037	7.445	91.857	1.669	-0.004	17.975	0.004
Ru	2.797	3.248	1.491	1.523	-16.636	27.29	7.096	93.374	1.641	-0.004	17.129	0.003
Ru^{3+}	70.847	5.205	-196.415	3.594	18.801	715.206	27.774	-0.001	3.929	169.8	197.173	0.041
Ru^{4+}	96.07	6.657	-218.813	3.764	26.07	741.022	33.155	-0.001	4.19	181.803	219.598	0.048
Rh	2.637	3.304	1.124	1.658	-19.003	29.676	7.405	103.988	1.748	-0.004	19.519	0.01
Rh^{3+}	70.797	5.122	-195.63	3.653	18.737	713.473	27.73	-0.001	3.871	169.127	196.395	0.041
Rh^{4+}	95.926	6.589	-217.178	3.811	25.898	737.793	32.927	-0.001	4.112	180.461	217.969	0.048
Pd	2.295	2.8	0.777	1.26	-18.422	16.377	5.183	49.432	1.312	-0.003	18.867	0.002
Pd^{2+}	46.737	4.06	-171.024	3.47	12.016	689.932	22.03	-0.001	3.509	156.003	171.764	0.033
Pd^{4+}	95.578	6.566	-434.772	3.858	25.946	737.281	33.055	-0	4.047	180.884	435.571	0.047
Ag	2.271	3.099	1.154	1.632	-37.933	24.945	6.535	88.467	1.649	-0.002	38.445	0.003
Ag^{1+}	22.663	3.481	-294.317	3.168	5.583	641.01	16.576	-0	3.074	132.634	295.02	0.023
Ag^{2+}	46.75	3.942	-352.677	3.524	12.058	691.458	22.176	-0	3.465	156.931	353.424	0.033
Cd	2.616	2.993	1.469	1.641	-35.272	24.494	6.249	76.72	1.611	-0.002	35.783	0.002
Cd^{2+}	46.741	3.818	-169.238	3.55	12.002	689.509	22.101	-0.001	3.393	156.233	169.991	0.033
In	3.276	3.021	1.663	1.924	-19.432	30.409	7.199	96.803	1.798	-0.004	19.978	0.003
In^{3+}	71.329	4.903	-196.823	3.792	18.995	721.937	28.696	-0.001	3.617	171.819	197.619	0.041
Sn	3.658	2.895	1.827	1.932	-18.376	27.836	6.921	83.115	1.756	-0.004	18.922	0.003
Sn^{2+}	46.688	4.589	-345.454	3.57	12.028	688.922	22.871	-0	3.278	155.599	346.224	0.033
Sn^{4+}	95.847	6.448	-216.07	3.932	26.021	740.165	34.16	-0.001	3.749	182.266	216.902	0.048
Sb	3.922	2.763	1.884	1.868	-15.79	24.494	6.379	69.25	1.661	-0.004	16.325	0.003
Sb^{3+}	71.168	5.475	-192.273	3.748	18.669	712.452	26.317	-0.001	3.443	166.509	193.081	0.042
Sb^{5+}	119.831	8.134	-225.38	3.977	32.792	745.276	36.053	-0.001	3.776	186.015	226.236	0.054
Te	4.088	2.636	1.97	1.782	-31.101	21.406	5.796	58.553	1.55	-0.002	31.621	0.002
I	4.243	2.588	1.75	1.803	-29.025	20.092	5.731	53.444	1.524	-0.002	29.546	0.002
I^{1-}	-12.09	-129.292	3.326	-35.761	6.367	361.413	4182.968	2.089	1279	18.53	0.375	0.05
Xe	4.3	2.509	1.707	1.765	-11.034	18.192	5.425	47.391	1.456	-0.006	11.547	0.001
Cs	3.822	4.979	4.323	2.7	-185.271	53.143	12.353	205.854	2.175	-0.001	185.945	0.01
Cs^{1+}	22.505	5.776	-145.2	3.264	5.538	625.532	17.079	-0.001	2.73	123.101	145.971	0.026
Ba	5.143	4.86	5.055	2.562	-31.152	50.164	11.041	157.662	1.988	-0.003	31.792	0.01
Ba^{2+}	46.327	5.968	-174.557	3.558	11.638	670.638	18.879	-0.001	2.996	146.145	175.384	0.037
La	5.391	4.929	4.482	2.618	-0.001	44.309	10.094	137.318	1.597	-1.156	0.375	0.028
La^{3+}	70.034	6.344	-206.979	3.883	17.947	687.974	21.346	-0.001	3.284	155.238	207.863	0.048
Ce	5.638	4.526	4.243	2.348	-16.373	41.462	9.17	137.779	1.76	-0.005	16.991	0.028
Ce^{3+}	69.931	6.206	-210.482	3.923	17.93	686.947	21.313	-0.001	3.275	155.116	211.382	0.048
Ce^{4+}	93.949	7.088	-103.287	4.268	24.647	704.222	25.058	-0.002	3.625	164.244	104.233	0.058
Pr	4.719	4.617	4.42	2.552	-72.699	47.534	10.189	147.304	1.908	-0.001	73.366	0.008
Pr^{3+}	70.049	6.064	-213.204	3.954	17.93	687.479	21.305	-0.001	3.261	154.93	214.118	0.048
Pr^{4+}	94.331	6.977	-246.881	4.295	24.682	706.183	25.219	-0.001	3.607	164.379	247.843	0.058

Nd	4.521	4.49	4.384	2.53	-69.971	45.68	9.828	142.342	1.863	-0.001	70.641	0.008
Nd^{3+}	70.063	5.938	-216.916	3.985	17.962	688.306	21.405	-0.001	3.254	155.409	217.846	0.049
Pm	4.438	4.402	4.192	2.523	-69.644	45.366	9.605	140.73	1.832	-0.001	70.319	0.008
Pm^{3+}	69.95	5.808	-220.788	4.008	17.955	687.886	21.515	-0.001	3.245	155.521	221.734	0.049
Sm	4.357	4.306	4.023	2.518	-28.796	44.991	9.391	139.102	1.802	-0.003	29.476	0.008
Sm^{3+}	69.923	5.691	-223.29	4.025	17.948	687.42	21.635	-0.001	3.233	155.618	224.251	0.049
Eu	4.238	4.166	3.911	2.544	-29.716	44.057	9.301	136.807	1.809	-0.003	30.413	0.008
Eu^{2+}	46.074	5.002	-362.512	3.686	11.464	663.625	17.773	-0	2.871	143.094	363.432	0.038
Eu^{3+}	70.019	5.576	-226.27	4.035	17.941	688.24	21.765	-0.001	3.218	155.665	227.246	0.049
Gd	4.442	4.154	3.606	2.389	-23.524	38.684	8.462	119.303	1.654	-0.004	24.189	0.006
Gd^{3+}	70.002	5.48	-230.041	4.046	17.993	688.846	21.984	-0.001	3.208	156.182	231.032	0.049
Tb	4.222	4.039	3.406	2.569	-73.636	45.692	9.202	139.592	1.793	-0.001	74.356	0.01
Tb^{3+}	70.204	5.388	-98.284	4.047	18.019	689.868	22.159	-0.002	3.19	156.096	99.288	0.049
Dy	3.95	3.923	3.574	2.478	-27.406	42.033	8.617	129.672	1.699	-0.004	28.111	0.007
Dy^{3+}	69.693	5.289	-233.862	4.041	17.949	686.781	22.269	-0.001	3.172	156.094	234.88	0.048
Ho	3.852	3.708	3.822	2.31	-21.81	32.422	7.542	101.578	1.555	-0.004	22.486	0.006
Ho^{3+}	69.893	5.217	-234.775	4.037	18.011	689.126	22.502	-0.001	3.156	156.914	235.807	0.049
Er	3.797	3.745	3.347	2.46	-27.137	41.074	8.327	126.217	1.659	-0.004	27.858	0.007
Er^{3+}	70.241	5.147	-239.624	4.038	18.112	693.467	22.833	-0.001	3.153	157.898	240.673	0.048
Tm	3.724	3.665	3.228	2.454	-27.05	40.788	8.217	124.285	1.643	-0.004	27.778	0.007
Tm^{3+}	69.99	5.073	-239.748	4.018	18.067	691.345	22.933	-0.001	3.126	157.612	240.807	0.048
Yb	3.639	3.573	3.169	2.432	-62.927	39.826	8.024	122.596	1.616	-0.002	63.661	0.006
Yb^{2+}	45.793	4.236	-204.331	3.695	11.478	662.546	18.148	-0.001	2.785	144.385	205.345	0.038
Yb^{3+}	70.304	5.032	-103.076	4.015	18.223	696.143	23.347	-0.002	3.119	159.195	104.149	0.049
Lu	3.899	3.502	2.975	2.373	-10.203	35.353	7.612	105.821	1.559	-0.009	10.929	0.005
Lu^{3+}	70.185	4.955	-487.356	3.989	18.124	693.886	23.417	-0	3.097	158.444	488.442	0.048
Hf	3.967	3.478	2.676	2.326	-22.887	32.062	7.325	95.666	1.518	-0.004	23.614	0.005
Hf^{4+}	94.609	6.257	-274.074	4.186	25.058	715.457	28.549	-0.001	3.328	169.764	275.215	0.055
Ta	3.969	3.482	2.384	2.287	-52.148	29.668	7.089	89.259	1.486	-0.002	52.877	0.005
Ta^{5+}	118.911	7.865	-127.023	4.32	32.057	729.899	32.328	-0.002	3.488	177.798	128.204	0.062
W	3.905	3.509	2.135	2.259	-50.636	27.876	6.915	84.457	1.461	-0.002	51.368	0.004
W^{6+}	144.136	9.623	-135.079	4.435	39.203	743.517	34.992	-0.002	3.623	183.787	136.295	0.069
Re	3.79	3.467	2.101	2.186	-7.812	24.889	6.462	76.112	1.393	-0.011	8.527	0.003
Os	3.7	3.508	1.88	2.167	-18.517	23.834	6.344	72.918	1.381	-0.005	19.242	0.004
Os^{4+}	94.783	6.58	-121.416	4.378	25.048	715.06	27.393	-0.002	3.39	168.528	122.609	0.057
Ir	3.599	3.503	1.765	2.121	-83.61	22.267	6.083	69.025	1.351	-0.001	84.338	0.003
Ir^{3+}	70.188	5.534	-109.913	4.238	18.115	692.941	22.688	-0.002	3.175	157.6	111.077	0.049
Ir^{4+}	94.38	6.563	-581.352	4.437	24.891	711.038	27.137	-0	3.404	167.515	582.558	0.057
Pt	3.191	3.553	1.258	2.087	-16.266	20.607	5.885	67.589	1.32	-0.005	16.99	0.003
Pt^{2+}	46.217	4.906	-227.347	4.029	11.599	668.2	18.481	-0.001	2.925	145.051	228.475	0.04
Pt^{4+}	95.629	6.991	-117.11	4.428	25.814	730.808	27.889	-0.002	3.313	175.516	118.306	0.081
Au	3.079	3.551	1.178	2.045	-15.081	19.365	5.639	63.89	1.285	-0.006	15.801	0.002
Au^{1+}	22.573	4.615	-186.645	3.7	5.432	618.312	14.647	-0.001	2.594	118.033	187.718	0.029
Au^{3+}	70.547	5.427	-261.685	4.373	18.142	695.15	22.567	-0.001	3.206	157.588	262.872	0.049
Hg	3.22	3.564	1.382	2.062	-15.386	19.56	5.609	61.516	1.299	-0.006	16.122	0.002
Hg^{1+}	22.313	4.751	-191.711	3.786	5.479	611.776	15.092	-0.001	2.633	115.746	192.801	0.03
Hg^{2+}	45.907	4.708	-474.597	4.131	11.472	662.662	17.996	-0	2.925	143.889	475.742	0.039
Tl	3.547	3.832	1.648	2.276	-22.02	24.73	6.405	83.815	1.454	-0.005	22.819	0.004
Tl^{1+}	22.33	4.914	-194.169	3.846	5.439	607.753	15.348	-0.001	2.649	113.569	195.271	0.03
Tl^{3+}	70.23	5.278	-537.074	4.511	18.117	693.947	22.724	-0	3.226	157.878	538.283	0.049
Pb	3.9	3.787	1.839	2.274	-8.696	24.097	6.235	76.222	1.433	-0.011	9.49	0.004
Pb^{2+}	46.004	5.192	-231.564	4.241	11.47	662.542	18.61	-0.001	2.944	143.205	232.731	0.04
Pb^{4+}	94.618	6.401	-297.09	4.773	24.991	713.908	27.641	-0.001	3.44	168.409	298.347	0.057
Bi	4.258	3.731	2.004	2.292	-21.076	23.582	6.151	71.227	1.444	-0.005	21.884	0.003
Bi^{3+}	69.891	5.786	-543.024	4.558	18.001	688.72	22.241	-0	3.186	156.291	544.245	0.049
Bi^{5+}	119.243	7.907	-646.283	4.941	32.016	729.868	31.583	-0	3.574	176.601	647.575	0.064
Po	4.523	3.595	2.244	2.208	-18.211	21.312	5.682	61.972	1.369	-0.005	19	0.003
At	4.782	3.513	2.184	2.198	-87.133	20.192	5.511	56.866	1.356	-0.001	87.926	0.003
Rn	4.991	3.456	2.073	2.186	-16.157	19.127	5.346	52.418	1.327	-0.006	16.942	0.002
Fr	4.652	5.462	4.325	3.259	-114.597	43.69	10.85	188.927	2.01	-0.001	115.597	0.013
Ra	5.593	5.497	5.263	3.201	-107.437	44.286	10.365	148.553	1.946	-0.001	108.427	0.011
Ra^{2+}	45.934	6.966	-235.738	4.409	11.464	658.602	18.342	-0.001	2.876	140.278	236.951	0.041

Ac	6.084	5.407	4.893	3.112	-97.44	39.974	9.694	126.834	1.864	-0.001	98.414	0.009
Ac^{3+}	69.798	7.3	-111.104	4.685	17.675	679.262	20.011	-0.002	3.065	150.692	112.363	0.052
Th	6.322	5.337	4.437	3.042	-37.487	36.091	9.16	111.734	1.795	-0.004	38.446	0.008
Pa	5.702	5.415	4.37	3.094	-202.793	37.407	9.162	119.457	1.812	-0.001	203.766	0.008
U	5.521	5.408	4.094	3.111	-89.961	36.982	9.003	118.142	1.804	-0.002	90.94	0.008
U^{3+}	69.619	7.03	-519.36	4.882	17.574	675.776	19.482	-0	3.074	149.272	520.65	0.053
U^{4+}	93.42	7.637	-300.004	5.167	24.053	690.81	22.27	-0.001	3.308	157.205	301.34	0.063
U^{6+}	142.495	9.895	-711.89	5.676	37.888	720.453	28.6	-0	3.76	171.549	713.309	0.08
Np	5.317	5.363	3.995	3.101	-36.766	35.918	8.722	114.677	1.768	-0.004	37.737	0.008
Pu	4.699	5.352	3.971	3.174	-37.906	37.554	8.754	125.515	1.792	-0.004	38.891	0.008
Am	4.577	5.303	3.754	3.2	-89.843	37.533	8.635	124.118	1.789	-0.002	90.836	0.008
Cm	4.853	5.164	3.571	3.132	-183.069	34.177	8.159	108.745	1.727	-0.001	184.049	0.007
Bk	4.723	5.09	3.462	3.138	-178.451	33.645	7.972	106.388	1.707	-0.001	179.431	0.007
Cf	4.235	4.348	4.814	2.675	-5.588	21.248	5.948	78.856	1.421	-0.018	6.464	0.026

Table 2.5: **Fitting coefficients for the 5 Gaussian + scalar constant [$f(s) = \sum_{j=1}^{5} a_j \exp(-b_j s^2) + c$] parameterizations from FAES, alongside corresponding RMSE values.**

REFERENCES

[1] Liebschner, D.; Afonine, P. V.; Baker, M. L.; Bunkóczi, G.; Chen, V. B.; Croll, T. I.; Hintze, B.; Hung, L.-W.; Jain, S.; McCoy, A. J.; Moriarty, N. W.; Oeffner, R. D.; Poon, B. K.; Prisant, M. G.; Read, R. J.; Richardson, J. S.; Richardson, D. C.; Sammito, M. D.; Sobolev, O. V.; Stockwell, D. H.; Terwilliger, T. C.; Urzhumtsev, A. G.; Videau, L. L.; Williams, C. J.; Adams, P. D. Macromolecular Structure Determination Using X-Rays, Neutrons and Electrons: Recent Developments in Phenix. *Acta Cryst. D* **2019**, 75 (10), 861–877. <DOI: 10.1107/S2059798319011471>

[2] Murshudov, G. N.; Skubák, P.; Lebedev, A. A.; Pannu, N. S.; Steiner, R. A.; Nicholls, R. A.; Winn, M. D.; Long, F.; Vagin, A. A. REFMAC5 for the Refinement of Macromolecular Crystal Structures. *Acta Cryst. D* **2011**, 67 (4), 355–367. <DOI: 10.1107/S0907444911001314>.

[3] Sheldrick, G. M. Crystal Structure Refinement with SHELXL. *Acta Cryst. C* **2015**, 71 (1), 3–8. <DOI: 10.1107/S2053229614024218>.

[4] Blum, T. B.; Housset, D.; Clabbers, M. T. B.; van Genderen, E.; Bacia-Verloop, M.; Zander, U.; McCarthy, A. A.; Schoehn, G.; Ling, W. L.; Abrahams, J. P. Statistically Correcting Dynamical Electron Scattering Improves the Refinement of Protein Nanocrystals, Including Charge Refinement of Coordinated Metals. *Acta Cryst. D* **2021**, 77, 75–85. <DOI: 10.1107/S2059798320014540>

[5] Levenberg, K. A method for the solution of certain non-linear problems in least squares. *Quart. Appl. Math.* **1944** 2, 164–168. <DOI: 10.1090/qam/10666>

[6] Marquardt, D. W. An algorithm for least-squares estimation of nonlinear parameters. *J. Soc. Ind. Appl. Math.* **1963,** 11, 431–441. <DOI: 10.1137/0111030>

[7] Ten Eyck, L. F. Efficient structure-factor calculation for large molecules by the fast Fourier transform. *Acta Cryst. A* **1977**, 33, 486–492. <DOI: 10.1107/S0567739477001211>

[8] Afonine, P. V.; Urzhumtsev, A. On a fast calculation of structure factors at a subatomic resolution. *Acta Cryst. A* **2004**, 60, 19–32. <DOI: 10.1107/S0108767303022062>

[9] Navaza, J. On the computation of structure factors by FFT techniques. *Acta Cryst. A* **2002**, 58, 568–573. <DOI: 10.1107/S0108767302016318>

[10] Yonekura, K.; Matsuoka, R.; Yamashita, Y.; Yamane, T.; Ikeguchi, M.; Kidera, A.; Maki-Yonekura, S. Ionic scattering factors of atoms that compose biological molecules. *IUCrJ* **2018**, 5, 348–353. <DOI: 10.1107/S2052252518005237>

[11] Colliex, C.; Cowley, J. M.; Dudarev, S. L.; Fink, M.; Gjønnes, J.; Hilderbrandt, R.; Howie, A.; Lynch, D. F.; Peng, L.-M.; Ren, G.; Ross, A. W.; Smith, V. H.; Spence, J. C. H.; Steeds,

J. W.; Wang, J.; Whelan, M. J.; Zvyagin, B. B. "Electron diffraction," in *International Tables for Crystallography*, Volume C, edited by E. Prince (Springer Netherlands, Dordrecht, **2004**) pp. 263–281.

[12] Rez, D.; Rez, P. Grant, I. Dirac–Fock calculations of X-ray scattering factors and contributions to the mean inner potential for electron scattering. *Acta Cryst.* **1994**, A50, 481–497. <DOI: 10.1107/S0108767393013200>

[13] Cordero, B.; Gómez, V.; Platero-Prats, A. E.; Revés, M.; Echeverría, J.; Cremades, E.; Barragán, F.; Alvarez, S. Covalent Radii Revisited. *Dalton Trans.* **2008**, 21, 2832–2838. <DOI: 10.1039/B801115J>

[14] Langmore, J. P.; Wall, J.; Isaacson, M. S. The collection of scattered electrons in dark-field electron microscopy. I: Elastic scattering. *Optik* **1973**, 38, 335–350.

[15] Langmore, J. P.; Smith, M. F. Quantitative Energy-Filtered Electron Microscopy of Biological Molecules in Ice. *Ultramicroscopy* **1992**, 46 (1), 349–373. <DOI: 10.1016/0304-3991(92)90024-E>

CHAPTER 3

Mapping Electron Beam-Induced Radiolytic Damage in Molecular Crystals

3.1 Abstract

Every electron diffraction experiment is fundamentally limited by radiation damage. Immediately as a molecular crystal is illuminated by the incident beam, a complex set of inelastic scattering events initiates a cascade of radiolytic reactions within the specimen, irreversibly breaking chemical bonds and ultimately destroying the long-range periodicity of the lattice. Despite its omnipresence, little is known about the mechanism of electron beam-induced radiolysis in molecular crystals, especially with respect to mapping its onset and progression in real space. Using 4D scanning transmission electron microscopy (4D–STEM), here we analyze a series of diffraction datasets acquired from repeated sampling of single nanocrystals formed by a range of organic and organometallic compounds. By acquiring a series of consecutive 4D-STEM scans on the same crystal, we explicitly visualize the spatial evolution of coherently diffracting zones as a function of accumulating electron fluence, providing an unprecedented, time-resolved map of the internal lattice reorientation induced by radiolysis. Our experiments also unveil the resolution-dependent propagation of amorphization from impact craters created by asymmetric, localized delivery of incident electrons.

3.2 Introduction to 4D–STEM on TEAM 0.5

All 4D–STEM experiments were conducted at an accelerating voltage of either 200 or 300 kV on the TEAM 0.5 instrument located at the National Center for Electron Microscopy at Lawrence Berkeley National Laboratory. TEAM 0.5 is a double-aberration-corrected FEI Titan 80–300 scanning transmission electron microscope (STEM) equipped with a Schottky-type field emission gun (XFEG) and a source monochromator (i.e., a continuously adjustable gun lens) capable of 0.15 eV energy resolution. In principle, its 2.3 mm ultra-twin pole piece gap enables sample tilting to atypically high angles (for the experiments conducted here, ±75° proved plausible). Two unique features distinguish TEAM 0.5 most prominently from comparable STEM instruments: (a) a specially engineered sample stage driven entirely by piezoelectric motors [1] and (b) a custom-built direct electron detector, the 4DCamera [2]. The sample holder consists of a pair of titanium chopsticks which can only accommodate metal pucks 1.0 mm in diameter; circular 1.0 mm sections must be hole-punched out of typical 3.05 mm TEM grids with a sharp blade and glued to the puck using a thin layer of fast-drying silver adhesive. This procedure can often destroy a range of flimsier TEM grids, so a metallic gold support is strongly recommended. Although the piezoelectric stage (Figure 3.1) is capable of very precise five-axis motion $(x, y, z, \alpha, \gamma)$, it is mostly overkill for the experiments described in this work, none of which require an ultrastable picometer-scale drift rate. Sacrificing precision for speed—i.e., by using a standard gear-driven compustage—would have significantly expedited much of this thesis without compromising the quality of the results.

Unlike the piezoelectric stage, however, the 4DCamera (Figure 3.3) is completely essential to the experiments described here. Based on the Gatan K3 platform, the 4DCamera is a custom-built direct electron detector designed at LBNL which operates at a frame rate of 87 kHz, corresponding to a very fast readout time of 11 μs (1.1×10^{-5} s). Compared to the typical frame rates of commercially available pixelated detectors (<1 kHz), the 4DCamera's readout speed is orders of magnitude faster, nicely matching the 10-μs dwell time conventionally used in monolithic

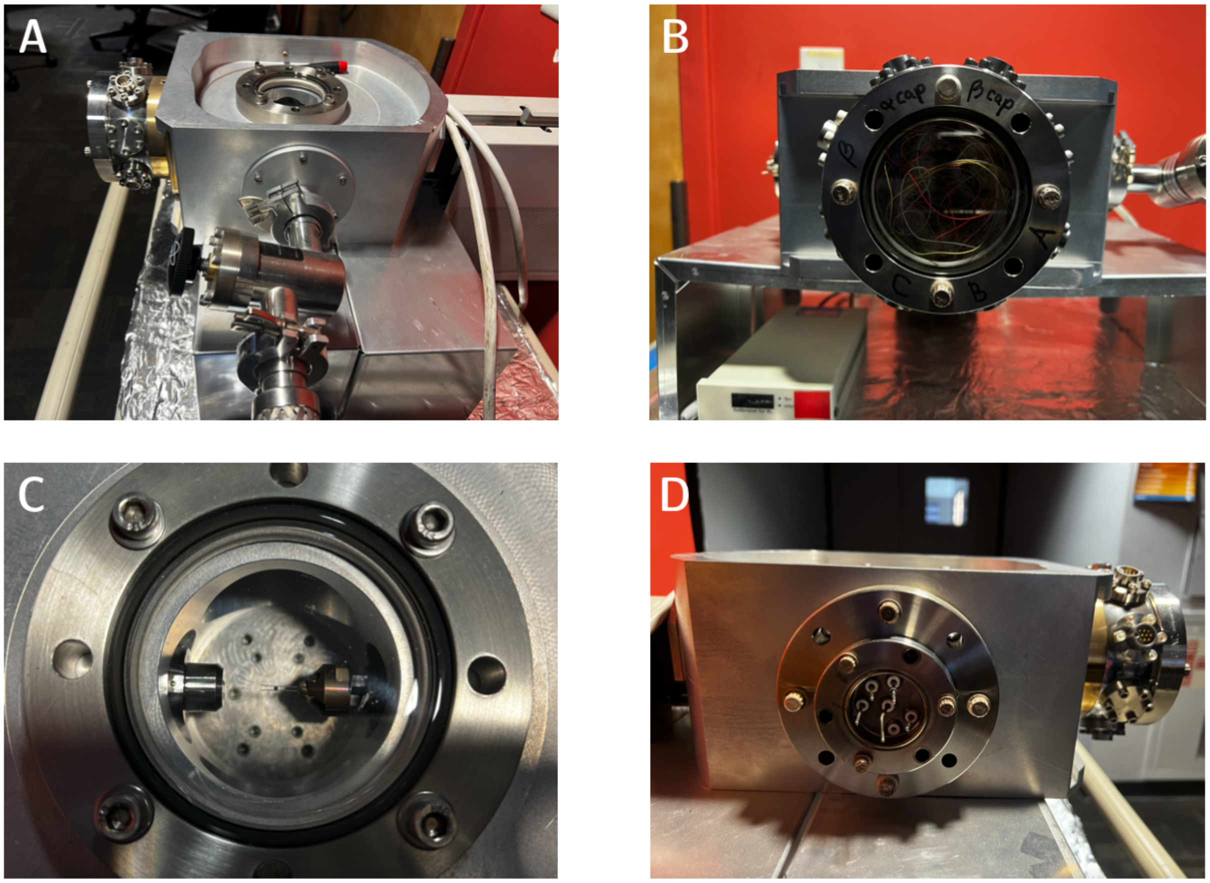

Figure 3.1: **Photographs of the piezoelectric stage apparatus in TEAM 0.5.** A: Side view of the vacuum casing designed to mimic the FEI "octagon," the cavity where the objective lens and the stage usually reside. B: Front-on view of the control module showing the internal wiring of the stage. C: Top-down view of the 1.0 mm metal puck sandwiched between the Ti chopsticks, effectively taken from the perspective of an incident electron. D: Remaining side view of the control module, displaying a flange with unused electrical feedthroughs. Photo credit: the author.

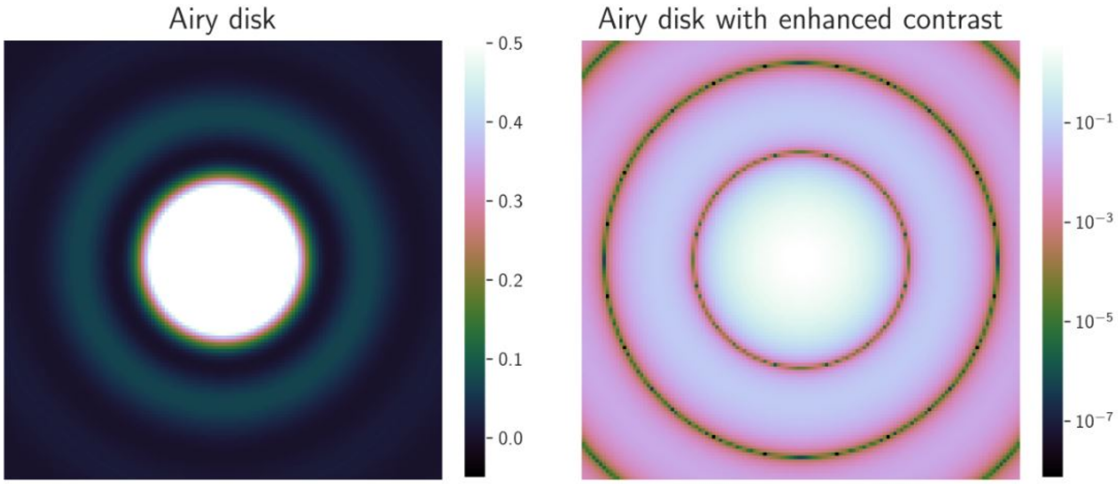

Figure 3.2: **Computationally generated Airy disk representing the shape of the probe in a STEM experiment.** A non-negligible fraction of the overall intensity is contained within the first ripple, which is exaggerated for contrast in the right image. After the first ripple—i.e., at the second zero of the first-order Bessel function $J_1(x)$—91% of the overall intensity has been accommodated.

high-angle annular dark field STEM detectors. This readout speed directly enables us to acquire 4D–STEM datasets on beam-sensitive molecular crystals on reasonable timescales (i.e., seconds instead of minutes), banishing the specter of immediately succumbing to radiolytic damage. Ensconced in retractable K3 housing, the 4DCamera features a backthinned complementary-metal-oxide semiconductor (CMOS) active-pixel sensor with 576 $\times$ 576 10 µm pixels tested for performance at a range of accelerating voltages from 30 to 300 kV.

3.2.1 Tuning STEM Parameters

Diffraction of light through a circular aperture—such as the prespecimen condenser apertures in a typical STEM instrument—yields a bright central disk surrounded by a series of concentric rings with decreasing intensities. This pattern, usually referred to as an *Airy disk*, is also an accurate approximation of the incident probe in a STEM experiment. Mathematically, the intensity I of the Airy disk varies as a function of the angle θ between the axis of the homogeneously illuminated circular aperture and an arbitrary point of evaluation:

$$I(\theta) = I_0 \left[\frac{2J_1(ka \sin\theta)}{ka \sin\theta} \right]^2 = I_0 \left[\frac{2J_1(x)}{x} \right]^2, \tag{3.1}$$

where the wavenumber $k = \frac{2\pi}{\lambda}$, a is the radius of the probe-forming aperture, I_0 is the maximum intensity at the centroid of the disk, and $J_1(x)$ is a first-order Bessel function of the first kind (Figure 3.2). Transposing the generic expression in equation 3.1 to the specific context of STEM, the full width at half maximum (FWHM) of the probe is given by

$$\text{FWHM of probe} = d_{\text{FWHM}} = 0.515 \left(\frac{\text{wavelength } \lambda \text{ in m}}{\text{semiconvergence angle } \alpha \text{ in rad}} \right), \tag{3.2}$$

implying that a significant fraction of the total intensity of the Airy disk is *not* encompassed by its FWHM [3]. A non-negligible quantity of electrons is contained within the first ripple of the Airy disk, which is enclosed by the first two zeroes of the Bessel function $J_1(x)$: 3.8317 and 7.0156. At the second zero of the Bessel function, however, 91% of the total fluence is encapsulated. This is generally a more accurate estimate for the genuine probe size than the FWHM, especially when assessing the level of overlap between adjacent probe positions in a STEM experiment. Nevertheless, simply for convenience's sake, the FWHM is more frequently used in the literature. Another plausible option is to use the degree of separation defined by the Rayleigh criterion, which involves substituting a prefactor of 0.61 in equation 3.2:

$$d_{\text{Rayleigh}} = 0.61 \left(\frac{\text{wavelength } \lambda \text{ in m}}{\text{semiconvergence angle } \alpha \text{ in rad}} \right). \tag{3.3}$$

This captures 59% of the delivered fluence [3]. If the real-space pixel size exceeds the size of the probe (as evaluated at the second zero of the Bessel function), this is equivalent to *undersampling*, indicating that portions of the specimen corresponding to gaps between consecutive probe positions receive no exposure to electrons. Conversely, if the size of the probe exceeds the real-space pixel size, this is equivalent to *oversampling*: some portions of the specimen receive an extra dose of electrons due to the overlap between adjacent Airy disks. Somewhat inadvertently, our experiments roughly straddle the line between undersampling and oversampling; none of the 4D–STEM parameters used in this work fall significantly toward either end of the spectrum.

Equation 3.2 clearly indicates an inverse relationship between the semiconvergence angle α and the minimum achievable probe size d_{FWHM}. Since the profile of a Bragg peak is essentially a Fourier transform of the shape of the probe at the specimen plane, a narrow semiconvergence angle—corresponding to a parallel electron beam with a larger FWHM—produces sharp, Gaussian-like Bragg reflections in reciprocal space. Conversely, a wide semiconvergence angle—corresponding to a convergent electron beam with a smaller FWHM—produces broad Bragg disks in reciprocal space. Convergent-beam electron diffraction (CBED) is a popular technique in materials science and condensed-matter physics. Nevertheless, our experiments leverage a parallel beam ($\alpha < 0.1$ mrad) to produce electron diffraction patterns comprehensible to indexing and integration routines originally developed for X-ray crystallography. Thanks to the tradeoff intrinsic to equation 3.2, however, this choice leads us to deliberately sacrifice the possibility of forming a smaller probe ($20\text{ nm} \geq d_{\mathsf{FWHM}} \geq 15\text{ nm}$). In other words, we forgo the prospect of especially granular real-space detail for the convenience of using well-established software from the X-ray community. Understandably, programs written for X-ray crystallography are (a) generally unaware of the existence of Bragg disks and (b) require clear separation between Bragg peaks to perform tasks such as spot-finding and space-group determination.

A final parameter in equation 3.1 worthy of discussion is the radius a of the probe-forming aperture. TEAM 0.5 is equipped with a slate of custom condenser apertures fabricated by Norcada, including bullseye-shaped apertures intended to form a patterned probe [5]. Our experiments leverage the second-smallest custom C2 aperture on TEAM 0.5, which is circular in shape with a diameter of 10 μm. Usage of a smaller C2 aperture grants us access to a set of narrower semiconvergence angles in the 0.07–0.15 mrad range, corresponding to a near-parallel beam. Notably, the second-smallest non-custom C2 aperture available on TEAM 0.5 has a diameter of 70 μm; trial experiments and vacuum scans quickly demonstrated that a 70 μm C2 yields an incident probe current roughly 100× greater than the custom 10 μm Norcada C2 for exactly the same

Current (pA)	Electrons delivered in 11 μs	Fluence per probe position (e^{-}Å^{-2})
1	68.75	0.003
10	**687.5**	**0.03**
20	**1375**	**0.06**
50	**3437.5**	**0.15**
100	6875	0.3
200	13750	0.6
500	34375	1.5
1000	68750	3

Table 3.1: **Range of probe currents typically used in the 4D–STEM experiments described in this dissertation**, alongside the corresponding number of electrons delivered within the readout time of the 4DCamera and the fluence delivered per probe position under "standard conditions." These values were calculated assuming a real-space pixel size of 15 nm × 15 nm and a matching FWHM.

monochromator focus and gun lens settings. Another immensely important consequence of the custom 10 μm C2 aperture, therefore, is the considerably lower fluence which it enables (Table 3.1).

3.2.2 Sparsification of 4D–STEM Data

Thanks to its very fast readout time, the 4DCamera produces a prodigious quantity of data at a daunting rate of approximately 480 Gbps. Depending on the dimensions of the scan, the incident beam current, and the scattering mass within the mean free path, the raw file sizes for the 4D–STEM data acquired in this work generally fall within the 20–400 GB range. Figure 3.4 summarizes the computational workflow for offloading, ingesting, and electron-counting these volumes of data. To transform the raw 4D–STEM scans—essentially massive four-dimensional arrays—into reasonably sized files easy to manipulate on a standard laptop computer, a sparsification routine is implemented on the Cori (now deceased) and Perlmutter supercomputers at the National Energy Research Scientific Computing Center (NERSC) using the open-source python-based software `stempy`. All `stempy` code is publicly available on Github.

We now turn to an oversimplified example to illustrate the sparsification process. Consider

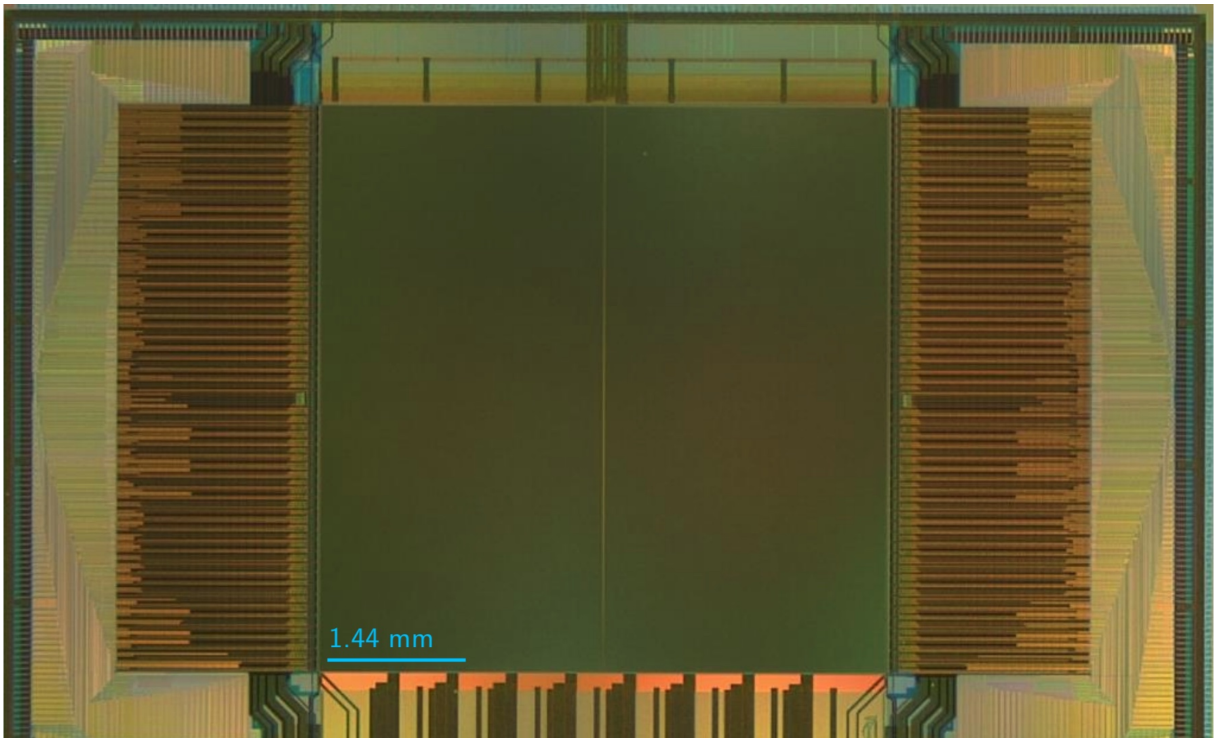

Figure 3.3: **Photograph of the first-generation backthinned complementary-metal-oxide semiconductor (CMOS) active-pixel sensor on the 4DCamera inside TEAM 0.5.** Thanks almost entirely to the experiments described in this dissertation, the central pixels absorbed many nanoamps of beam current over the course of 18 months. As a result, this venerable sensor has been recently replaced with a second-generation variant. Photo credit: P. Denes.

the 3 × 3 matrix in equation 3.4 as a toy dataset:

$$\begin{bmatrix} 8 & 5 & 3 \\ 4 & 2 & 1 \\ 7 & 6 & 9 \end{bmatrix} \rightarrow \begin{bmatrix} 8 & 5 & 3 & 4 & 2 & 1 & 7 & 6 & 9 \end{bmatrix} \tag{3.4}$$

To encode this 3 × 3 matrix in computer memory, we generally collapse it into a one-dimensional row and use some meta-level indexing code to associate each number in this flattened 1D representation with its location in its 2D counterpart. In other words, an N-dimensional array is stored in computer memory as one contiguous block, and some indexing system simply tells the computer which element to summon. Since each element of this matrix is populated with a nonzero (and therefore presumably meaningful) value, this type of data is typically referred to as a *dense array* in scientific computing.

Conversely, consider the 3 × 3 matrix in equation 3.5:

$$\begin{bmatrix} 0 & 0 & 0 \\ 0 & 1 & 0 \\ 0 & 0 & 0 \end{bmatrix} \rightarrow \begin{bmatrix} 0 & 0 & 0 & 0 & 1 & 0 & 0 & 0 & 0 \end{bmatrix} \tag{3.5}$$

In this 3 × 3 matrix, only 1 out of 9 elements is nonzero, corresponding to a *sparse array*. (Although competing definitions of sparsity exist, the simplest approach is to consider any matrix where the majority of entries are zeroes as a *sparse array*, which is what we'll do here.) If we were to encode this information in computer memory in a dense format analogous to the array in equation 3.4, all 9 elements would require explicit storage. Thankfully, 4D–STEM operates within a very constrained parameter space in which we can only encounter one of two possible outcomes. Either an electron *did* strike a given pixel during the 11 μs readout time of the 4DCamera—in which case we record a 1—or no electron struck that pixel, which means we record a 0. Therefore, in lieu of a brute-force approach in which every single element is saved, we can exclusively record the locations of the 1s:

$$\begin{bmatrix} 0 & 0 & 0 \\ 0 & 1 & 0 \\ 0 & 0 & 0 \end{bmatrix} \rightarrow \begin{bmatrix} 5 \end{bmatrix} \tag{3.6}$$

Here the number 5 simply represents that the nonzero element of the original array was the fifth entry in the matrix. A number of indexing ambiguities immediately arise, especially for nonsquare matrices (i.e., do we start counting at 0 or 1, do we progress through rows and columns horizontally or vertically, etc.), but suffice to say picking one convention and sticking to it is immensely important. For instance, C and C++ cycle through multidimensional arrays using the most rapidly changing index *last*, whereas Fortran does the reverse. Our choice is python's `numpy.ndarray` class, which is actually interpretable either way.

Overall, this tactic still conveys all the underlying information present in the original array but stores it in a hugely more efficient manner, often consuming up to 10–300× less disk space. Sparsification of the raw 4D–STEM data ultimately generates eminently manageable sub-200 MB HDF5 files amenable to short-term storage and data analysis on standard laptop computers. The simple internal architecture of these HDF5 files is described in the `stempy` documentation available on Github. In brief, a supercategory called `electron_events` contains an array of arrays called `frames`, in which the first index corresponds to the scan position (also stored as a 2D array in a separate subcategory called `scan_positions`) and the second index holds a sparsified array corresponding to the locations of the electron strikes in the diffraction pattern (i.e., following the logic laid out in equation 3.6).

3.3 Radiolysis Discussion

A specter is haunting electron microscopy—the specter of radiation damage. Immediately as a molecular crystal is illuminated within a transmission electron microscope, it confronts the

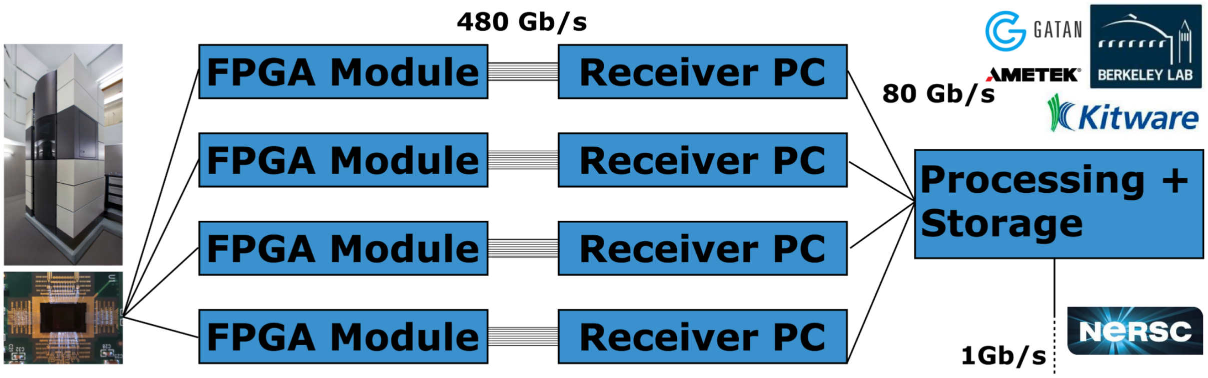

Figure 3.4: **Computational workflow for acquiring and processing 4D–STEM data on TEAM 0.5 using the 4DCamera [4].** Each dataset is streamed via field-programmable gate array (FPGA) modules into the RAM of four receiver PCs, offloaded into flash storage on a fifth PC, and transferred to the Cori (now deceased) and Perlmutter supercomputers at the National Energy Research Scientific Computing Center (NERSC) over 1 km of fiber-optic cables. Open-source `stempy` routines then reduce the raw data to a sparse linear-index-encoded electron event representation (EER) in HDF5 format, resulting in an overall compression from 100 GB files to 100 MB files viewable on a mediocre laptop computer.

bleak prospect of sustained bombardment with extremely harsh levels of ionizing radiation. As electrons accelerated to relativistic speeds impinge on the sample, they typically disseminate quantities of energy per unit mass in the range of megagrays (MGy; 10^6 J kg^{-1}) [6], several orders of magnitude greater than the lethal Gy-scale doses (10^1 J kg^{-1}) imbibed by victims of the nuclear disaster at Chernobyl [7]. Thus, electron beam-induced radiolytic damage has long been heralded as the "fundamental limit" [8] constraining fields such as single-particle analysis, cryo-electron tomography, and electron crystallography.

Nevertheless, despite its crucial importance, little is rigorously understood about the onset and progression of radiolytic damage in beam-sensitive materials. This is partially due to the sheer complexity of the myriad phenomena involved. Electrons accelerated to 300 keV move at comfortably relativistic speeds ($0.77c$, or 2.327×10^8 m s^{-1}), making their transit time through a 300 nm thick crystal virtually instantaneous—on the order of 1–2 femtoseconds (10^{-15} s). If a primary inelastic collision during this timeframe involves sufficient energy loss to cause electronic excitation of an atom within the specimen, a dizzyingly wide array of consequences can ensue, each with their own characteristic timescales and probabilities. These include direct ionization, excitation and decay of plasmon and phonon oscillations, secondary electron emission, homolytic scission of covalent bonds, and subsequent formation of reactive free radicals. A helpful timeline of some of these events has been provided by Grubb [9] and Flannigan [10]. From a chemical perspective, however, by far the most consequential downstream effect of primary excitation is the generation, thermal diffusion, and propagation of itinerant free radicals. This is a markedly slower process, generally thought to occur on the picosecond timescale (10^{-12} s: still many orders of magnitude faster than the 1.1×10^{-5} s readout time of the 4DCamera). Furthermore, some fraction of radical fragments generated by radiolysis likely undergoes rapid recombination, especially if steric bulk renders thermal diffusion kinetically unfavorable. Nevertheless, the subset of free radicals which do undergo thermal diffusion—predominantly low molecular weight species—can migrate into the interstitial space of the crystal lattice and initiate a cascade of further homolytic reactions elsewhere in the specimen. This process is generally considered the prevailing emissary of radiolytic damage in molecular crystals [11, 12]. In sum, inelastic scattering events initiate a cascade of radiolytic reactions within the sample, irreversibly breaking chemical bonds and ultimately destroying the long-range periodicity of the lattice.

In electron crystallography, the primary metric used for assessing the extent of degradation induced by radiolysis is the disappearance of Bragg reflections in electron diffraction patterns [13, 14, 15, 16, 17, 18]. Upon prolonged exposure to incident electrons, the Bragg reflections ultimately recede into the noise floor, corresponding to the permanent loss of long-range periodicity in the lattice. To quantify some arbitrary crystalline material's susceptibility to radiolysis, a commonly used parameter is the *critical fluence*, corresponding to the number of electrons delivered per unit area which causes the intensities of the Bragg peaks to fade to e^{-1} of their original values. Egerton [19] has tabulated critical fluences for a wide gamut of materials, ranging from fragile organic small molecules (e.g., 1.6 $e^{-}\text{Å}^{-2}$ for glycine) to robust inorganic salts (e.g., 50000 $e^{-}\text{Å}^{-2}$ for NaCl). A few consistent trends have emerged from Egerton's analysis. Compounds bearing aromatic functional groups, for instance, tend to have significantly higher critical fluence

Compound	Critical fluence ($e^{-}\text{Å}^{-2}$)
Bacteriorhodopsin	0.5
Glycine	1.6
Polyethylene	6.0
Coronene	70
Phthalocyanine	120
Cu(II) phthalocyanine	1600
Perchlorinated phthalocyanine	12000
NaCl	50000

Table 3.2: **Critical fluences for a range of materials**, tabulated by Egerton [19]. Two sharp jumps in critical fluence merit discussion here. The disparity between polyethylene and coronene is an illustrative example of the difference between aliphatic and aromatic compounds, whereas the remarkable 100× discrepancy between phthalocyanine and its perchlorinated derivative demonstrates the powerful advantage conferred by perhalogenation.

values than their aliphatic counterparts, and dose tolerance is generally lifted by perhalogenation of C–H bonds. Apart from these scattered, hard-won insights, however, existing data from the TEM community sparingly samples the vast complexity of chemical space, and most previous studies do not meaningfully venture beyond indirect observation via the back focal plane. Little is known about the concomitant changes in real space which *drive* the deterioration of Bragg peaks. A *simultaneous* visualization of the effects of beam-induced radiolysis—in both real and reciprocal space—remains elusive.

In this work, we leverage the dual-space imaging power of scanning nanobeam electron diffraction—also known as 4D scanning transmission electron microscopy (4D–STEM)—to provide an incisive new perspective on this longstanding problem. 4D-STEM involves raster-scanning a focused electron nanobeam across a user-selected region of interest in real space, partitioned into an $n \times n$ array of scan points [20, 21]. At every single probe position in this two-dimensional grid, a diffraction pattern is recorded, exploiting recent improvements in detector sensitivity and speed. We utilize a back-thinned CMOS-based direct electron detector operating at 87,000 frames per second, corresponding to a readout speed of 11 microseconds. This yields a four-dimensional dataset consisting of 2^n sparse diffraction patterns (indexed by reciprocal-space coordinates q_x and q_y), each linked with an associated pair of probe positions (x, y) in real space. By computationally summing signal from specific regions of a crystal *ex post facto*, 4D–STEM empowers us to construct custom virtual apertures, functionally permitting direct visualization of exactly which coherently diffracting zones (CDZs) gave rise to Bragg signal in reciprocal space.

Here we expand the scope of conventional 4D-STEM in three critical ways. Firstly, our experiments add a crucial fifth dimension: time. By acquiring a series of consecutive 4D-STEM scans on the same crystal, we explicitly visualize the spatial evolution of CDZ contours as a function of accumulating electron fluence, providing an unprecedented, time-resolved map of the internal lattice changes induced by radiolysis. Secondly, in lieu of the wide semiconvergence angles typically used in convergent-beam electron diffraction (CBED)—a standard technique in materials science—we utilize a near-parallel beam to generate sharp, Gaussian-like Bragg peaks. Thirdly, we broaden the ambit of the technique by analyzing a range of organic and organometallic compounds relevant to synthetic chemists, none of which have been previously investigated using 4D-STEM.

3.3.1 Spatial Migration of Coherently Diffracting Zones

We began our studies by conducting exploratory 4D-STEM scans on nanocrystals of (+)–biotin, a beam-sensitive organic molecule typically used as a standard in 3D electron crystallography. As long-range order in the crystal lattice was destroyed, we observed that new diffraction signal was frequently unmasked from dormant, initially Bragg-silent CDZs. We found that beam damage-induced lattice reorientation causes a continuously shifting array of reciprocal lattice vectors to intersect the surface of the Ewald sphere, leading to several distinct patterns of decay. Broadly, we classify these into two groups: monotonic (type 1) and nonmonotonic (type 2) decay. To identify these two groups of reflections, we generated a synthetic diffraction pattern where the intensity of each pixel represented a projection of its maximum value during the time series. We then placed virtual apertures around the centroids of every individual Bragg reflection. Next, we reconstructed virtual dark-field (VDF) images to visualize the corresponding real-space signal, displayed as a horizontal montage with increasing electron fluence applied from left to right.

An emblematic example of type 1 decay is depicted in Figure 3.14A. In type 1 decay, the recorded intensity for a given Bragg peak has already reached its global maximum in scan zero. From this apex, it then undergoes simple, nearly linear deterioration, a trend well-known in the literature. For instance, the twisted striation in Figure 3.14A—corresponding to a 2.36 Å Bragg reflection (Supplementary Video S1)—migrates to the right fringe of the crystal while thinning rapidly into a narrow sliver. As the intensity of this Bragg peak becomes indistinguishable from noise, its CDZ disintegrates in lockstep. These VDF images indicate that reflections which undergo type 1 decay originate from CDZs which also diminish monotonically in size.

Conversely, in type 2 decay, the global maximum of the recorded intensity is linearly offset from scan zero, resulting in a delayed-onset decay pattern which most frequently resembles a skewed Gaussian distribution. These reflections represent reciprocal lattice vectors which do not precisely fulfill the Bragg condition in scan zero. Nevertheless, their excitation error is effectively reduced in whatever radiolysis-induced orientation the lattice has progressed to in a later scan, causing them to paradoxically appear stronger for some ephemeral period before ultimately succumbing to monotonic decay. For instance, somewhat unexpectedly, the Friedel mate of the 2.36 Å type 1 reflection considered earlier follows a type 2 decay pattern (Figure 3.14B, Supplementary Video S2). Although this CDZ is morphologically similar to that of its Friedel mate, it clearly unfurls into a more expansive striation in scans 1 and 2 relative to its shape in scan 0. Consistent with this transient boost in size, the intensity of this reflection also withstands an extra 0.6 $e^{-}\text{Å}^{-2}$ compared to its Friedel mate before it fades to nothingness.

Another subset of type 2 decay involves Bragg peaks completely absent in scan 0 which proceed to materialize midway in the time series before beginning to deteriorate. For instance, the boomerang-shaped CDZ in Figure 3.14C is not observable in scan 0 and begins to form only after ca. 0.45 $e^{-}\text{Å}^{-2}$ have been delivered (Supplementary Video S3). This CDZ then extends across the surface of the crystal and appears to recede back into the upper left corner as it decays. Intriguingly, although this 2.61 Å reflection's Friedel mate activates a similar type 2 decay pattern (Figure 3.14D), its lifetime is a truncated subset of its counterpart in Figure 3.14C, and its shape is not quite as expansive (Supplementary Video S4). This disparate behavior mirrors the asymmetry observed in the decay patterns of reflections A and B.

Following these case studies on individual Bragg peaks, we then moved on to reconstructing the aggregate signal from clusters of reflections. We began by assembling a composite VDF image corresponding to the CDZs linked to all identified Bragg peaks. These formed an intricate network of veins and striations meandering across the (+)-biotin crystal, with an especially intense and long-lived swath located at the center (Figure 3.14E). Next, by summoning signal exclusively from reflections obeying type 1 decay, we observed that the intense central band dimmed considerably (Figure 3.14F), unveiling a weaker group of striated CDZs underneath. Since reflections undergoing type 1 decay fade earlier than their type 2 counterparts, we reasoned that the most robust CDZs likely produce Bragg peaks inclined to experience nonmonotonic decay. As expected, the VDF images corresponding to the CDZs associated with type 2 reflections recapitulated most of the real-space signal in the central band (Figure 3.14G). Collectively, our analysis indicates that CDZs in molecular crystals display a profound degree of internal movement upon irradiation, suggesting that the orientation of the lattice is far from static. Instead, the nanoscale topography of the lattice is constantly evolving immediately as it is illuminated.

3.3.2 Implications for 3D ED

Previous analyses of electron beam-induced radiolytic damage in organic crystals have generally coalesced around a model involving monotonic decay of Bragg peak intensities [17, 18]. Critically, however, these studies exclusively monitored the fading of Bragg peaks, with little to no corroborating analysis conducted in real space. Our 4D–STEM results expand this body of work by visualizing a crucial missing piece in this puzzle: beam-induced lattice reorientation, driven by damaged CDZs engaging in a complex dance choreographed by radiolysis. A key consequence of this effect is that monotonic decay—the ultimate fate of every reflection—is initially coincident within an ephemeral phase where lattice reorientation reshuffles the intensities of some recorded Bragg peaks. Subsequently, after enough rotationally misoriented CDZs have been ablated, the lattice relaxes to a more stagnant consensus orientation, and the intensities of the remaining Bragg peaks fade monotonically.

In 1971, Glaeser disclosed an analogous scenario in uranyl acetate-stained catalase crystals, where he briefly observed "relative changes in diffraction intensities" upon irradiation by 80 keV electrons [13]. Glaeser's prescient speculation that a "significant portion of the matter within the unit cell of the structure changes to some more stable configuration" is partially consistent with our 4D–STEM data. Slight changes *within* individual unit cells—equivalent, for instance, to a global increase in atomic B-factors—would indeed affect the intensities of the recorded Bragg peaks. 4D–STEM does not offer an easy way to deconvolute such contributions. Nevertheless, unit cell-level effects cannot adequately rationalize the sudden appearance of Bragg peaks completely absent in earlier scans, and *ab initio* structures determined from multipass 3D ED datasets do not display drastic deviations in the RMSDs of atomic positions. Therefore, our results point more definitively to macroscopic motion of the CDZs themselves—i.e., at the level of *lattice* subregions—as the primary driving force behind type 2 decay. We note that precedent for nonmonotonic fluctuations in Bragg peak intensities—as well as hypothesized lattice reorientation—has also been documented by Thorne and co-workers in the context of macromolecular X-ray crystallography [22, 23].

These observations lead to critical implications for 3D electron diffraction (3D ED) experiments, where an irradiated nanocrystal is continuously rotated while reciprocal space is periodically sampled in regular intervals. We reasoned that some "catalytic" amount of beam-induced damage could potentially mold the initial distribution of CDZs into a more self-consistent lattice, transiently producing higher-quality data. To test this hypothesis, we collected a series of 3D ED datasets on three species we had also surveyed by 4D—STEM: Ni(dppf)Cl_2 (Figure 3.5), (+)–biotin (Figure 3.6), and Jacobsen's ligand (Figure 3.7). In Ni(dppf)Cl_2, we found that three key metrics typically used to assess crystallographic data quality—R_{meas}, $<I/\sigma(I)>$, and $CC_{1/2}$—improved for the second pass relative to the first pass, followed by a steady and incremental decline. As a measurement of internal consistency [24], lower R_{meas} is particularly suggestive of the possibility that radiolysis can ablate rotationally misoriented CDZs, leading to an ensemble of more accurately sampled intensities produced from a more monolithic lattice. Conversely, recording a full 3D ED dataset before the lattice has relaxed to a consensus orientation—i.e., while the underlying distribution of CDZs is still *actively shifting* due to beam-induced radiolysis—causes R_{meas} to suffer, rationalizing the sharp difference between the first and second passes. For (+)–biotin, results were mixed: $<I/\sigma(I)>$ and $CC_{1/2}$ deteriorated monotonically, whereas overall R_{meas} was still slightly ameliorated for the second and third passes. For Jacobsen's ligand, overall $<I/\sigma(I)>$ and R_{meas} also improved for the second pass, although not quite as convincingly as $Ni(dppf)Cl_2$.

In other words, if the substrate under interrogation is sufficiently robust, a full 3D ED dataset is obtainable during the critical window after lattice reorientation has concluded but before monotonic decay has attenuated sub-1.2 Å resolution reflections. $Ni(dppf)Cl_2$ nicely fits these criteria. In especially beam-sensitive samples, however, this window is exceptionally narrow, because lattice reorientation occurs simultaneously alongside both type 1 and type 2 decay. For instance, even under cryogenic conditions at 100 K, radiolytic damage in (+)–biotin propagates too quickly to productively exploit, as most CDZs have already progressed deep into the monotonic decay phase by the time a second-pass movie can be acquired. This leads to uniformly lower-quality data in terms of $<I/\sigma(I)>$ and $CC_{1/2}$, despite the fact that lower overall R_{meas} suggests that the lattice has relaxed to a stable consensus orientation more suitable for crystallographic data reduction. Intriguingly, Chiu and co-workers have reported that transient strengthening of Bragg peak intensities in frozen-hydrated catalase is much more widespread at 4 K than 100 K [25]. Although Chiu and co-workers speculatively attribute these effects to "specimen movement or charging," our 4D–STEM analysis suggests that beam-induced lattice reorientation is an equally if not more plausible interpretation of their results. A detailed investigation of temperature as an independent variable is beyond the scope of our current work, but simply slowing the thermal diffusion of damaging free radicals is likely to elongate the lattice reorientation phase and enhance its visibility.

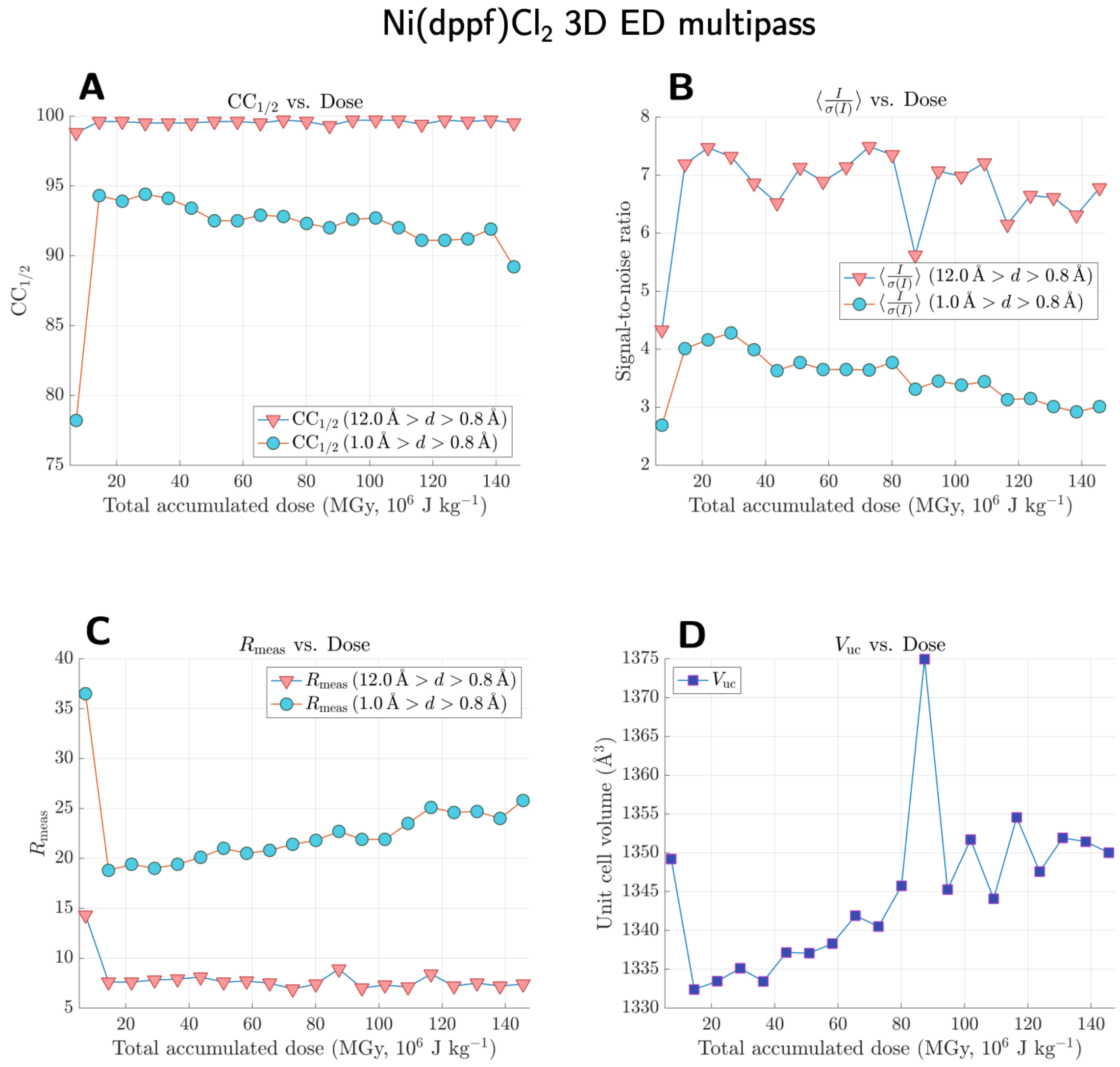

Figure 3.5: **Data reduction statistics for 20 consecutive 3D ED movies collected on a single crystal of Ni(dppf)Cl$_2$**, where each point represents a full continuous-rotation dataset. A fluence of approximately 2.2 e^{-}Å^{-2} was delivered per movie, which was converted to a substrate-specific dose of 7.3 MGy using the program RADDOSE-EM [26]. After 20 consecutive passes, the Ni(dppf)Cl$_2$ crystal has endured a total accumulated fluence of 44 e^{-}Å^{-2}, or 146 MGy. A clear improvement to a better value is seen between movies 1 and 2 for CC$_{1/2}$ (A), $<I/\sigma(I)>$ (B), and R_{meas} (C), accompanied by a contraction in unit cell volume (D). From movie 2 onwards, all statistical metrics tend to uniformly get worse, and unit cell volume begins to expand. A plausible interpretation of these statistics is that data acquisition during the first movie is coterminous with lattice reorientation, whereas the remainder of the movies represent the initial stages of slow, steady monotonic decay after the lattice has relaxed to a consensus orientation.

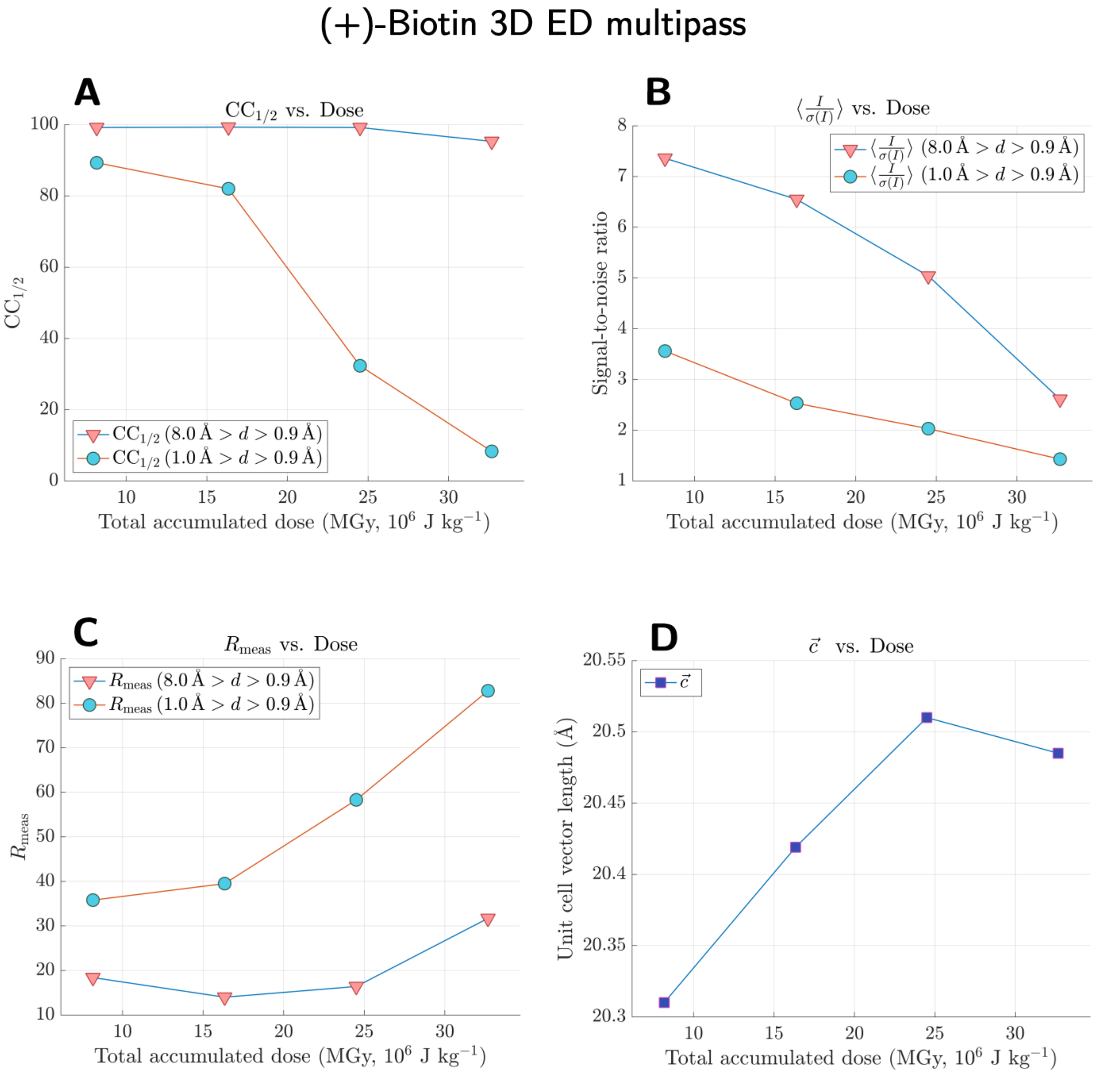

Figure 3.6: **Data reduction statistics for 4 consecutive 3D ED movies collected on a single crystal of (+)–biotin at 100 K**, where each point represents a full continuous-rotation dataset. A fluence of approximately 2.3 e^{-}Å^{-2} was delivered per movie, which was converted to a substrate-specific dose of 8.2 MGy per movie using the program RADDOSE-EM [26]. After 4 consecutive passes, the (+)–biotin crystal has endured a total accumulated fluence of 9.2 e^{-}Å^{-2}, or 32.8 MGy. Unlike Ni(dppf)Cl_2, (+)–biotin is too beam-sensitive to allow acquisition of multiple movies from the same crystal at RT, necessitating slow-cooling to cryogenic temperatures. Interestingly, these statistics appear mixed, with $CC_{1/2}$ (A) and $<I/\sigma(I)>$ (B) deteriorating monotonically but overall R_{meas} (C) getting slightly better in movie 2. A plausible interpretation of these statistics is that lattice reorientation has definitely concluded by the time movie 2 is acquired—thus the slightly better R_{meas}—but monotonic decay has also rapidly progressed to the point where $CC_{1/2}$ (A) and $<I/\sigma(I)>$ have diminished, leading to overall lower-quality data.

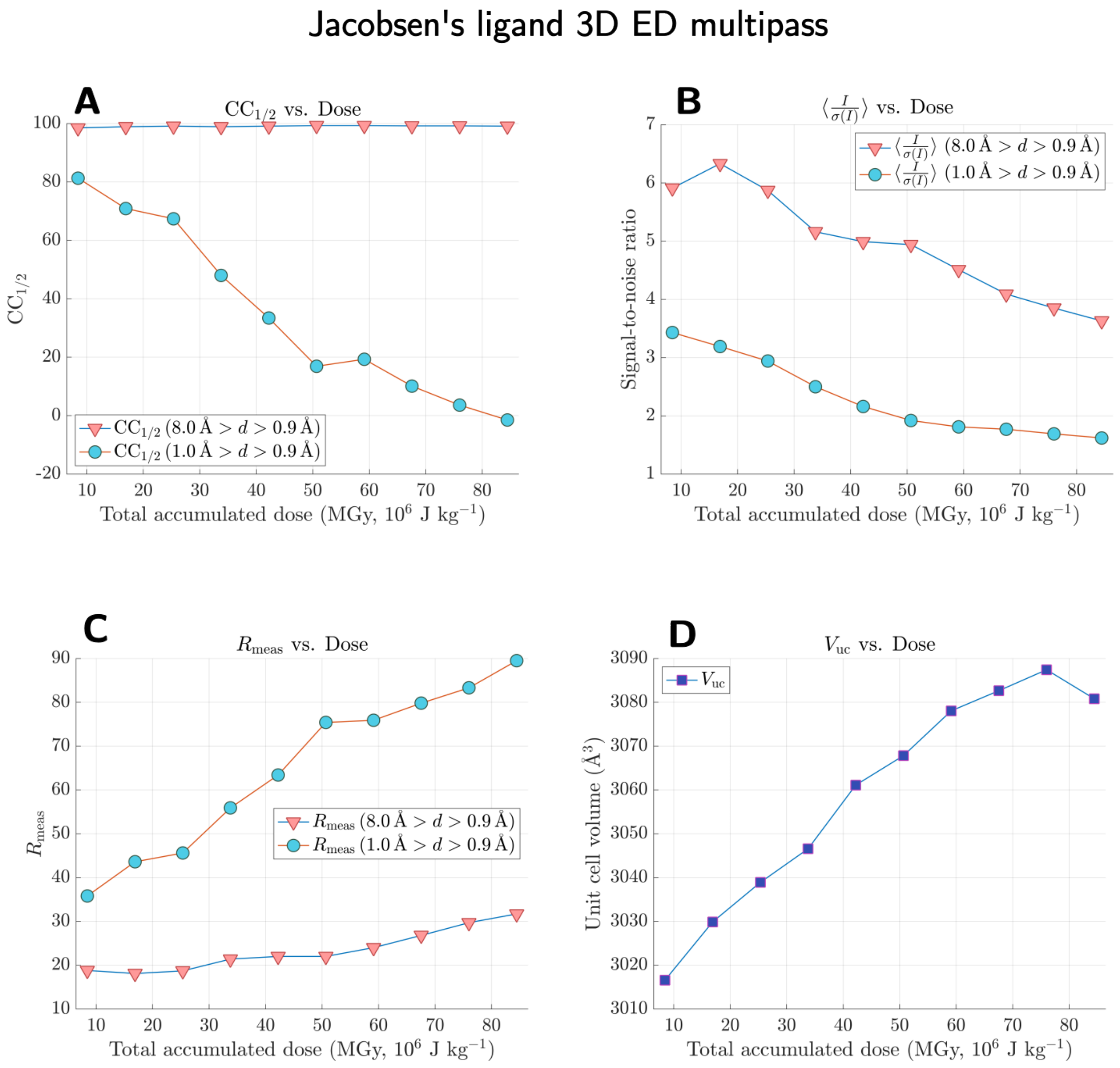

Figure 3.7: **Data reduction statistics for 10 consecutive 3D ED movies collected on a single crystal of Jacobsen's ligand at 100 K**, where each point represents a full continuous-rotation dataset. A fluence of approximately 2.3 e^{-}Å^{-2} was delivered per movie, which was converted to a substrate-specific dose of 8.4 MGy using the program RADDOSE-EM [26]. After 10 consecutive passes, the Jacobsen's ligand crystal has endured a total accumulated fluence of 23 e^{-}Å^{-2}, or 84 MGy. A slight improvement to a better value is seen between movies 1 and 2 for overall R_{meas} (C), accompanied by a more substantial improvement in $<I/\sigma(I)>$ (B). Although not exactly a smoking gun, this is consistent with lattice reorientation. Interestingly, unit cell volume—historically considered an unreliable metric—appears to expand very consistently in this case.

3.4 Radial Propagation of Amorphization

We then sought to explore whether 4D–STEM was sufficiently sensitive to visualize any effects arising from the asymmetric, localized delivery of incident fluence. Our initial foray into this area was inadvertent. Due to a consistent delay in the activation of the pre-specimen beam blanker, a single region of the Ni(dppf)Cl_2 nanocrystal—corresponding to the dwell point of the 15 nm FWHM probe in between consecutive scans—received an extra dose of electrons between the acquisition of each 4D–STEM dataset. Although the exact duration of this intercalary period is difficult to determine retroactively, a conservative estimate based on the sleep time in our multiscan script is approximately 200 ms. This created a highly localized "dead zone" in which diffraction signal was quickly extinguished, despite the simultaneous presence of strong Bragg reflections originating from CDZs distal to this region (e.g., 200 nm away). Corroborating evidence from concurrently acquired high-angle annular dark field (HAADF) images revealed a blot of contamination emerging at scan 30 which proceeded to darken in contrast throughout all subsequent scans. To our astonishment, the corresponding VDF images reconstructed from all Bragg reflections displayed a tide of amorphization radially propagating from this area, suggesting that the "dead zone" at the dwell point acts as a concentrated reservoir of reactive free radicals. With each consecutive scan, these destructive radicals diffused into areas of the lattice increasingly far removed from the original source, ablating all CDZs in their wake. Each time, their advances were thwarted by molecular bulwarks such as aromatic rings, which can temporarily arrest a cascade of further radiolytic reactions via several postulated quenching pathways [27, 28]. Nevertheless, since these mechanisms cannot quench propagating free radicals indefinitely, each consecutive 4D–STEM scan maps the outward progression of an expanding frontier of amorphization, representing a set of finite defenses steadily overwhelmed by fresh bursts of radiolysis.

Crucially, we then discovered that the rate of expansion also varies as a function of scattering angle. VDF images reconstructed from a series of progressively higher-resolution Bragg reflections—at 4.45 Å (Figure 3.23B, Supplementary Video S5), 2.94 Å (Figure 3.23C, Supplementary Video S6), and 2.22 Å (Figure 3.23D, Supplementary Video S7), respectively—unveiled that the radius of the growing impact crater was clearly larger in the latter two cases *for an identical point in the time series*. CDZs producing low-resolution Bragg peaks generally appear larger in size and stronger in diffracting power than their high-resolution counterparts. This is because these CDZs correspond to a crude level of long-range order present more uniformly within many regions of the lattice. Consequently, these CDZs tend to dominate the real-space signal in composite VDF images generated from all reflections. Therefore, this remarkable resolution-dependent effect is visible only when placing virtual apertures around individual peaks and is obscured when summing aggregate signal from groups of reflections. Our physical interpretation of this phenomenon is that a small vanguard of itinerant free radicals diffuses significantly farther than the frontier delineated by the composite VDF images—on the order of 50–100 nm—before being quenched. Although these species represent a minority of overall radicals produced, the weaker CDZs corresponding to high-resolution reflections require fewer radiolytic reactions to ablate, since these CDZs represent a granular level of long-range order present much more sporadically within the lattice. As a result, the extent to which the tide of amorphization appears to have progressed is strongly resolution-dependent, and the radius of the impact crater grows considerably when reconstructing VDF images from higher-resolution Bragg reflections.

We note that this phenomenon manifests only when the probe consistently delivers more fluence to one localized region of the illuminated crystal. If the dwell point of the probe were placed somewhere on the adjacent lacey carbon support—i.e., not directly on the surface of the crystal—smaller pockets of localized damage would stochastically distribute themselves throughout the lattice, preventing the formation of a singular impact crater. Furthermore, in compounds significantly more beam-sensitive than Ni(dppf)Cl_2, amorphization would likely have occurred far too rapidly for us to visualize on a scan-by-scan basis. Nevertheless, we successfully reproduced the radial propagation of amorphization in two related organometallic complexes—Pd(dppf)Cl_2 (Figure 3.29) and Pd(dcyf)Cl_2 (Figure 3.32)—suggesting that this is a property intrinsic to systems which undergo radiolytic decay.

An especially salient point illustrated by the corresponding sequence of HAADF images is that the gross morphology of the specimen stayed entirely intact, with virtually no changes in shape, size, or thickness apart from the accumulating contamination at the dwell point. Furthermore, each irradiated crystal remained completely stationary, definitively ruling out gross specimen movement as a plausible confounding variable. In other words, the total fluence applied in this study was far from catastrophic; no significant evidence of mass loss was observed. Given the seeming invariance of the crystal's real-space morphology, we were then confronted with lingering questions about the chemical identity of the substrate post-irradiation. Although 4D–STEM generates a wealth of insights relating to the beam-induced ablation of long-range order within the crystal lattice, we recognized at this point that diffraction alone could not provide a complete picture of the chemical effects of radiolytic damage. Inspired by Li and Egerton's analysis of cathodoluminescence decay in polycyclic aromatic hydrocarbons [29], we set out to briefly investigate whether electron energy-loss spectroscopy (EELS) could serve as a parallel metric for assessing beam-induced chemical destruction. In particular, aromaticity is known to produce an EELS resonance at an energy loss of ca. 6 eV, corresponding to the same π—π* electronic transition typically probed at the macroscopic level by ultraviolet-visible spectroscopy.

Gratifyingly, we successfully recorded EEL spectra displaying a clear peak in the 6 eV range for both dppf and Ni(dppf)Cl_2. (Since these compounds possess two types of aromatic moieties—the negatively charged cyclopentadienyl ligands and the neutral phenyl rings—this peak presumably represents an aggregate signal corresponding to both π—π* transitions, which we cannot distinguish without superior energy resolution.) Furthermore, our EEL spectra also indicated that a typical inelastic collision during irradiation of Ni(dppf)Cl_2 involves an energy loss of approximately 22 eV (Figure 3.8). To contextualize, this value is at least 4× higher than the homolytic bond dissociation free enthalpy (BDFE) of an average C—F bond (ca. 5 eV), generally considered one of the strongest bonds in organic chemistry. After the initial acquisition of an EEL spectrum from an individual nanocrystal (Figure 3.9), each specimen was continuously irradiated until the corresponding diffraction patterns had completely faded. For both compounds, the subsequent acquisition of another EEL spectrum revealed that the 6 eV π—π* peak remained intact (Figure 3.10), indicating that crystallographic destruction precedes chemical destruction in these species. Although it is unclear whether this progression of events will hold in nonaromatic compounds, we note that the recent development of low-loss HREELS in the infrared regime [30] provides an excellent range of spectroscopic handles (e.g., the decay of a C–H stretching mode) for assessing this.

In other words, upon irradiation by a 300 keV electron beam, no covalent bond in an organic molecule is safe. An average inelastic scattering event deposits more than enough kinetic energy to induce homolytic scission of any single bond. Why, then, is radiolytic damage in 3D electron crystallography not immediately cataclysmic? Any molecular crystal illuminated by a parallel electron beam likely enters a transient state characterized by constant "fission and recombination" of radical fragments produced by radiolytic cleavage of covalent bonds. In the solid state, most of these ephemeral open-shell species possess sufficient steric bulk such that they remain immobilized within the crystal lattice once formed. This level of spatial proximity facilitates radical recombination and subsequent regeneration of the damaged bonds. A select few bonds, however, present a more perilous outcome once cleaved. Scission of any bond involving hydrogen, for instance, generates a sterically unobtrusive and highly mobile H· radical, which can quickly diffuse away into the interstitial space of the unit cell and initiate a cascade of homolytic reactions elsewhere in the crystal lattice. If an itinerant H· radical goes on to abstract a proton (e.g. from a labile heteroatom—H bond involved in hydrogen bonding), H_2 gas is formed, which in X-ray diffraction is thought to accumulate within the lattice and induce unit cell expansion.

3.5 Substrate Scope and Experimental Methods

This section serves as a roadmap for all substrates investigated via multipass 4D–STEM and 3D ED experiments (Figure 3.11). Unless otherwise specified, all 4D–STEM experiments were conducted using 300 mesh Au grids with an ultrathin ($\leq$ 3 nm) carbon film stretched over a lacey

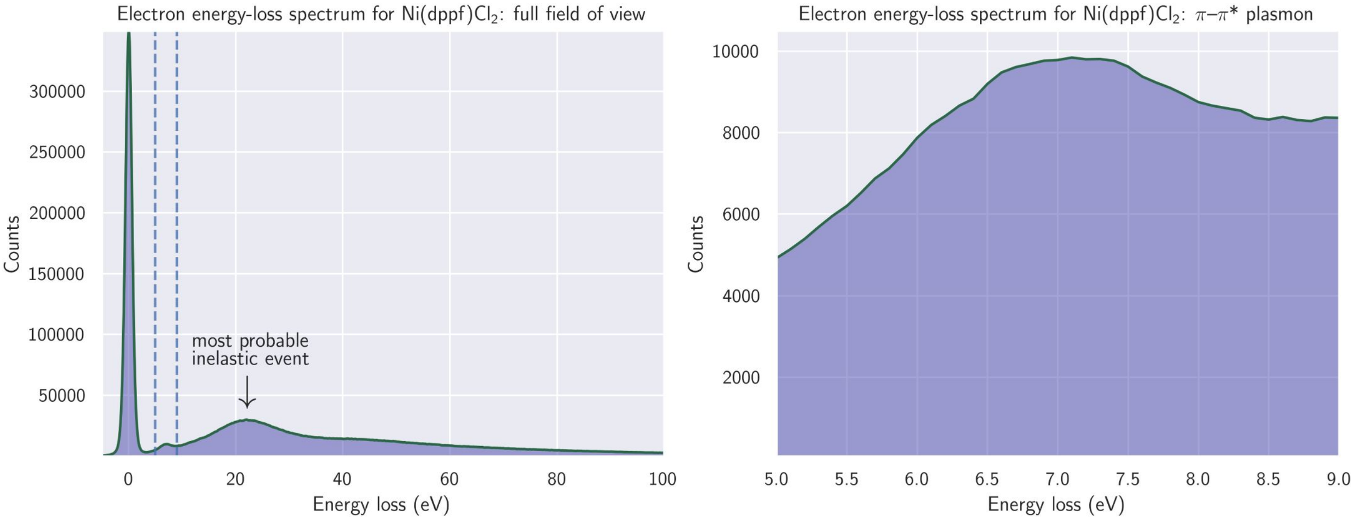

Figure 3.8: **Electron energy-loss spectrum acquired from a single crystal of Ni(dppf)Cl$_2$, demonstrating that the most probable inelastic scattering event involves an energy loss of 22 eV.** Dashed vertical lines represent the π—π* plasmon corresponding to the presence of aromaticity. Spectra were acquired using a JEOL JEM–2100F TEM equipped with a Gatan Quantum SE operating at an accelerating voltage of 200 kV.

carbon support (Ted Pella product no. 01824G).

3.5.1 Tecnai F30 Specifications

All 3D ED experiments were conducted at an accelerating voltage of 300 kV on an FEI Tecnai F30 transmission electron microscope (TEM) located in Boyer Hall at the UCLA–DOE Institute for Genomics and Proteomics. This particular Tecnai F30 is equipped with a Schottky-type field emission gun (XFEG) and a bottom-mount TVIPS TemCam-XF416 camera. Generally, the workflow for 3D ED involved the dispersion of a nanocrystalline powder onto a lacey carbon grid, subsequent insertion of the grid into the TEM, and then a prolonged search to find well-diffracting samples. After a suitable single crystal was identified, usually in overfocused diffraction (i.e., shadow imaging) mode, a 1 μm postspecimen selected area aperture was inserted to isolate the specimen of interest. Next, the crystal was exposed to parallel illumination and unidirectionally rotated at an angular speed of roughly 0.3 degrees per second. During this process, diffraction

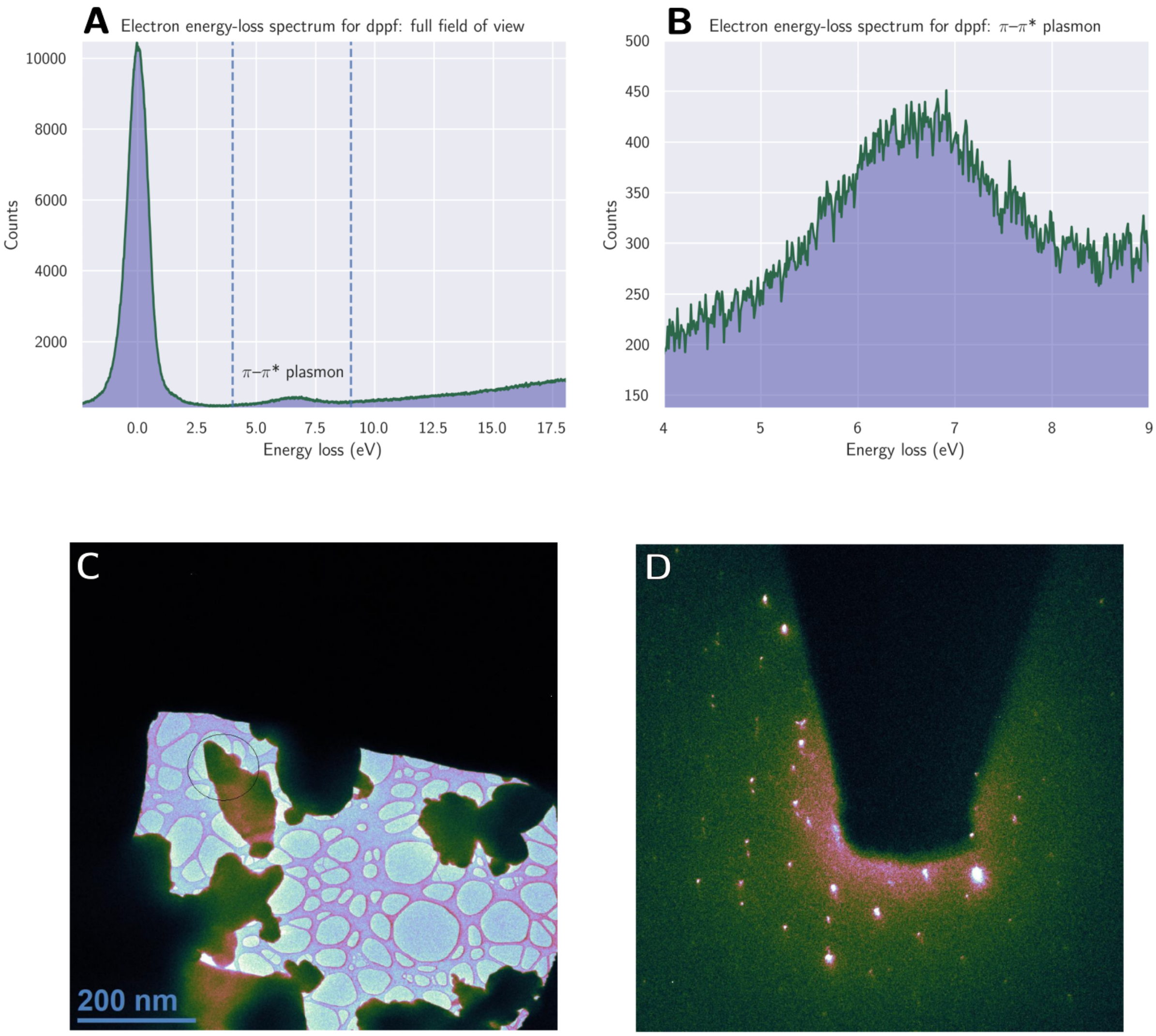

Figure 3.9: **Electron energy-loss spectrum (A, B) and selected-area diffraction pattern (D) acquired from a single crystal of dppf (C) before sustained irradiation.** π—π* plasmon is visible at 6.5 eV energy loss, with an estimated peak width of around 2.3 eV. This dispersion is fairly broad, and superior energy resolution would likely split this peak into several subsidiary maxima representing the different energy levels of the π—π* transitions in the cyclopentadienyl rings vs. the phenyl rings. Spectra were acquired using an FEI Tecnai F20 TEM equipped with a Gatan Imaging Filter (GIF) operating at an accelerating voltage of 200 kV. Unmonochromated, the energy resolution of EEL spectra acquired on this instrument is 500 meV, which is fairly coarse.

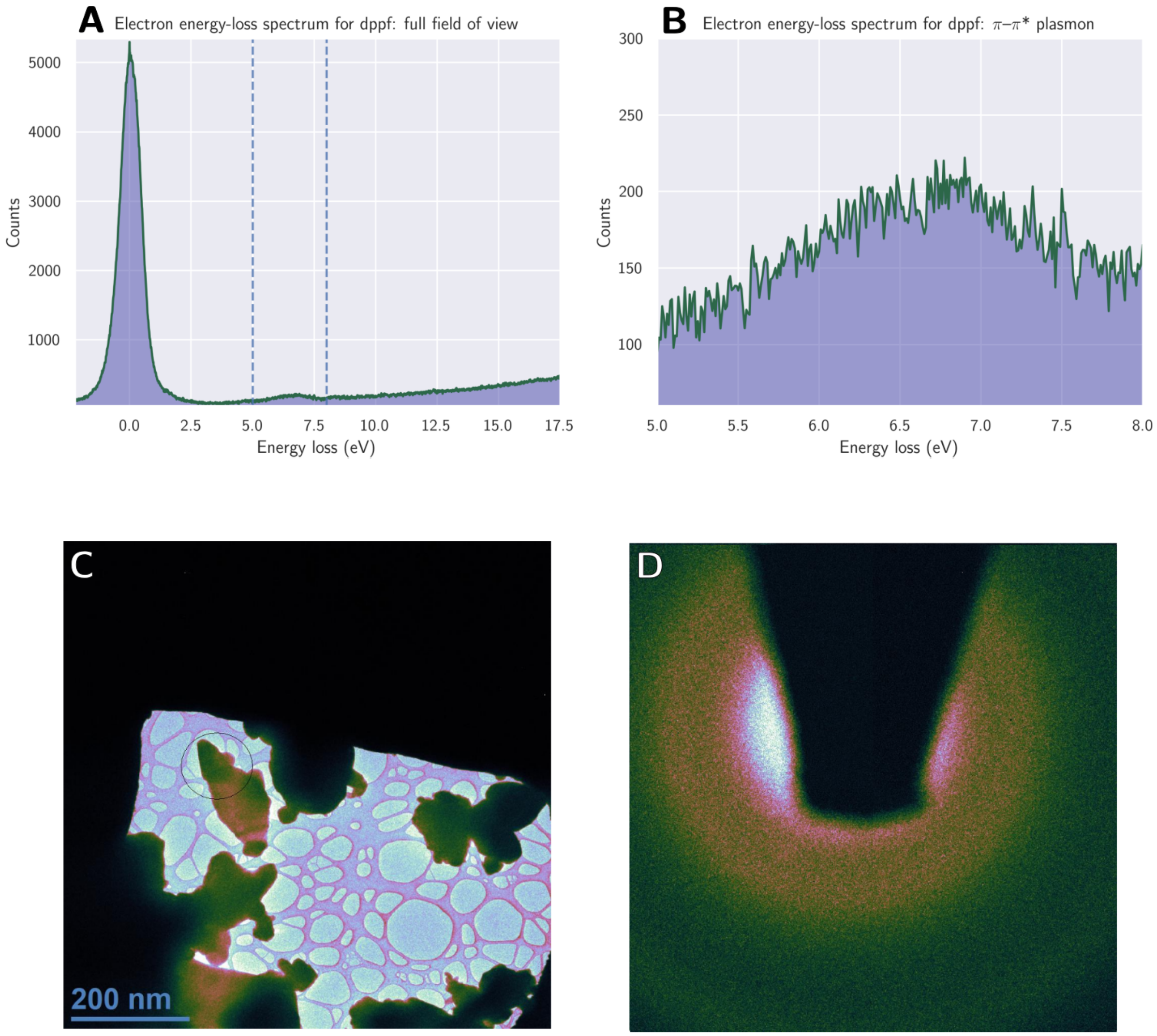

Figure 3.10: **Electron energy-loss spectrum (A, B) and selected-area diffraction pattern (D) acquired from a single crystal of dppf (C) after sustained irradiation for 10 minutes at spot size 6, corresponding to an estimated delivered fluence of at least 200 $e^{-}\text{Å}^{-2}$.** Although the diffraction pattern has disappeared—indicating complete loss of crystallinity—the π—π^* plasmon remains intact, indicating that crystallographic destruction precedes chemical destruction in this species. Interestingly, the π—π^* peak is somewhat shifted and narrowed compared to the pre-irradiation spectrum, now appearing at 6.3 eV energy loss with a peak with of 2 eV. Without superior energy resolution, chemical interpretation of this shift is premature, but an intriguing question to explore involves whether the negatively charged Cp rings decay at different rates than the neutral Ph rings. Spectra were acquired using an FEI Tecnai F20 TEM equipped with a Gatan Imaging Filter (GIF) operating at an accelerating voltage of 200 kV; since the battery attached to the screen ammeter was depleted, a direct measurement of the delivered fluence was not possible.

patterns were continuously acquired throughout the angular wedge sampled. Typical parameters involved 3-second exposures over an angular wedge of 100 degrees for a single movie.

3.5.2 Organic and Biomolecular Compounds

3.5.2.1 (+)–Biotin

(+)–Biotin (Sigma–Aldrich) is a visibly microcrystalline white to off-white powder. Since the distribution of well-diffracting nanocrystals by simple shake-n-bake was subpar, (+)–biotin was recrystallized by dissolving 10 mg in 5 mL boiling nanopure deionized water and allowing the resultant colorless solution to gradually cool to RT. Showers of high-quality, colorless single crystals precipitated after 10 minutes; the resultant suspension was diluted 10× with ethanol and dropcast onto lacey carbon grids.

3.5.2.2 EYNNQNNFV

EYNNQNNFV (GenScript) is an amorphous white powder that was recrystallized and dropcast onto lacey carbon grids as previously described [31] by Calina Glynn.

3.5.2.3 *Trans*-1,2-bis(*n*-pyridyl)ethylene/4,6-dichlororesorcinol cocrystal

Trans-1,2-bis(*n*-pyridyl)ethylene/4,6-dichlororesorcinol (abbreviated as BPE/dichlororesorcinol) is a pink microcrystalline powder. Cocrystals were synthesized as previously described [32] by Krzysztof Konieczny, crushed between siliconized glass coverslips, and gently applied onto lacey carbon grids.

3.5.2.4 (*S*,*S*)–Jacobsen's ligand

(*S*,*S*)–Jacobsen's ligand (Sigma–Aldrich) is a visibly microcrystalline pale yellow powder. Since the distribution of well-diffracting nanocrystals by simple shake-n-bake was mediocre, (*S*,*S*)–

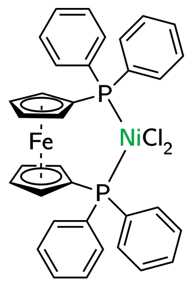

Ni(dppf)Cl$_2$

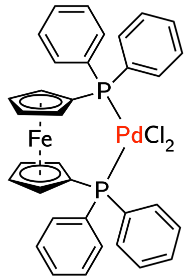

Pd(dppf)Cl$_2$

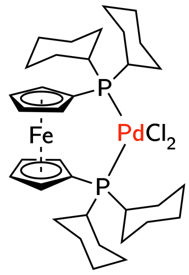

Pd(dcyf)Cl$_2$

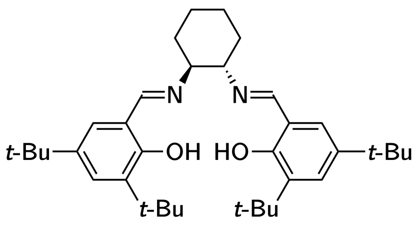

(*S*,*S*)-Jacobsen's ligand

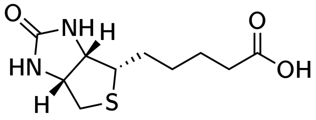

(+)-biotin

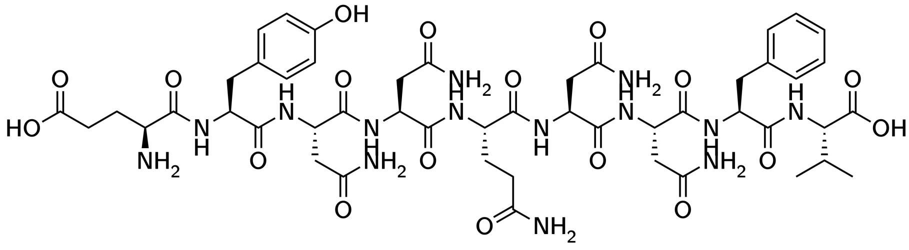

EYNNQNNFV

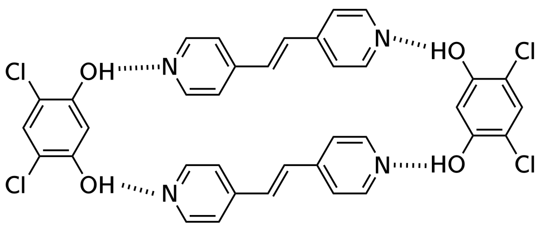

BPE/dichlororesorcinol

Figure 3.11: **Schematics of all molecules within the 4D–STEM radiolytic damage substrate scope.**

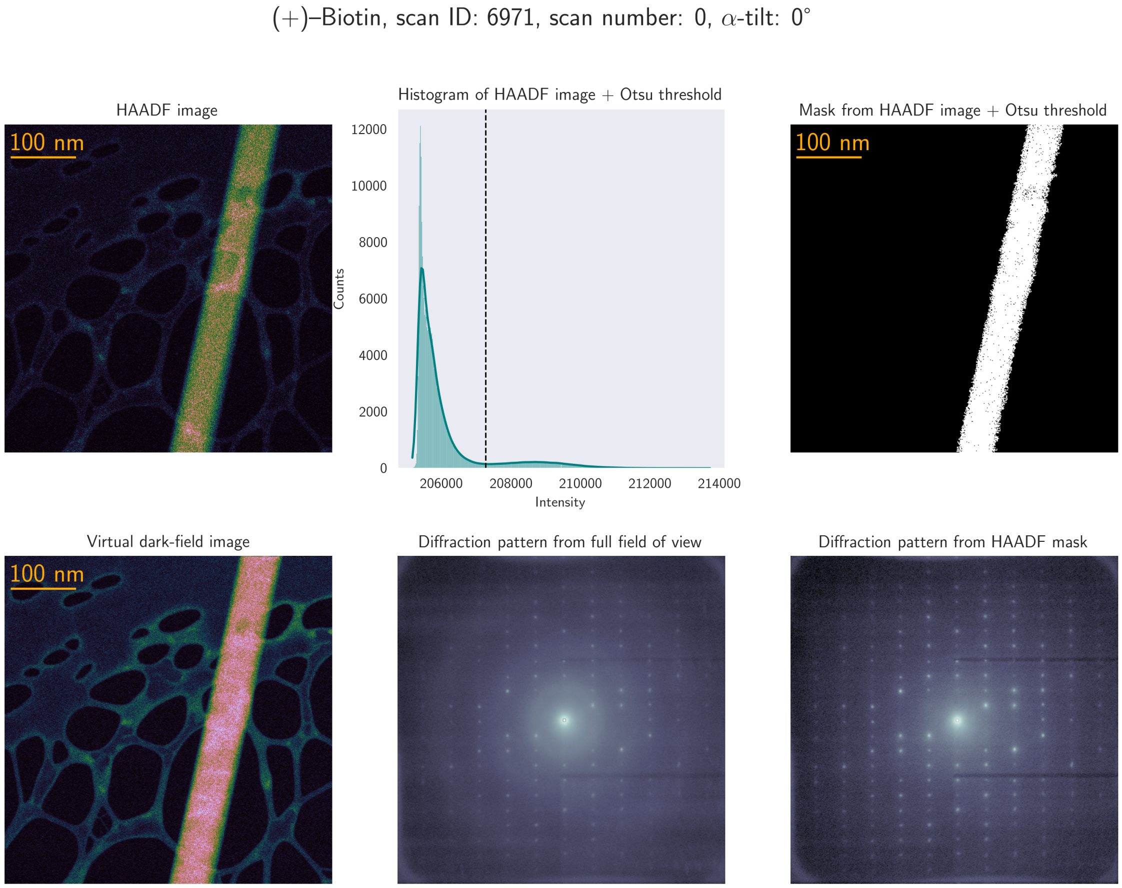

Figure 3.12: **VDF image, simultaneously acquired HAADF image, and corresponding diffraction patterns for the first representative 4D–STEM scan in the 40 kx (+)–biotin multiscan dataset.** Since the target crystal was sufficiently isolated, applying the Otsu threshold to the HAADF image worked nicely, and the resultant binary mask was used to generate the diffraction pattern in the bottom right.

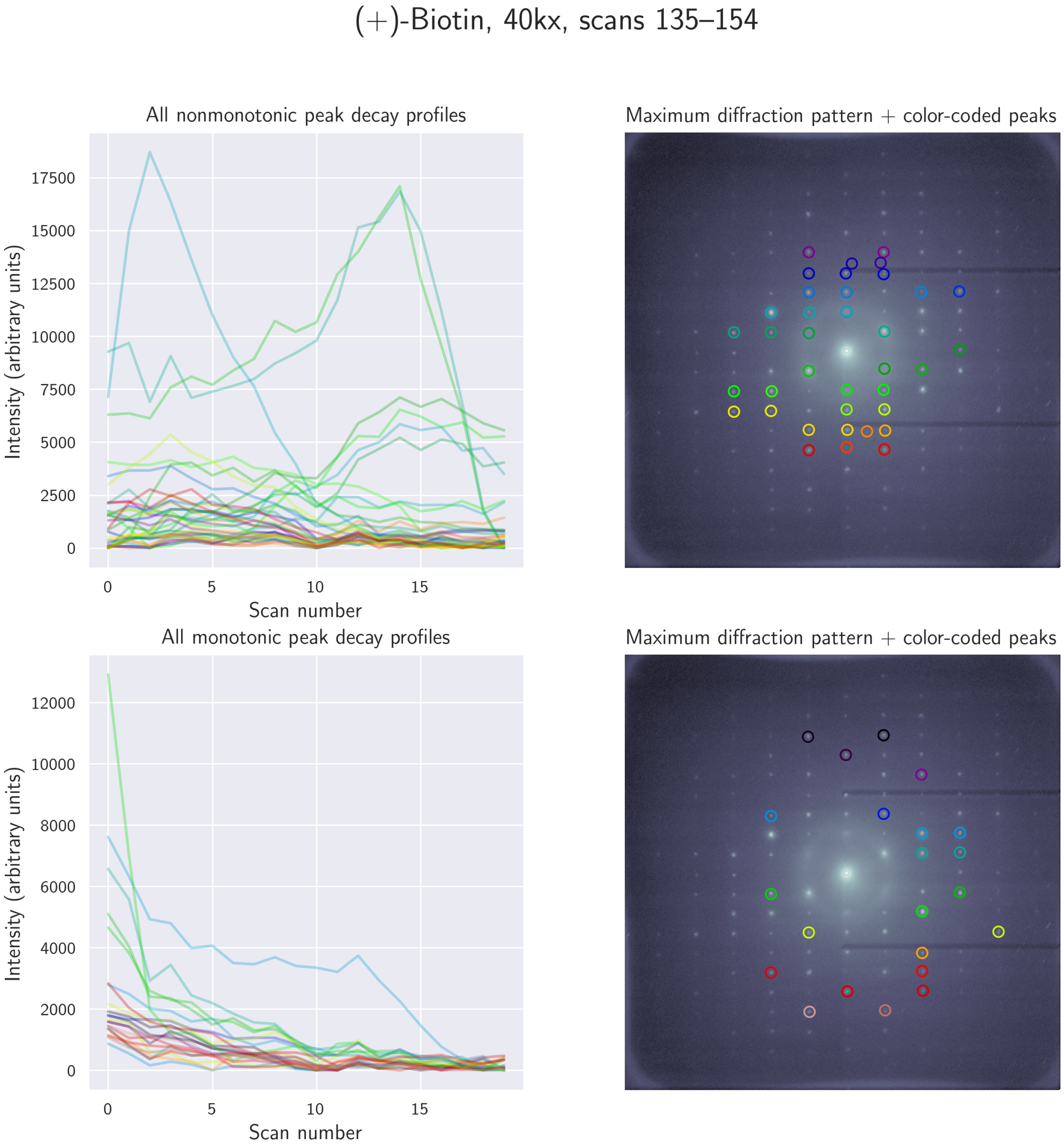

Figure 3.13: **Decay profiles of Bragg peak intensities in the 40 kx (+)–biotin multiscan dataset** whose unnormalized maximum values exceeded a cutoff of 3000, clustered by monotonic (22 clearly identified reflections) vs. nonmonotonic (37 clearly identified reflections) decay. 62% of overall Bragg reflections decay nonmonotonically. Without accounting for overlap between adjacent probe positions, the estimated fluence delivered was 0.15 $e^{-}\text{Å}^{-2}$ per scan.

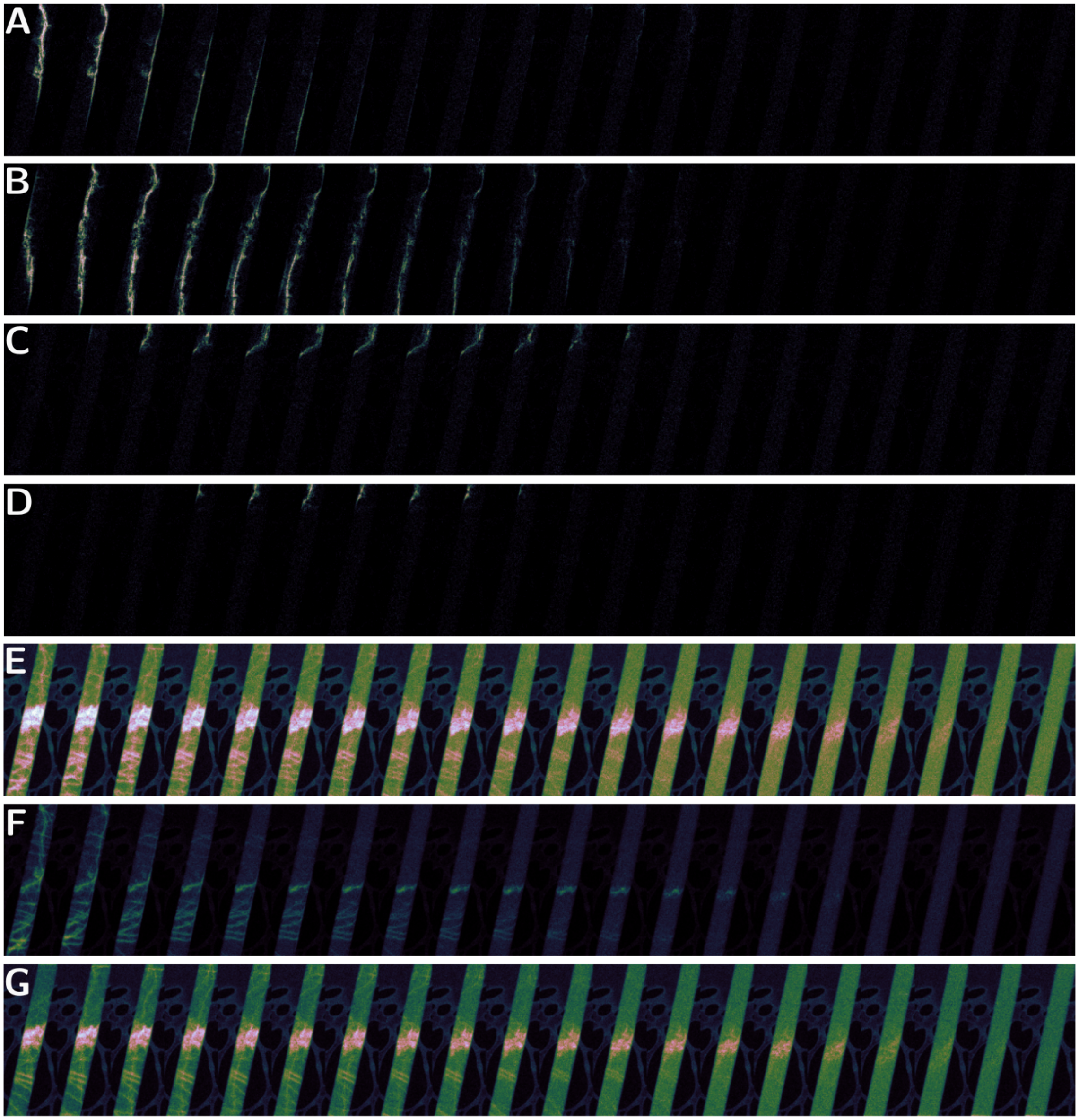

Figure 3.14: **VDF images visualizing the spatial decay of CDZs in the 40 kx (+)–biotin multiscan dataset**, with a sampling interval of 1 4D–STEM scan per displayed image. A: VDF images reconstructed by placing a single virtual aperture around a 2.36 Å resolution Bragg peak. B: VDF images reconstructed by placing a single virtual aperture around the Friedel mate of the reflection isolated in A. C: VDF images reconstructed by placing a single virtual aperture around a 2.61 Å resolution Bragg peak. D: VDF images reconstructed by placing a single virtual aperture around the Friedel mate of the reflection isolated in C. E: VDF images reconstructed by placing virtual apertures around all 59 clearly identified Bragg peaks from Figure 3.13. F: VDF images reconstructed by placing virtual apertures around all 22 clearly identified reflections from Figure 3.13 which underwent monotonic decay. G: VDF images reconstructed by placing virtual apertures around all 37 clearly identified reflections from Figure 3.13 which underwent nonmonotonic decay.

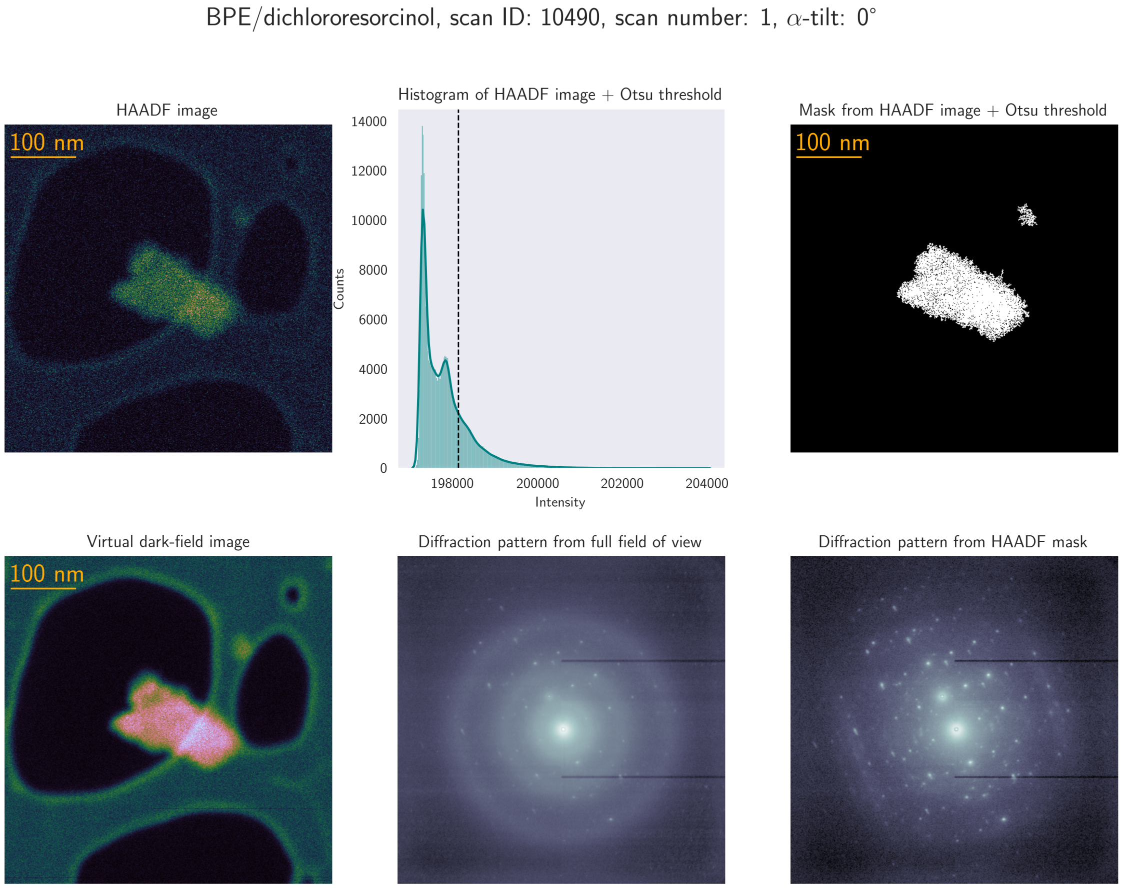

Figure 3.15: **VDF image, simultaneously acquired HAADF image, and corresponding diffraction patterns for the first representative 4D–STEM scan in the 40 kx BPE/dichlororesorcinol multiscan dataset.** Since the target crystal was sufficiently isolated, applying the Otsu threshold to the HAADF image worked nicely, and the resultant binary mask was used to generate the diffraction pattern in the bottom right. Unfortunately this specimen was suboptimally defocused, leading to a blurry image; reconstructed CDZs did not show sharp contrast.

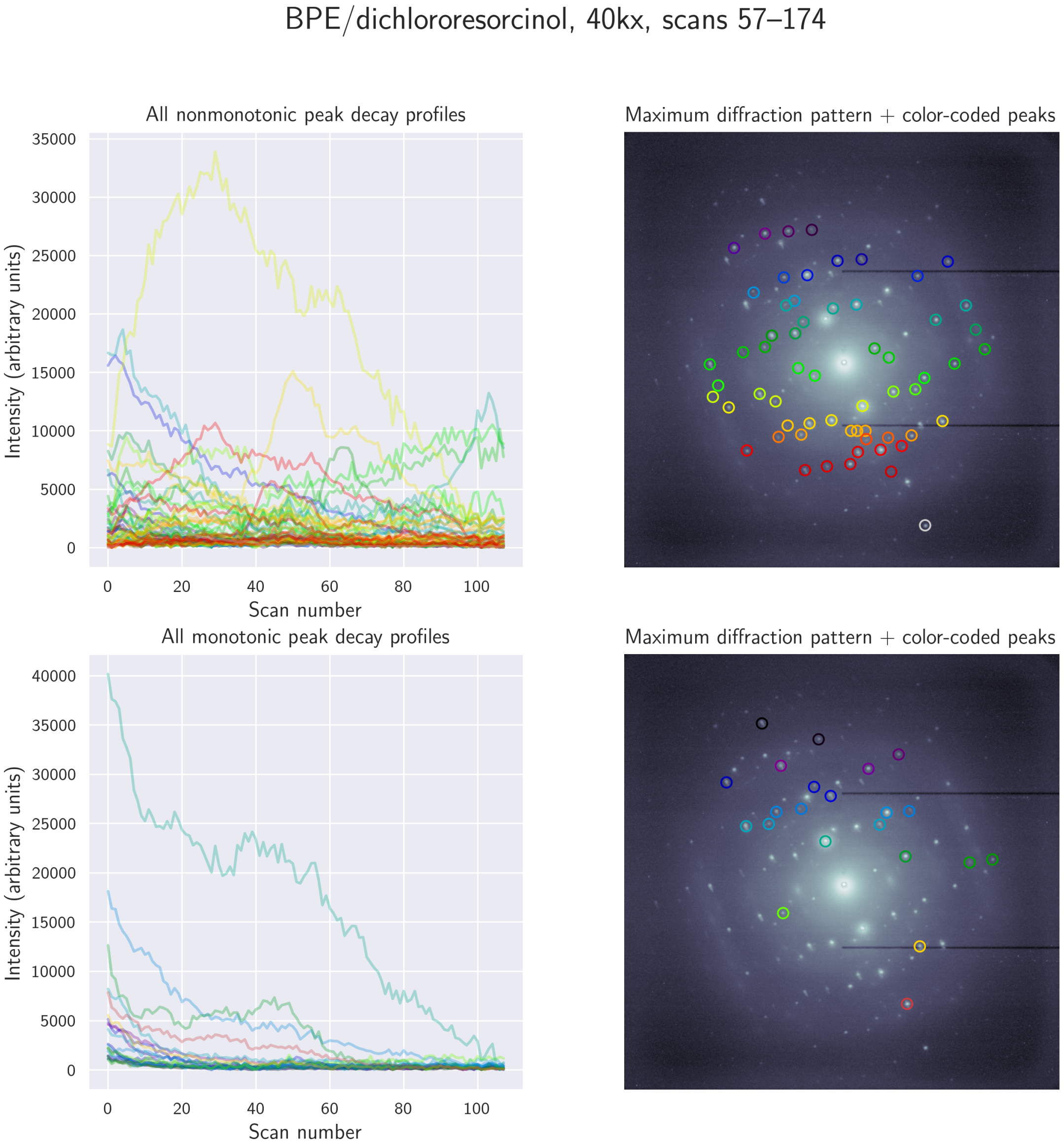

Figure 3.16: **Decay profiles of Bragg peak intensities in the 40 kx BPE/dichlororesorcinol multiscan dataset** whose unnormalized maximum values exceeded a cutoff of 2500, clustered by monotonic (22 clearly identified reflections) vs. nonmonotonic (60 clearly identified reflections) decay. 73% of overall Bragg reflections decay nonmonotonically. Without accounting for overlap between adjacent probe positions, the estimated fluence delivered was 0.15 $e^{-}\text{Å}^{-2}$ per scan.

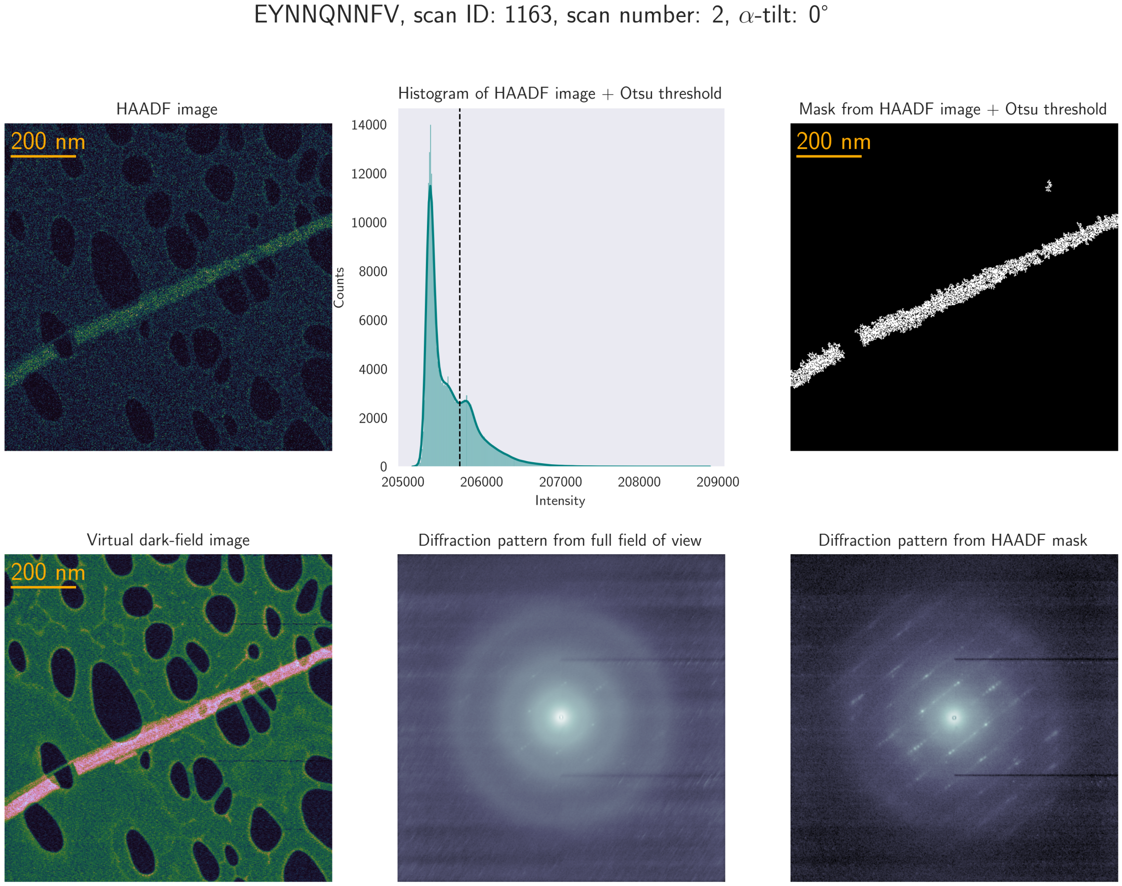

Figure 3.17: **VDF image, simultaneously acquired HAADF image, and corresponding diffraction patterns for the first representative 4D–STEM scan in the 40 kx EYNNQNNFV multiscan dataset.** EYNNQNNFV nanocrystals exhibit strong orientation bias. As a result, diffraction patterns acquired at 0 degrees tend to overwhelmingly sample the long (31.56 Å) *c* parameter, leading to streaky Bragg peaks difficult to resolve at this camera length. Placing individual virtual apertures around these streaks did not yield clearly defined CDZs in the corresponding VDF images, so this sample was suboptimal for 4D–STEM. Furthermore, the thickness contrast in the simultaneously recorded HAADF images was only slightly stronger than the lacey carbon support, suggesting that the EYNNQNNFV nanocrystals were probably too thin to generate sufficiently robust signal to reconstruct a decent VDF image. This also led to thresholding issues when generating the HAADF mask; the Otsu threshold required constant tweaking from scan to scan, generally by a factor of 1.1–1.2. Without accounting for overlap between adjacent probe positions, the estimated fluence delivered was 0.15 e^{-}Å^{-2} per scan.

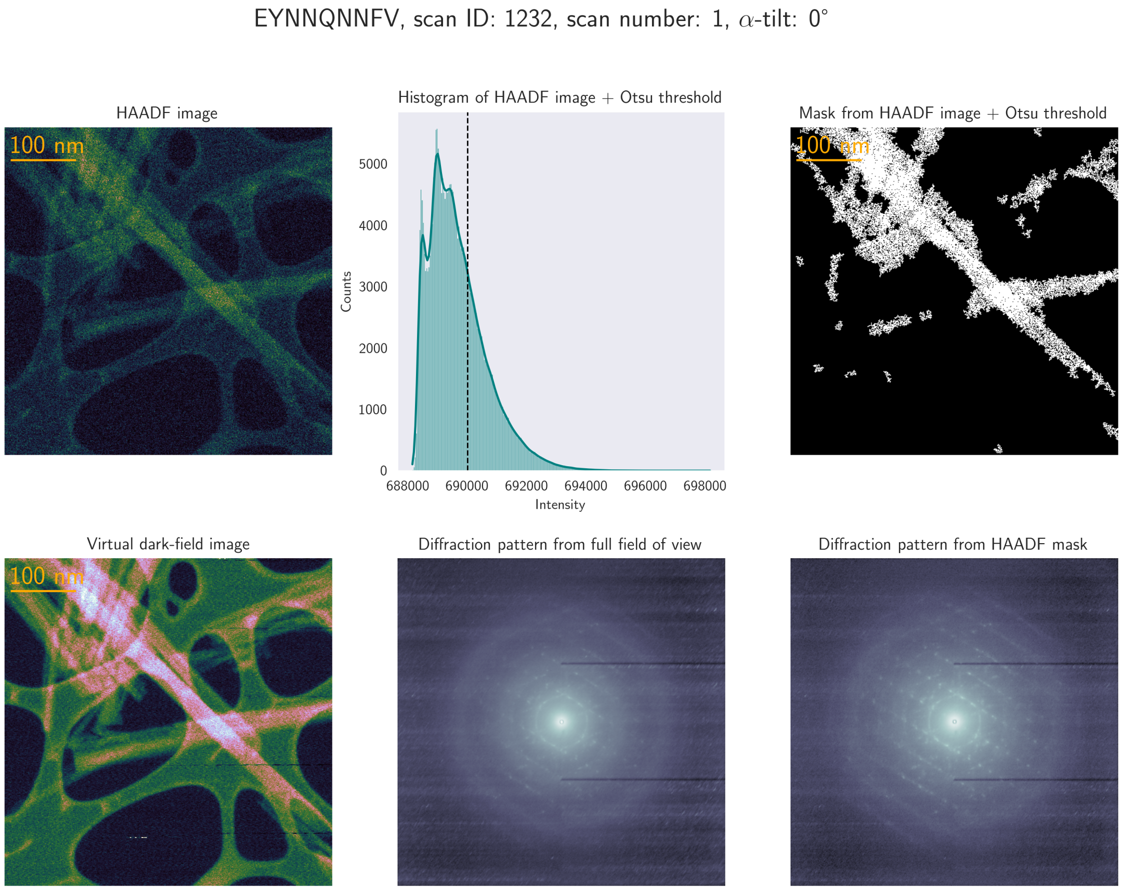

Figure 3.18: **VDF image, simultaneously acquired HAADF image, and corresponding diffraction patterns for the first representative 4D–STEM scan in the 80 kx EYNNQNNFV multiscan dataset.** All single crystals within this conglomerate decay at roughly the same rate.

Jacobsen's ligand was recrystallized by dissolving 10 mg in 3 mL 2:1 dichloromethane:ethanol and allowing the resultant yellow solution to slowly evaporate in a loosely sealed scintillation vial. High-quality, bright yellow single crystals grew in 24 hours. These crystals were crushed between siliconized glass coverslips and gently applied onto lacey carbon grids.

3.5.3 Organometallic Complexes

Three organometallic complexes, based on either a 1,1'-*bis*(diphenylphosphino)ferrocene (dppf) or 1,1'-*bis*(dicyclohexylphosphino)ferrocene (dcyf) scaffold, were surveyed by 4D–STEM. These molecules were selected based on their modularity, commercial availability, and broad relevance to synthesis and catalysis.

3.5.3.1 Ni(dppf)Cl_2

Ni(dppf)Cl_2 (Sigma–Aldrich) is a visibly microcrystalline, dark green iridescent powder. 10 mg of this compound was crushed between siliconized glass coverslips and gently applied to a lacey carbon grid. No formal recrystallization was necessary.

3.5.3.2 Pd(dppf)Cl_2 and Pd(dcyf)Cl_2

Pd(dppf)Cl_2 and Pd(dcyf)Cl_2 (Sigma–Aldrich) are visibly microcrystalline, reddish-orange iridescent powders. 10 mg of each compound was crushed between siliconized glass coverslips and gently applied to a lacey carbon grid. No formal recrystallization was necessary.

Two sets of multipass 4D–STEM data were collected on both these substrates: two at 40 kx STEM magnification and two at 80 kx. Due to pressing time constraints during this particular session, these experiments utilized a relatively high incident probe current (80 pA). Under these conditions, the total fluence delivered per probe position was estimated at around 3 $e^{-}\text{Å}^{-2}$. We then set out to investigate whether beam-induced lattice reorientation varies as a function of the dose absorbed by the specimen. By solely increasing the STEM magnification—i.e., without

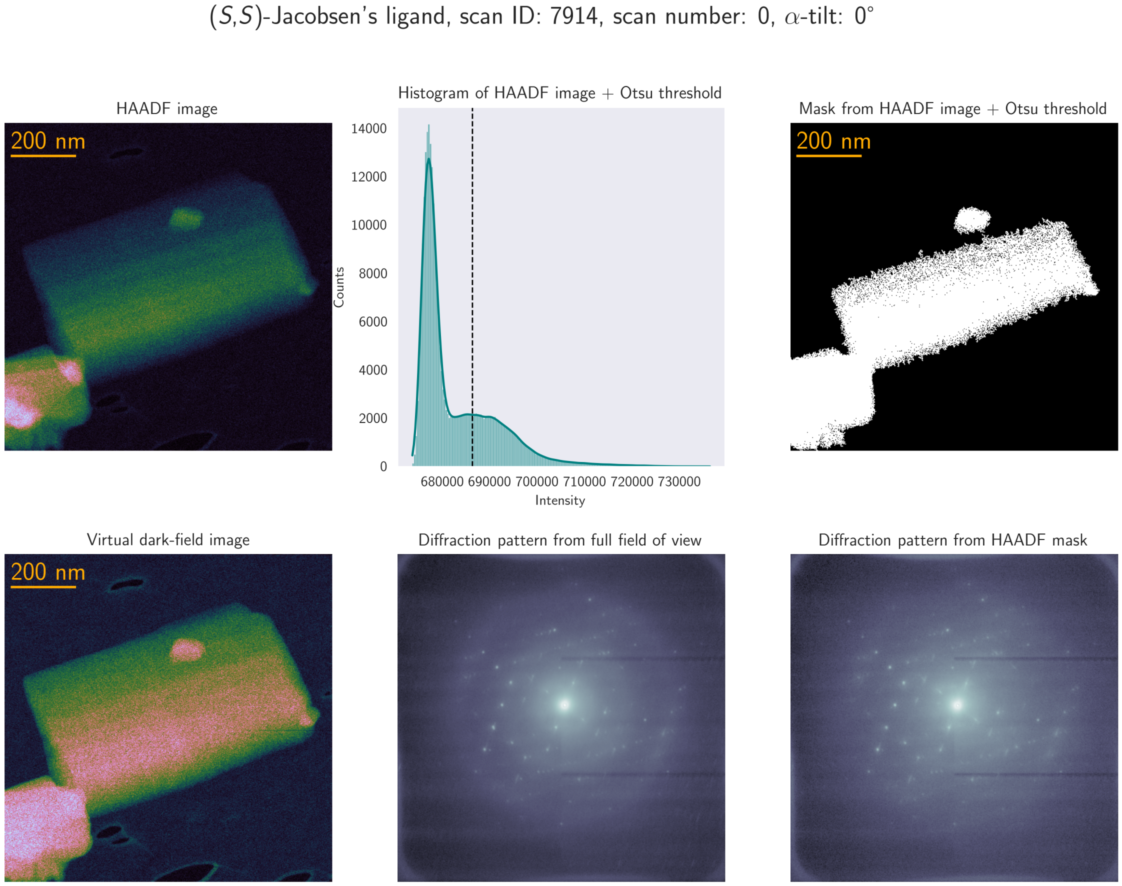

Figure 3.19: **VDF image, simultaneously acquired HAADF image, and corresponding diffraction patterns for the first representative 4D–STEM scan in the 40 kx (*S*,*S*)–Jacobsen's ligand multiscan dataset.**

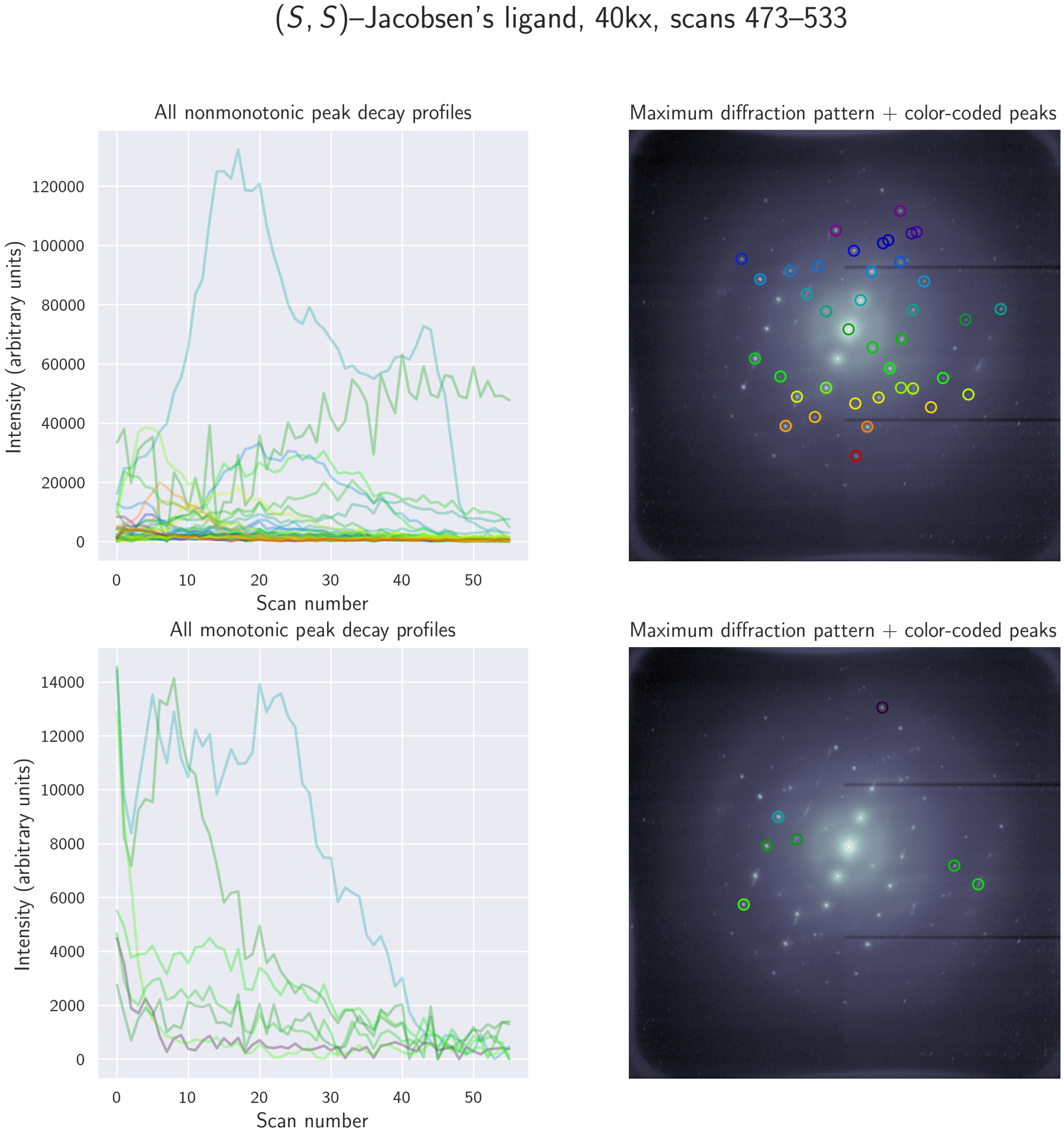

Figure 3.20: **Decay profiles of Bragg peak intensities in the 40 kx (S, S)–Jacobsen's ligand multiscan dataset** whose unnormalized maximum values exceeded a cutoff of 7000, clustered by monotonic (7 clearly identified reflections) vs. nonmonotonic (39 clearly identified reflections) decay. 82% of overall Bragg reflections decay nonmonotonically. The two strongest peaks identified as monotonic are spurious as well, since they clearly fluctuate nonmonotonically; this is because the clustering code looks for whether or not the maximum intensity for a given Bragg reflection is observed during the first scan. Without accounting for overlap between adjacent probe positions, the estimated fluence delivered was 0.15 $e^{-}\text{Å}^{-2}$ per scan.

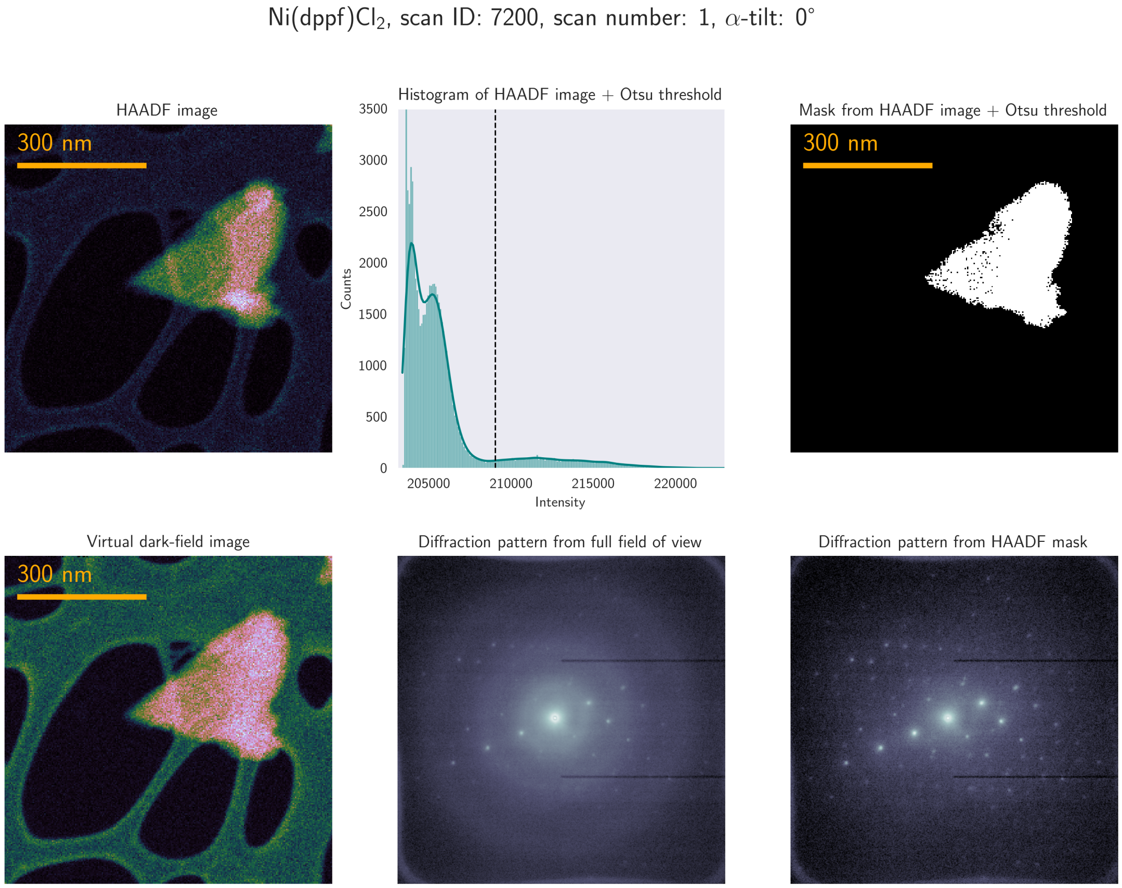

Figure 3.21: **VDF image, simultaneously acquired HAADF image, and corresponding diffraction patterns for the first representative 4D–STEM scan in the 40 kx Ni(dppf)Cl$_2$ multiscan dataset.** Since the target crystal was sufficiently isolated, applying the Otsu threshold to the HAADF image worked nicely, and the resultant binary mask was used to generate the diffraction pattern in the bottom right.

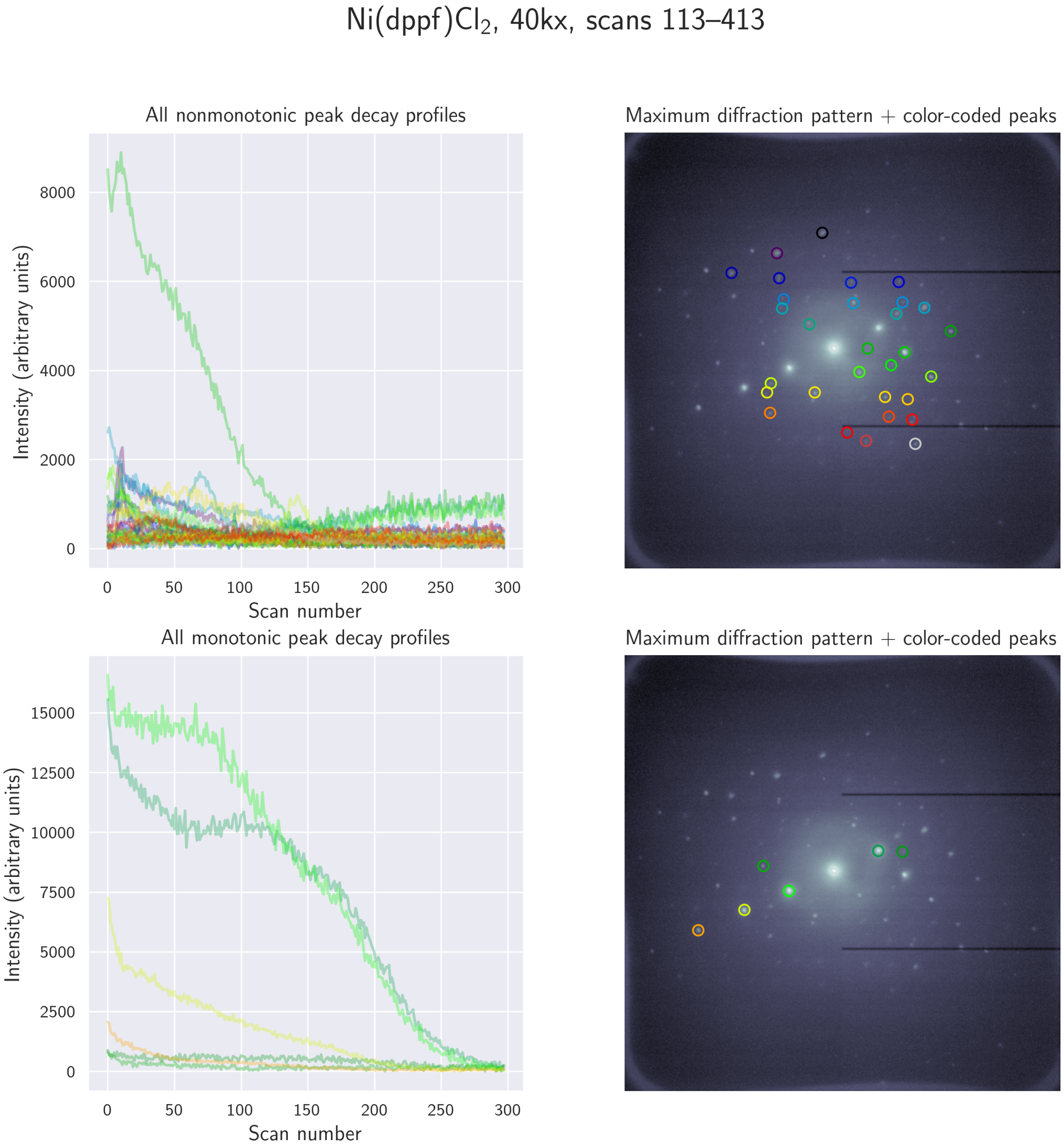

Figure 3.22: **Decay profiles of Bragg peak intensities in the 40 kx Ni(dppf)Cl_2 multiscan dataset** whose unnormalized maximum values exceeded a cutoff of 1600, clustered by monotonic (6 clearly identified reflections) vs. nonmonotonic (30 clearly identified reflections) decay. 83% of overall Bragg reflections decay nonmonotonically. Without accounting for overlap between adjacent probe positions, the estimated fluence delivered was 0.3 $e^{-}Å^{-2}$ per scan.

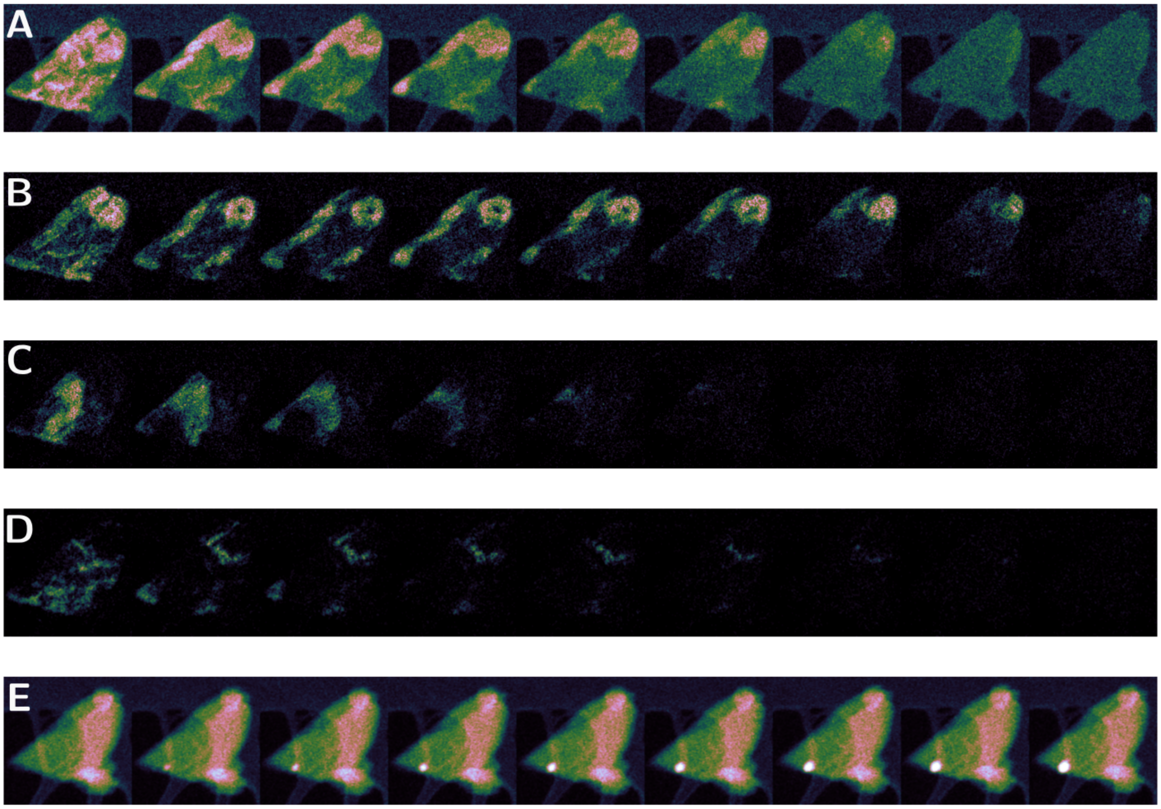

Figure 3.23: **VDF images visualizing the radial propagation of the tide of amorphization in the 40 kx Ni(dppf)Cl$_2$ multiscan dataset**, with a sampling interval of 30 4D–STEM scans per displayed image. A: VDF images reconstructed by placing virtual apertures around all 36 clearly identified Bragg peaks from Figure 3.22. B: VDF images reconstructed by placing a single virtual aperture around one of the strongest, lowest-resolution Bragg peaks ($d = 4.45$ Å). Impact crater is notably more conspicuous than in A. C: VDF images reconstructed by placing a single virtual aperture around a weaker, higher-resolution Bragg peak ($d = 2.94$ Å). D: VDF images reconstructed by placing a single virtual aperture around another weaker, higher-resolution Bragg peak ($d = 2.22$ Å). In both C and D, the frontier of amorphization has clearly propagated farther into the lattice than in either A or B. E: Simultaneously acquired HAADF images.

altering the semiconvergence angle, the incident beam current, or the dimensions of the scan—an identical number of probe positions (e.g., 256×256) is now partitioned across a smaller field of view. This leads to a 4× increase in total accumulated fluence for every corresponding 2× increase in magnification, causing the crystal to absorb a significantly higher dose. Generally, we observed that the rate of radiolytic decay—as well as the corresponding degree of beam-induced lattice reorientation—was around 3.5 × faster for the 80 kx datasets relative to the 4x datasets. Some of this variation from 4× is likely rationalized by mismatches between the FWHM of the probe and the corresponding real-space step size, leading either to oversampling (i.e., overlap between consecutive probe positions) or undersampling (i.e., separation between consecutive probe positions).

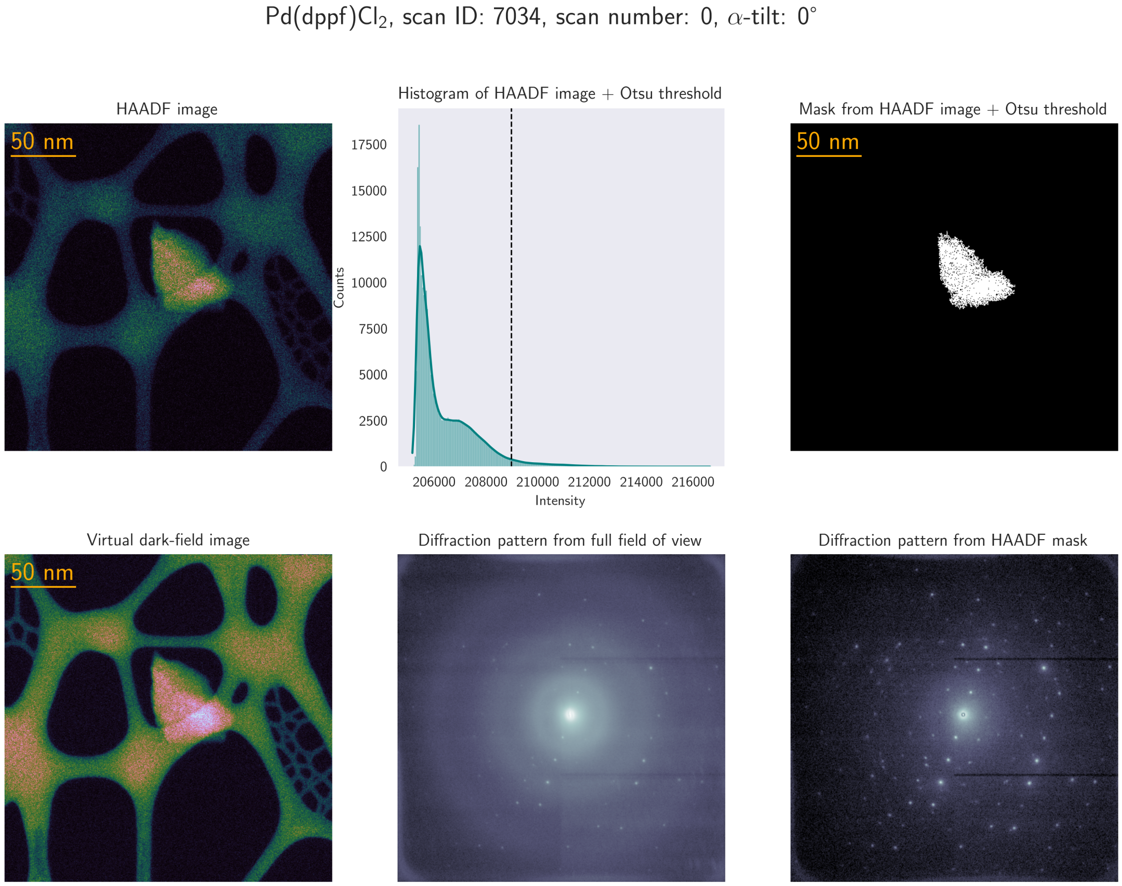

Figure 3.24: **VDF image, simultaneously acquired HAADF image, and corresponding diffraction patterns for the first representative 4D–STEM scan in the 80 kx Pd(dcyf)Cl$_2$ multiscan dataset.** Since the target crystal was sufficiently isolated, applying the Otsu threshold to the HAADF image worked nicely, and the resultant binary mask was used to generate the diffraction pattern in the bottom right.

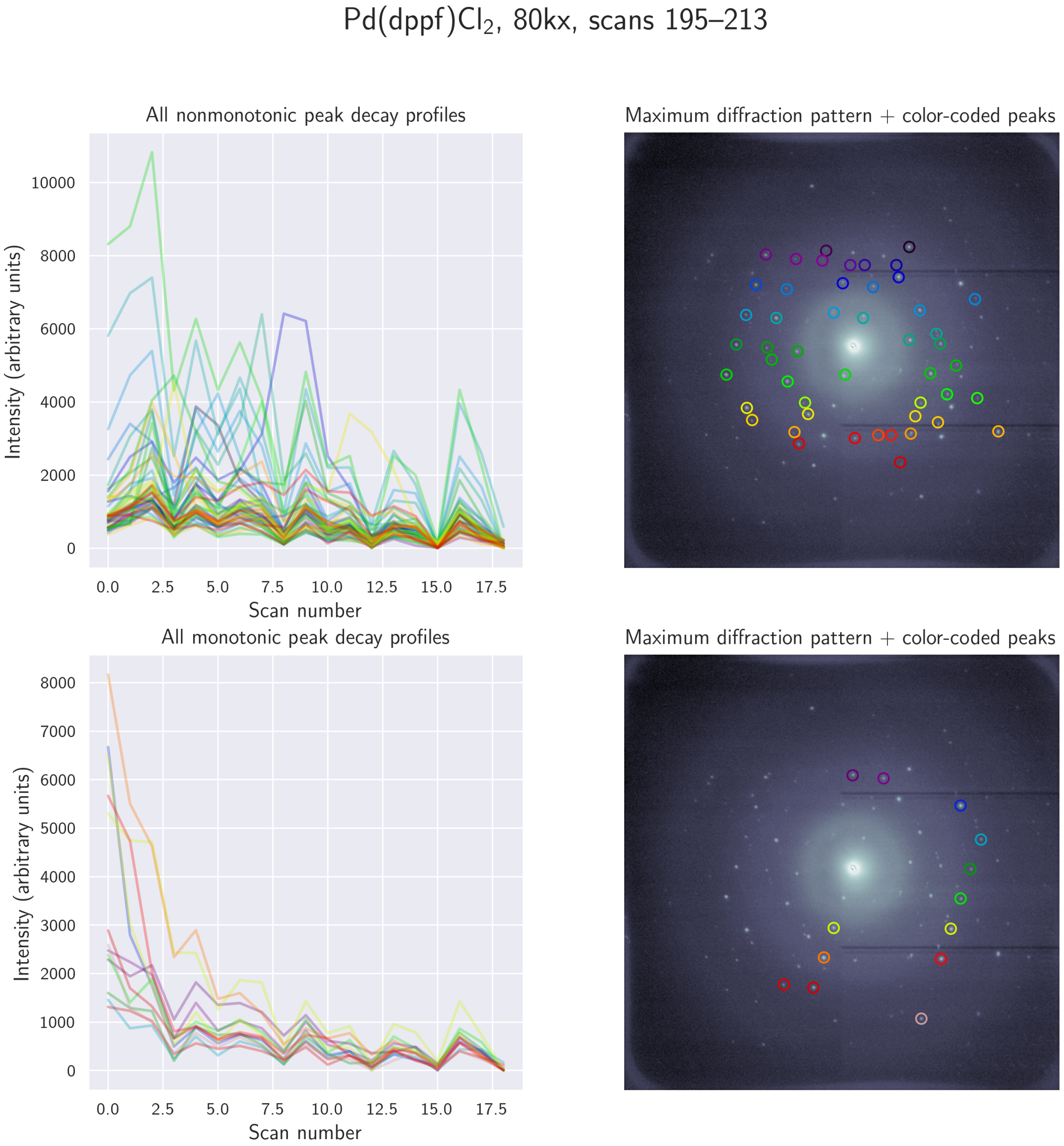

Figure 3.25: **Decay profiles of Bragg peak intensities in the 80 kx Pd(dppf)Cl$_2$ multiscan dataset** whose unnormalized maximum values exceeded a cutoff of 2300, clustered by monotonic (13 clearly identified reflections) vs. nonmonotonic (48 clearly identified reflections) decay. 78% of overall Bragg reflections decay nonmonotonically. Without accounting for overlap between adjacent probe positions, the estimated fluence delivered was 3 $e^{-}\text{Å}^{-2}$ per scan.

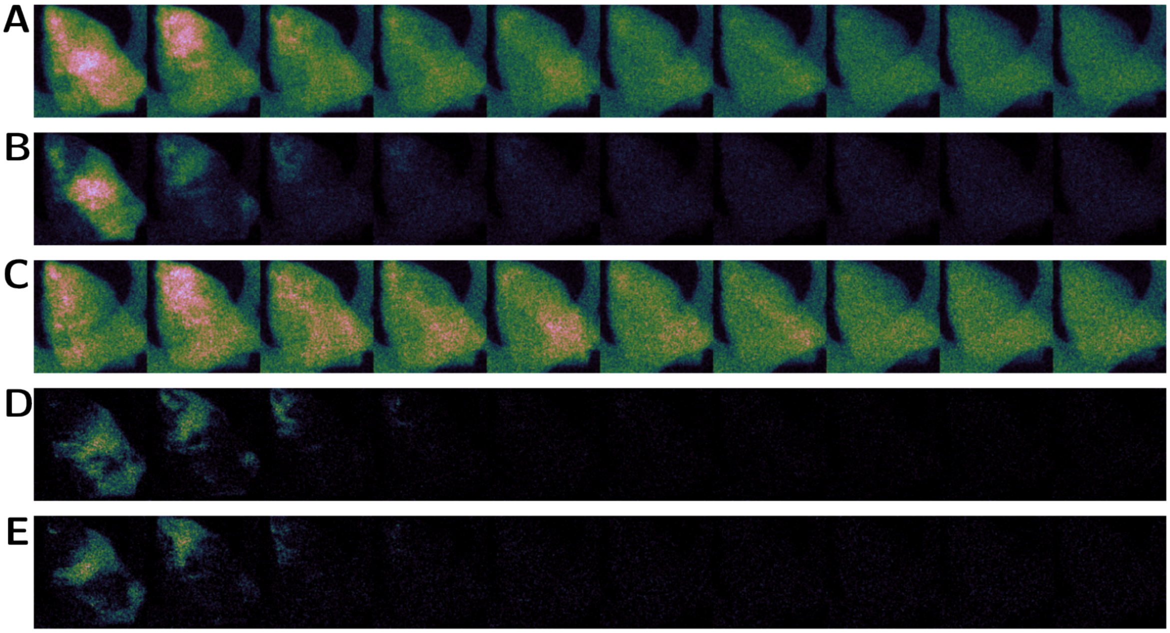

Figure 3.26: **VDF images visualizing the spatial decay of coherently diffracting zones in the 80 kx Pd(dppf)Cl$_2$ multiscan dataset**, with a sampling interval of 2 4D–STEM scans per displayed image. A: VDF images reconstructed by placing virtual apertures around all 61 clearly identified Bragg peaks from Figure 3.25. B: VDF images reconstructed by placing virtual apertures around all 13 clearly identified reflections from Figure 3.25 which underwent monotonic decay. C: VDF images reconstructed by placing virtual apertures around all 48 clearly identified reflections from Figure 3.25 which underwent nonmonotonic decay. D: VDF images reconstructed by placing a single virtual aperture around a weaker, higher-resolution Bragg peak ($d = 2.15$ Å). E: VDF images reconstructed by placing a single virtual aperture around a stronger, lower-resolution Bragg peak ($d = 3.22$ Å).

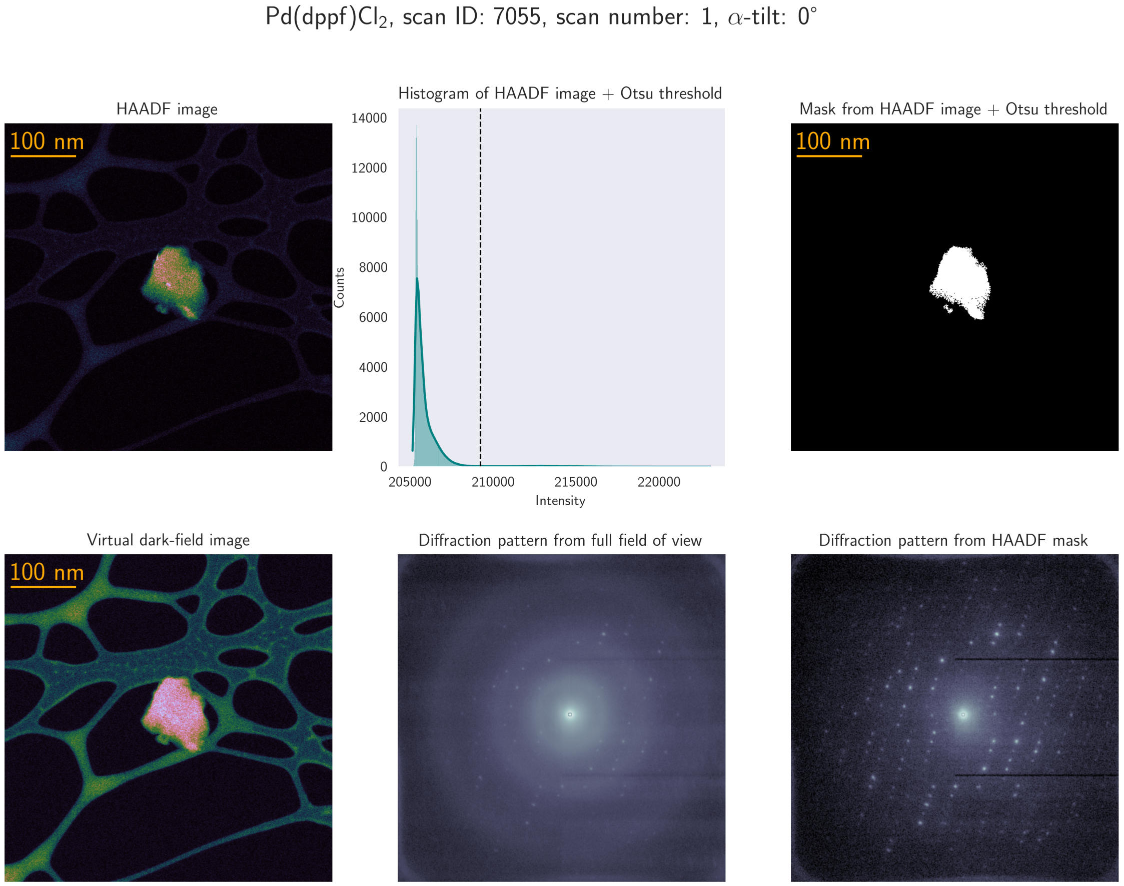

Figure 3.27: **VDF image, simultaneously acquired HAADF image, and corresponding diffraction patterns for the first representative 4D–STEM scan in the 40 kx Pd(dppf)Cl$_2$ multiscan dataset.** Since the target crystal was sufficiently isolated, applying the Otsu threshold to the HAADF image worked nicely, and the resultant binary mask was used to generate the diffraction pattern in the bottom right.

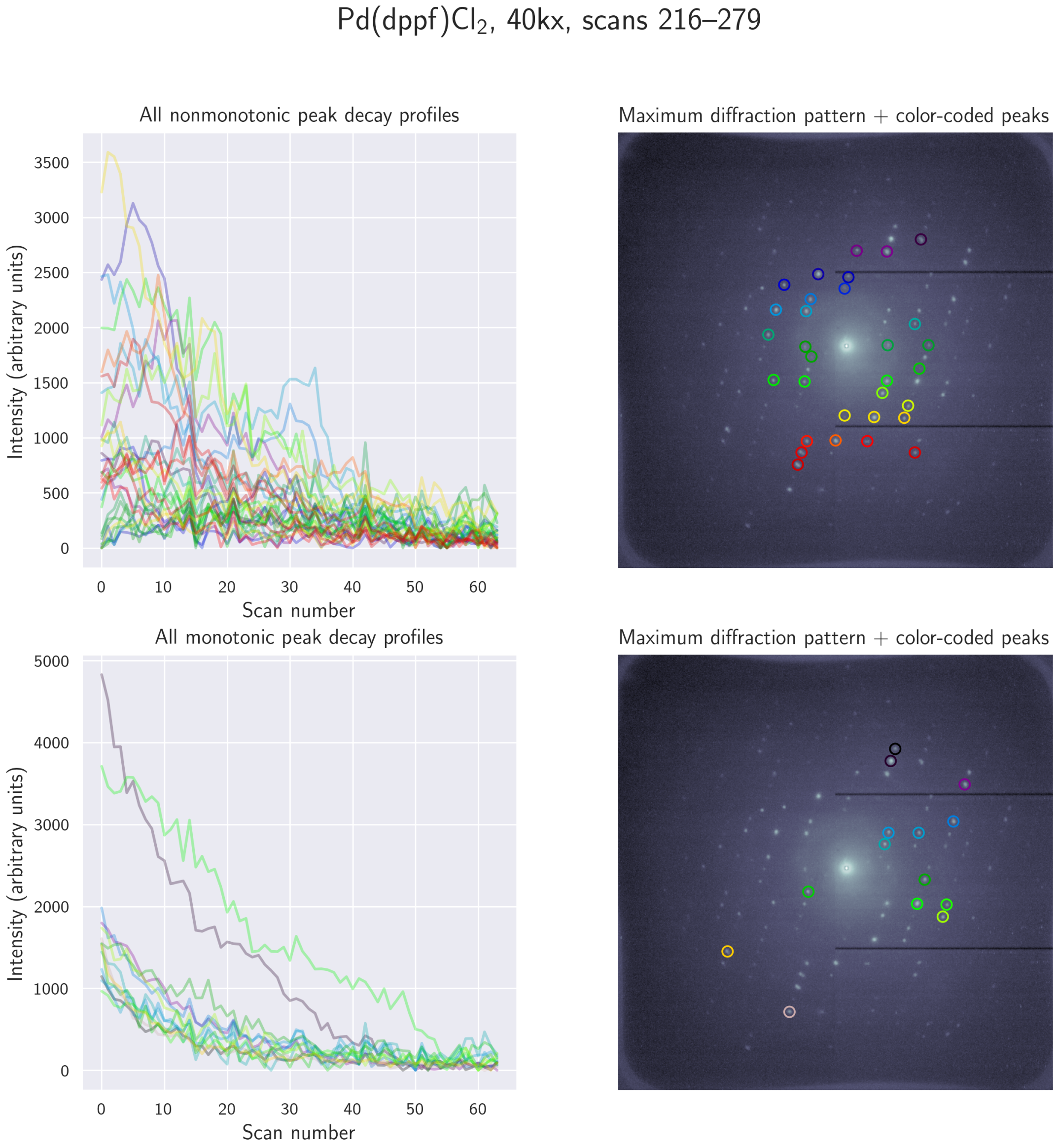

Figure 3.28: **Decay profiles of Bragg peak intensities in the 40 kx Pd(dppf)Cl$_2$ multiscan dataset** whose unnormalized maximum values exceeded a cutoff of 1500, clustered by monotonic (14 clearly identified reflections) vs. nonmonotonic (31 clearly identified reflections) decay. 68% of overall Bragg reflections decay nonmonotonically. Without accounting for overlap between adjacent probe positions, the estimated fluence delivered was 3 e^{-}Å^{-2} per scan.

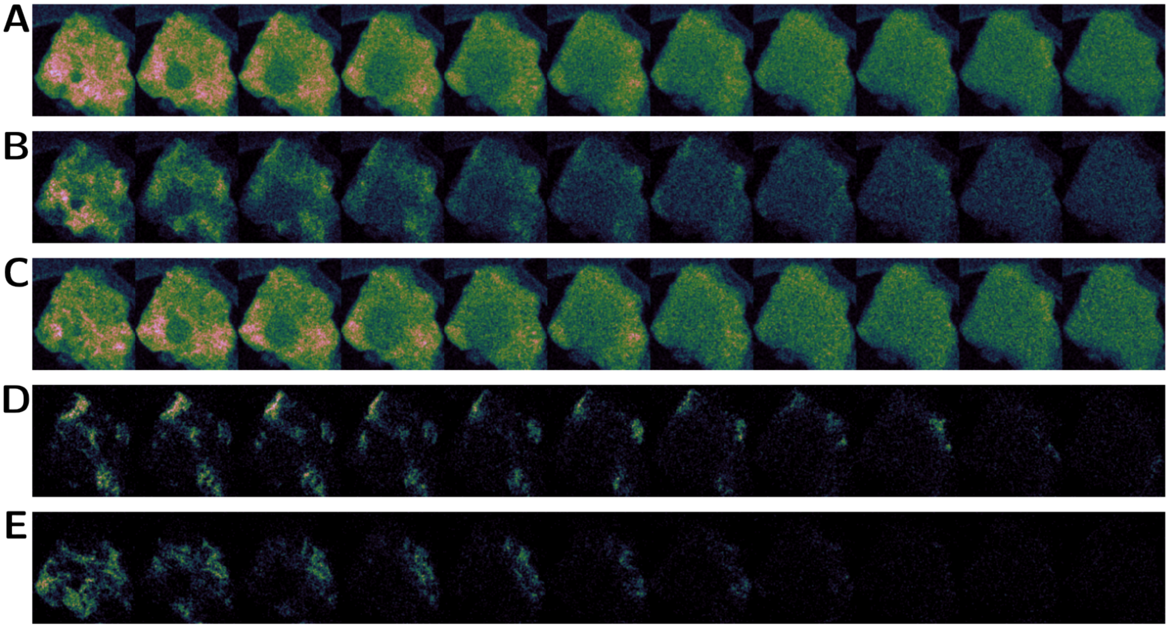

Figure 3.29: **VDF images visualizing the radial propagation of a tide of amorphization in the 40 kx Pd(dppf)Cl$_2$ multiscan dataset**, with a sampling interval of 6 4D–STEM scans per displayed image. A: VDF images reconstructed by placing virtual apertures around all 45 clearly identified Bragg peaks from Figure 3.28. B: VDF images reconstructed by placing virtual apertures around all 14 clearly identified reflections from Figure 3.28 which underwent monotonic decay. C: VDF images reconstructed by placing virtual apertures around all 31 clearly identified reflections from Figure 3.28 which underwent nonmonotonic decay. D: VDF images reconstructed by placing a single virtual aperture around a weaker, higher-resolution Bragg peak ($d = 2.58$ Å). E: VDF images reconstructed by placing a single virtual aperture around another weaker, higher-resolution Bragg peak ($d = 1.75$ Å).

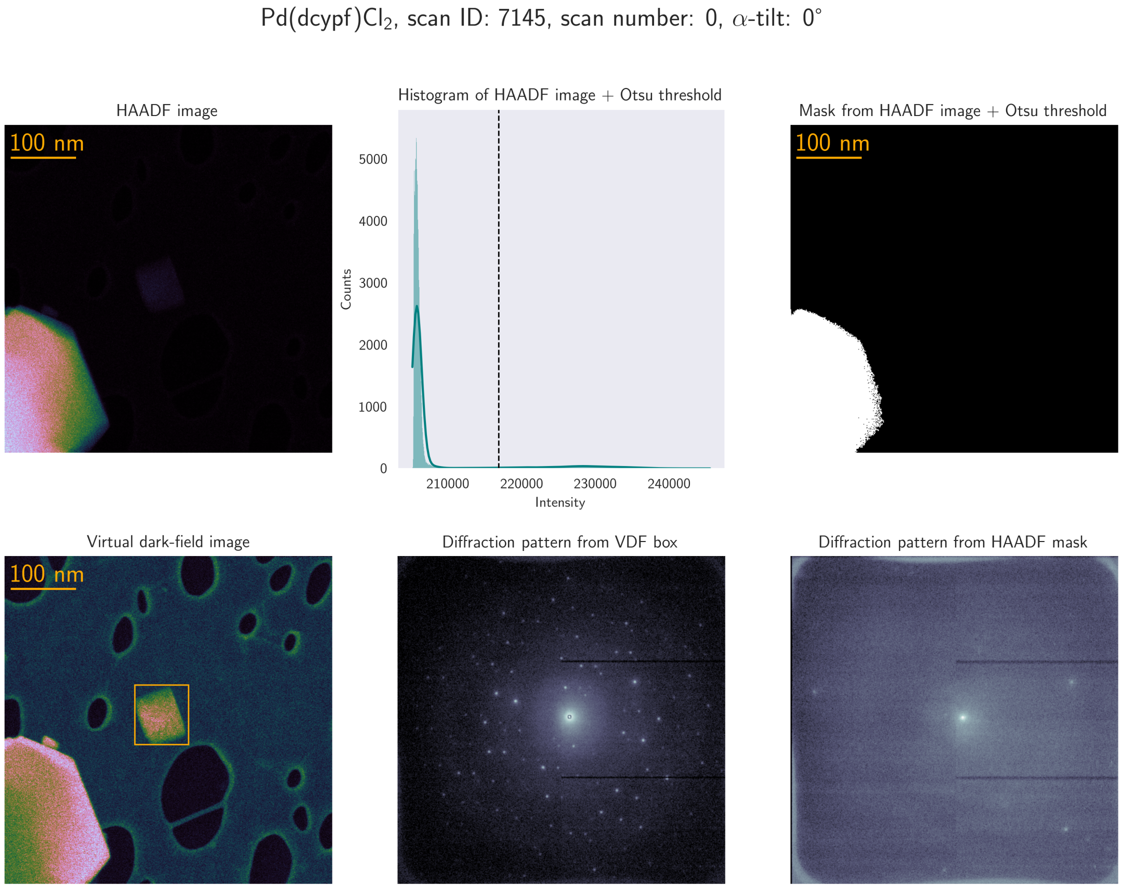

Figure 3.30: **VDF image, simultaneously acquired HAADF image, and corresponding diffraction patterns for the first representative 4D–STEM scan in the 40 kx Pd(dcyf)Cl$_2$ multiscan dataset.** Since the target crystal was very proximal to an extremely thick specimen, it's barely visible in the HAADF image. This represents a clear case where generating a simple binary mask from applying the Otsu threshold to the HAADF image was not feasible. Instead, diffraction signal was exported from a virtual aperture hand-drawn around the crystal of interest using the VDF image, where both specimens featured more comparable contrast.

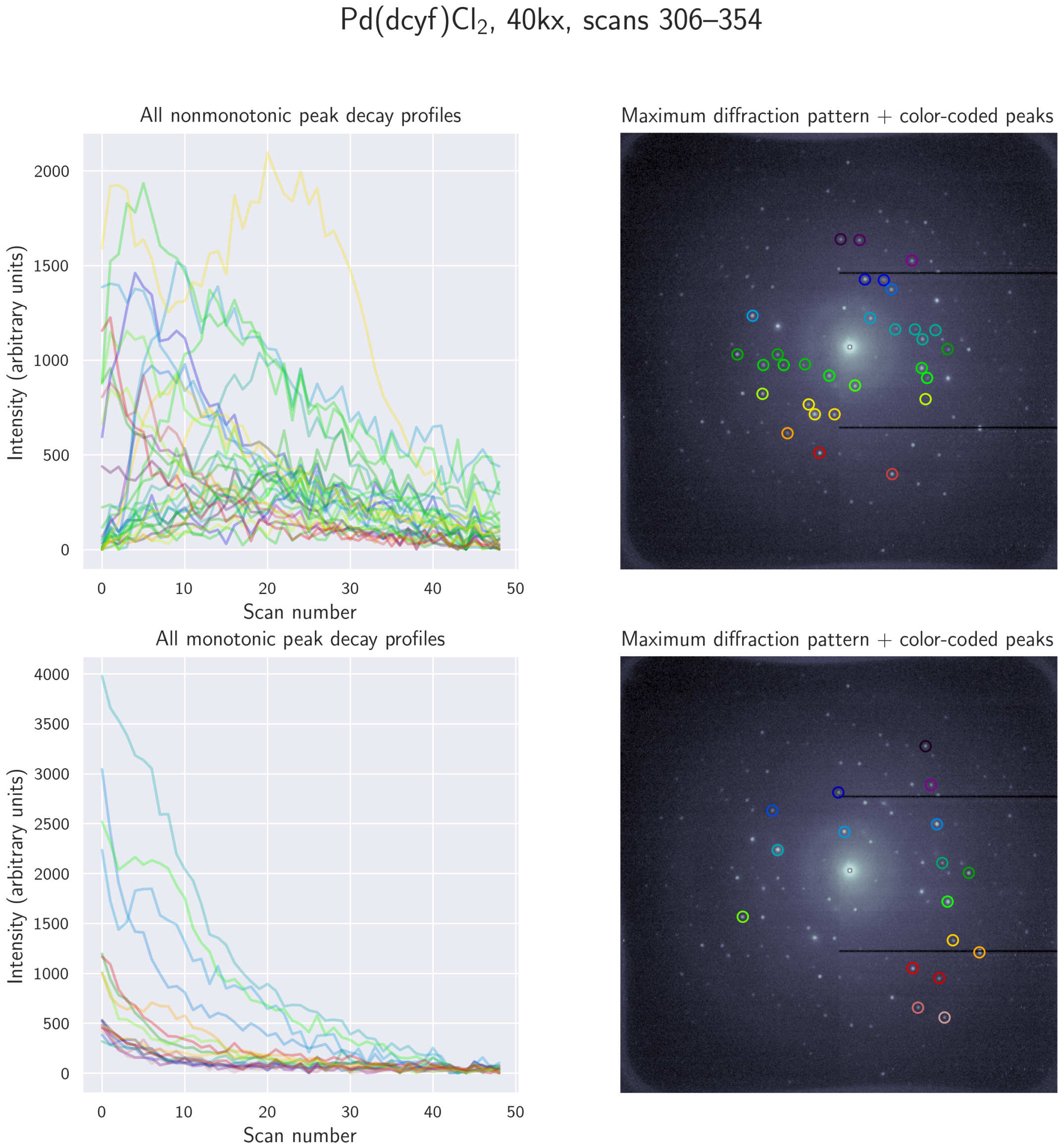

Figure 3.31: **Decay profiles of Bragg peak intensities in the 40 kx Pd(dcyf)Cl$_2$ multiscan dataset** whose unnormalized maximum values exceeded a cutoff of 700, clustered by monotonic (17 clearly identified reflections) vs. nonmonotonic (30 clearly identified reflections) decay. 64% of overall Bragg reflections decay nonmonotonically. Without accounting for overlap between adjacent probe positions, the estimated fluence delivered was 3 $e^{-}\text{Å}^{-2}$ per scan.

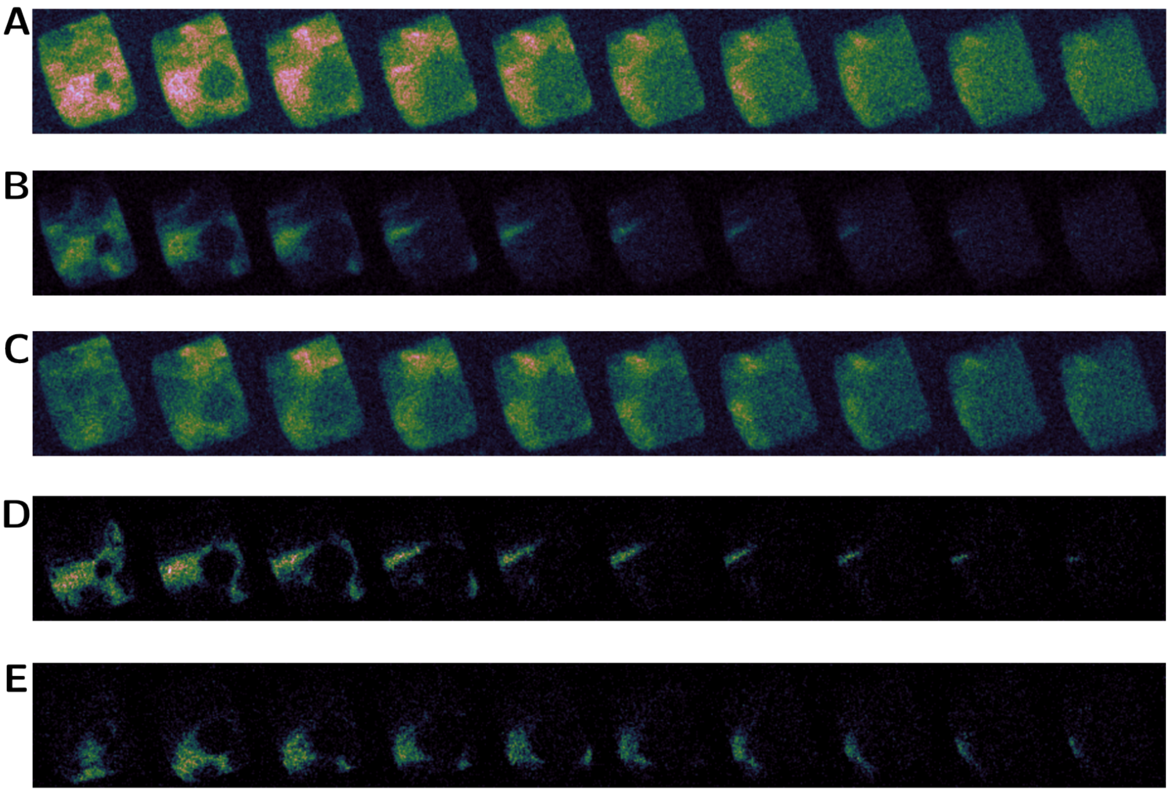

Figure 3.32: **VDF images visualizing the radial propagation of a tide of amorphization in the 40 kx Pd(dcyf)Cl_2 multiscan dataset**, with a sampling interval of 5 4D–STEM scans per displayed image. A: VDF images reconstructed by placing virtual apertures around all 47 clearly identified Bragg peaks from Figure 3.31. B: VDF images reconstructed by placing virtual apertures around all 17 clearly identified reflections from Figure 3.31 which underwent monotonic decay. C: VDF images reconstructed by placing virtual apertures around all 30 clearly identified reflections from Figure 3.31 which underwent nonmonotonic decay. D: VDF images reconstructed by placing a single virtual aperture around a weaker, higher-resolution Bragg peak. E: VDF images reconstructed by placing a single virtual aperture around another weaker, higher-resolution Bragg peak.

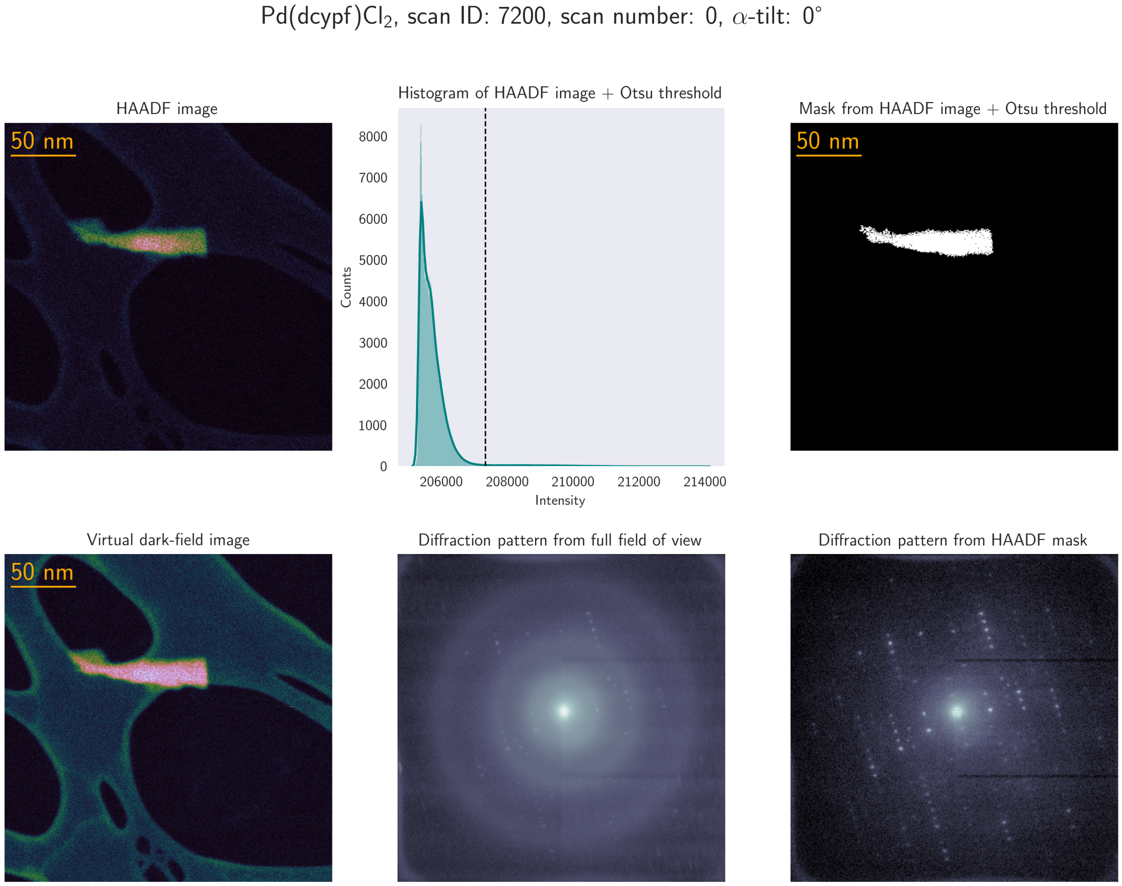

Figure 3.33: **VDF image, simultaneously acquired HAADF image, and corresponding diffraction patterns for the first representative 4D–STEM scan in the 80 kx Pd(dcyf)Cl$_2$ multiscan dataset.**

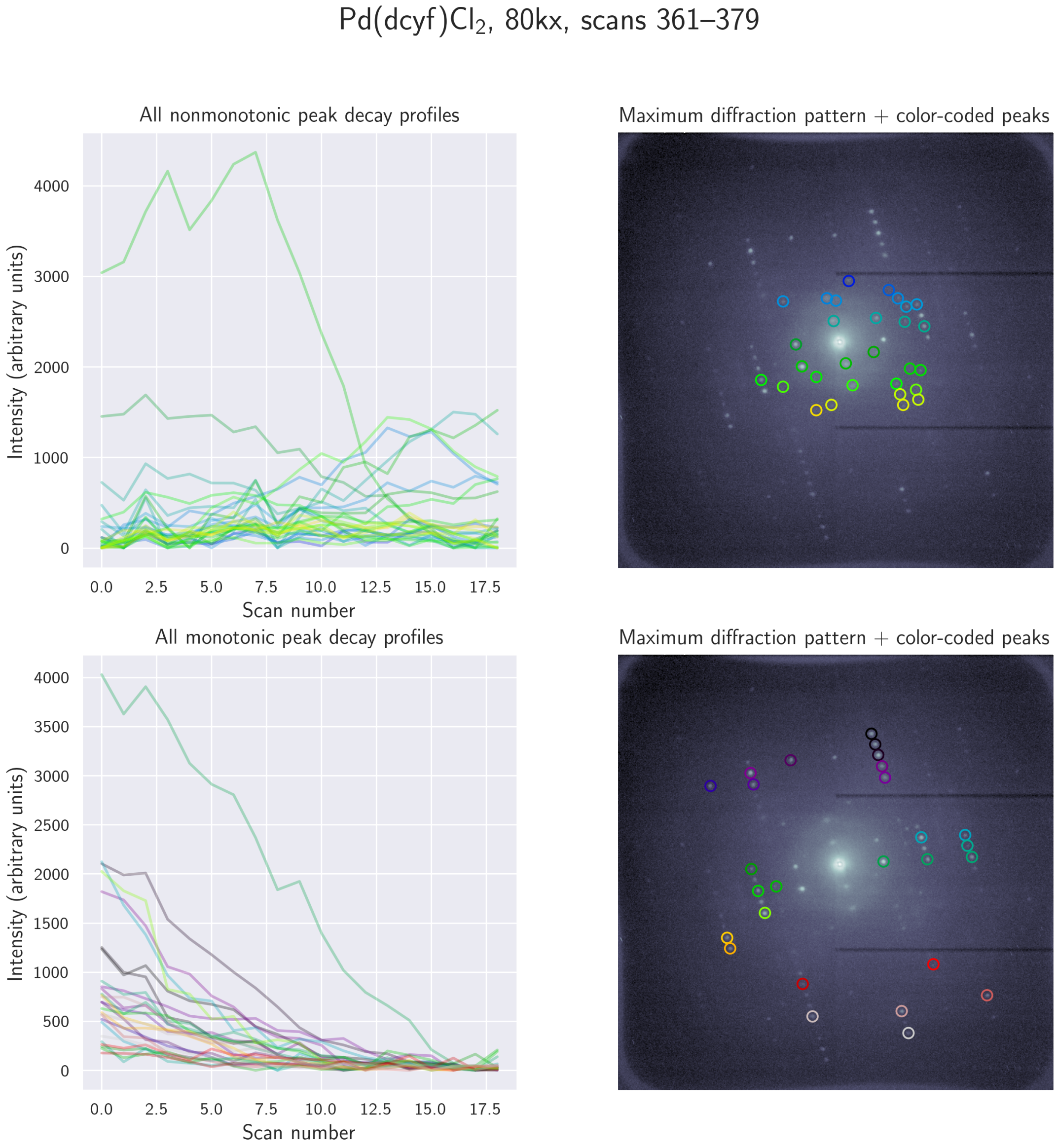

Figure 3.34: **Decay profiles of Bragg peak intensities in the 80 kx Pd(dcyf)Cl$_2$ multiscan dataset** whose unnormalized maximum values exceeded a cutoff of 700, clustered by monotonic (27 clearly identified reflections) vs. nonmonotonic (29 clearly identified reflections) decay. 51% of overall Bragg reflections decay nonmonotonically. Without accounting for overlap between adjacent probe positions, the estimated fluence delivered was 3 $e^{-}\text{Å}^{-2}$ per scan.

3.6 Supplementary Code

This section contains several sample Python scripts used to parse and analyze the 4D–STEM data discussed earlier in the chapter.

```
import os
import numpy as np
import matplotlib as mpl
import matplotlib.pyplot as plt
import ncempy
import seaborn as sns
from matplotlib.colors import LogNorm
from scipy.special import j1, jn, jn_zeros

mpl.rcParams[’text.usetex’] = True
mpl.rcParams[’text.latex.preamble’] = r"\usepackage{sfmath}"
mpl.rcParams[’font.family’] = ’sans-serif’
mpl.rcParams[’font.sans-serif’] = ’cm’
sns.set_style(’darkgrid’)

c = 2.99792e8  # speed of light in m/s
h = 6.626070e-34  # planck’s constant in J*s
m0 = 9.1094e-31  # electron rest mass in kg
kev2j = 1.60218e-16  # conversion factor for keV to J


# this function takes energy in keV and semiconvergence angle in rad (NOT
    mrad)
def fwhm_probe(energy, semicon):
    wavelength = (h * c) / (np.sqrt((2 * m0 * (c ** 2) * energy * kev2j) +
    (energy * kev2j) ** 2))  # in meters
    wavelength_ang = wavelength * 1e10  # converts wavelength from m to
    angstroms
```

```
    fwhm = 0.515 * (wavelength / semicon)  # in meters, see DOI: 10.1016/j
   .ultramic.2021.113440 for a reference
    # rayleigh separation = distance between first zero of airy disk and
   center: this is 59% of total probe intensity
    rayleigh = 0.61 * (wavelength / semicon)
    fwhm_nm = fwhm * 1e9  # converts fwhm from m to nm
    print(f"At {energy} keV, the corresponding relativistic wavelength = {
   wavelength_ang} angstroms")
    print(f"Estimated FWHM of the probe = {fwhm_nm} nm")
    return fwhm


def airy_from_fwhm(fwhm, size=128):
    radius = fwhm / 3.232
    s = 3.83 / radius
    x = np.arange(size, dtype=np.float64) * s
    x -= x.mean()
    y, x = np.meshgrid(x, x)
    r = np.sqrt(x ** 2 + y ** 2)
    result = np.ones(r.shape)
    result[r != 0] = (2 * j1(r[r != 0]) / r[r != 0]) ** 2
    return result, y, x

for scan_num in range(343, 348):
    dm4_path = f"/home/ambarneil/NCEM/dm4/2022.08.13/scan{scan_num}.dm4"
    if os.path.isfile(dm4_path):
        haadf = ncempy.read(dm4_path)
        with ncempy.io.dm.fileDM(dm4_path) as f0:
            metadata = f0.getMetadata(0)
        for key, val in metadata.items():
            print(f'{key} = {val}')
        print(f"---------------------------------------------------------
   ")
```

```
    print(f"Real-space probe step size = {haadf['pixelSize'][0]} {
haadf['pixelUnit'][0]}")
    print(f"Dimensions of HAADF image = {np.shape(haadf['data'])}")
    print(f"Maximum value in HAADF image = {np.max(haadf['data'])}")
    print(f"Minimum value in HAADF image = {np.min(haadf['data'])}")
    print(f"Mean value in HAADF image = {np.mean(haadf['data'])}")
    print(f"Median value in HAADF image = {np.median(haadf['data'])}")

    if haadf['pixelUnit'][0] and metadata['Calibrations Dimension 1
Units'] == r" m ":
        pixelsize_m = haadf['pixelSize'][0] / 1e6
        print(f"Overall field of view = {metadata['Microscope Info
Field of View ( m )'] ** 2} square microns")
    elif haadf['pixelUnit'][0] and metadata['Calibrations Dimension 1
Units'] == r"nm":
        pixelsize_m = haadf['pixelSize'][0] / 1e9
        print(f"Overall field of view = {metadata['Microscope Info
Field of View (nm)'] ** 2} square nm")

    if metadata[r"Microscope Info Operation Mode"] == r"microprobe
large":
        pass
    elif metadata[r"Microscope Info Operation Mode"] == r"SCANNING":
        pixelsize_m = pixelsize_m * 2
    else:
        raise ValueError("Whoa there, partner. Unexpected metadata
encountered")

    rows = 1
    columns = 1
    fig = plt.figure(figsize=(5, 5), constrained_layout=True)

    fig.add_subplot(rows, columns, 1)
```

```
    ax = plt.gca()
    plt.axis('off')

    plt.imshow(haadf['data'], cmap='cubehelix', vmin=203399, vmax
=224623)

    #plt.show()
    plt.savefig(f"craterfig_haadf_0_{scan_num}.svg", format='svg', dpi
=300)

    voltage_keV = metadata['Microscope Info Voltage'] / 1e3
    alpha = 7e-5  # for some reason semiconvergence angle is not
stored in metadata: supply manually
    fwhm = fwhm_probe(voltage_keV, alpha)
    fwhm_nm = fwhm * 1e9
    print(fwhm_nm)

    # if fwhm is small (e.g. 1-2 nm for CBED) plot won't look great,
but airy disk looks nice for larger probe sizes
    airy, yy, xx = airy_from_fwhm(fwhm=fwhm_nm, size=128)

    rows = 1
    columns = 2
    fig = plt.figure(figsize=(10, 10))
    plt.tight_layout()

    fig.add_subplot(rows, columns, 1)
    plt.imshow(airy, vmin=-0.05, vmax=0.5, cmap='cubehelix')
    plt.title(f"Airy disk", fontdict={'size': 16})
    plt.colorbar(fraction=0.045, pad=0.045)
    plt.axis('off')

    fig.add_subplot(rows, columns, 2)
```

```
        plt.imshow(airy, cmap='cubehelix', norm=LogNorm())
        plt.title(f"Airy disk with enhanced contrast", fontdict={'size':
   16})
        plt.colorbar(fraction=0.045, pad=0.045)
        plt.axis('off')
        plt.savefig(r"airy_example_lognorm.png", dpi=300)
        plt.show()

        if pixelsize_m > fwhm:
            print(f"Real-space probe step size ({pixelsize_m} m) is {round
   ((pixelsize_m / fwhm) * 100)} percent larger than estimated FWHM of
   probe ({fwhm} m): undersampling")
        elif pixelsize_m < fwhm:
            print(f"Real-space probe step size ({pixelsize_m} m) is {round
   ((pixelsize_m / fwhm) * 100)} percent smaller than estimated FWHM of
   probe ({fwhm} m): oversampling")
        else:
            print(f"Real-space probe step size ({pixelsize_m} m) matches
   estimated FWHM of probe ({fwhm} m)")
        """


    elif not os.path.isfile(dm4_path):
        print(f"DM4 file at {dm4_path} not found, skipping ahead to scan {
   str(scan_num + 1)}")
```

Listing 3.1: Sample code used to calculate FWHM of probe (Airy disk) and estimate undersampling vs. oversampling from the metadata contained in the HAADF image.

```
"""
this script:
[1] loads 4D-STEM scans and corresponding HAADF images
[2] thresholds HAADF image and generates binary mask
[3] applies HAADF mask to 4D-STEM scan and generates diffraction pattern
```

```
[4] plots VDF, HAADF, full diffraction pattern, masked DP, and HAADF
   histogram
[5] exports diffraction pattern as SMV
questions? contact <ambarneil@mbi.ucla.edu>
"""

import stempy.image as stim
from pathlib import Path
import stempy.io as stio
import ncempy
import os
import numpy as np
import skimage
from scipy import ndimage
from skimage.filters import threshold_otsu
from skimage.filters import threshold_multiotsu
from skimage.filters import try_all_threshold
import matplotlib as mpl
import matplotlib.pyplot as plt
from matplotlib.patches import Rectangle
import seaborn as sns

mpl.rcParams['text.usetex'] = True
mpl.rcParams['text.latex.preamble'] = r"\usepackage{sfmath}"
mpl.rcParams['font.family'] = 'sans-serif'
mpl.rcParams['font.sans-serif'] = 'cm'
sns.set_style('dark')



def write_smv(out_path, im, mag=110, lamda=0.019687576525122874,
   pixel_size=0.01):
    # Write out diffraction as SMV formatted file
    # Header is 512 bytes of zeros and then filled with ASCII
```

```
 #
 # camera length, wavelength, and pixel_size are hard coded.
 # Hard coded metadata

 if im.max() > 65535:
     im[im > 65535] = 65535  # maximum 16 bit value allowed
     im[im < 0] = 0  # just in case
     print('warning. Loss of dynamic range due to conversion from 32
bit to 16 bit')
 im = im.astype(np.uint16)
 dtype = 'unsigned_short'

 # Write 512 bytes of zeros
 with open(out_path, 'wb') as f0:
     f0.write(np.zeros(512, dtype=np.uint8))
 # Write the header over the zeros as needed
 with open(out_path, 'r+') as f0:
     f0.write("{\nHEADER_BYTES=512;\n")
     f0.write("DIM=2;\n")
     f0.write("BYTE_ORDER=little_endian;\n")
     f0.write(f"TYPE={dtype};\n")
     f0.write(f"SIZE1={im.shape[1]};\n")  # size1 is columns
     f0.write(f"SIZE2={im.shape[0]};\n")  # size 2 is rows
     f0.write(f"PIXEL_SIZE={pixel_size};\n")  # physical pixel size in
micron
     f0.write(f"WAVELENGTH={lamda};\n")  # wavelength
     if mag:
         f0.write(f"DISTANCE={int(mag)};\n")
     f0.write("PHI=0.0;\n")
     f0.write("BEAM_CENTER_X=146;\n")
     f0.write("BEAM_CENTER_Y=142;\n")
     f0.write("BIN=1x1;\n")
     f0.write("DATE=Sat Mar 11 02:33:22 2023;\n")
```

```
        f0.write("DETECTOR_SN=unknown;\n")
        f0.write("OSC_RANGE=1.0;\n")
        f0.write("OSC_START=0;\n")
        f0.write("IMAGE_PEDESTAL=0;\n")
        f0.write("TIME=10.0;\n")
        f0.write("TWOTHETA=0;\n")
        f0.write("}\n")
    # Append the binary image data at the end of the header
    with open(out_path, 'rb+') as f0:
        f0.seek(512, 0)
        f0.write(im)

rsx_min = 47
rsx_max = 47 + 58
rsy_min = 79
rsy_max = 79 + 124
scan_id = 7200
alpha = 0
counter = 1

start = 417
stop = 655

dm4_path = f"/home/ambarneil/NCEM/dm4/2023.05.13/scan{start}.dm4"
dm4_ref = ncempy.read(dm4_path)
haadf_ref = dm4_ref['data']
dims = np.shape(haadf_ref)
stack = np.zeros((stop - start, 3, dims[0], dims[1]))

for ii, scan_num in enumerate(range(start, stop)):
    hdf5_path = f"/home/ambarneil/NCEM/2022.08.13_manual/data_scan{
   scan_num}_th5.0_electrons_centered.h5"
    dm4_path = f"/home/ambarneil/NCEM/dm4/2022.08.14/scan{scan_num}.dm4"
```

```
 if os.path.isfile(hdf5_path) and os.path.isfile(dm4_path):
     sp = stio.load_electron_counts(hdf5_path)
     dp_full = sp.sum(axis=(0, 1))
     dp_box = sp[rsy_min:rsy_max, rsx_min:rsx_max, :, :]
     dp_box = dp_box.sum(axis=(0, 1))
     sums = sp.sum(axis=(2, 3))
     stem_images = stim.create_stem_images(sp, (0, 150), (10, 270),
center=(282, 299))
     dm4 = ncempy.io.read(dm4_path)
     haadf = dm4['data']
     pixelsize = dm4['pixelSize'][0]

     otsu = skimage.filters.threshold_otsu(haadf)
     binary_otsu = haadf > otsu
     binary_otsu_img = skimage.morphology.remove_small_objects(
binary_otsu)

     print(f"Otsu threshold = {otsu}")
     temp = ndimage.gaussian_filter(dm4['data'].astype(np.float32), 3)
>= otsu
     mask = np.zeros_like(dm4['data'])
     mask[temp] = 1
     dp_mask = stim.mask_real_space(sp, mask)

     rows = 2
     columns = 3
     fig = plt.figure(figsize=(14, 10))
     plt.tight_layout(pad=5)

     fig.add_subplot(rows, columns, 1)
     ax = plt.gca()
     plt.title(r"HAADF image")
```

```
    plt.axis('off')

    scaleL = pixelsize * 199
    scaleH = 100
    scaleR = Rectangle((10, 30), scaleH, scaleL, color=r"#ffab01")
    ax.add_patch(scaleR)
    ax.text(10, 20, str(int(np.round(scaleL * scaleH) * 2)) + r" nm",
            fontdict={'size': 18, 'weight': 'bold', 'color': r"#ffab01
"})
    haadf_align, shifts = ncempy.algo.image_correlate(haadf, haadf_ref
)
    plt.imshow(haadf_align, cmap='cubehelix')
    # plt.imshow(haadf, cmap='cubehelix')

    fig.add_subplot(rows, columns, 2)
    plt.title(r"Histogram of HAADF image + Otsu threshold")
    plt.xlabel(r"Intensity")
    plt.ylabel(r"Counts")
    sns.histplot(data=haadf.ravel(), kde=True, stat='count', color='
#008080')
    plt.axvline(otsu, color='k', linestyle='dashed', linewidth=1)

    fig.add_subplot(rows, columns, 3)
    ax = plt.gca()
    plt.axis('off')
    scaleL = pixelsize * 199
    scaleH = 100
    scaleR = Rectangle((10, 30), scaleH, scaleL, color=r"#ffab01")
    ax.add_patch(scaleR)
    ax.text(10, 20, str(int(np.round(scaleL * scaleH) * 2)) + r" nm",
            fontdict={'size': 18, 'weight': 'bold', 'color': r"#ffab01
"})
    ax.get_xaxis().set_visible(False)
```

```
    ax.get_yaxis().set_visible(False)
    plt.title(r"Mask from HAADF image + Otsu threshold")
    binary_otsu_img_align = ndimage.interpolation.shift(
binary_otsu_img, shifts)
    plt.imshow(binary_otsu_img_align, cmap='gray')
    # plt.imshow(binary_otsu_img, cmap='gray')

    fig.add_subplot(rows, columns, 4)
    ax = plt.gca()
    plt.axis('off')
    scaleL = pixelsize * 199
    scaleH = 100
    scaleR = Rectangle((10, 30), scaleH, scaleL, color=r"#ffab01")
    ax.add_patch(scaleR)
    ax.text(10, 20, str(int(np.round(scaleL * scaleH) * 2)) + r" nm",
            fontdict={'size': 18, 'weight': 'bold', 'color': r"#ffab01
"})
    ax.add_patch(
        Rectangle((rsy_min, rsx_min), rsy_max - rsy_min, rsx_max -
rsx_min, fc='none', color='#ffab01', lw=1))
    vdf_align = ndimage.interpolation.shift(stem_images[1,], shifts)
    plt.imshow(vdf_align, cmap='cubehelix')
    # plt.imshow(stem_images[1,], cmap='cubehelix')
    plt.title(r"Virtual dark-field image")

    fig.add_subplot(rows, columns, 5)
    ax = plt.gca()
    plt.axis('off')
    ax.get_xaxis().set_visible(False)
    ax.get_yaxis().set_visible(False)
    plt.matshow(np.log(dp_box + 1), cmap='bone', fignum=False,
interpolation='gaussian')
    # plt.title(r"Diffraction pattern from full field of view")
```

```
    plt.title(r"Diffraction pattern from VDF box")

    fig.add_subplot(rows, columns, 6)
    ax = plt.gca()
    plt.axis('off')
    ax.get_xaxis().set_visible(False)
    ax.get_yaxis().set_visible(False)
    plt.matshow(np.log(dp_mask + 1), cmap='bone', fignum=False,
interpolation='gaussian')
    plt.title(r"Diffraction pattern from HAADF mask")
    # plt.suptitle(r"BPE/dichlororesorcinol, " + r"scan ID: " + str(
scan_id) + r", scan number: " + str(
    #   scan_num) + r", $\alpha$-tilt: " + str(alpha) + r"  ",
fontsize=18)

    plt.suptitle(
        r"Ni(dppf)Cl$_{2}$, " + r"scan number: " + str(
            scan_num - 224) + r", $\alpha$-tilt: " + str(alpha) + r"
", fontsize=18)

    plt.savefig(f"otsu_nidppf_OGmultiscan_{scan_num}_{scan_id}.png",
dpi=300)
    outpath = Path(f"/home/ambarneil/PycharmProjects/4DSTEM/
nidppf_OGmultiscan/")
    outpath.mkdir(exist_ok=True)
    dp_mask_500 = dp_mask + 500
    dp_box_500 = dp_box + 500

    write_smv(outpath / Path(f"nidppf_multiscan40kx_081322_mov2_{
scan_num}.img"), dp_mask)
    write_smv(outpath / Path(f"
nidppf_multiscan40kx_plus500_081322_mov2_{scan_num}.img"), dp_mask_500)
```

```
        stack[ii, 0, :, :] = haadf_new
        stack[ii, 1, :, :] = haadf_mask
        stack[ii, 2, :, :] = vdf_new

        scan_id = scan_id + 1
        counter = counter + 1
        plt.show()
        # alpha = alpha - 1
        plt.figure().clear()
        plt.close()
        plt.cla()
        plt.clf()

    elif not os.path.isfile(hdf5_path):
        print(f"HDF5 file at {hdf5_path} not found, skipping ahead to scan {str(scan_num + 1)}")
        scan_id = scan_id + 1
        # this only works if i messed up, not if distiller messes up: then the IDs will be out of sync and you have to restart from scratch

    elif not os.path.isfile(dm4_path):
        print(f"DM4 file at {dm4_path} not found, skipping ahead to scan {str(scan_num + 1)}")
        scan_id = scan_id + 1
```

Listing 3.2: Sample code used to create binary mask from simultaneously acquired HAADF image and export diffraction patterns in SMV format from HAADF mask.

```
from pathlib import Path
from collections import namedtuple
from scipy.optimize import curve_fit
import matplotlib as mpl
import matplotlib.pyplot as plt
```

```
from matplotlib.colors import LogNorm,PowerNorm
from matplotlib.patches import Rectangle, Polygon
import numpy as np
from numpy.linalg import svd
import imageio
from scipy import ndimage
import stempy
import stempy.io as stio
import stempy.image as stim
import ncempy

mpl.rcParams['text.usetex'] = True
mpl.rcParams['text.latex.preamble'] = r"\usepackage{sfmath}"
mpl.rcParams['font.family'] = 'sans-serif'
mpl.rcParams['font.sans-serif'] = 'cm'
plt.rcParams['figure.dpi'] = 300
plt.rcParams['savefig.dpi'] = 300

dir_path = Path(r"C:\Users\eicn_user\Desktop\ambarneil\4DSTEM_20230209
   \2023.02.08")
id0 = 6971
file_names = []
for ii in range(135, 155):
    filename = f'data_scan{ii}_id{id0}_electrons_centered.h5'
    full_path = dir_path / Path(filename)
    file_names.append(full_path)
    id0 += 1
print(file_names)

# Load the data and create full diffraction patterns

threshold = 200
```

```
masks = []
full_dps = []
dfs = []
mask_dps = []
sorted_filenames = []
for full_path in sorted(file_names):
    print(full_path)
    sorted_filenames.append(str(full_path))
    sp = stio.load_electron_counts(full_path)
    df = sp.sum(axis='frame')
    full_dp = sp.sum(axis='scan')
    full_dps.append(full_dp)
    dfs.append(df)

    mask = df.copy()
    mask[df < threshold] = 0
    mask[df >= threshold] = 1

    ndimage.binary_fill_holes(mask, output=mask)

    mask_dp = stim.mask_real_space(sp, mask)
    mask_dps.append(mask_dp)

mask_dps_max = np.max(mask_dps, axis=0)
import seaborn as sns
sns.set_style('darkgrid')
#plt.figure()
#plt.imshow(rr * mask_dps_max)
#mask_dps_max_hole = rr * mask_dps_max
mask_dps_max_smooth = ndimage.gaussian_filter(mask_dps_max.astype(np.
   float32), 3.2)

numpeaks = []
```

```
threshold = 25
threshold = threshold / mask_dps_max_smooth.max()
peaks = ncempy.algo.peak_find.peakFind2D(mask_dps_max_smooth, threshold)
print(threshold)

keep = []

# keep peaks if they fall outside central beam and 5 pixel outer border
for peak in peaks:
    if np.sqrt((peak[0] - centerx) ** 2 + (peak[1] - centery) ** 2) >= 20
   and peak[0] > 50 and peak[1] > 50 and peak[0] < 536 and peak[1] < 536:
        keep.append(peak)

peaks = np.asarray(keep)
print(peaks)
np.savetxt("peaks_biotin.csv", peaks, delimiter=",")

# peaks = ncempy.algo.peak_find.enforceMinDist(peaks, mask_dps_max[peaks],
    25)
#plt.figure()
#plt.plot(numpeaks)

rows = 1
columns = 2
fig = plt.figure(figsize=(13, 5))
fig.add_subplot(rows, columns, 1)
ax = plt.gca()
plt.imshow(mask_dps_max, norm=LogNorm(), cmap=’bone’, interpolation=’
   gaussian’)
plt.scatter(peaks[:,1], peaks[:, 0], c=’#00acd5’)
plt.title(r"Maximum diffraction pattern + peak coordinates", fontsize=14)
ax.axis(’off’)
```

```
fig.add_subplot(rows, columns, 2)
ax = plt.gca()
sns.histplot(np.log(mask_dps_max.ravel() + 1), bins=50, color=r"#00acd5")
plt.title(r"Histogram of maximum diffraction pattern", fontsize=14)
plt.ylabel(r"Counts", fontsize=14)
plt.xlabel("Logarithm of pixel intensity", fontsize=14)
plt.yticks(fontsize=14)
plt.xticks(fontsize=14)

#ax.axis('off')


plt.tight_layout()
plt.savefig(r"mmm_biotinhist.png", format='png', dpi=300)
plt.cla()
plt.clf()

r = 5
sns.set_style('darkgrid')

fg, ax = plt.subplots(2, 2)
ax[0, 1].axis('off')
ax[1, 1].axis('off')
plt.rcParams['figure.figsize'] = [10, 10]
plt.rcParams['figure.dpi'] = 300
#plt.tight_layout()
ax[0, 1].imshow(mask_dps_max, norm=LogNorm(), cmap='bone')
ax[1, 1].imshow(mask_dps_max, norm=LogNorm(), cmap='bone')
lim = (len(peaks))
colors = plt.cm.nipy_spectral(np.linspace(0, 1, lim))
peaks_record = []
monoints_record = []
nonmonoints_record = []
plt.suptitle(r"(+)-Biotin, 40kx, scans 135--154", fontsize=18)
```

```
for ii, peak in enumerate(peaks[0:lim,:]):
    chooseX, chooseY = peak
    intensity = mask_dps[:, chooseX-r:chooseX+r+1, chooseY-r:chooseY+r+1].
  sum(axis=(1, 2))
    if np.max(intensity) > 3000 and np.max(intensity) != intensity[0]:
        print(peak)
        print(intensity)
        intensity = intensity - np.min(intensity)
        info = np.concatenate((peak, intensity))
        nonmonoints_record.append(info)
        p = ax[0, 0].plot(intensity, alpha=0.3, color=colors[ii])
        ax[0, 0].set_title(r"All nonmonotonic peak decay profiles")
        #plt.xlim(0, 25)
        ax[0, 1].scatter(chooseY, chooseX,  edgecolor = p[0].get_color(),
  marker='o', facecolor = 'none')
        ax[0, 1].set_title(r"Maximum diffraction pattern + color-coded
  peaks")
        ax[0, 0].set_box_aspect(1)
        ax[0, 0].set_ylabel(r"Intensity (arbitrary units)", fontsize=12)
        ax[0, 0].set_xlabel(r"Scan number", fontsize=12)
    elif np.max(intensity) > 3000 and np.max(intensity) == intensity[0]:
        print(peak)
        print(intensity)
        intensity = intensity - np.min(intensity)
        info = np.concatenate((peak, intensity))
        monoints_record.append(info)
        p = ax[1, 0].plot(intensity, alpha=0.3, color=colors[ii])
        ax[1, 0].set_title(r"All monotonic peak decay profiles")
        #plt.xlim(0, 25)
        ax[1, 1].scatter(chooseY, chooseX, edgecolor = p[0].get_color(),
  marker='o', facecolor = 'none')
        ax[1, 1].set_title(r"Maximum diffraction pattern + color-coded
```

```
   peaks")
        ax[1, 0].set_box_aspect(1)
        ax[1, 0].set_ylabel(r"Intensity (arbitrary units)", fontsize=12)
        ax[1, 0].set_xlabel(r"Scan number", fontsize=12)

print(f"Number of nonmonotonically decaying intensities: {int(len(
   nonmonoints_record))}")
print(f"Number of monotonically decaying intensities: {int(len(
   monoints_record))}")

count_nonmono = int(len(nonmonoints_record))
count_mono = int(len(monoints_record))
ratio_nonmono = (count_nonmono / (count_mono + count_nonmono)) * 100
print(f"{ratio_nonmono} percent nonmonotonic")


np.savetxt("peaks_biotin135_mono.csv", monoints_record, delimiter=",")
np.savetxt("peaks_biotin135_nonmono.csv", nonmonoints_record, delimiter=",
   ")
plt.savefig(r"mmm_biotin135_decayprofiles_mono.pdf", format='pdf', dpi
   =300)
```

Listing 3.3: Sample code used to generate a binary mask based on a VDF image and find all peaks within a maximum projection diffraction pattern stitched together from all scans across a full time series. Decay profiles of the identified Bragg reflections are sorted into monotonic and nonmonotonic groups and the results are plotted.

REFERENCES

[1] Ercius, P.; Boese, M.; Duden, T.; Dahmen, U. Operation of TEAM I in a user environment at NCEM. *Microsc. Microanal.* **2012**, 18 (4), 676-683. <DOI: 10.1017/S1431927612001225>

[2] Ercius, P.; Johnson, I.; Brown, H.; Pelz, P.; Hsu, S.-L.; Draney, B.; Fong, E.; Goldschmidt, A.; Joseph, J.; Lee, J.; Ciston, J.; Ophus, C.; Scott, M.; Selvarajan, A.; Paul, D.; Skinner, D.; Hanwell, M.; Harris, C.; Avery, P.; Stezelberger, T.; Tindall, C.; Ramesh, R.; Minor, A.; Denes, P. The 4D Camera: an 87 kHz direct electron detector for scanning/transmission electron microscopy. *Microsc. Microanal.* **2020**, 26, 1896–1897. <DOI: 10.1017/S1431927620019753>

[3] Sagawa, R.; Yasuhara, A.; Hashiguchi, H.; Naganuma, T.; Tanba, S.; Ishikawa, T.; Riedel, T.; Hartel, P.; Linck, M.; Uhlemann, S.; Müller, H.; Sawada, H. Exploiting the Full Potential of the Advanced Two-Hexapole Corrector for STEM Exemplified at 60 kV. *Ultramicroscopy* **2022**, 233, 113440. <DOI: 10.1016/j.ultramic.2021.113440>

[4] Ercius, P.; Johnson, I. J.; Pelz, P.; Savitzky, B. H.; Hughes, L.; Brown, H. G.; Zeltmann, S. E.; Hsu, S.-L.; Pedroso, C. C. S.; Cohen, B. E.; Ramesh, R.; Paul, D.; Joseph, J. M.; Stezelberger, T.; Czarnik, C.; Lent, M.; Fong, E.; Ciston, J.; Scott, M. C.; Ophus, C.; Minor, A. M.; Denes, P. The 4D Camera–An 87 kHz Frame-rate Detector for Counted 4D-STEM Experiments. *arXiv* **2023**. <DOI: 10.48550/arXiv.2305.11961>

[5] Zeltmann, S. E.; Müller, A.; Bustillo, K. C.; Savitzky, B.; Hughes, L.; Minor, A. M.; Ophus, C. Patterned Probes for High Precision 4D-STEM Bragg Measurements. *Ultramicroscopy* **2020**, 209, 112890. <DOI: 10.1016/j.ultramic.2019.112890>

[6] Hattne, J. Low-Dose Data Collection and Radiation Damage in MicroED. In *cryoEM: Methods and Protocols*; Gonen, T., Nannenga, B. L., Eds.; *Methods in Molecular Biology*; Springer US: New York, NY, **2021**; pp 309–319. DOI: 10.1007/978-1-0716-0966-8_15

[7] Drozdovitch, V. Radiation Exposure to the Thyroid After the Chernobyl Accident. *Frontiers in Endocrinology* **2021**, 11. <DOI: 10.3389/fendo.2020.569041>

[8] Baker, L. A.; Rubinstein, J. L. Chapter Fifteen - Radiation Damage in Electron Cryomicroscopy. In *Methods in Enzymology*; Jensen, G. J., Ed.; Cryo-EM Part A Sample Preparation and Data Collection; Academic Press, **2010**; Vol. 481, pp. 371–388. <DOI: 10.1016/S0076-6879(10)81015-8>

[9] Grubb, D. T. Radiation Damage and Electron Microscopy of Organic Polymers. *J. Mater. Sci.* **1974**, 9 (10), 1715–1736. <DOI: 10.1007/BF00540772>

[10] Flannigan, D. J.; VandenBussche, E. J. Pulsed-Beam Transmission Electron Microscopy and Radiation Damage. *Micron* **2023**, 172, 103501. <DOI: 10.1016/j.micron.2023.103501>

[11] Fryer, J. R. The Effect of Dose Rate on Imaging Aromatic Organic Crystals. *Ultramicroscopy* **1987**, 23 (3), 321–327. <DOI: 10.1016/0304-3991(87)90242-7>

[12] Talmon, Y. Electron Beam Radiation Damage to Organic and Biological Cryospecimens. In *Cryotechniques in Biological Electron Microscopy*; Steinbrecht, R. A., Zierold, K., Eds.; Springer: Berlin, Heidelberg, **1987**; pp 64–84. <DOI: 10.1007/978-3-642-72815-0_3>

[13] Glaeser, R. M. Limitations to significant information in biological electron microscopy as a result of radiation damage. *J. Ultrastructure Res.* **1971**, 36, 466–482. <DOI: 10.1016/S0022-5320(71)80118-1>

[14] Glaeser, R. M.; Taylor, K. A. Radiation Damage Relative to Transmission Electron Microscopy of Biological Specimens at Low Temperature: A Review. *Journal of Microscopy* **1978**, 112 (1), 127–138. <DOI: 10.1111/j.1365-2818.1978.tb01160.x>

[15] Reimer, L.; Spruth, J. Interpretation of the Fading of Diffraction Patterns from Organic Substances Irradiated with 100 KeV Electrons at 10-300 K. *Ultramicroscopy* **1982**, 10 (3), 199–210. <DOI: 10.1016/0304-3991(82)90039-0>

[16] S'ari, M.; Blade, H.; Brydson, R.; Cosgrove, S. D.; Hondow, N.; Hughes, L. P.; Brown, A. Toward Developing a Predictive Approach To Assess Electron Beam Instability during Transmission Electron Microscopy of Drug Molecules. *Mol. Pharmaceutics* **2018**, 15, 5114–5123. <DOI: 10.1021/acs.molpharmaceut.8b00693>

[17] Peet, M. J.; Henderson, R.; Russo, C. J. The Energy Dependence of Contrast and Damage in Electron Cryomicroscopy of Biological Molecules. *Ultramicroscopy* **2019**, 203, 125–131. <DOI: 10.1016/j.ultramic.2019.02.007>

[18] Naydenova, K.; Kamegawa, A.; Peet, M. J.; Henderson, R.; Fujiyoshi, Y.; Russo, C. J. On the Reduction in the Effects of Radiation Damage to Two-Dimensional Crystals of Organic and Biological Molecules at Liquid-Helium Temperature. *Ultramicroscopy* **2022**, 237, 113512. <DOI: 10.1016/j.ultramic.2022.113512>

[19] Egerton, R. F. Radiation Damage to Organic and Inorganic Specimens in the TEM. *Micron* **2019**, 119, 72–87. <DOI: 10.1016/j.micron.2019.01.005>

[20] Ophus, C. Four-Dimensional Scanning Transmission Electron Microscopy (4D-STEM): From Scanning Nanodiffraction to Ptychography and Beyond. *Microscopy and Microanalysis* **2019**, 25 (3), 563–582. <DOI: 10.1017/S1431927619000497>

[21] Bustillo, K. C.; Zeltmann, S. E.; Chen, M.; Donohue, J.; Ciston, J.; Ophus, C.; Minor, A. M. 4D-STEM of Beam-Sensitive Materials. *Acc. Chem. Res.* **2021**, 54 (11), 2543–2551. `<DOI: 10.1021/acs.accounts.1c00073>`

[22] Warkentin, M. A.; Atakisi, H.; Hopkins, J. B.; Walko, D.; Thorne, R. E. Lifetimes and spatio-temporal response of protein crystals in intense X-ray microbeams. *IUCrJ* **2017**, 4 (6), 785–794. `<DOI: 10.1107/S2052252517013495>`

[23] Warkentin, M.; Hopkins, J. B.; Badeau, R.; Mulichak, A. M.; Keefe, L. J.; Thorne, R. E. Global Radiation Damage: Temperature Dependence, Time Dependence and How to Outrun It. *J. Synchrotron Rad.* **2013**, 20 (1), 7–13. `<DOI: 10.1107/S0909049512048303>`

[24] Diederichs, K.; Karplus, P. A. Improved R-Factors for Diffraction Data Analysis in Macromolecular Crystallography. *Nat. Struct. Mol. Biol.* **1997**, 4 (4), 269–275. `<DOI: 10.1038/nsb0497-269>`

[25] Bammes, B. E.; Jakana, J.; Schmid, M. F.; Chiu, W. Radiation Damage Effects at Four Specimen Temperatures from 4 to 100K. *Journal of Structural Biology* **2010**, 169 (3), 331–341. `<DOI: 10.1107/S0909049512048303>`

[26] Dickerson, J. L. Dose calculations to optimise atomic resolution protein structure determination at new sources. University of Oxford master's thesis, 2019.

[27] Liming, F. G.; Gordy, W. Hydrogen-Addition Radicals Formed in the Aromatic Rings of Amino Acids, Polyamino Acids, and Proteins. *Proceedings of the National Academy of Sciences* **1968**, 60 (3), 794–801. `<DOI: 10.1073/pnas.60.3.794>`

[28] Lin, S. D. Electron Radiation Damage of Thin Films of Glycine, Diglycine, and Aromatic Amino Acids. *Radiation Research* **1974**, 59 (3), 521–536. `<DOI: 10.2307/3574071>`

[29] Li, P.; Egerton, R. F. Radiation Damage in Coronene, Rubrene and p-Terphenyl, Measured for Incident Electrons of Kinetic Energy between 100 and 200kev. *Ultramicroscopy* **2004**, 101 (2), 161–172. `<DOI: 10.1016/j.ultramic.2004.05.010>`

[30] Hachtel, J. A.; Huang, J.; Popovs, I.; Jansone-Popova, S.; Keum, J. K.; Jakowski, J.; Lovejoy, T. C.; Dellby, N.; Krivanek, O. L.; Idrobo, J. C. Identification of Site-Specific Isotopic Labels by Vibrational Spectroscopy in the Electron Microscope. *Science* **2019**, 363 (6426), 525–528. `<DOI: 10.1126/science.aav5845>`

[31] Glynn, C.; Hernandez, E.; Gallagher-Jones, M.; Miao, J.; Sigurdson, C. J.; Rodriguez, J. A. Structural Consequences of Sequence Variation in Mammalian Prion $\beta 2 \alpha 2$ Loop Segments. *Frontiers in Neuroscience* **2022**, 16. `<DOI: 10.3389/fnins.2022.960322`

[32] Sokolov, A. N.; Bucar, D.-K.; Baltrusaitis, J.; Gu, S. X.; MacGillivray, L. R. Supramolecular Catalysis in the Organic Solid State through Dry Grinding. *Angew. Chem. Int. Ed.* **2000** 49 (25), 4273–4277. `<DOI: 10.1002/anie.201000874>`

CHAPTER 4

Beyond MicroED: *Ab Initio* Crystal Structures Using 4D–STEM

4.1 Abstract

Microcrystal electron diffraction (microED) has recently morphed into an increasingly mainstream technique in structural chemistry. MicroED's ability to interrogate nanocrystals orders of magnitude too small for conventional X-ray diffraction has enabled solid-state structure elucidation of several species previously considered impossible to solve using X-ray crystallography. Nevertheless, selected area aperture-enabled microED remains thwarted by the presence of disordered, overlapping, or otherwise poorly diffracting domains, all of which routinely conspire to diminish data quality. Just as insufficient crystal size historically stymied conventional X-ray methods, these nanoscale defects frequently prohibit structure solution using classical microED. To overcome this, we apply the 4D scanning electron microscopy (4D–STEM) technique nanobeam electron diffraction tomography (nanoEDT). Our results represent the first 4D–STEM structures phased ab initio by direct methods. Critically, 4D–STEM's unique ability to pinpoint a specific nanoscale volume for data analysis enables pixel-by-pixel spatial exclusion of unwanted signal from Bragg-silent regions, empowering us to simply pick and choose whichever coherently diffracting zones (CDZs) of crystal generate the highest-quality diffraction patterns. Furthermore, our analysis unveils that CDZs form an intricate topography of unpredictably distributed striations. CDZs appear as randomly shaped slivers often embedded within relatively Bragg-silent domains, even in nanocrystals anticipated to contain well-ordered, monolithic lattices. The ubiquity of these

imperfections indicates sharp deviation from the defect-free crystals assumed in computational simulations of electron diffraction patterns, providing an explanation for the current chasm between theory and experiment.

4.2 Motivation and Background

MicroED's ability to extract atomic-resolution diffraction from nanocrystals has proved liberating to synthetic chemists and structural biologists, both of whom frequently encounter species recalcitrant to X-ray-scale crystallization. Nevertheless, 3D ED remains thwarted by disordered crystalline samples that contain significant defects or imperfections in lattice structure. Furthermore, continuous-rotation 3D ED data is typically recorded using a sizeable (e.g., 50-100 microns) selected-area (SA) aperture. As a result, conventional microED diffraction patterns contain signal averaged over all materials isolated within the confines of the SA aperture. This frequently leaves the experimentalist frustratingly unable to circumvent random obstacles, such as the inopportune presence of multiple crystals located very close together (an especially common phenomenon at high tilt angles). Additionally, the positional instability of the substrate during rotation sets a lower bound on the SA aperture size. Disordered, overlapping, or pathologically twinned domains—all features which microED is powerless to deconvolute—can also significantly diminish diffraction data quality, potentially prohibiting structure solution by *ab initio* phasing.

Our experimental approach features key distinctions from both continuous-rotation microED and convergent-beam 4D–STEM. Conventional microED utilizes parallel illumination in microprobe mode, resulting in a floodlit electron beam approximately 5-10 μm in diameter (Figure 4.1). Under these conditions, the full width at half maximum (FWHM) of the probe generally dwarfs the dimensions of the crystal under irradiation, yielding an aggregate diffraction pattern averaged across the entirety of the specimen. Conversely, our 4D–STEM approach leverages aberration-corrected optics to produce a scanning electron nanobeam with a narrow semiconvergence angle [1, 2], focused to a FWHM of approximately 20 nm. This nanoscale probe is then raster-scanned across the specimen at an $n \times n$ array of real-space points separated by a sub-20 nm step size, allowing for much more granular spatial subsampling of the illuminated crystal. A single 4D–STEM dataset consists of 2^n sparse diffraction patterns (indexed by reciprocal-space coordinates q_x and q_y), each linked with an associated pair of scan positions (x, y) in real space. These four parameters correspond to the four eponymous "dimensions" in 4D–STEM. Contrary to the convergent-beam electron diffraction (CBED) technique typically used in materials science, our method features a near-parallel beam to generate point-like Bragg peaks in lieu of Bragg disks, producing ED patterns comprehensible to indexing and integration routines originally developed for X-ray crystallography. Furthermore, to minimize beam-induced radiolytic damage, our experiments exploit a continuously adjustable gun lens to generate an ultra-low probe current.

A central aspect of our method involves the strategic placement of virtual apertures over specific Bragg peaks. This procedure—equivalent to masking out signal corresponding to all electrons scattered within an arbitrarily chosen solid angle (in millisteradians)—effectively causes the associated subset of pixels in the virtual dark-field image to "light up." If the selected solid angle encompasses a Bragg peak, we can directly pinpoint the contours of the corresponding CDZ which produced it. We describe these pixels in terms of two defining properties: their location and their intensity. Their intensity is linearly related to the strength of the corresponding diffraction-space signal within the selected solid angle, whereas their location is given by the relevant x, y probe positions associated with the q_x and q_y coordinates of that region in reciprocal space. Such spatial detail is inaccessible to SA aperture-enabled microED, which would return an averaged diffraction pattern (a) indiscriminately blending signal from all CDZs and (b) devoid of any corresponding real-space information. Our analysis shows that CDZs resemble an intricate mosaic of unpredictably shaped striations. Generally, the lattice coherence area represented by these striations tends to shrink as a monotonic function of increasing scattering angle. As we place virtual apertures around Bragg peaks corresponding to progressively higher-resolution information, smaller slivers of crystal "light up" in real space, suggesting that sub-Sheldrick reflections originate from a minuscule fraction of ordered unit cells within an already nanoscale volume.

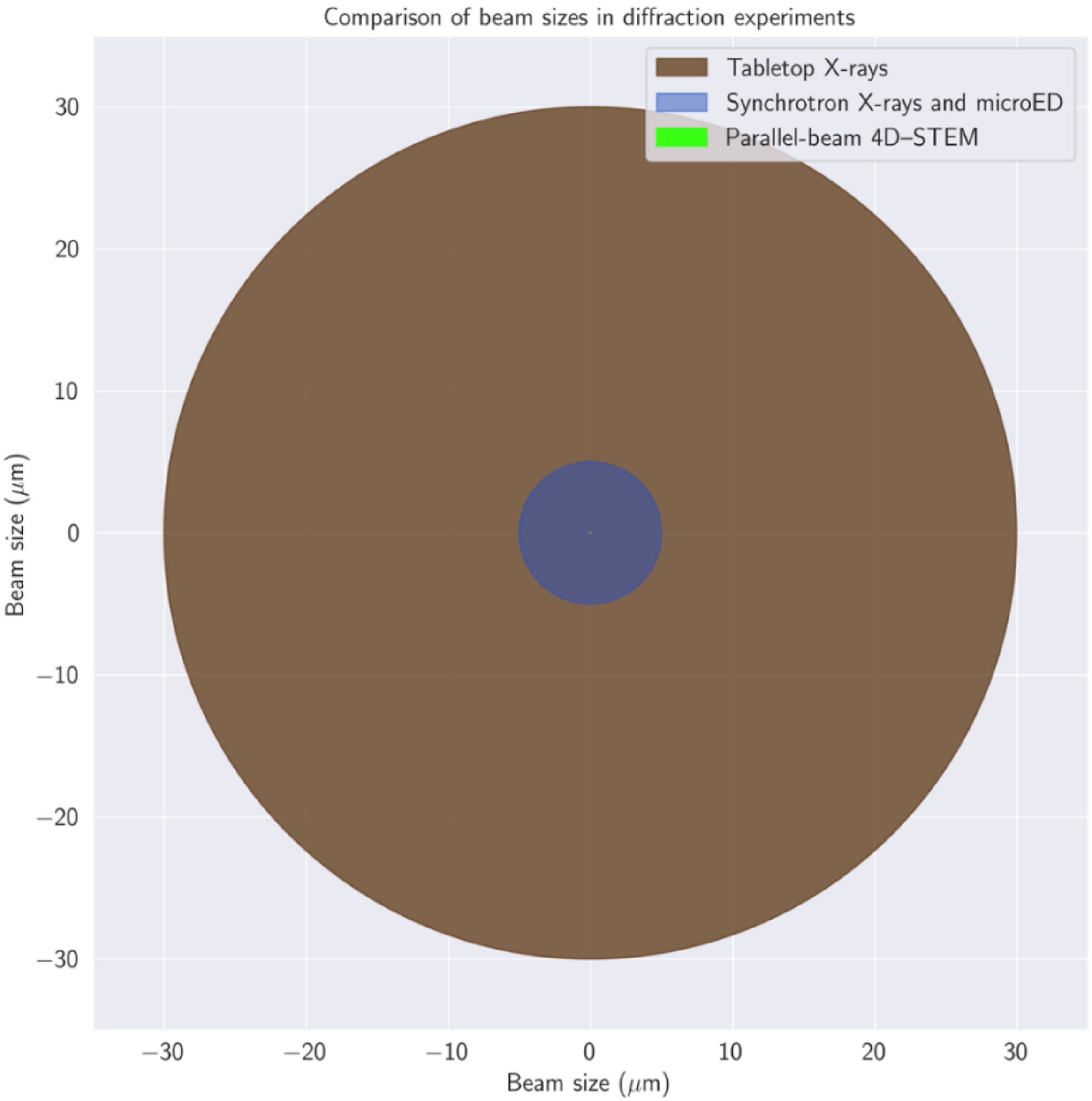

Figure 4.1: **Comparison of beam sizes between in-house X-ray diffractometers, synchrotron X-rays at microfocus beamlines/microED, and 4D–STEM.**

4.3 Substrate Scope and Experimental Methods

This section serves as a roadmap for the Ni(dppf)Cl_2 4D–STEM tilt series experiments. Although several other tilt series were acquired on a range of other substrates, a persistent issue with an overheating projector lens on TEAM 0.5 prevented us from using the correct virtual camera length, rendering many of those datasets unusable due to an inability to sample sufficiently high-resolution Bragg reflections at the periphery of the detector. In the two tilt series recorded in this chapter, the resolution at the edge of the 4DCamera is approximately 0.8 Å. Unless otherwise specified, all 4D–STEM experiments were conducted using 300 mesh Au grids with an ultrathin ($\leq$ 3 nm) carbon film stretched over a lacey carbon support (Ted Pella product no. 01824G).

Navigation on TEAM 0.5 is performed using a PS2 controller, which pains me as a Nintendo loyalist. To collect a dataset, the TEAM Stage GUI was used to manually adjust the alpha tilt in increments of 1 degree between frames. This is surprisingly time-consuming thanks to the piezoelectric stage; it can take 5-10 seconds to complete. Once the rectangular box labeled "Approach" stops flashing green, the software has essentially given up (i.e., determined that it's close enough to the target angle), and data acquisition can proceed. Each crystal was roughly realigned and centered for each successive frame, since the stage nearly always drifts in the interim. During this process, the crystal unfortunately receives an extra dose of electrons.

4.3.1 Ni(dppf)Cl_2

Two viable 4D–STEM tilt series were acquired on the organometallic complex Ni(dppf)Cl_2, both at an accelerating voltage of 300 kV: one at 28.5 kx (movie 1, from -50 to +60 degrees) and one at 57 kx (movie 2, from +60 to -66 degrees). Five representative 4D–STEM scans at selected angles are displayed in Figures 4.4–4.8 (movie 1) and Figures 4.9–4.13 (movie 2). Diffraction patterns were (a) exported in SMV format, (b) indexed and integrated with DIALS, (c) merged and scaled with XSCALE, and (d) phased using direct methods in shelxd. Gratifyingly, indexing proceeded relatively smoothly, correctly identifying a triclinic polymorph of Ni(dppf)Cl_2 previously

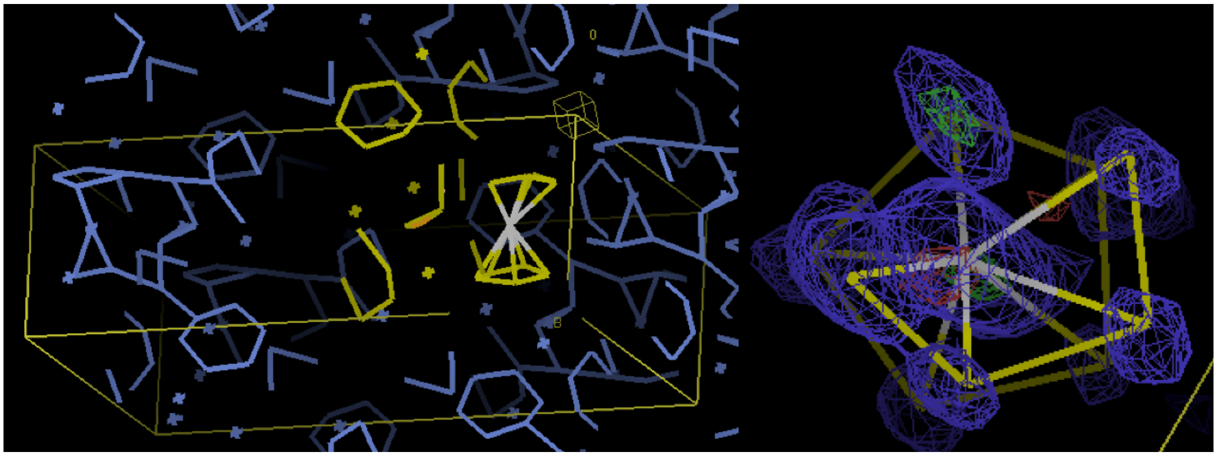

Figure 4.2: **Raw shelxd output for the first 4D–STEM tilt series, representing an ab initio structure of Ni(dppf)Cl_2.** Barring a single carbon atom clearly identifiable in the Fourier difference map (right inset), all of the ferrocenyl moiety is correctly placed, along with the nickel dichloride. Coot fails to draw the phosphorus–carbon bonds in the dppf ligand adequately, but most of the carbon atoms in the four phenyl rings also pop out *ab initio*.

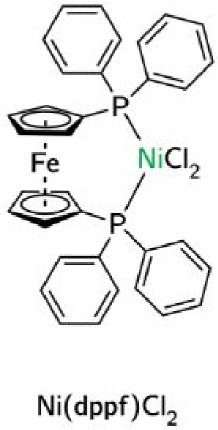

Figure 4.3: **Schematic of Ni(dppf)Cl_2.**

solved via single-crystal X-ray diffraction [4]. Many runs of shelxd yielded a range of *ab initio* structure solutions in which the majority of atoms in Ni(dppf)Cl_2 were correctly placed (Figure 4.2). Although 0.8 Å resolution *ab initio* structures were successfully obtained (Figure 4.14–4.15), refinement statistics were generally worse than comparable 3D ED structures, generally in the $R1 = 30$–40% range despite no errors in atomic placement or assignment. A consistent problem observed during data reduction of these 4D–STEM tilt series involved inaccurate integration of subangstrom resolution Bragg reflections, which were clearly visible by eye but inadequately scaled such that $\mathrm{CC}_{1/2}$ in the outermost shells was generally quite poor, close to e^{-1}. Development of new processing routines, especially to account for partiality of Bragg reflections sampled discretely, is probably necessary to extract the highest-quality structures possible from these 4D–STEM data. Nevertheless, these results represent the first 4D–STEM structures phased by direct methods—a significant advance given the consistent usage of software designed for X-ray crystallography, a much more mature field.

4.4 Discussion and Implications for 3D ED

Consider a perfectly monolithic crystal oriented perpendicular to the impinging beam. In such an idealized system, every single region of the crystal would constitute one unbroken real-space lattice—thus generating identical diffraction patterns in reciprocal space no matter where the crystal was sampled. Averaging signal over the entirety of such a crystal would linearly amplify the recorded intensities without altering their underlying statistical distribution. Furthermore, if such a crystal were sufficiently thick (i.e., >2 elastic mean free paths), a significant fraction of incident electrons would begin to undergo multiple elastic or "dynamical" scattering. Conversely, however, if the irradiated crystal contained significant deviations from perfection—for instance, mechanical deformations such as bend contours—individual regions would begin to produce appreciably different diffraction patterns relative to their neighbors. Averaging signal over a highly imperfect crystal would effectively subsume a range of overlapping reciprocal lattices, causing

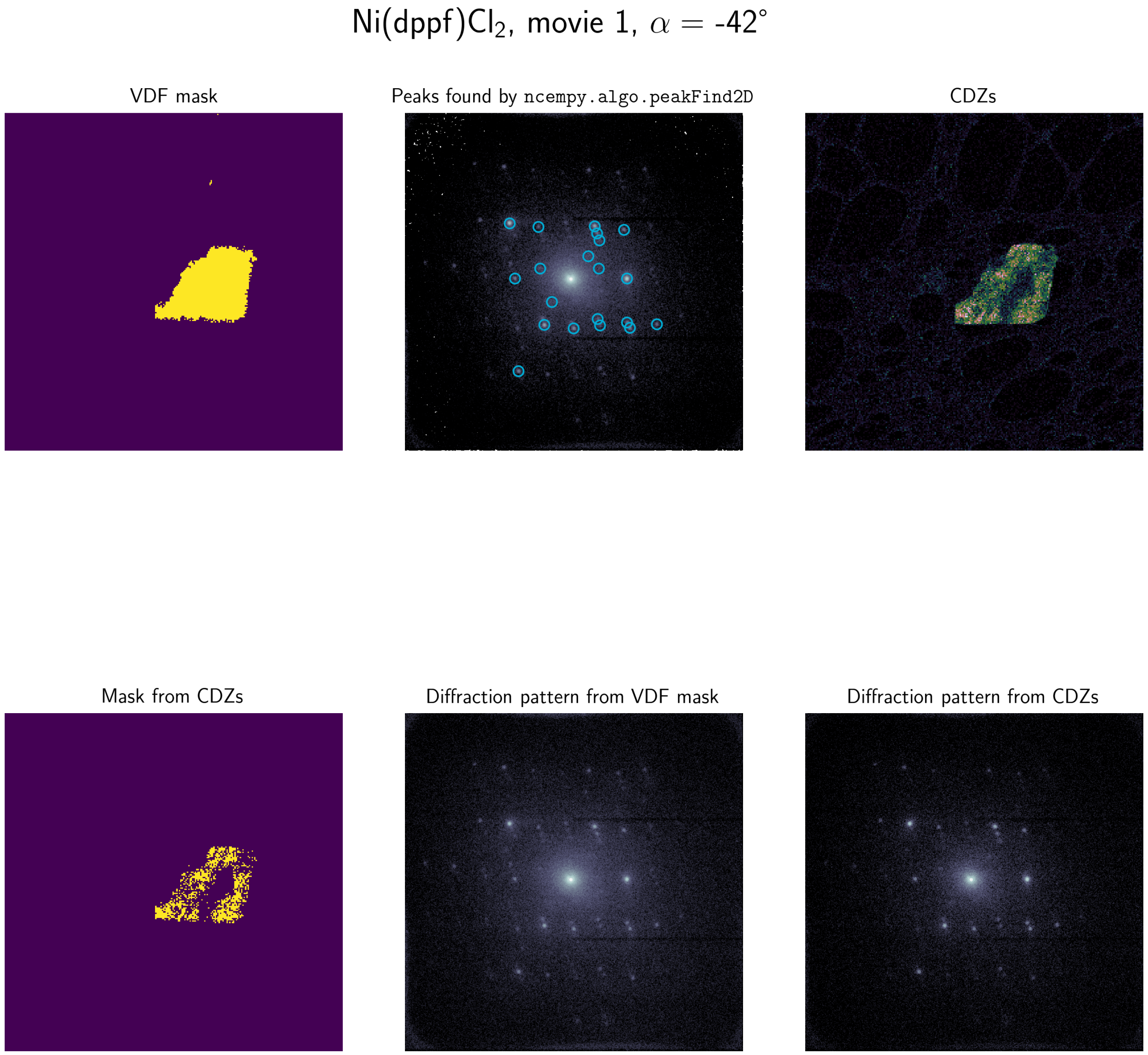

Figure 4.4: **VDF mask, coherently diffracting zones corresponding to circled peaks, mask corresponding to identified CDZs, and corresponding diffraction patterns for the 9th 4D–STEM scan in the 28.5 kx Ni(dppf)Cl$_2$ tilt series.** At this particular angular orientation, a central swath of the crystal is mostly Bragg-silent and is excluded from the mask generated by the CDZs. The resultant diffraction pattern features better SNR than its counterpart from the full VDF mask, with a reduction in background noise especially noticeable around the unscattered beam.

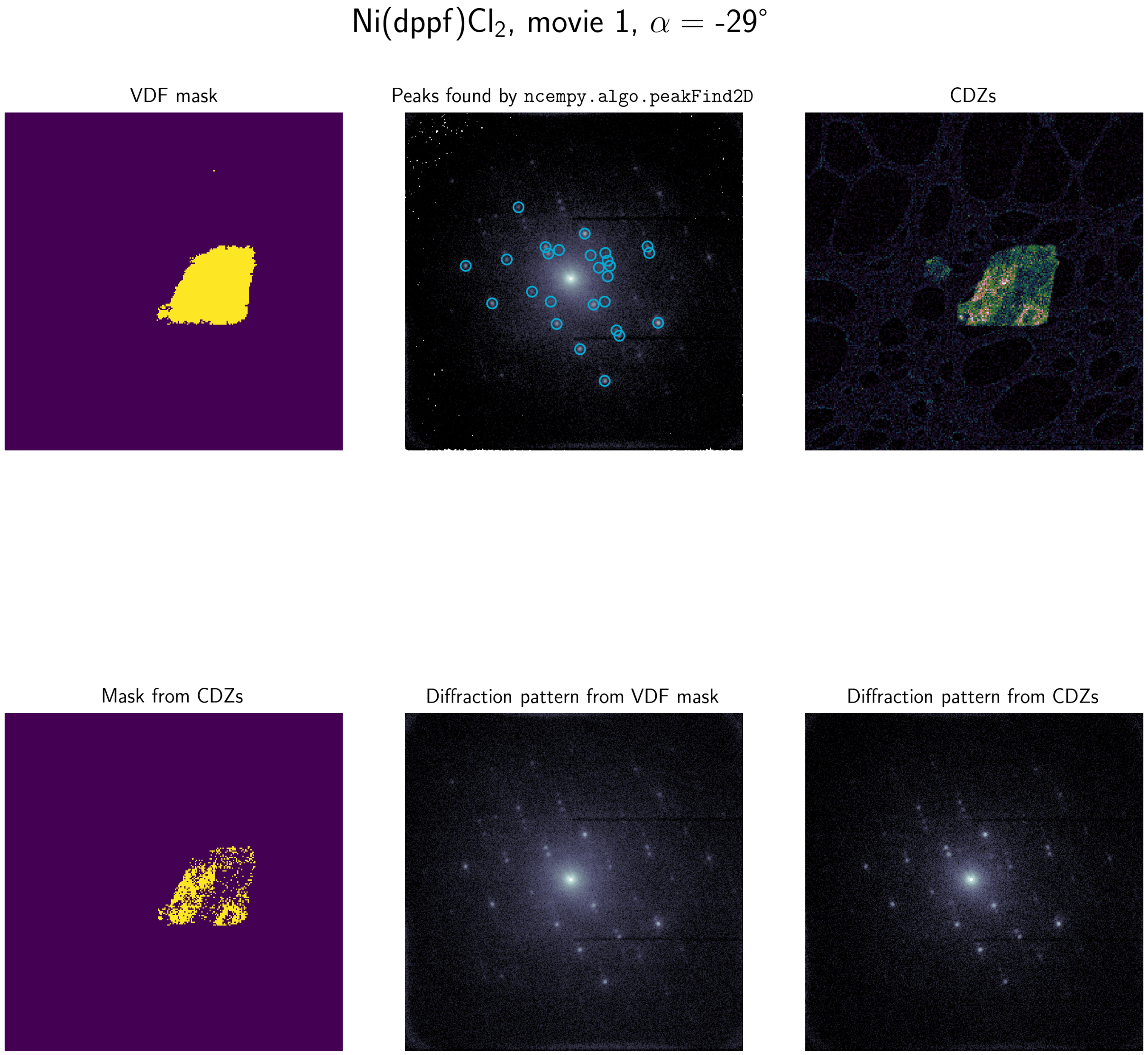

Figure 4.5: **VDF mask, coherently diffracting zones corresponding to circled peaks, mask corresponding to identified CDZs, and corresponding diffraction patterns for the 22nd 4D–STEM scan in the 28.5 kx Ni(dppf)Cl$_2$ tilt series.** After an extra 13 degrees of tilting, the central Bragg-silent swath from Figure 4.4 has shifted orientation slightly.

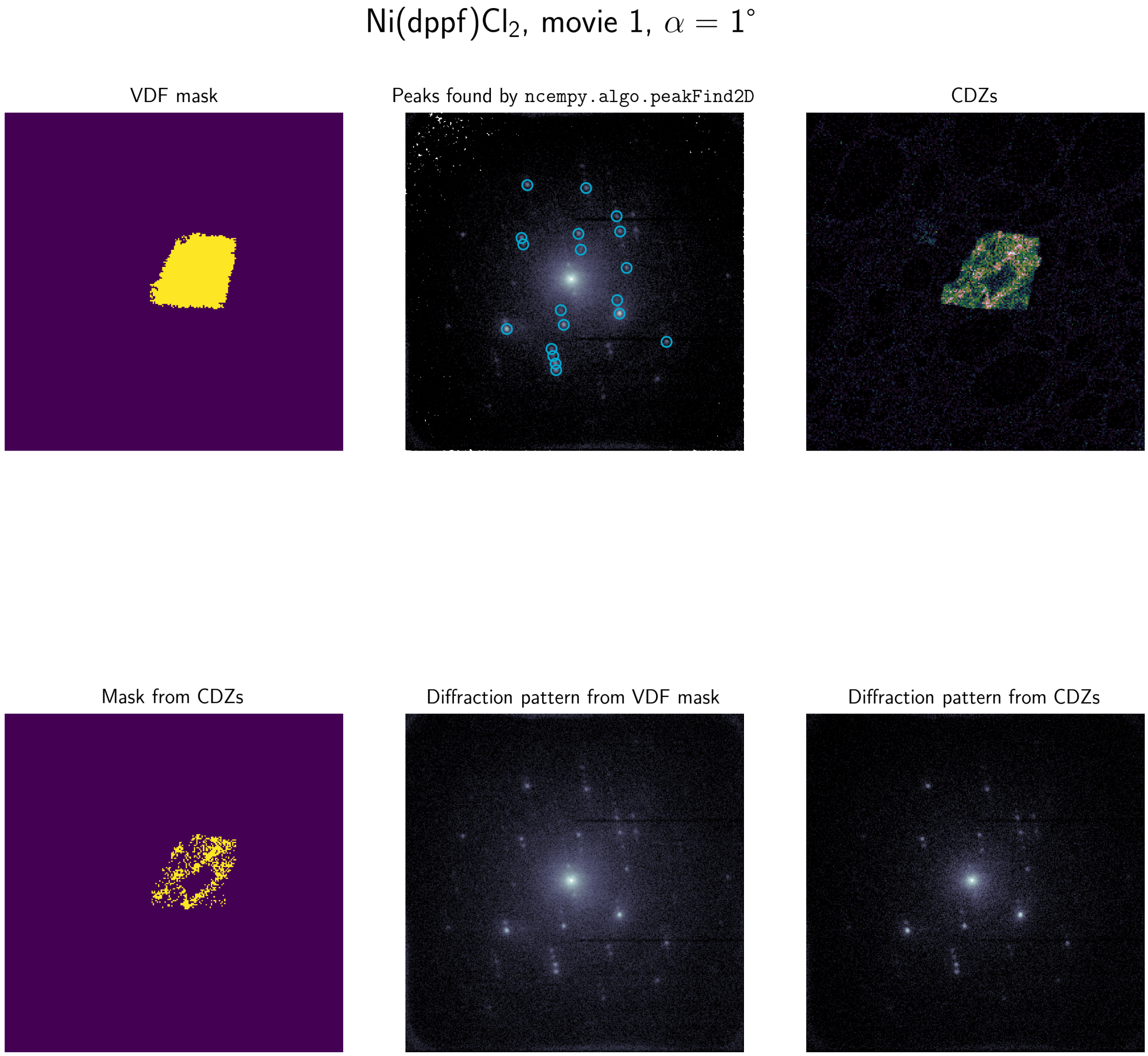

Figure 4.6: **VDF mask, coherently diffracting zones corresponding to circled peaks, mask corresponding to identified CDZs, and corresponding diffraction patterns for the 52nd 4D–STEM scan in the 28.5 kx Ni(dppf)Cl_2 tilt series.** At this angle, the Bragg-silent region resembles a valley which has migrated toward the center of the crystal relative to Figure 4.5.

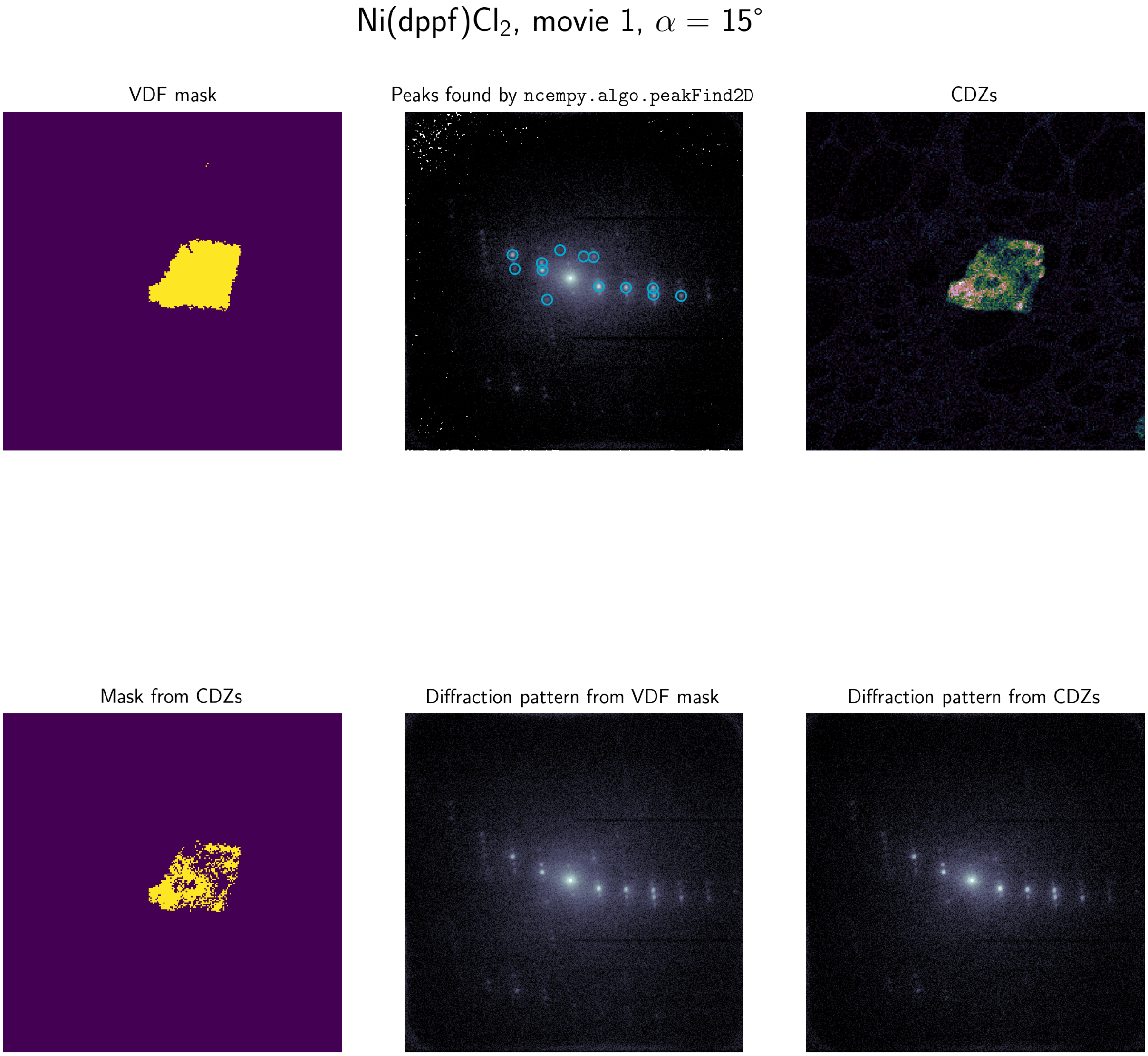

Figure 4.7: **VDF mask, coherently diffracting zones corresponding to circled peaks, mask corresponding to identified CDZs, and corresponding diffraction patterns for the 65th 4D–STEM scan in the 28.5 kx Ni(dppf)Cl$_2$ tilt series.**

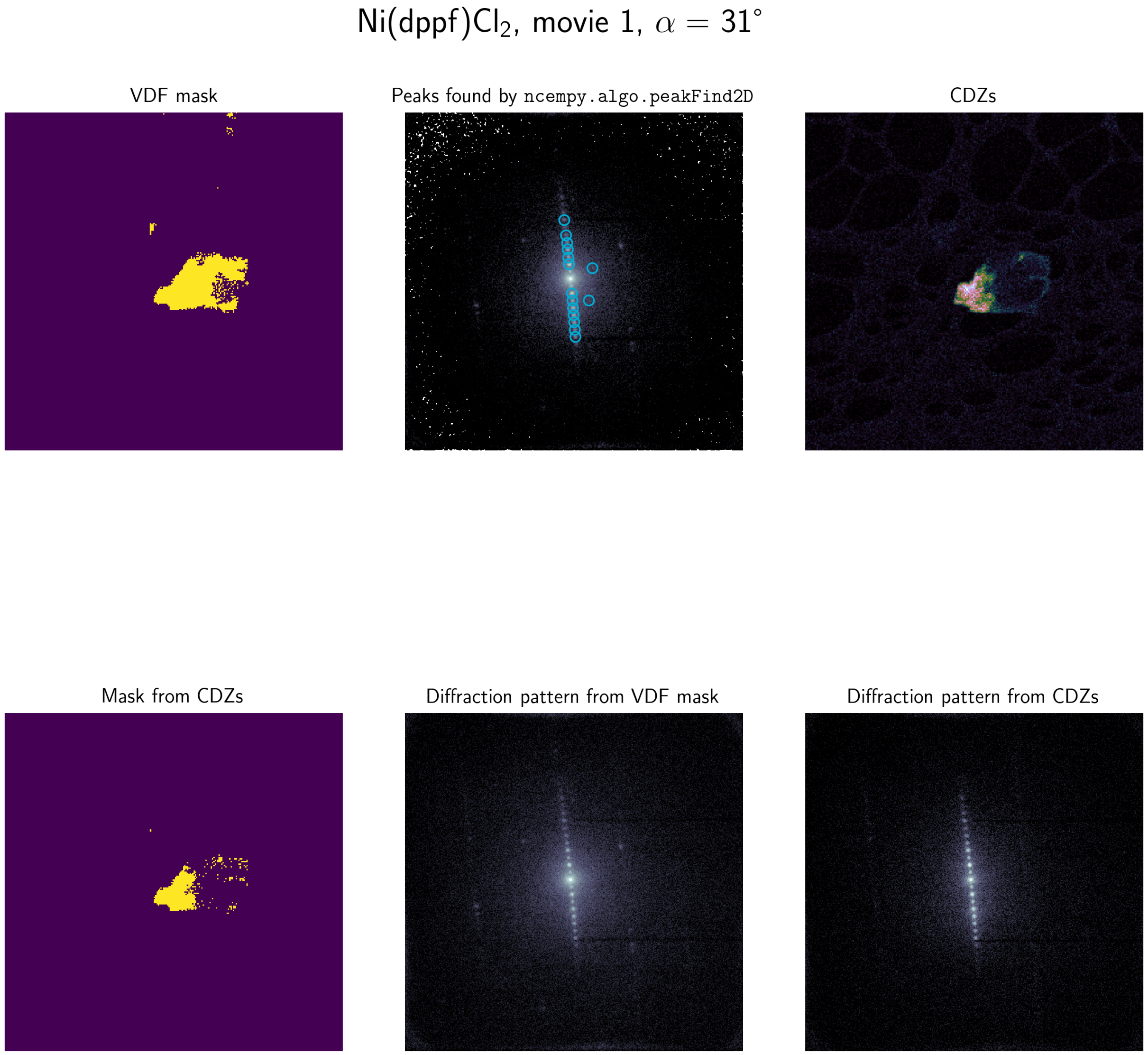

Figure 4.8: **VDF mask, coherently diffracting zones corresponding to circled peaks, mask corresponding to identified CDZs, and corresponding diffraction patterns for the first representative 4D–STEM scan in the 28.5 kx Ni(dppf)Cl_2 tilt series.** At this point in the tilt series, a crater had emerged on the right flank of the crystal due to inappropriate placement of the dwell point, and the remaining CDZs cluster toward the left half.

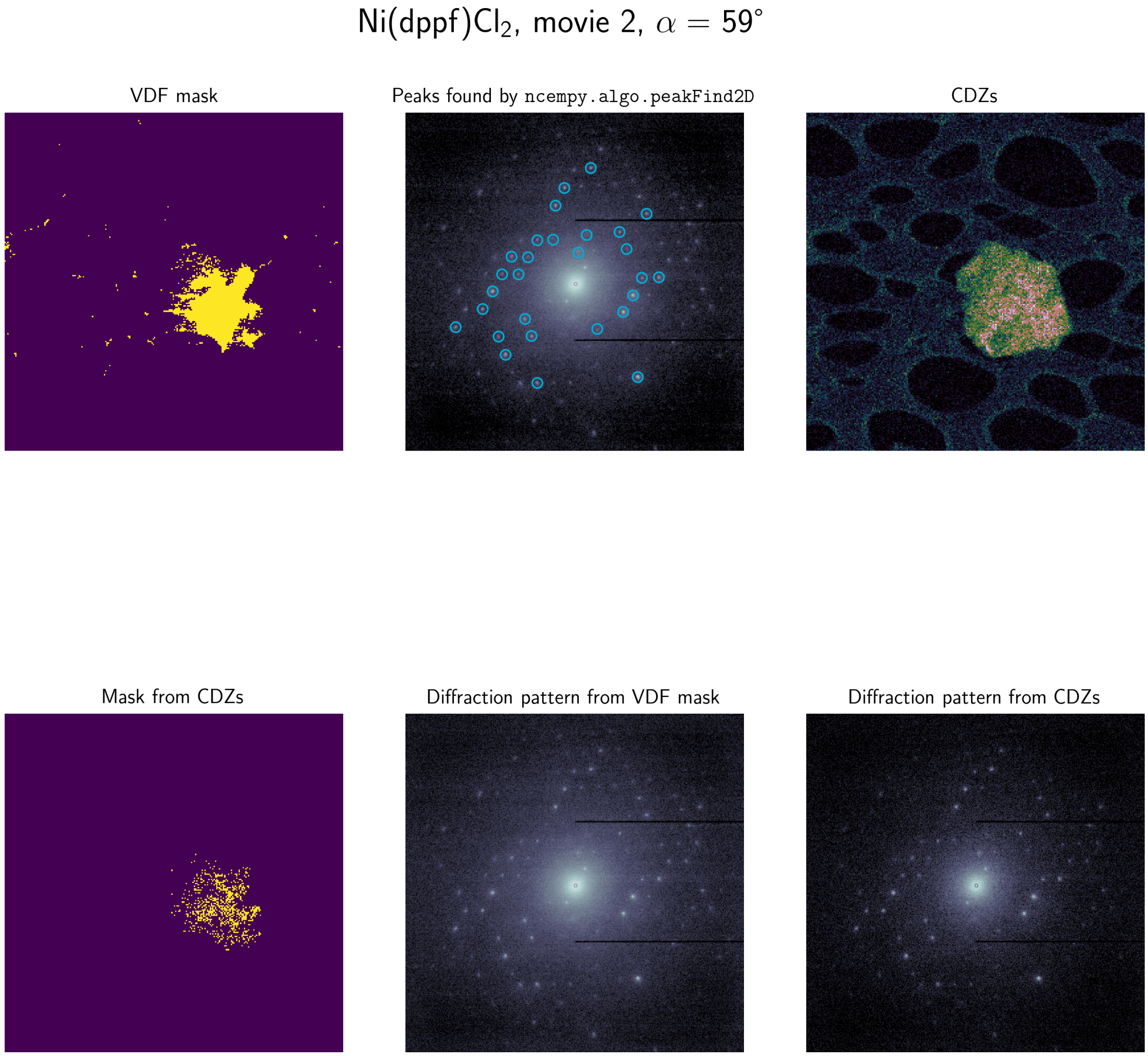

Figure 4.9: **VDF mask, coherently diffracting zones corresponding to circled peaks, mask corresponding to identified CDZs, and corresponding diffraction patterns for the 1st 4D–STEM scan in the 57 kx Ni(dppf)Cl$_2$ tilt series.** Since this crystal is fairly thin, the VDF mask is difficult to generate via thresholding. In this case, the CDZs form a mottled distribution more evenly spread out throughout the crystal, as opposed to the fjords and valleys in the previous Ni(dppf)Cl$_2$ dataset. Nevertheless, spatial subsampling is still decent when generating signal from the CDZs, and the resultant diffraction pattern is less noisy.

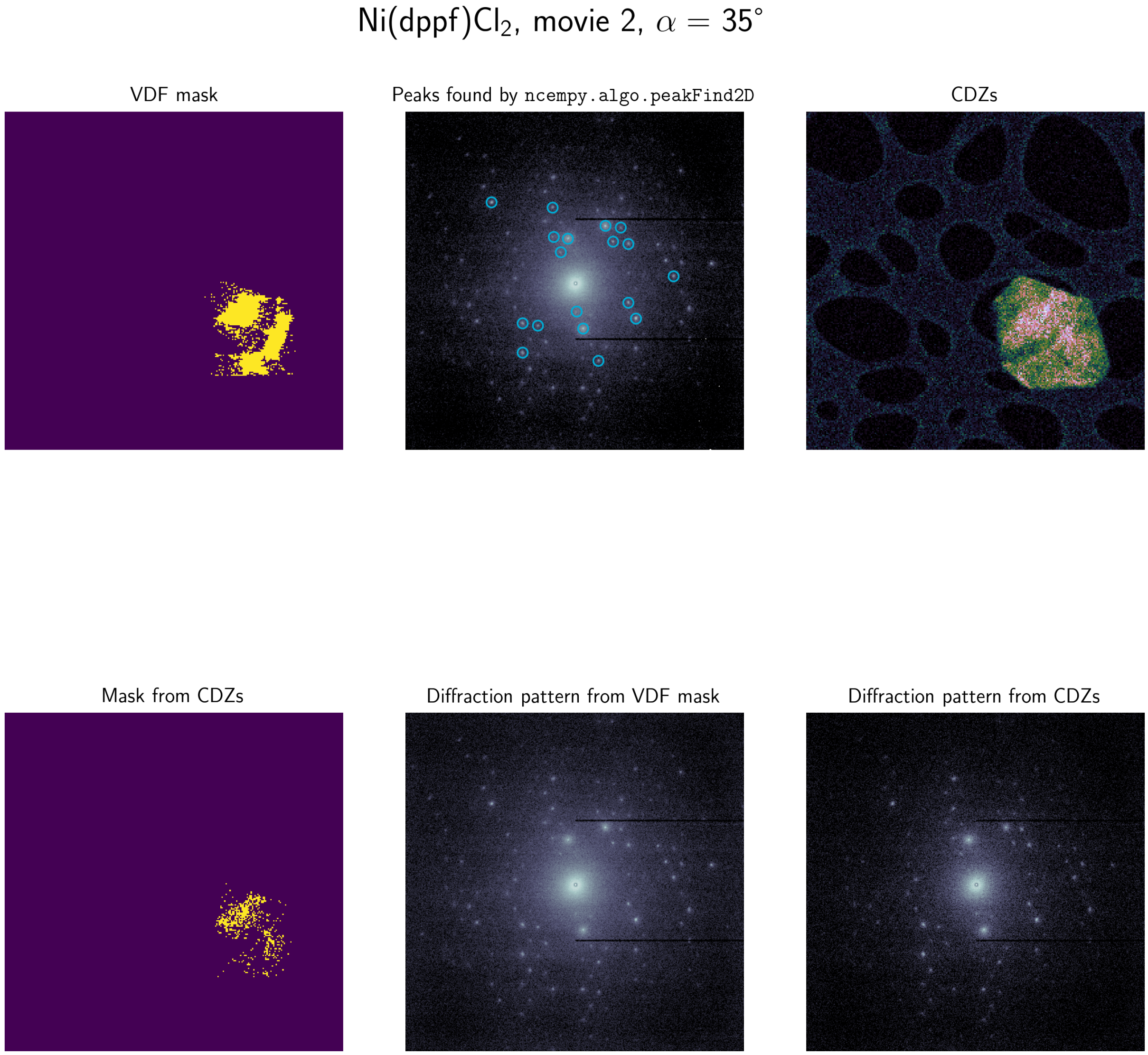

Figure 4.10: **VDF mask, coherently diffracting zones corresponding to circled peaks, mask corresponding to identified CDZs, and corresponding diffraction patterns for the 25th representative 4D–STEM scan in the 57 kx Ni(dppf)Cl_2 tilt series.**

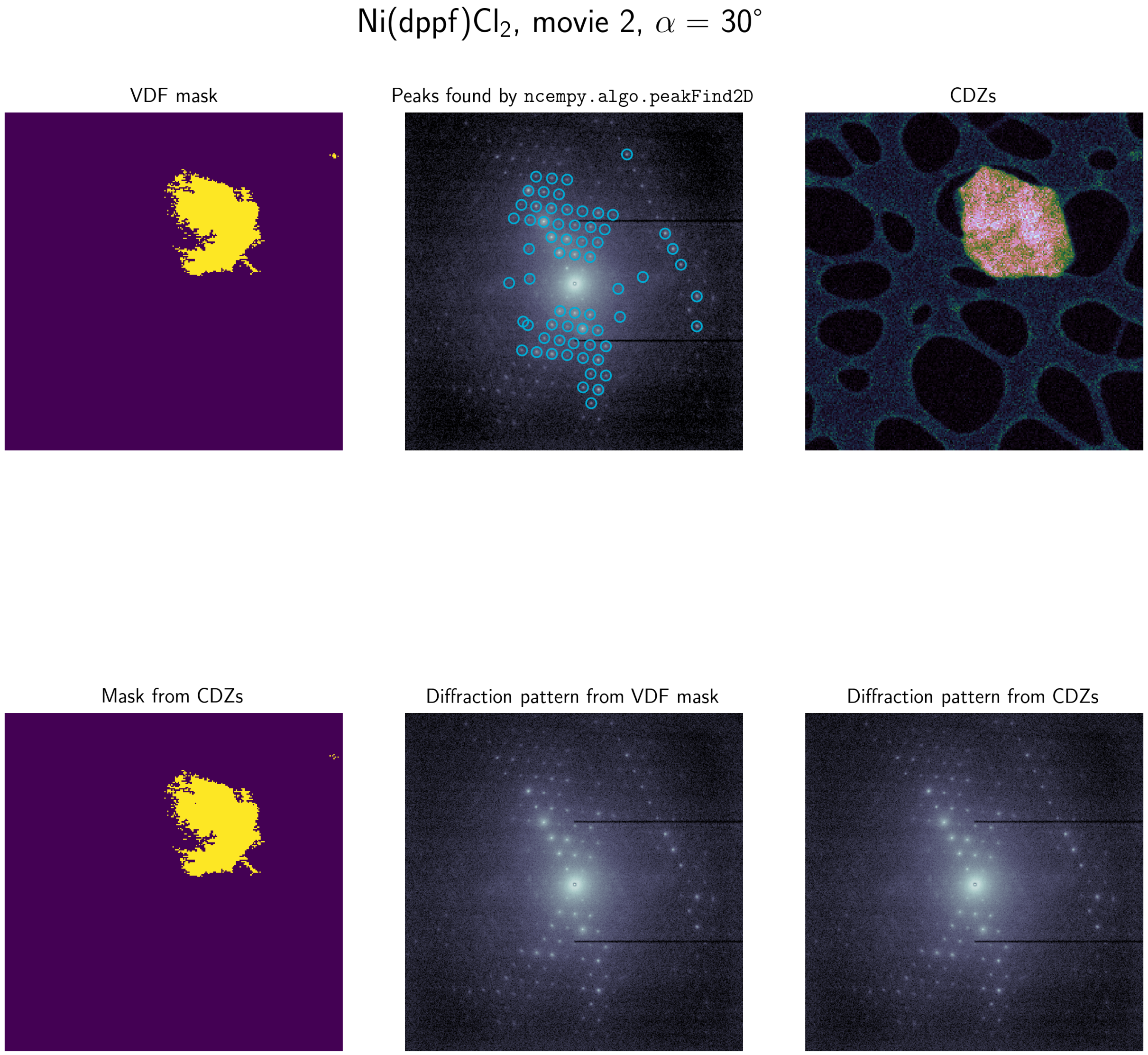

Figure 4.11: **VDF mask, coherently diffracting zones corresponding to circled peaks, mask corresponding to identified CDZs, and corresponding diffraction patterns for the 30th 4D–STEM scan in the 57 kx Ni(dppf)Cl$_2$ tilt series.** At this angular orientation, the CDZs appear more or less uniformly distributed, and the mask generated from the CDZs is not appreciably different from the VDF mask itself.

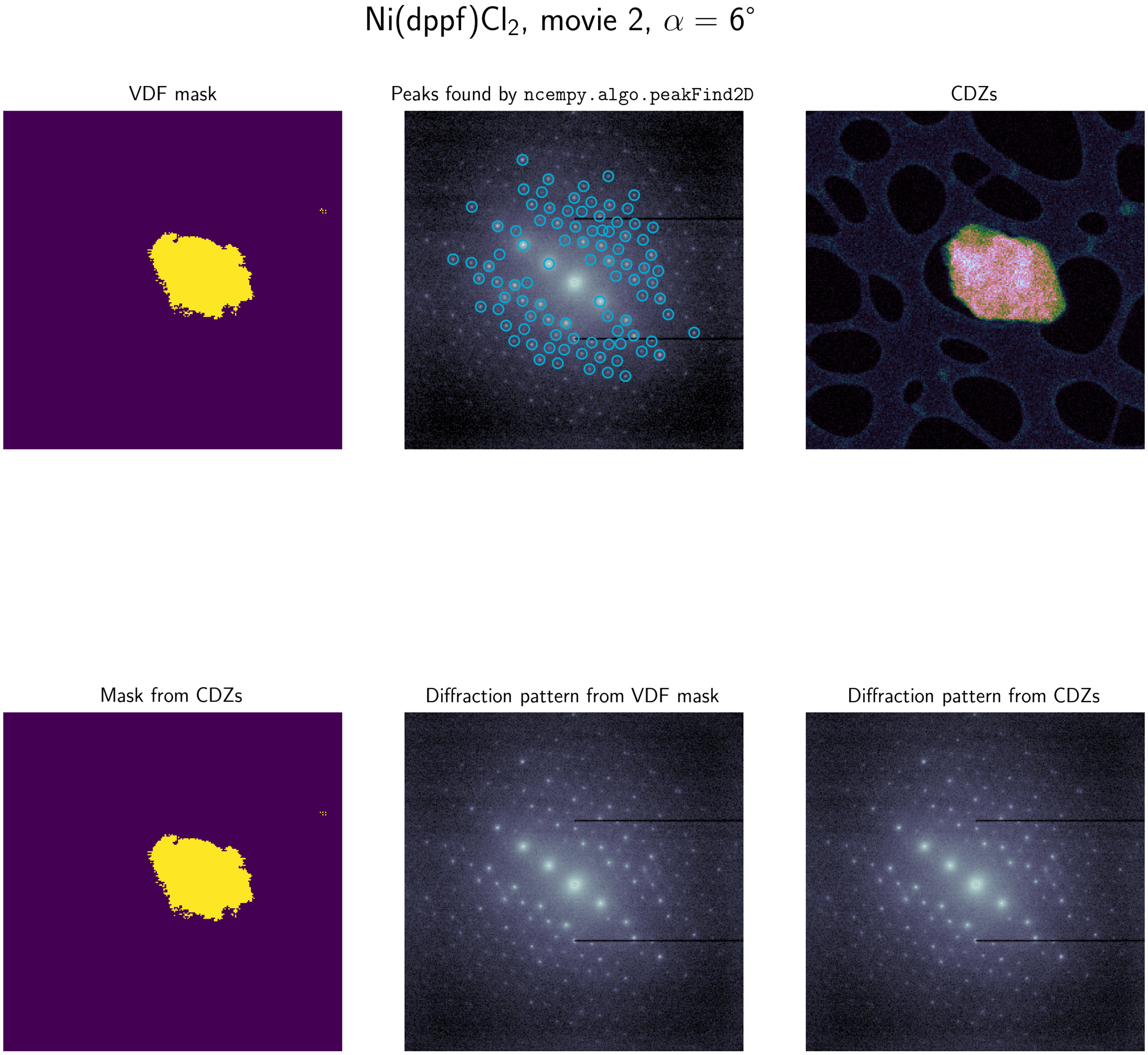

Figure 4.12: **VDF mask, coherently diffracting zones corresponding to circled peaks, mask corresponding to identified CDZs, and corresponding diffraction patterns for the 54th 4D–STEM scan in the 57 kx Ni(dppf)Cl$_2$ tilt series.** At this angular orientation, the CDZs appear especially uniformly distributed, and the mask generated from the CDZs is almost identical to the VDF mask itself.

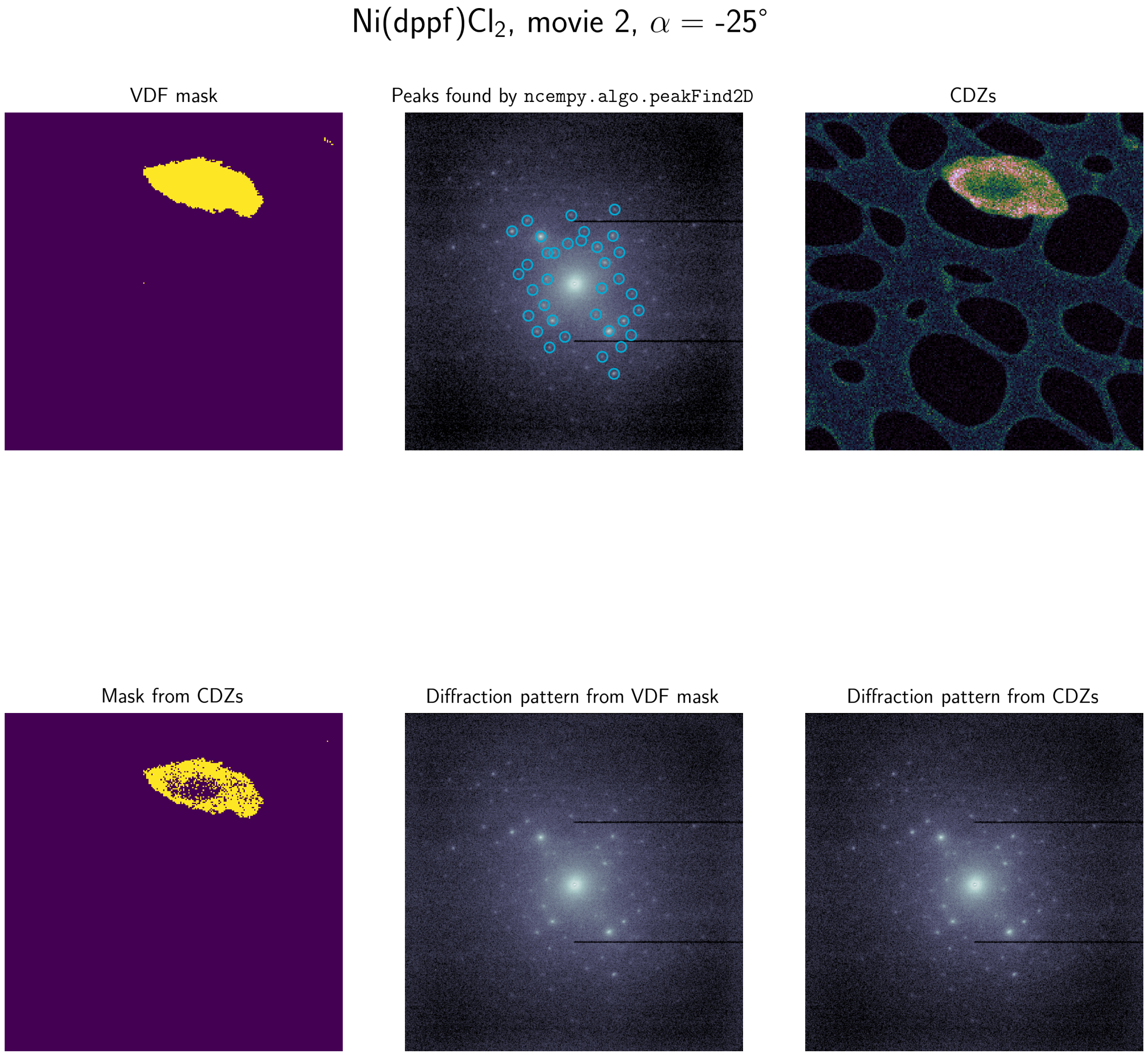

Figure 4.13: **VDF mask, coherently diffracting zones corresponding to circled peaks, mask corresponding to identified CDZs, and corresponding diffraction patterns for the 85th 4D–STEM scan in the 57 kx Ni(dppf)Cl$_2$ tilt series.** At this angular orientation, the crystal has rotated away from the uniform distribution of CDZs observed earlier in the tilt series and now displays an ellipsoidal depression in its center.

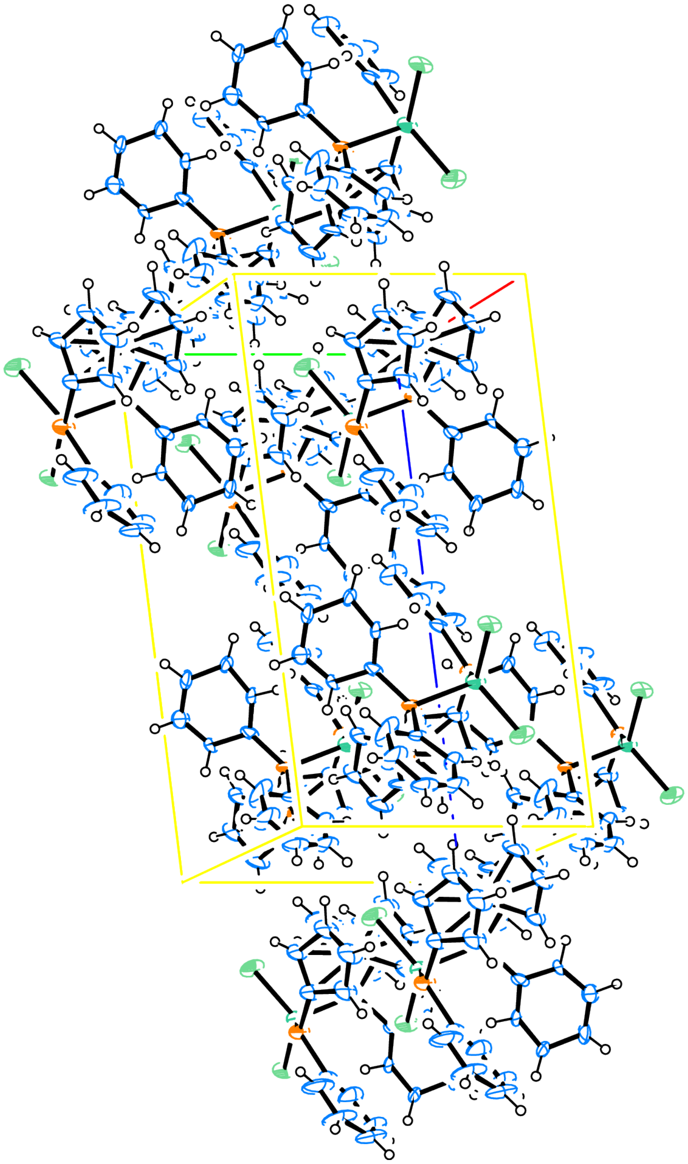

Figure 4.14: **ORTEP diagram of an *ab initio* structure of Ni(dppf)Cl$_2$ solved from the 4D–STEM tilt series, viewed orthogonal to the [001] set of Bragg planes.** See Listing 4.3 for associated CIF file used to generate this image.

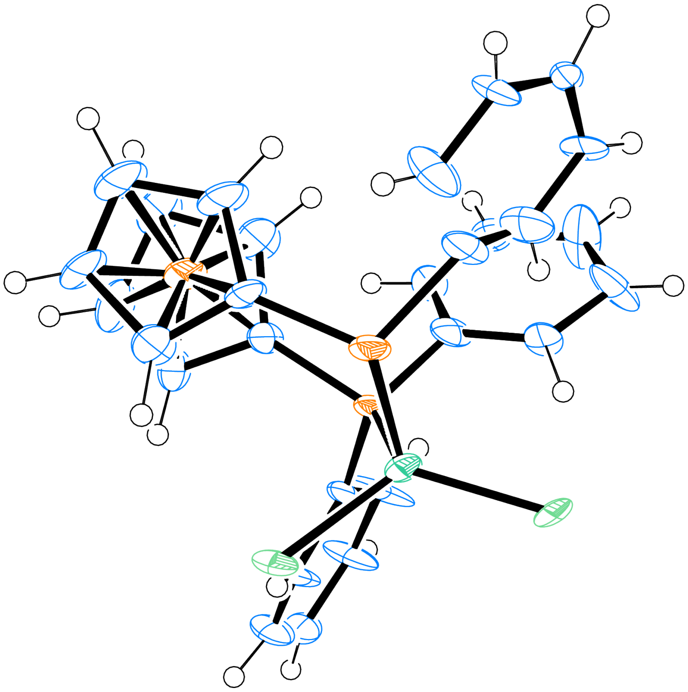

Figure 4.15: **ORTEP diagram of an *ab initio* structure of Ni(dppf)Cl_2 solved from the first 4D–STEM tilt series, displaying the asymmetric unit.** Despite reasonable anisotropic displacement parameters and many attempts at further refinement of this structure and others, the $R1$ value generally did not drop below the 35% mark. See Listing 4.3 for associated CIF file used to generate this image.

ideally point-like Bragg peaks to expand into anisotropic ellipsoids.

In conventional X-ray crystallography, mosaicity is commonly invoked to rationalize these effects, dating back to C. G. Darwin's 1922 monograph on X-ray diffraction from imperfect crystals [5]. Darwin's theory conceptualizes a single crystal as a conglomerate of smaller crystallites, each rotationally misoriented relative to some mean position. Modern X-ray data processing software7 attempts to estimate the angular spread of these putative "mosaic blocks," usually by assessing the broadening of Bragg peak profiles. Nevertheless, a typical X-ray diffraction or SAED experiment neither measures the size nor pinpoints the location of an individual "mosaic block." Moreover, mosaicity makes no attempt either to count the constituent crystallites or to model whatever implicit boundaries or discontinuities must have delineated them [6]. In practice, mosaicity functions more as a broad-spectrum "fudge factor" which captures the influence of many sources of disorder simultaneously. For instance, in tandem with crystal-specific parameters such as lattice strain, mosaicity also encompasses instrumental variables unrelated to crystal quality, such as beam divergence and spectral dispersion [7]. Although conceptually useful, Darwin's model predated the development of methods capable of directly isolating the sub-micrometric contours of a coherently diffracting zone.

Broadly, the ubiquity of the nanoscale imperfections described in this dissertation strongly contradicts the idealized models of perfect crystals typically used in simulations of ED data. These simulations predicted that multiple elastic or "dynamical" scattering events would fatally corrupt signal from Bragg peaks, untethering the measured intensities from genuine structure-factor amplitudes [8]. However, an expansive body of experimental work has since demonstrated perfectly viable 3D ED data collection from crystals much thicker than the theoretical limit suggested in 2015. Our work adds a uniquely topographic perspective to this discussion. At a range of angular orientations, we consistently observed different swathes of crystal remaining mostly Bragg-silent, suggesting a complex three-dimensional topography of interlocking CDZs in which the effective coherence volume of the lattice was generally substantially smaller than the gross dimensions of the crystal itself. In other words, in 3D molecular crystals, few regions of the lattice contain unit cells oriented perfectly enough to generate genuinely dynamical scattering. In standard SAED, rotational misorientation between CDZs would also affect the measured intensities, which would essentially reflect a weighted average of signal blended from all CDZs within the SA aperture. This underlying heterogeneity helps rationalize why dynamical scattering has never functioned as a prohibitive impediment to solving the structures of molecular crystals using 3D ED.

4.5 Supplementary Code

This section contains several sample bash and Python scripts used to parse and analyze the 4D–STEM data discussed earlier in the chapter, as well as a refined CIF file containing atomic coordinates for the 4D–STEM structure of Ni(dppf)Cl_2.

```
%matplotlib notebook

from pathlib import Path
from collections import namedtuple
from scipy.optimize import curve_fit
import matplotlib as mpl
import matplotlib.pyplot as plt
from matplotlib.colors import LogNorm,PowerNorm
from matplotlib.patches import Rectangle, Polygon
import numpy as np
from numpy.linalg import svd
import imageio
from scipy import ndimage
import stempy
import stempy.io as stio
import stempy.image as stim
import ncempy

mpl.rcParams['text.usetex'] = True
mpl.rcParams['text.latex.preamble'] = r"\usepackage{sfmath}"
```

```
mpl.rcParams['font.family'] = 'sans-serif'
mpl.rcParams['font.sans-serif'] = 'cm'
plt.rcParams['figure.dpi'] = 300
plt.rcParams['savefig.dpi'] = 300

dir_path = Path(r"C:\Users\eicn_user\Desktop\ambarneil\4DSTEM_20220223\4
    dstem_nidppf_mov02\counted_hdf5")
file_names = []
file_names = list(dir_path.glob('*centered.h5'))

print(file_names)
threshold = 170

masks = []
full_dps = []
dfs = []
mask_dps = []
mask_dps_bin2 = []
sorted_filenames = []
for full_path in sorted(file_names):
    print(full_path)
    sorted_filenames.append(str(full_path))
    sp = stio.load_electron_counts(full_path)
    df = sp.sum(axis='frame')
    full_dp = sp.sum(axis='scan')
    full_dps.append(full_dp)
    dfs.append(df)

    mask = df.copy()
    mask[df < threshold] = 0
    mask[df >= threshold] = 1

    mask0 = np.zeros((256,256), dtype=bool)
```

```
    mask0[:,110:220] = 1
    mask_crystal = mask * mask0

    ndimage.binary_fill_holes(mask_crystal, output=mask_crystal)
    mask_dp = stim.mask_real_space(sp, mask_crystal)
    masks.append(mask_crystal)
    mask_dps.append(mask_dp)
    mask_dps_bin2.append(ncempy.algo.rebin(mask_dp, 2))

def write_smv(out_path, dp, frame_dimensions=(576, 576)):
    mag = 110  # camera length in mm
    lamda = 0.019687576525122874  # angstrom
    pixel_size = 0.01  # mm

    im = dp.reshape(frame_dimensions)
    if im.max() > ((2 ** 16) - 1):
        im[im > ((2 ** 16) - 1)] = ((2 ** 16) - 1)  # maximum 16 bit value
    allowed
        im[im < 0] = 0  # just in case
        print('warning. Loss of dynamic range due to conversion from 32
   bit to 16 bit')
    im = im.astype(np.uint16)
    dtype = 'unsigned_short'

    # if self.dp.dtype == np.uint16:
    #    dtype = 'unsigned_short'
    # elif im.dtype == np.uint32:
    #    dtype = 'unsigned_long'
    # else:
    #    raise TypeError('Unsupported dtype: {}'.format(im.dtype))

    # Write 512 bytes of zeros
    with open(out_path, 'wb') as f0:
```

```
        f0.write(np.zeros(512, dtype=np.uint8))
    # Write the header over the zeros as needed
    with open(out_path, ’r+’) as f0:
        f0.write("{\nHEADER_BYTES=512;\n")
        f0.write("DIM=2;\n")
        f0.write("BYTE_ORDER=little_endian;\n")
        f0.write(f"TYPE={dtype};\n")
        f0.write(f"SIZE1={im.shape[1]};\n")  # size1 is columns
        f0.write(f"SIZE2={im.shape[0]};\n")  # size 2 is rows
        f0.write(f"PIXEL_SIZE={pixel_size};\n")  # physical pixel size in
   micron
        f0.write(f"WAVELENGTH={lamda};\n")  # wavelength
        if mag:
            f0.write(f"DISTANCE={int(mag)};\n")
        f0.write("PHI=0.0;\n")
        f0.write("BEAM_CENTER_X=1.0;\n")
        f0.write("BEAM_CENTER_Y=1.0;\n")
        f0.write("BIN=1x1;\n")
        f0.write("DATE=Thu Oct 21 23:06:09 2021;\n")
        f0.write("DETECTOR_SN=unknown;\n")
        f0.write("OSC_RANGE=1.0;\n")
        f0.write("OSC_START=0;\n")
        f0.write("IMAGE_PEDESTAL=0;\n")
        f0.write("TIME=10.0;\n")
        f0.write("TWOTHETA=0;\n")
        f0.write("}\n")
    # Append the binary image data at the end of the header
    with open(out_path, ’rb+’) as f0:
        f0.seek(512, 0)
        f0.write(im)

for ii in range(len(mask_dps)):
    print(ii)
```

```
    out = Path(f"C:/Users/eicn_user/Desktop/ambarneil/4DSTEM_20220223/4
   dstem_nidppf_mov02/counted_hdf5/scan_vdf_{ii:04}.img")
    write_smv(out, mask_dps[ii])
    out2 = Path(f"C:/Users/eicn_user/Desktop/ambarneil/4DSTEM_20220223/4
   dstem_nidppf_mov02/counted_hdf5/scan_fulldp_{ii:04}.img")
    write_smv(out2, full_dps[ii])

jj = -50
import skimage
from skimage.filters import threshold_otsu

for ii in range(len(mask_dps)):
    sp = stempy.io.load_electron_counts(file_names[ii])
    dp = mask_dps[ii]
    dp_smooth = ndimage.gaussian_filter(dp.astype(np.float32), 3)

    numpeaks = []
    threshold = 5
    threshold = threshold / dp_smooth.max()
    peaks = ncempy.algo.peak_find.peakFind2D(dp_smooth, threshold)
    print(threshold)

    keep = []

    centerx = 278
    centery = 283

    # keep peaks if they fall outside central beam and 5 pixel outer
   border
    for peak in peaks:
        if np.sqrt((peak[0] - centerx) ** 2 + (peak[1] - centery) ** 2) >=
    20 and peak[0] > 50 and peak[1] > 50 and peak[0] < 536 and peak[1] <
   536:
```

```
         keep.append(peak)

 peaks = np.asarray(keep)
 #print(peaks)

 radius = 5

 radii = (radius,)*peaks.shape[0]
 #peaks_labeled = stempy.image.plot_virtual_darkfield(dp, peaks[:,1],
peaks[:,0], radii)
 find_cdz = stempy.image.virtual_darkfield(sp, peaks[:,1], peaks[:,0],
radii)
 mask_cdz = find_cdz * masks[ii]
 mask_cdz[mask_cdz < 7] = 0
 mask_cdz[mask_cdz >= 7] = 1
 dp_cdz = stempy.image.mask_real_space(sp, mask_cdz)

 fig, axs = plt.subplots(2, 3, figsize=(10, 10));
 # just mask
 fig.tight_layout()
 axs[0, 0].imshow(masks[ii])
 axs[0, 0].axis('off')
 axs[0, 0].set_title('VDF mask')

 # mask + CDZs
 axs[0, 1].imshow(dp, norm=LogNorm(), cmap='bone', interpolation='
gaussian')
 axs[0, 1].scatter(peaks[:,1], peaks[:, 0], marker='o', facecolor='none
', edgecolor='#00acd5')
 axs[0, 1].axis('off')
 axs[0, 1].set_title(r'Peaks found by \texttt{ncempy.algo.peakFind2D}')

 axs[0, 2].imshow(find_cdz, cmap='cubehelix')
```

```
    axs[0, 2].axis(’off’)
    axs[0, 2].set_title(’CDZs’)

    # just DP
    axs[1, 0].imshow(mask_cdz)
    axs[1, 0].axis(’off’)
    axs[1, 0].set_title(’Mask from CDZs’)



    # just DP from mask + CDZs
    axs[1, 1].imshow(np.log(dp + 1), cmap=’bone’)
    axs[1, 1].set_title(’Diffraction pattern from VDF mask’)
    axs[1, 1].axis(’off’)

    axs[1, 2].imshow(np.log(dp_cdz + 1), cmap=’bone’)
    axs[1, 2].set_title(’Diffraction pattern from CDZs’)
    axs[1, 2].axis(’off’)

    plt.suptitle(r"Ni(dppf)Cl$_{2}$, movie 1, $\alpha =$ " + str(jj) + r"
     ", fontsize=20)
    out = Path(f"C:/Users/eicn_user/Desktop/ambarneil/4DSTEM_20220223/4
   dstem_nidppf_mov02/counted_hdf5/scan_cdz_{ii:04}.img")
    write_smv(out, dp_cdz)
    plt.savefig(f"mov1_scan_cdz_{ii:04}.png", format=’png’)
    jj = jj + 1
```

Listing 4.1: Sample python code used to generate the SMV format diffraction patterns and figures presented earlier in this chapter.

```
#!/bin/bash
set -e

# Check script input
```

```
if [ "$#" -ne 1 ]; then
    echo "You must supply the location of the data directory (
   nidppf_4dstem/) only"
    exit 1
fi

DATAROOT=$(realpath "$1")
if [ ! -d "$DATAROOT" ]; then
    echo "$DATAROOT is not found"
    exit 1
fi

# Install/update format class and set env var to force its use
dxtbx.install_format -u \
  https://raw.githubusercontent.com/dials/dxtbx_ED_formats/master/
   FormatSMV4DSTEM.py
export FORCE_SMV_AS_4DSTEM=1

# Renumber files to be a sequential series matching template image_###.img
i=1
for file in "$DATAROOT"/*.img
do
    ln -sf "$file" "$(printf "image_%03d.img" $i)"
    i=$((i+1))
done

# Import
dials.import template=image_###.img\
  geometry.scan.oscillation=-50,1\
  fast_slow_beam_centre=141,142\
  panel.pixel_size=0.02,0.02
dials.find_spots imported.expt\
  threshold.algorithm=dispersion d_min=0.8
```

```
dials.find_rotation_axis imported.expt strong.refl
dials.index optimised.expt strong.refl detector.fix=distance
dials.refine indexed.expt indexed.refl detector.fix=distance
dials.integrate refined.expt refined.refl prediction.d_min=0.8
dials.scale integrated.expt integrated.refl\
  physical.absorption_correction=False error_model=None
dials.export scaled.expt scaled.refl format=xds
```

Listing 4.2: Sample bash script used to feed 4D-STEM SMV files into DIALS. Many thanks to David Waterman for assistance with this and all DIALS-related issues.

```
_audit_creation_method            'SHELXL-2018/3'
_shelx_SHELXL_version_number      '2018/3'
_chemical_name_systematic         ?
_chemical_name_common             ?
_chemical_melting_point           ?
_chemical_formula_moiety          ?
_chemical_formula_sum
 'C34 H28 Cl2 Fe Ni P2'
_chemical_formula_weight          684.23

loop_
 _atom_type_symbol
 _atom_type_description
 _atom_type_scat_dispersion_real
 _atom_type_scat_dispersion_imag
 _atom_type_scat_source
 'C'  'C'   0.0000   0.0000
 'International Tables Vol C Tables 4.2.6.8 and 6.1.1.4'
 'Cl'  'Cl'   0.0000   0.0000
 'International Tables Vol C Tables 4.2.6.8 and 6.1.1.4'
 'Fe'  'Fe'   0.0000   0.0000
 'International Tables Vol C Tables 4.2.6.8 and 6.1.1.4'
```

```
 'Ni'  'Ni'   0.0000   0.0000
 'International Tables Vol C Tables 4.2.6.8 and 6.1.1.4'
 'P'  'P'   0.0000   0.0000
 'International Tables Vol C Tables 4.2.6.8 and 6.1.1.4'
 'H'  'H'   0.0000   0.0000
 'International Tables Vol C Tables 4.2.6.8 and 6.1.1.4'

_space_group_crystal_system       triclinic
_space_group_IT_number            2
_space_group_name_H-M_alt         'P -1'
_space_group_name_Hall            '-P 1'

_shelx_space_group_comment
;
The symmetry employed for this shelxl refinement is uniquely defined
by the following loop, which should always be used as a source of
symmetry information in preference to the above space-group names.
They are only intended as comments.
;

loop_
 _space_group_symop_operation_xyz
 'x, y, z'
 '-x, -y, -z'

_cell_length_a                    9.610(2)
_cell_length_b                    9.5500(19)
_cell_length_c                    18.260(3)
_cell_angle_alpha                 97.02
_cell_angle_beta                  101.62
_cell_angle_gamma                 115.23
_cell_volume                      1443.3(5)
_cell_formula_units_Z             1
```

```
_cell_measurement_temperature     293(2)
_cell_measurement_reflns_used     ?
_cell_measurement_theta_min       ?
_cell_measurement_theta_max       ?

_exptl_crystal_description        ?
_exptl_crystal_colour             ?
_exptl_crystal_density_meas       ?
_exptl_crystal_density_method     ?
_exptl_crystal_density_diffrn     0.787
_exptl_crystal_F_000              134
_exptl_transmission_factor_min    ?
_exptl_transmission_factor_max    ?
_exptl_crystal_size_max           ?
_exptl_crystal_size_mid           ?
_exptl_crystal_size_min           ?
_exptl_absorpt_coefficient_mu     0.000
_shelx_estimated_absorpt_T_min    ?
_shelx_estimated_absorpt_T_max    ?
_exptl_absorpt_correction_type    ?
_exptl_absorpt_correction_T_min   ?
_exptl_absorpt_correction_T_max   ?
_exptl_absorpt_process_details    ?
_exptl_absorpt_special_details    ?
_diffrn_ambient_temperature       293(2)
_diffrn_radiation_wavelength      0.01969
_diffrn_radiation_type            ?
_diffrn_source                    ?
_diffrn_measurement_device_type   ?
_diffrn_measurement_method        ?
_diffrn_detector_area_resol_mean  ?
_diffrn_reflns_number             6589
_diffrn_reflns_av_unetI/netI      0.8421
```

```
_diffrn_reflns_av_R_equivalents   0.4389
_diffrn_reflns_limit_h_min        -12
_diffrn_reflns_limit_h_max        12
_diffrn_reflns_limit_k_min        -11
_diffrn_reflns_limit_k_max        11
_diffrn_reflns_limit_l_min        -22
_diffrn_reflns_limit_l_max        22
_diffrn_reflns_theta_min          0.065
_diffrn_reflns_theta_max          0.705
_diffrn_reflns_theta_full         0.677
_diffrn_measured_fraction_theta_max   0.574
_diffrn_measured_fraction_theta_full  0.575
_diffrn_reflns_Laue_measured_fraction_max    0.574
_diffrn_reflns_Laue_measured_fraction_full   0.575
_diffrn_reflns_point_group_measured_fraction_max   0.574
_diffrn_reflns_point_group_measured_fraction_full  0.575
_reflns_number_total              3381
_reflns_number_gt                 440
_reflns_threshold_expression      'I > 2\s(I)'
_reflns_Friedel_coverage          0.000
_reflns_Friedel_fraction_max      .
_reflns_Friedel_fraction_full     .

_reflns_special_details
;
 Reflections were merged by SHELXL according to the crystal
 class for the calculation of statistics and refinement.

 _reflns_Friedel_fraction is defined as the number of unique
 Friedel pairs measured divided by the number that would be
 possible theoretically, ignoring centric projections and
 systematic absences.
;
```

```
_computing_data_collection        ?
_computing_cell_refinement        ?
_computing_data_reduction         ?
_computing_structure_solution     ?
_computing_structure_refinement 'SHELXL-2018/3 (Sheldrick, 2018)'
_computing_molecular_graphics     ?
_computing_publication_material   ?
_refine_special_details           ?
_refine_ls_structure_factor_coef  Fsqd
_refine_ls_matrix_type            full
_refine_ls_weighting_scheme       calc
_refine_ls_weighting_details
'w=1/[\s^2^(Fo^2^)+(0.1000P)^2^] where P=(Fo^2^+2Fc^2^)/3'
_atom_sites_solution_primary      ?
_atom_sites_solution_secondary    ?
_atom_sites_solution_hydrogens    geom
_refine_ls_hydrogen_treatment     constr
_refine_ls_extinction_method      'SHELXL-2018/3 (Sheldrick 2018)'
_refine_ls_extinction_coef        53731(96)
_refine_ls_extinction_expression
 'Fc^*^=kFc[1+0.001xFc^2^\l^3^/sin(2\q)]^-1/4^'
_refine_ls_number_reflns          3381
_refine_ls_number_parameters      308
_refine_ls_number_restraints      381
_refine_ls_R_factor_all           0.4950
_refine_ls_R_factor_gt            0.3976
_refine_ls_wR_factor_ref          0.7169
_refine_ls_wR_factor_gt           0.6406
_refine_ls_goodness_of_fit_ref    0.961
_refine_ls_restrained_S_all       0.910
_refine_ls_shift/su_max           2.094
_refine_ls_shift/su_mean          0.333
```

```
loop_
 _atom_site_label
 _atom_site_type_symbol
 _atom_site_fract_x
 _atom_site_fract_y
 _atom_site_fract_z
 _atom_site_U_iso_or_equiv
 _atom_site_adp_type
 _atom_site_occupancy
 _atom_site_site_symmetry_order
 _atom_site_calc_flag
 _atom_site_refinement_flags_posn
 _atom_site_refinement_flags_adp
 _atom_site_refinement_flags_occupancy
 _atom_site_disorder_assembly
 _atom_site_disorder_group
Fe1 Fe 0.158(3) 0.477(2) 0.1492(7) 0.057(5) Uani 1 1 d . . . . .
C1 C -0.687(8) 0.113(8) -0.001(2) 0.053(13) Uani 1 1 d . . . . .
H1 H -0.783135 0.065850 -0.039954 0.063 Uiso 1 1 calc R U . . .
P1 P -0.223(4) 0.324(4) 0.1923(9) 0.051(5) Uani 1 1 d . . . . .
P0 P 0.114(4) 0.698(4) 0.2931(10) 0.052(6) Uani 1 1 d . . . . .
Ni0 Ni -0.150(2) 0.585(2) 0.2447(7) 0.049(5) Uani 1 1 d . . . . .
C222 C 0.036(8) 0.255(7) 0.167(2) 0.063(7) Uani 1 1 d . . . . .
H222 H 0.056225 0.225140 0.216171 0.076 Uiso 1 1 calc R U . . .
C212 C 0.179(8) 0.642(7) 0.385(2) 0.062(12) Uani 1 1 d . . . . .
C201 C -0.224(7) 0.207(6) 0.2573(18) 0.037(10) Uani 1 1 d . . . . .
C33 C 0.183(10) 0.507(10) 0.479(3) 0.096(16) Uani 1 1 d . . . . .
H33 H 0.119068 0.426655 0.499065 0.115 Uiso 1 1 calc R U . . .
Cl4 Cl -0.133(4) 0.729(4) 0.1502(10) 0.057(9) Uani 1 1 d . . . . .
C3 C 0.337(8) 0.617(8) 0.236(2) 0.063(8) Uani 1 1 d . . . . .
H3 H 0.367311 0.582510 0.282030 0.076 Uiso 1 1 calc R U . . .
C333 C 0.384(10) 0.777(10) 0.419(2) 0.086(14) Uani 1 1 d . . . . .
```

```
H333 H 0.438780 0.857243 0.396289 0.103 Uiso 1 1 calc R U . . .
Cl5 Cl -0.272(4) 0.597(4) 0.3322(10) 0.067(9) Uani 1 1 d . . . . .
C006 C -0.395(8) 0.249(7) 0.1197(17) 0.049(7) Uani 1 1 d . . . . .
C008 C -0.084(7) 0.304(7) 0.1411(18) 0.056(7) Uani 1 1 d . . . . .
C009 C -0.276(7) 0.209(6) 0.321(2) 0.049(14) Uani 1 1 d . . . . .
H009 H -0.315174 0.282025 0.327310 0.059 Uiso 1 1 calc R U . . .
C010 C -0.236(8) 0.059(7) 0.233(2) 0.053(15) Uani 1 1 d . . . . .
H010 H -0.226463 0.031318 0.184408 0.064 Uiso 1 1 calc R U . . .
C011 C -0.437(8) 0.338(7) 0.068(2) 0.056(13) Uani 1 1 d . . . . .
H011 H -0.369447 0.446770 0.076143 0.067 Uiso 1 1 calc R U . . .
C014 C -0.077(8) 0.326(8) 0.067(2) 0.064(8) Uani 1 1 d . . . . .
H014 H -0.139499 0.367985 0.037053 0.077 Uiso 1 1 calc R U . . .
C015 C 0.226(8) 0.721(8) 0.154(2) 0.062(8) Uani 1 1 d . . . . .
H015 H 0.161715 0.766496 0.127996 0.074 Uiso 1 1 calc R U . . .
C016 C 0.449(10) 0.745(10) 0.484(3) 0.102(16) Uani 1 1 d . . . . .
H016 H 0.554725 0.812478 0.512368 0.123 Uiso 1 1 calc R U . . .
C017 C -0.260(8) -0.049(7) 0.279(2) 0.047(13) Uani 1 1 d . . . . .
H017 H -0.256960 -0.142868 0.261475 0.056 Uiso 1 1 calc R U . . .
C021 C 0.127(9) 0.261(8) 0.109(3) 0.072(9) Uani 1 1 d . . . . .
H021 H 0.208213 0.224433 0.108067 0.086 Uiso 1 1 calc R U . . .
C21 C -0.557(9) 0.277(9) 0.014(2) 0.060(13) Uani 1 1 d . . . . .
H21 H -0.569054 0.338253 -0.020324 0.071 Uiso 1 1 calc R U . . .
C022 C 0.407(8) 0.617(8) 0.174(2) 0.068(8) Uani 1 1 d . . . . .
H022 H 0.487914 0.581520 0.168912 0.081 Uiso 1 1 calc R U . . .
C023 C -0.521(10) 0.087(9) 0.112(3) 0.087(15) Uani 1 1 d . . . . .
H023 H -0.514855 0.023929 0.146283 0.105 Uiso 1 1 calc R U . . .
C024 C 0.346(9) 0.594(10) 0.509(2) 0.093(16) Uani 1 1 d . . . . .
H024 H 0.396950 0.561107 0.546885 0.112 Uiso 1 1 calc R U . . .
C025 C 0.022(9) 0.287(8) 0.043(2) 0.069(9) Uani 1 1 d . . . . .
H025 H 0.042651 0.296190 -0.007081 0.083 Uiso 1 1 calc R U . . .
C028 C 0.244(7) 0.698(7) 0.231(2) 0.052(7) Uani 1 1 d . . . . .
C029 C -0.290(10) -0.025(7) 0.349(3) 0.07(2) Uani 1 1 d . . . . .
H029 H -0.313705 -0.103931 0.376190 0.080 Uiso 1 1 calc R U . . .
```

```
C032 C -0.283(9) 0.128(6) 0.379(2) 0.053(19) Uani 1 1 d . . . . .
H032 H -0.283170 0.164373 0.428235 0.064 Uiso 1 1 calc R U . . .
C035 C 0.124(9) 0.548(8) 0.418(3) 0.081(14) Uani 1 1 d . . . . .
H035 H 0.013964 0.485930 0.396956 0.097 Uiso 1 1 calc R U . . .
C036 C -0.642(9) 0.043(9) 0.052(2) 0.078(14) Uani 1 1 d . . . . .
H036 H -0.716158 -0.063332 0.043662 0.093 Uiso 1 1 calc R U . . .
C037 C 0.318(8) 0.649(8) 0.120(3) 0.064(7) Uani 1 1 d . . . . .
H037 H 0.327167 0.646450 0.067560 0.077 Uiso 1 1 calc R U . . .

loop_
 _atom_site_aniso_label
 _atom_site_aniso_U_11
 _atom_site_aniso_U_22
 _atom_site_aniso_U_33
 _atom_site_aniso_U_23
 _atom_site_aniso_U_13
 _atom_site_aniso_U_12
Fe1 0.088(12) 0.100(11) 0.038(6) 0.022(6) 0.028(7) 0.088(11)
C1 0.06(3) 0.12(3) 0.023(16) 0.02(2) 0.009(18) 0.07(3)
P1 0.084(13) 0.103(12) 0.017(7) 0.019(7) 0.018(7) 0.088(12)
P0 0.080(13) 0.101(16) 0.028(8) 0.022(9) 0.019(8) 0.084(13)
Ni0 0.073(12) 0.090(11) 0.033(6) 0.023(6) 0.026(6) 0.075(11)
C222 0.11(2) 0.098(15) 0.042(14) 0.019(15) 0.035(16) 0.093(17)
C212 0.12(3) 0.11(3) 0.021(13) 0.013(14) 0.017(13) 0.11(3)
C201 0.05(3) 0.055(19) 0.013(10) -0.006(12) -0.008(14) 0.04(3)
C33 0.14(3) 0.19(4) 0.06(2) 0.07(3) 0.05(2) 0.16(4)
Cl4 0.06(3) 0.11(2) 0.036(9) 0.033(12) 0.012(12) 0.07(2)
C3 0.082(17) 0.11(2) 0.049(12) 0.017(11) 0.025(11) 0.088(16)
C333 0.11(3) 0.17(4) 0.024(16) 0.03(2) 0.008(18) 0.10(3)
Cl5 0.10(2) 0.13(2) 0.040(9) 0.030(12) 0.037(12) 0.11(2)
C006 0.089(16) 0.096(17) 0.015(10) 0.020(11) 0.019(11) 0.087(15)
C008 0.079(14) 0.117(18) 0.011(11) 0.010(12) 0.012(11) 0.084(13)
C009 0.09(4) 0.06(3) 0.040(14) 0.027(17) 0.03(2) 0.07(3)
```

```
C010 0.10(5) 0.07(2) 0.031(16) 0.018(15) 0.03(2) 0.08(3)
C011 0.08(3) 0.08(2) 0.034(15) 0.016(17) -0.001(17) 0.07(3)
C014 0.088(17) 0.13(2) 0.021(10) 0.020(11) 0.028(10) 0.087(16)
C015 0.11(3) 0.107(14) 0.037(13) 0.025(14) 0.036(16) 0.099(19)
C016 0.12(3) 0.23(5) 0.037(19) 0.06(2) 0.028(19) 0.15(3)
C017 0.07(4) 0.07(3) 0.042(15) 0.019(18) 0.02(2) 0.06(3)
C021 0.12(2) 0.107(16) 0.053(15) 0.020(14) 0.047(15) 0.10(2)
C21 0.07(3) 0.11(3) 0.022(15) 0.02(2) 0.002(17) 0.07(3)
C022 0.085(14) 0.12(2) 0.054(16) 0.016(16) 0.030(14) 0.091(14)
C023 0.10(2) 0.106(19) 0.08(2) 0.05(2) -0.005(18) 0.077(16)
C024 0.14(3) 0.22(5) 0.033(19) 0.06(2) 0.05(2) 0.17(4)
C025 0.10(2) 0.11(2) 0.041(11) 0.012(11) 0.040(12) 0.08(2)
C028 0.069(18) 0.103(16) 0.033(11) 0.021(10) 0.022(12) 0.078(15)
C029 0.14(8) 0.04(3) 0.07(2) 0.04(2) 0.07(3) 0.06(5)
C032 0.11(6) 0.04(3) 0.023(14) 0.009(15) 0.00(2) 0.05(4)
C035 0.12(3) 0.15(3) 0.06(2) 0.05(2) 0.034(18) 0.12(3)
C036 0.08(3) 0.12(2) 0.05(2) 0.04(2) 0.00(2) 0.075(18)
C037 0.08(2) 0.115(18) 0.047(14) 0.017(15) 0.033(15) 0.086(16)

_geom_special_details
;
 All esds (except the esd in the dihedral angle between two l.s. planes)
 are estimated using the full covariance matrix.  The cell esds are taken
 into account individually in the estimation of esds in distances, angles
 and torsion angles; correlations between esds in cell parameters are only
 used when they are defined by crystal symmetry.  An approximate (
   isotropic)
 treatment of cell esds is used for estimating esds involving l.s. planes.
;

loop_
 _geom_bond_atom_site_label_1
 _geom_bond_atom_site_label_2
```

```
 _geom_bond_distance
 _geom_bond_site_symmetry_2
 _geom_bond_publ_flag
Fe1 C3 1.92(6) . ?
Fe1 C037 1.94(7) . ?
Fe1 C021 1.97(5) . ?
Fe1 C222 2.04(7) . ?
Fe1 C022 2.11(7) . ?
Fe1 C015 2.12(6) . ?
Fe1 C008 2.16(7) . ?
Fe1 C028 2.15(5) . ?
Fe1 C014 2.18(7) . ?
Fe1 C025 2.20(6) . ?
C1 C036 1.34(6) . ?
C1 C21 1.48(10) . ?
P1 C006 1.70(6) . ?
P1 C201 1.73(5) . ?
P1 C008 1.83(5) . ?
P1 Ni0 2.30(3) . ?
P0 C028 1.85(5) . ?
P0 C212 1.88(4) . ?
P0 Ni0 2.21(4) . ?
Ni0 Cl5 2.18(2) . ?
Ni0 Cl4 2.32(3) . ?
C222 C008 1.44(6) . ?
C222 C021 1.50(7) . ?
C212 C035 1.14(8) . ?
C212 C333 1.75(11) . ?
C201 C009 1.36(6) . ?
C201 C010 1.37(5) . ?
C33 C035 1.32(6) . ?
C33 C024 1.37(11) . ?
C3 C028 1.40(5) . ?
```

```
C3 C022 1.43(7) . ?
C333 C016 1.35(5) . ?
C006 C023 1.47(10) . ?
C006 C011 1.46(5) . ?
C008 C014 1.40(6) . ?
C009 C032 1.37(6) . ?
C010 C017 1.38(7) . ?
C011 C21 1.21(8) . ?
C014 C025 1.29(7) . ?
C015 C028 1.44(5) . ?
C015 C037 1.51(5) . ?
C016 C024 1.55(12) . ?
C017 C029 1.37(6) . ?
C021 C025 1.53(7) . ?
C022 C037 1.32(6) . ?
C023 C036 1.30(8) . ?
C029 C032 1.47(5) . ?

loop_
 _geom_angle_atom_site_label_1
 _geom_angle_atom_site_label_2
 _geom_angle_atom_site_label_3
 _geom_angle
 _geom_angle_site_symmetry_1
 _geom_angle_site_symmetry_3
 _geom_angle_publ_flag
C3 Fe1 C037 68(3) . . ?
C3 Fe1 C021 120(2) . . ?
C037 Fe1 C021 116(2) . . ?
C3 Fe1 C222 112(2) . . ?
C037 Fe1 C222 158.7(17) . . ?
C021 Fe1 C222 44(2) . . ?
C3 Fe1 C022 41(2) . . ?
```

```
C037 Fe1 C022 38(2) . . ?
C021 Fe1 C022 102(2) . . ?
C222 Fe1 C022 128(2) . . ?
C3 Fe1 C015 67(2) . . ?
C037 Fe1 C015 43.2(19) . . ?
C021 Fe1 C015 157(2) . . ?
C222 Fe1 C015 158(2) . . ?
C022 Fe1 C015 67(2) . . ?
C3 Fe1 C008 132(2) . . ?
C037 Fe1 C008 154.7(19) . . ?
C021 Fe1 C008 71(2) . . ?
C222 Fe1 C008 39.9(18) . . ?
C022 Fe1 C008 167.2(18) . . ?
C015 Fe1 C008 123(2) . . ?
C3 Fe1 C028 39.8(16) . . ?
C037 Fe1 C028 70(2) . . ?
C021 Fe1 C028 157.4(19) . . ?
C222 Fe1 C028 125.4(19) . . ?
C022 Fe1 C028 68(2) . . ?
C015 Fe1 C028 39.4(16) . . ?
C008 Fe1 C028 114(2) . . ?
C3 Fe1 C014 167.2(19) . . ?
C037 Fe1 C014 120(2) . . ?
C021 Fe1 C014 68(2) . . ?
C222 Fe1 C014 65(2) . . ?
C022 Fe1 C014 150.7(19) . . ?
C015 Fe1 C014 111(2) . . ?
C008 Fe1 C014 37.7(18) . . ?
C028 Fe1 C014 130.5(17) . . ?
C3 Fe1 C025 157.8(18) . . ?
C037 Fe1 C025 105(2) . . ?
C021 Fe1 C025 43(2) . . ?
C222 Fe1 C025 66(2) . . ?
```

```
C022 Fe1 C025 120(2) . . ?
C015 Fe1 C025 124(2) . . ?
C008 Fe1 C025 62(2) . . ?
C028 Fe1 C025 159.9(16) . . ?
C014 Fe1 C025 34.2(18) . . ?
C036 C1 C21 108(6) . . ?
C006 P1 C201 115(3) . . ?
C006 P1 C008 102(2) . . ?
C201 P1 C008 103(2) . . ?
C006 P1 Ni0 108.7(16) . . ?
C201 P1 Ni0 115.6(15) . . ?
C008 P1 Ni0 112(3) . . ?
C028 P0 C212 110(2) . . ?
C028 P0 Ni0 120.9(19) . . ?
C212 P0 Ni0 113(3) . . ?
Cl5 Ni0 P0 112.6(11) . . ?
Cl5 Ni0 P1 109.8(14) . . ?
P0 Ni0 P1 104.5(10) . . ?
Cl5 Ni0 Cl4 123.8(8) . . ?
P0 Ni0 Cl4 93.0(13) . . ?
P1 Ni0 Cl4 110.6(9) . . ?
C008 C222 C021 110(3) . . ?
C008 C222 Fe1 75(3) . . ?
C021 C222 Fe1 66(3) . . ?
C035 C212 C333 119(5) . . ?
C035 C212 P0 138(6) . . ?
C333 C212 P0 103(4) . . ?
C009 C201 C010 109(4) . . ?
C009 C201 P1 127(3) . . ?
C010 C201 P1 119(2) . . ?
C035 C33 C024 114(8) . . ?
C028 C3 C022 114(4) . . ?
C028 C3 Fe1 79(3) . . ?
```

```
C022 C3 Fe1 76(3) . . ?
C016 C333 C212 109(7) . . ?
C023 C006 C011 116(5) . . ?
C023 C006 P1 119(3) . . ?
C011 C006 P1 125(5) . . ?
C014 C008 C222 105(4) . . ?
C014 C008 P1 128(3) . . ?
C222 C008 P1 127(3) . . ?
C014 C008 Fe1 72(4) . . ?
C222 C008 Fe1 66(4) . . ?
P1 C008 Fe1 129(3) . . ?
C201 C009 C032 134(3) . . ?
C201 C010 C017 122(3) . . ?
C21 C011 C006 123(7) . . ?
C025 C014 C008 114(4) . . ?
C025 C014 Fe1 74(4) . . ?
C008 C014 Fe1 70(3) . . ?
C028 C015 C037 105(3) . . ?
C028 C015 Fe1 71(3) . . ?
C037 C015 Fe1 62(3) . . ?
C333 C016 C024 119(7) . . ?
C029 C017 C010 123(4) . . ?
C222 C021 C025 99(4) . . ?
C222 C021 Fe1 70(3) . . ?
C025 C021 Fe1 77(3) . . ?
C011 C21 C1 125(5) . . ?
C037 C022 C3 103(4) . . ?
C037 C022 Fe1 64(4) . . ?
C3 C022 Fe1 62(4) . . ?
C036 C023 C006 112(5) . . ?
C33 C024 C016 123(4) . . ?
C014 C025 C021 110(4) . . ?
C014 C025 Fe1 72(3) . . ?
```

```
C021 C025 Fe1 61(3) . . ?
C3 C028 C015 103(3) . . ?
C3 C028 P0 125(3) . . ?
C015 C028 P0 127(3) . . ?
C3 C028 Fe1 61(3) . . ?
C015 C028 Fe1 69(3) . . ?
P0 C028 Fe1 115(4) . . ?
C017 C029 C032 118(4) . . ?
C009 C032 C029 108(3) . . ?
C212 C035 C33 134(8) . . ?
C023 C036 C1 136(8) . . ?
C022 C037 C015 111(4) . . ?
C022 C037 Fe1 78(4) . . ?
C015 C037 Fe1 75(4) . . ?

_refine_diff_density_max    0.239
_refine_diff_density_min   -0.237
_refine_diff_density_rms    0.063

_shelx_res_file
;
REM Best SHELXD solution   FINAL CC 50.73
REM Fragments: 35 3 1
REM
TITL GGYMLG       in space group P 1 21 1    .
    a.res
    created by SHELXL-2018/3 at 19:31:58 on 14-Sep-2023
REM The peptide contains 6 residues with formula C26 H38 N6 O8 S1.
REM The molecular weight of the peptide is   594.7 Da.
REM The asymmetric unit contains   1 peptides.
REM Vm=  1.3 A^3/Da, solvent content=  3.2%.
CELL 0.019687 9.61     9.55    18.26  97.023 101.625 115.230
ZERR    1.00   0.0020   0.0019   0.0033   0.000   0.0  0.000
```

```
LATT 1
SFAC C 0.600 40.938 0.136 0.374 0.547 3.278 1.225 13.013 0 0 0 0 0.76
   12.011
SFAC Cl 1.232 33.612 0.341 0.339 0.893 2.625 2.391 11.095 0 0 0 0 1.02
   35.453
SFAC Fe 2.177 71.621 0.563 0.387 1.966 3.307 2.453 18.670 0 0 0 0 1.52
   55.845
SFAC Ni 1.890 65.305 0.582 0.373 1.870 3.009 2.221 16.917 0 0 0 0 1.24
   58.933
SFAC P 1.567 49.607 0.354 0.394 0.941 3.189 2.622 15.680 0 0 0 0 1.07
   30.974
SFAC H 0.129 37.737 0.036 0.553 0.127 3.772 0.236 13.518 0 0 0 0 0.31
   1.008 H
UNIT 34 2 1 1 2 28
LIST 6 ! automatically inserted. Change 6 to 4 for CHECKCIF!!
XNPD 0.01
RIGU
L.S. 1
ACTA
WGHT    0.100000
EXTI53731.183594
FVAR      18.78447
FE1   3    0.157579    0.476535    0.149152    11.00000    0.08818
   0.10023 =
         0.03814    0.02170    0.02763    0.08751
C1    1   -0.687264    0.112694   -0.000810    11.00000    0.05705
   0.11505 =
         0.02292    0.01997    0.00868    0.07260
AFIX  43
H1    6   -0.783135    0.065850   -0.039954    11.00000   -1.20000
AFIX   0
P1    5   -0.222769    0.323967    0.192288    11.00000    0.08442
   0.10316 =
```

```
         0.01669    0.01876    0.01752    0.08790
P0    5    0.114006    0.697744    0.293067    11.00000    0.07987
   0.10063 =
         0.02778    0.02186    0.01937    0.08420
NI0   4   -0.149795    0.585437    0.244741    11.00000    0.07327
   0.09041 =
         0.03326    0.02347    0.02622    0.07521
C222  1    0.035896    0.255428    0.167264    11.00000    0.10719
   0.09765 =
         0.04239    0.01855    0.03516    0.09267
AFIX  13
H222  6    0.056225    0.225140    0.216171    11.00000   -1.20000
AFIX   0
C212  1    0.178931    0.642238    0.384716    11.00000    0.11592
   0.10629 =
         0.02124    0.01260    0.01662    0.10518
C201  1   -0.223735    0.206540    0.257345    11.00000    0.04760
   0.05459 =
         0.01317   -0.00557   -0.00778    0.03843
C33   1    0.182755    0.507100    0.478649    11.00000    0.14407
   0.19164 =
         0.06135    0.06532    0.04709    0.15900
AFIX  43
H33   6    0.119068    0.426655    0.499065    11.00000   -1.20000
AFIX   0
CL4   2   -0.132886    0.728966    0.150163    11.00000    0.06092
   0.11199 =
         0.03612    0.03261    0.01220    0.07192
C3    1    0.336895    0.617252    0.235781    11.00000    0.08211
   0.11092 =
         0.04854    0.01737    0.02523    0.08832
AFIX  13
H3    6    0.367311    0.582510    0.282030    11.00000   -1.20000
```

```
AFIX   0
C333  1    0.383604    0.776559    0.418982    11.00000    0.10914
   0.16796 =
         0.02441    0.03367    0.00801    0.10500
AFIX  43
H333  6    0.438780    0.857243    0.396289    11.00000   -1.20000
AFIX   0
CL5   2   -0.271681    0.597285    0.332201    11.00000    0.09934
   0.13236 =
         0.03957    0.03044    0.03665    0.10638
C006  1   -0.394907    0.248867    0.119749    11.00000    0.08922
   0.09606 =
         0.01539    0.01971    0.01898    0.08714
C008  1   -0.083760    0.304439    0.141139    11.00000    0.07933
   0.11728 =
         0.01133    0.01041    0.01159    0.08364
C009  1   -0.275655    0.209130    0.321164    11.00000    0.09081
   0.06471 =
         0.04049    0.02687    0.03152    0.07111
AFIX  43
H009  6   -0.315174    0.282025    0.327310    11.00000   -1.20000
AFIX   0
C010  1   -0.235524    0.059175    0.233191    11.00000    0.10063
   0.07336 =
         0.03144    0.01778    0.02679    0.07672
AFIX  43
H010  6   -0.226463    0.031318    0.184408    11.00000   -1.20000
AFIX   0
C011  1   -0.437489    0.338457    0.067657    11.00000    0.07930
   0.08250 =
         0.03359    0.01601   -0.00144    0.06870
AFIX  43
H011  6   -0.369447    0.446770    0.076143    11.00000   -1.20000
```

```
AFIX   0
C014  1   -0.076667    0.325609    0.067210    11.00000    0.08798
   0.13129 =
         0.02059    0.01990    0.02809    0.08690
AFIX  13
H014  6   -0.139499    0.367985    0.037053    11.00000   -1.20000
AFIX   0
C015  1    0.226142    0.720886    0.153991    11.00000    0.10747
   0.10682 =
         0.03664    0.02486    0.03639    0.09852
AFIX  13
H015  6    0.161715    0.766496    0.127996    11.00000   -1.20000
AFIX   0
C016  1    0.449214    0.744856    0.483642    11.00000    0.11825
   0.23473 =
         0.03731    0.06198    0.02811    0.14600
AFIX  43
H016  6    0.554725    0.812478    0.512368    11.00000   -1.20000
AFIX   0
C017  1   -0.260346   -0.048972    0.278803    11.00000    0.06579
   0.07036 =
         0.04170    0.01937    0.01784    0.06263
AFIX  43
H017  6   -0.256960   -0.142868    0.261475    11.00000   -1.20000
AFIX   0
C021  1    0.127252    0.260706    0.109225    11.00000    0.11675
   0.10712 =
         0.05301    0.02040    0.04738    0.09700
AFIX  13
H021  6    0.208213    0.224433    0.108067    11.00000   -1.20000
AFIX   0
C21   1   -0.557411    0.277255    0.014147    11.00000    0.07180
   0.11325 =
```

```
         0.02205    0.02029    0.00205    0.07224
AFIX  43
H21   6   -0.569054    0.338253   -0.020324    11.00000   -1.20000
AFIX   0
C022  1    0.407353    0.616526    0.173815    11.00000    0.08463
   0.11831 =
         0.05354    0.01649    0.03010    0.09075
AFIX  13
H022  6    0.487914    0.581520    0.168912    11.00000   -1.20000
AFIX   0
C023  1   -0.520930    0.087278    0.112176    11.00000    0.09891
   0.10648 =
         0.08205    0.04750   -0.00518    0.07709
AFIX  43
H023  6   -0.514855    0.023929    0.146283    11.00000   -1.20000
AFIX   0
C024  1    0.345845    0.594111    0.509110    11.00000    0.13853
   0.22398 =
         0.03275    0.06384    0.04676    0.16823
AFIX  43
H024  6    0.396950    0.561107    0.546885    11.00000   -1.20000
AFIX   0
C025  1    0.022176    0.287247    0.043024    11.00000    0.09662
   0.11439 =
         0.04118    0.01207    0.03994    0.08180
AFIX  13
H025  6    0.042651    0.296190   -0.007081    11.00000   -1.20000
AFIX   0
C028  1    0.244092    0.697664    0.231054    11.00000    0.06902
   0.10301 =
         0.03314    0.02142    0.02163    0.07828
C029  1   -0.289877   -0.025009    0.348669    11.00000    0.13738
   0.04213 =
```

```
         0.07013    0.03952    0.06810    0.06168
AFIX  43
H029  6   -0.313705   -0.103931    0.376190    11.00000   -1.20000
AFIX   0
C032  1   -0.282835    0.128140    0.378654    11.00000    0.10573
   0.04449 =
         0.02346    0.00940    0.00460    0.05230
AFIX  43
H032  6   -0.283170    0.164373    0.428235    11.00000   -1.20000
AFIX   0
C035  1    0.124211    0.547844    0.417664    11.00000    0.11851
   0.14591 =
         0.06011    0.05086    0.03433    0.12396
AFIX  43
H035  6    0.013964    0.485930    0.396956    11.00000   -1.20000
AFIX   0
C036  1   -0.642245    0.043180    0.052020    11.00000    0.08294
   0.12425 =
         0.05150    0.03790   -0.00090    0.07475
AFIX  43
H036  6   -0.716158   -0.063332    0.043662    11.00000   -1.20000
AFIX   0
C037  1    0.318116    0.649053    0.120160    11.00000    0.08252
   0.11464 =
         0.04703    0.01749    0.03304    0.08563
AFIX  13
H037  6    0.327167    0.646450    0.067560    11.00000   -1.20000
AFIX   0
HKLF 4
```

```
REM  GGYMLG       in space group P 1 21 1    .
REM wR2 = 0.7169, GooF = S = 0.961, Restrained GooF = 0.910 for all data
REM R1 = 0.3976 for 440 Fo > 4sig(Fo) and 0.4950 for all 3381 data
REM 308 parameters refined using 381 restraints

END

WGHT      0.2000      0.0000
```

Listing 4.3: CIF file containing atomic coordinates of the 4D–STEM structure of Ni(dppf)Cl_2.

REFERENCES

[1] Gallagher-Jones, M.; Ophus, C.; Bustillo, K. C.; Boyer, D. R.; Panova, O.; Glynn, C.; Zee, C.-T.; Ciston, J.; Mancia, K. C.; Minor, A. M.; Rodriguez, J. A. Nanoscale Mosaicity Revealed in Peptide Microcrystals by Scanning Electron Nanodiffraction. *Commun. Biol.* **2019**, 2, 1–8. `<DOI: 10.1038/s42003-018-0263-8>`

[2] Gallagher-Jones, M.; Bustillo, K. C.; Ophus, C.; Richards, L. S.; Ciston, J.; Lee, S.; Minor, A. M.; Rodriguez, J. A. Atomic Structures Determined from Digitally Defined Nanocrystalline Regions. *IUCrJ* **2020**, 7, 490–499. `<DOI: 10.1107/S2052252520004030>`

[3] Hattne, J.; Reyes, F. E.; Nannenga, B. L.; Shi, D.; de la Cruz, M. J.; Leslie, A. G. W.; Gonen, T. MicroED Data Collection and Processing. *Acta Cryst. A* **2015**, 71 (4), 353–360. `<DOI: 10.1107/S2053273315010669>`

[4] Casellato, U.; Ajo, D.; Valle, G.; Corain, B.; Longato, B.; Graziani, R. *Journal of Crystallographic and Spectroscopic Research*, **1988**, 18, 583. `<DOI: 10.1007/BF01161151>`

[5] Darwin, C. G. XCII. The Reflexion of X-Rays from Imperfect Crystals. *The London, Edinburgh, and Dublin Philosophical Magazine and Journal of Science* **1922**, 43 (257), 800–829. `<DOI: 10.1080/14786442208633940>`

[6] Boggon, T. J.; Helliwell, J. R.; Judge, R. A.; Olczak, A.; Siddons, D. P.; Snell, E. H.; Stojanoff, V. Synchrotron X-Ray Reciprocal-Space Mapping, Topography and Diffraction Resolution Studies of Macromolecular Crystal Quality. *Acta Cryst. D* **2000**, 56 (7), 868–880. `<DOI: 10.1107/S0907444900005837`

[7] Bellamy, H. D.; Snell, E. H.; Lovelace, J.; Pokross, M.; Borgstahl, G. E. O. The High-Mosaicity Illusion: Revealing the True Physical Characteristics of Macromolecular Crystals. *Acta Cryst. D* **2000**, 56 (8), 986–995. `<DOI: 10.1107/S0907444900007356>`

[8] Subramanian, G.; Basu, S.; Liu, H.; Zuo, J.-M.; Spence, J. C. H. Solving Protein Nanocrystals by Cryo-EM Diffraction: Multiple Scattering Artifacts. *Ultramicroscopy* **2015**, 148, 87–93. `<DOI: 10.1016/j.ultramic.2014.08.013>`

APPENDIX A

Structural Elucidation of TEMPO-N_3, a Transient Organic Charge-Transfer Complex

This appendix contains material referenced in H. M. Nelson, J. C. Siu, **A. Saha**, D. Cascio, S. N. MacMillan, S.-B. Wu, C. Lu, J. A. Rodríguez, K. N. Houk, and S. Lin, Isolation and X-ray crystal structure of an electrogenerated TEMPO–N_3 charge-transfer complex. *Org. Lett.* **23**, 454–458 (2021). `<DOI: 10.1021/acs.orglett.0c03966>`

TEMPO–N_3 is a metastable organic charge-transfer complex (CTC) with a half-life of ca. 7 minutes in acetonitrile solution at RT. We first encountered this species while investigating the electrochemical azidooxygenation of alkenes (Figure A.1), a CTC-mediated transformation [1]. Our previous attempts to isolate and characterize TEMPO–N_3 in the solid state all proved futile. Hypothesizing that TEMPO–N_3's inherent instability may hamper its ability to aggregate into crystals large enough for X-ray diffraction (XRD), we turned to continuous-rotation 3D electron diffraction (3D ED) in an attempt to interrogate any possible nanocrystalline domains. Although

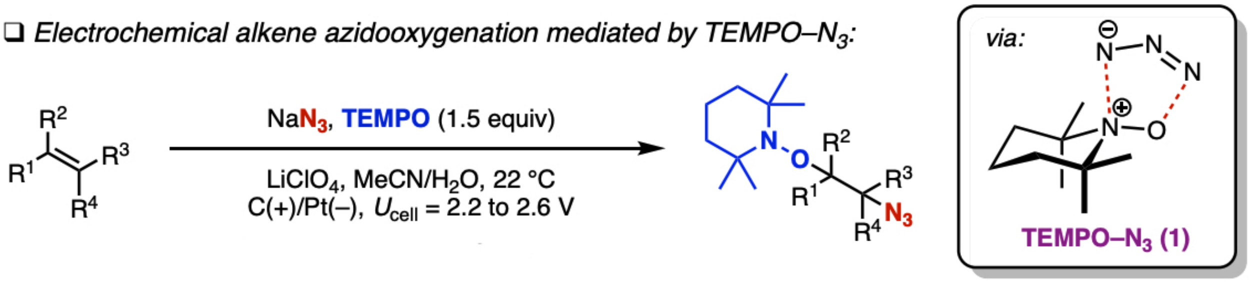

Figure A.1: **Schematic of the electrochemical azidooxygenation reaction mediated by TEMPO–N_3**, adapted from [1].

3D ED has rapidly made significant contributions to chemical crystallography since its revival in 2018, it has yet to contribute meaningfully to the study of reactive intermediates—ephemeral species naturally predisposed not to form macroscopic X-ray-scale crystals. During the course of our 3D ED investigations, we inadvertently discovered TEMPO–N_3's solid-state volatility. This breakthrough allowed us to generate pure crystals of TEMPO–N_3 via sublimation, which proved stable for ca. 6 hours at RT. We then solved the structure of this transient charge-transfer complex via single-crystal XRD.

To generate TEMPO–N_3 in solution, we mixed equimolar quantities of NaN_3 with TEMPO$^+$ oxopiperidinium perchlorate (TEMPO$^+$ ClO_4^-) in nanopure DI water. We then flash-froze the resultant blood-red solution by immersion in liquid N_2, followed by lyophilization to sublimate the solid bulk solvent. This yielded a pale-yellow, hygroscopic powder which regenerated CTC when dissolved in H_2O or MeCN. Months of attempts at recrystallization of this material failed, as re-dissolution in any solvent capable of accommodating solution-state CTC merely kick-started its decay. We originally suspected that this seemingly amorphous lyophilized powder may contain microcrystalline domains invisible to XRD or optical microscopy. Indeed, direct application of powder to an EM grid—followed by quickly transferring the grid to the TEM under argon—revealed a landscape replete with microcrystalline deposits. We then subjected these microcrystals to ambient-temperature continuous-rotation 3D electron diffraction (3D ED). However, due to an array of confounding variables—such as severe orientation bias, inherent disorder, and persistent contamination with TEMPO$^+$ ClO_4^-—we were unable to solve a 3D ED structure which we could unambiguously assign as TEMPO–N_3 (Figure A.2).

To banish the specter of lingering TEMPO$^+$ ClO_4^-, we turned to electrochemistry. Constant-current electrolysis ($I = 5$ mA) allowed us to generate TEMPO–N_3 directly from TEMPO· and NaN_3 via anodic oxidation of TEMPO· to TEMPO$^+$, obviating the need for a preoxidized TEMPO$^+$ salt. To exclude inherently crystalline impurities from our system, we conducted this reaction in the absence of supporting electrolyte (such as $LiClO_4$), necessitating usage of a slightly higher cell potential ($E_{cell} = 4.1$ V) versus our standard azidooxygenation conditions ($E_{cell} = 2.6$

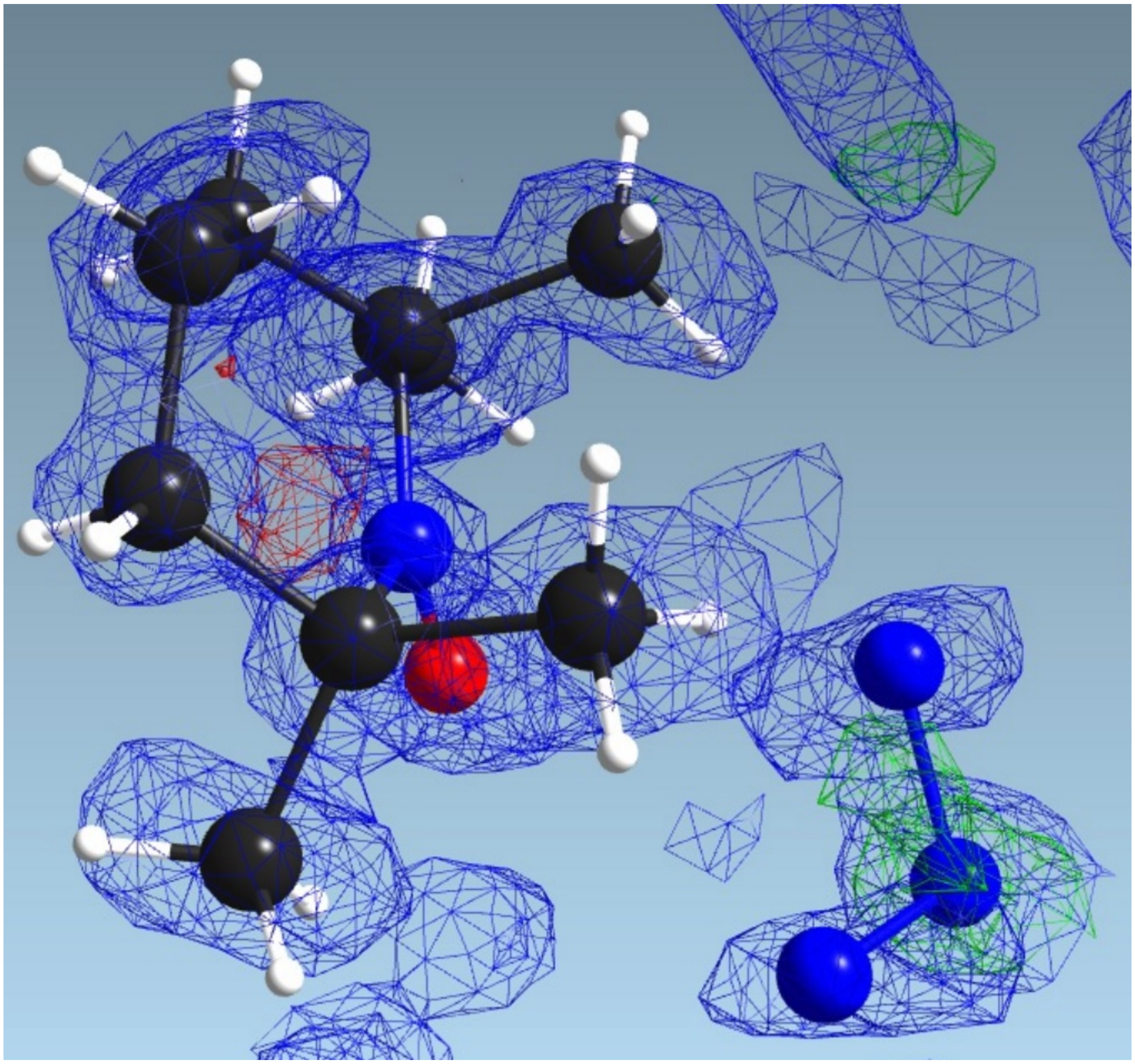

Figure A.2: **3D ED structure of disordered TEMPO$^+$ ClO$_4^-$, initially misinterpreted as TEMPO–N$_3$.** Due to its delocalization of charge across the four oxygen atoms, the perchlorate anion is considered relatively weakly coordinating; therefore, it often exhibits site-specific disorder in crystallographic structures because no strong intermolecular forces tether it to one particular spot in the unit cell. Many attempts were made to fit a bent azide moiety in the blob-like density corresponding to the perchlorate; some were vaguely promising, but all resulted in awkward bond angles. Following the key discovery of TEMPO–N$_3$'s solid-state volatility even under mild reduced pressure (200 mtorr in the Kugelrohr distillation apparatus), this structure was deemed extremely unlikely to be TEMPO–N$_3$, which would probably never survive the ultrahigh vacuum of the TEM.

V). Upon full conversion of TEMPO· to $TEMPO^+$ (1 F mol^{-1}), we plunge-froze an aliquot of this reaction mixture in liquid N_2 and subjected it to lyophilization. To our chagrin, this yielded a free-flowing white powder clearly distinct from the pale-yellow material obtained upon lyophilization of chemically generated CTC. Furthermore, this granular white solid (later identified as NaOH, a byproduct of electrolysis) proved insoluble in MeCN, indicating the absence of CTC. These results cast further doubt upon our earlier 3D ED solutions, as TEMPO–N_3 generated under electrochemical conditions was clearly too volatile to survive lyophilization. Additionally, consecutive MeCN extractions of electrochemically generated CTC followed by evaporation *in vacuo* left behind a brownish-red residue which also proved volatile under vacuum. Therefore, we concluded that the pale-yellow lyophilized powder generated via chemical methods was simply a heterogeneous mixture of $TEMPO^+$ ClO_4^- and NaN_3 which most likely did *not* contain any solid-state TEMPO–N_3. Even if some residual TEMPO–N_3 remained in this mixture, it was extremely unlikely to survive the ultrahigh vacuum of the TEM.

Recalibrating our strategy, we then sought to exploit this newfound volatility, reasoning that TEMPO· and TEMPO–N_3 likely sublime at markedly different rates under isothermal and isobaric conditions. Using a short-path Kugelrohr distillation apparatus, we subjected electrochemically generated TEMPO–N_3 to sublimation at 50 °C and 200 mtorr static vacuum. Initially, we observed nucleation of several pale orange, millimeter-sized crystals of TEMPO·, which we discarded. After 2 hours, however, we observed deposition of several dark, opaque specks of a seemingly reddish-black solid. Promisingly, dissolution of this material in MeCN regenerated CTC, producing a UV-vis absorption at 380 nm diagnostic of TEMPO–N_3 [1]. However, this solid also proved difficult to handle, as it either dissolved or decomposed in a range of solvents with drastically disparate dielectric constants (H_2O, MeCN, hexanes, heptanes, paratone oil). Nevertheless, optical microscopy revealed crystalline deposits hundreds of μm thick. We then subjected these sublimated crystals to Cu K_α X-ray diffraction and successfully solved the structure of TEMPO–N_3 using direct methods. These results were also successfully reproduced using synchrotron X-ray radiation, which generated a higher-resolution structure in excellent agreement with our Cu $K\alpha$

solution (all-atom non-H rmsd = 0.012 Å), albeit with a higher refinement R-factor due to its sampling of many higher-resolution Bragg reflections A.1.

Several observations here strike us as noteworthy. Firstly, our X-ray structure accurately replicates the [3+2] cycloadduct-like motif [2, 3] adumbrated by density functional theory (DFT) calculations, with the azide moiety positioned directly over the oxoammonium bond. Such electrostatic coordination yields a nonlinear azide, with an N–N–N bond angle of 170°. Although sporadic reports of bent azides exist in the literature [4, 5], ours is a unique example of azide nonlinearity in the context of a charge-transfer complex. Furthermore, the interatomic distances between azide and oxoammonium (2.31 Å, 2.44 Å) appear contracted in our X-ray structure versus DFT predictions (2.51 Å, 2.47 Å). These distances remain too elongated for a formal covalent bond, but such proximity suggests an interaction stronger than a typical electrostatic attraction, such as pancake bonding. Secondly, the N—O bond length (1.25 Å) of TEMPO–N_3 appears closer in length to the N—O bond (1.28 Å) of TEMPO· than the N=O bond (1.19 Å) of the $TEMPO^+$ salt precursor [6].

In closing, although we ultimately solved a single-crystal X-ray structure of TEMPO–N_3, electron diffraction still played a consequential role in providing a key breakthrough. We turned to electrochemistry in an attempt to probe the validity of our original 3D ED structure. As a result of that impetus, we inadvertently discovered TEMPO–N_3's solid-state volatility—a finding we likely would have never made otherwise. This story thus serves as a testament to the anfractuous but ultimately didactic path science often takes *en route* to hard-won conclusions.

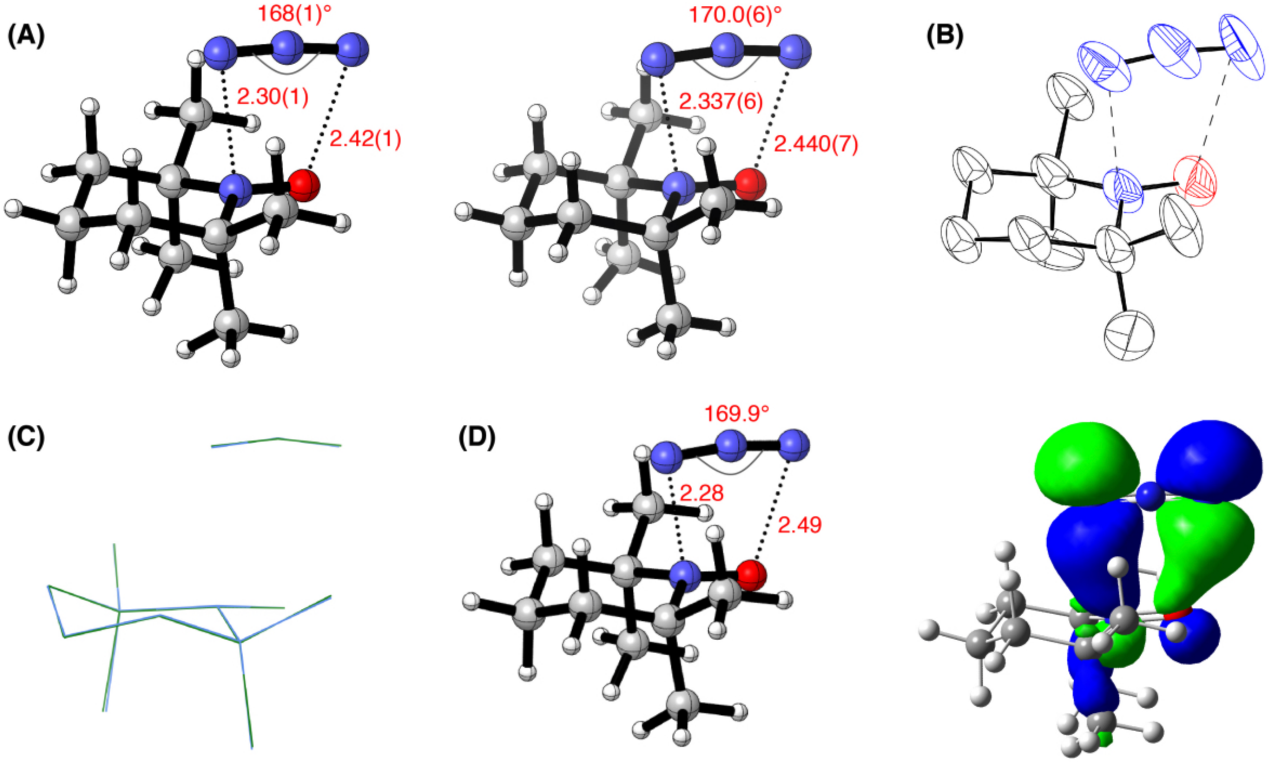

Figure A.3: **Experimental and computational structures of TEMPO–N$_3$.** (A) X-ray crystal structure of the CTC, Cu Kα (1.5418 Å) (left) and synchrotron radiation (0.7749 Å) (right); (B) ORTEP diagram of the synchrotron X-ray structure of 1 with thermal ellipsoids shown at the 30% probability level, with H atoms omitted for clarity; (C) overlay of structures obtained from Cu Kα (green) and synchrotron radiation (blue), root-mean-square deviation (RMSD) = 0.028 Å (for all non-hydrogen atoms) or 0.015 Å for the N=O–N$_3$ motif; (D) DFT-predicted structure at B3LYP-D3/6-311++G(d,p) level of density functional theory; (E) electronic structure (HOMO-1) of 1 calculated at the B3LYP-D3/6-311++G(d,p) level of theory.

Structure	1a	1b
Empirical formula	C_9H_{18} N_4O	C_9H_{18} N_4O
Formula weight (gmol^{-1})	198.27	198.27
Crystal system	Monoclinic	Monoclinic
Space group	$P2_1/n$ (14)	$P2_1/n$ (14)
Point group	2/m	2/m
Laue symmetry	2/m	2/m
Temperature (K)	100	100
Unit cell lengths a, b, c (Å)	7.360(2), 14.330(2), 10.670(3)	7.310(8), 14.220(5), 10.600(5)
Unit cell angles α, β, γ (°)	90, 100.72(2), 90	90, 100.66(4), 90
Unit cell volume (Å^3)	1105.7(4)	1082.8(14)
$F(000)$ [calculated]	432	432
Z	4	4
Radiation source, wavelength	Synchrotron, $\lambda = 0.77490$ Å	CuK_α, $\lambda = 1.5418$ Å
Resolution (Å)	1.05	1.35
Measured reflections	12603	2956
Unique reflections	990	398
Reflections with $I > 2\sigma(I)$	946	317
Completeness	99.5%	85.6%
I/σ	9.20	11.52
$\Theta_{\mathrm{max}}, \Theta_{\mathrm{min}}$ (°)	21.7, 2.6	34.8, 5.3
Index ranges	$-7 \leq h \leq 7, -13 \leq k \leq 13$ $-10 \leq l \leq 10$	$-5 \leq h \leq 5, -10 \leq k \leq 10$ $-7 \leq l \leq 7$
Refinement method	Full-matrix least-squares on F^2	Full-matrix least-squares on F^2
H-atom treatment	H-atom parameters constrained	H-atom parameters constrained
$R\,[F^2 > 2\sigma\,(F^2)]$	0.105	0.049
$wR\,(F^2)$	0.354	0.136
S	1.79	1.05
$\Delta\rho_{\mathrm{max}}, \Delta\rho_{\mathrm{min}}$ (e^{-3})	0.40, −0.29	0.13, −0.10

Table A.1: Refinement results and associated crystallographic statistics for the synchrotron (1a) and in-house (1b) structures of TEMPO–N_3.

REFERENCES

[1] Siu, J. C.; Sauer, G. S.; Saha, A.; Macey, R. L.; Fu, N.; Chauviré, T.; Lancaster, K. M.; Lin, S. Electrochemical Azidooxygenation of Alkenes Mediated by a TEMPO–N_3 Charge-Transfer Complex. *J. Am. Chem. Soc.* **2018**, 140 (39), 12511–12520. <DOI: 10.1021/jacs.8b06744>

[2] Schoenebeck, F.; Ess, D. H.; Jones, G. O.; Houk, K. N. Reactivity and Regioselectivity in 1,3-Dipolar Cycloadditions of Azides to Strained Alkynes and Alkenes: A Computational Study. *J. Am. Chem. Soc.* **2009**, 131, 8121–8133. <DOI: 10.1021/10.1021/ja9003624>

[3] Xie, S.; Lopez, S. A.; Ramstrom, O.; Yan, M.; Houk, K. N. 1,3–Dipolar Cycloaddition Reactivities of Perfluorinated Aryl Azides with Enamines and Strained Dipolarophiles. *J. Am. Chem. Soc.* **2015**, 137, 2958–2966. <DOI: 10.1021/ja511457g>

[4] Oz, S.; Kurtaran, R.; Arici, C.; Ergun, U.; Kaya, F. N. D.; Emregul, K. C.; Atakol, O.; Ulku, D. Two Non-Linear Azide Containing Heteronuclear Complexes: Crystal Structure and Thermal Decomposition. *J. Therm. Anal. Calorim.* **2010**, 99, 363–368. <DOI: 10.1007/s10973-009-0172-7>

[5] Seok, W. K.; Klapotke, T. M. Inorganic and Transition Metal Azides. *Bull. Korean Chem. Soc.* **2010**, 31, 781– 788. <DOI: 10.5012/bkcs.2010.31.04.781>

[6] Yonekuta, Y.; Oyaizu, K.; Nishide, H. Structural Implication of Oxoammonium Cations for Reversible Organic One-Electron Redox Reaction to Nitroxide Radicals. *Chem. Lett.* **2007**, 36, 866–867. <DOI: 10.1246/cl.2007.866>